frontiers
RESEARCH TOPICS

FRACTAL ANALYSES: STATISTICAL AND METHODOLOGICAL INNOVATIONS AND BEST PRACTICES

Topic Editors
John G. Holden, Michael A. Riley,
Jianbo Gao and Kjerstin Torre

frontiers in
PHYSIOLOGY

Cover image provided by Ibbl sarl, Lausanne CH

ISSN 1664-8714
ISBN 978-2-88919-138-3
DOI 10.3389/978-2-88919-138-3

ABOUT FRONTIERS

Frontiers is more than just an open-access publisher of scholarly articles: it is a pioneering approach to the world of academia, radically improving the way scholarly research is managed. The grand vision of Frontiers is a world where all people have an equal opportunity to seek, share and generate knowledge. Frontiers provides immediate and permanent online open access to all its publications, but this alone is not enough to realize our grand goals.

FRONTIERS JOURNAL SERIES

The Frontiers Journal Series is a multi-tier and interdisciplinary set of open-access, online journals, promising a paradigm shift from the current review, selection and dissemination processes in academic publishing.
All Frontiers journals are driven by researchers for researchers; therefore, they constitute a service to the scholarly community. At the same time, the Frontiers Journal Series operates on a revolutionary invention, the tiered publishing system, initially addressing specific communities of scholars, and gradually climbing up to broader public understanding, thus serving the interests of the lay society, too.

DEDICATION TO QUALITY

Each Frontiers article is a landmark of the highest quality, thanks to genuinely collaborative interactions between authors and review editors, who include some of the world's best academicians. Research must be certified by peers before entering a stream of knowledge that may eventually reach the public - and shape society; therefore, Frontiers only applies the most rigorous and unbiased reviews.
Frontiers revolutionizes research publishing by freely delivering the most outstanding research, evaluated with no bias from both the academic and social point of view.
By applying the most advanced information technologies, Frontiers is catapulting scholarly publishing into a new generation.

WHAT ARE FRONTIERS RESEARCH TOPICS?

Frontiers Research Topics are very popular trademarks of the Frontiers Journals Series: they are collections of at least ten articles, all centered on a particular subject. With their unique mix of varied contributions from Original Research to Review Articles, Frontiers Research Topics unify the most influential researchers, the latest key findings and historical advances in a hot research area!
Find out more on how to host your own Frontiers Research Topic or contribute to one as an author by contacting the Frontiers Editorial Office: researchtopics@frontiersin.org

FRACTAL ANALYSES: STATISTICAL AND METHODOLOGICAL INNOVATIONS AND BEST PRACTICES

Topic Editors:
John G. Holden, University of Cincinnati, USA
Michael A. Riley, University of Cincinnati, USA
Jianbo Gao, Wright State University, USA
Kjerstin Torre, Montpellier-1 University, France

Many statistical and methodological developments regarding fractal analyses have appeared in the scientific literature since the publication of the seminal texts introducing Fractal Physiology. However, the lion's share of more recent work is distributed across many outlets and disciplines, including aquatic sciences, biology, computer science, ecology, economics, geology, mathematics, medicine, neuroscience, physics, physiology, psychology, and others.

The purpose of this special topic is to solicit submissions regarding fractal and nonlinear statistical techniques from experts that span a wide range of disciplines. The articles will aggregate extensive cross-discipline expertise into comprehensive and broadly applicable resources that will support the application of fractal methods to physiology and related disciplines.

The articles will be organized with respect to a continuum defined by the characteristics of the empirical measurements a given analysis is intended to confront. At one end of the continuum are stochastic techniques directed at assessing scale invariant but stochastic data. The next step in the continuum concerns self-affine random fractals and methods directed at systems that entail scale-invariant or $1/f$ patterns or related patterns of temporal and spatial fluctuation. Analyses directed at (noisy) deterministic signals correspond to the final stage of the continuum that relates the statistical treatments of nonlinear stochastic and deterministic signals. Each section will contain introductory articles, advanced articles, and application articles so readers with any level of expertise with fractal methods will find the special topic accessible and useful.

Example stochastic methods include probability density estimation for the inverse power-law, the lognormal, and related distributions. Articles describing statistical issues and tools for discriminating different classes of distributions will be included. An example issue is distinguishing power-law distributions from exponential distributions. Modeling issues and problems regarding statistical mimicking will be addressed as well.

The random fractal section will present introductions to several one-dimensional monofractal time-series analysis. Introductory articles will be accompanied by advanced articles that will supply comprehensive treatments of all the key fractal time series methods such as dispersion analysis, detrended fluctuation analysis, power spectral density analysis, and wavelet techniques. Box counting and related techniques will be introduced and described for spatial analyses of two and three dimensional domains as well. Tutorial articles on the execution and interpretation of multifractal analyses will be solicited. There are several standard wavelet based and detrended fluctuation based methods for estimating a multifractal spectrum. We hope to include articles that contrast the different methods and compare their statistical performance as well.

The deterministic methods section will include articles that present methods of phase space reconstruction, recurrence analysis, and cross-recurrence analysis. Recurrence methods are widely applicable, but motivated by signals that contain deterministic patterns. Nonetheless recent developments such as the analysis of recurrence interval scaling relations suggest applicability to fractal systems. Several related statistical procedures will be included in this section. Examples include average mutual information statistics and false nearest neighbor analyses.

Table of Contents

frontiers in
PHYSIOLOGY

EDITORIAL
published: 08 May 2013
doi: 10.3389/fphys.2013.00097

Fractal analyses: statistical and methodological innovations and best practices

***John G. Holden*[1]**, *Michael A. Riley*[2]*, *Jianbo Gao*[3,4,5] *and Kjerstin Torre*[6]

[1] *Complexity Group, Department of Psychology, CAP center for Cognition, Action, and Perception, University of Cincinnati, Cincinnati, OH, USA*
[2] *Department of Psychology, CAP Center for Cognition, Action, and Perception, University of Cincinnati, Cincinnati, OH, USA*
[3] *PMB Intelligence LLC, West Lafayette, IN, USA*
[4] *Department of Mechanical and Materials Engineering, Wright State University, Dayton, OH, USA*
[5] *State Key Laboratory of Non-linear Mechanics, Institute of Mechanics, Chinese Academy of Sciences, Beijing, China*
[6] *Movement to Health, University Montpellier, Montpellier, France*
**Correspondence: holdenjn@ucmail.uc.edu*

Edited by:
Bruce J. West, U.S. Army Research Laboratory, USA

Reviewed by:
Bruce J. West, U.S. Army Research Laboratory, USA

Fractal statistics now routinely appear in the scientific literature. Examples originate from many disciplines, including aquatic sciences, biology, computer science, ecology, economics, geology, mathematics, medicine, neuroscience, physics, physiology, and psychology. This eBook provides a broad range of resources to support the application of fractal methods and theory in physiology and related disciplines. It is comprised of a set of research topic articles that appeared in the *Frontiers in Physiology* specialty section: Fractal Physiology. Our eBook chapters are organized along a loose continuum defined by the characteristics of the empirical measurements a given statistical technique is intended to confront.

At one end of the continuum are techniques designed for application to stochastic systems. van Rooij et al. (2013) describe histograms, probability distributions, and scaling distributions in fractal terms. The next step on the continuum concerns self-affine random fractals and methods intended for outcome measures that entail scale-invariant $1/f$ patterns or related patterns of temporal fluctuation. Stadnitski (2012) overviews several statistical procedures available for the analysis of fractal time-series measurements. Riley et al. (2012) discuss an adaptive fractal analysis that broadens the potential range of bio-signals that can be understood from a fractal perspective. Likewise, Marmelat et al. (2012) illustrate a relative roughness scale, helpful in determining the applicability of a monofractal description to a given signal. Wijnants et al. (2013) examines how of signal sampling rate artifacts influence spectrally derived scaling exponents. Hasselman (2013) discusses relationships among a set of common fractal time-series analyses, and advocates reliance on theory-driven predictions as a route to understanding the systems that yield empirical patterns. Eke et al. (2012) bridge the monofractal and multifractal frameworks with a special emphasis on the appropriate and accurate characterization of measured signals. Ihlen (2012) supplies a detailed tutorial on multifractal detrended fluctuation analysis.

The deterministic end of the statistical continuum emphasizes techniques used to investigate systems that express differentiable trajectories. Webber (2012) illustrates recurrence analysis on time-series derived from several multi-dimensional dynamic systems. Gao et al. (2012) introduces a very general analysis that is suitable for use on both stochastic and continuous measurements. Finally, Richardson et al. (2012) describe techniques that assess relative dynamic synchrony among multiple coupled oscillatory time-series. Taken together, the chapters offer a gamut of analytic strategies alongside contemporary expertise on how to best conduct and interpret the outcomes of fractal analyses.

REFERENCES

Eke, A., Herman, P., Sanganahalli, B. G., Hyder, F., Mukli, P., and Nagy, Z. (2012). Pitfalls in fractal time series analysis: fMRI BOLD as an exemplary case. *Front. Physiol.* 3:417. doi: 10.3389/fphys.2012.00417

Gao, J., Hu, J., Tung, W.-W., and Blasch, E. (2012). Multiscale analysis of biological data by scale-dependent Lyapunov exponent. *Front. Physiol.* 2:110. doi: 10.3389/fphys.2011.00110

Hasselman, F. (2013). When the blind curve is finite: dimension estimation and model inference based on empirical waveforms. *Front. Physiol.* 4:75. doi: 10.3389/fphys.2013.00075

Ihlen, E. A. (2012). Introduction to multifractal detrended fluctuation analysis in Matlab. *Front. Physiol.* 3:141. doi: 10.3389/fphys.2012.00141

Marmelat, V., Torre, K., and Delignières, D. (2012). Relative roughness: an index for testing the suitability of the monofractal model. *Front. Physiol.* 3:208. doi: 10.3389/fphys.2012.00208

Richardson, M. J., Garcia, R. L., Frank, T. D., Gergor, M., and Marsh, K. L. (2012). Measuring group synchrony: a cluster-phase method for analyzing multivariate movement time-series. *Front. Physiol.* 3:405. doi: 10.3389/fphys.2012.00405

Riley, M. A., Bonnette, S., Kuznetsov, N., Wallot, S., and Gao, J. (2012). A tutorial introduction to adaptive fractal analysis. *Front. Physiol.* 3:371. doi: 10.3389/fphys.2012.00371

Stadnitski, T. (2012). Measuring fractality. *Front. Physiol.* 3:127. doi: 10.3389/fphys.2012.00127

van Rooij, M. M. J. W., Nash, B. A., Rajaraman, S., and Holden, J. G. (2013). A fractal approach to dynamic inference and distribution analysis. *Front. Physiol.* 4:1. doi: 10.3389/fphys.2013.00001

Webber, C. L. Jr. (2012). Recurrence quantification of fractal structures. *Front. Physiol.* 3:382. doi: 10.3389/fphys.2012.00382

Wijnants, M. L., Cox, R. F. A., Hasselman, F., Bosman, A. M. T., and Van Orden, G. (2013). Does sample rate introduce an artifact in spectral analysis of continuous processes? *Front. Physiol.* 3:495. doi: 10.3389/fphys.2012.00495

Received: 17 April 2013; accepted: 20 April 2013; published online: 08 May 2013.

Citation: Holden JG, Riley MA, Gao J and Torre K (2013) Fractal analyses: statistical and methodological innovations and best practices. Front. Physiol. ***4****:97. doi: 10.3389/fphys.2013.00097*

This article was submitted to Frontiers in Fractal Physiology, a specialty of Frontiers in Physiology.

frontiers in
PHYSIOLOGY

METHODS ARTICLE
published: 29 January 2013
doi: 10.3389/fphys.2013.00001

A fractal approach to dynamic inference and distribution analysis

Marieke M. J. W. van Rooij, Bertha A. Nash, Srinivasan Rajaraman and John G. Holden*

Department of Psychology, CAP Center for Cognition, Action, and Perception, University of Cincinnati, Cincinnati, OH, USA

Edited by:
Michael A. Riley, University of Cincinnati, USA

Reviewed by:
James A. Dixon, University of Connecticut, USA
Fred Hasselman, Radboud University Nijmegen, Netherlands

****Correspondence:***
John G. Holden, Department of Psychology, CAP Center for Cognition, Action, and Perception, University of Cincinnati, PO Box 210376, Cincinnati, OH 45221-0376, USA.
e-mail: john.holden@uc.edu

Event-distributions inform scientists about the variability and dispersion of repeated measurements. This dispersion can be understood from a complex systems perspective, and quantified in terms of fractal geometry. The key premise is that a distribution's shape reveals information about the governing dynamics of the system that gave rise to the distribution. Two categories of characteristic dynamics are distinguished: additive systems governed by component-dominant dynamics and multiplicative or interdependent systems governed by interaction-dominant dynamics. A logic by which systems governed by interaction-dominant dynamics are expected to yield mixtures of lognormal and inverse power-law samples is discussed. These mixtures are described by a so-called cocktail model of response times derived from human cognitive performances. The overarching goals of this article are twofold: First, to offer readers an introduction to this theoretical perspective and second, to offer an overview of the related statistical methods.

Keywords: scaling relations, distribution analysis, dynamic systems, cognitive performance, response time distributions, fractal analysis

Many biological, physiological, and psychological phenomena display time evolving dynamics among their governing processes. Very often these dynamics are straightforwardly observable, as in the back-and-fourth limb movements that are typical of human gait. The most successful and transparent contemporary models of human gait originated in the mathematics of harmonic oscillatory systems such as the driven-pendulum (e.g., Haken et al., 1985; Kugler and Turvey, 1987). The late 15th century research on pendulum behavior was originally motivated by a need for reliable clocks (e.g., Huygens, 1673/1986). The resulting mathematical framework was subsequently adapted to the problem of biological locomotion (among other things). The new application was accommodated by the straightforward observation that, like the pendulum of a clock, both human and animal gaits exhibit relatively regular oscillatory movements (e.g., von Holst, 1939/1973). Clearly, gait's accessibility to measurement facilitated progress in this domain.

Unlike locomotor activity, however, the dynamic evolution of other biological and behavioral systems is, for various reasons, relatively opaque, or simply unobservable. For instance, time evolving dynamics likely support cognitive activity, but those dynamics are more difficult to measure. Worse yet, many stochastic processes entail statistical independence across time. In these cases, scientists may only have access to distributions of measurements that characterize either the same or categorically similar events. They can be utterly disconnected events, related by identity only, not by an obvious adjacent connection in time or space. Thus, a typical outcome measure might index event durations, frequencies, magnitudes, or similar variables. Examples include earthquake magnitudes, computer network traffic, war durations, and countless others. Nevertheless, the shapes of the event-distributions that arise in many systems are often quite lawful. Perhaps the best-known example is when they conform to a Gaussian probability density function.

This article is motivated by the insight that the shape of probability distributions of events reveals information about the dynamics that govern a system's output. The approach leverages the fact that the essential nature of the dynamics that govern many natural *stochastic* systems can be understood without specific knowledge of the components that comprise the system itself (Holden et al., 2009; Holden and Rajaraman, 2012). Inferences about dynamics follow from the statistical behavior of random variables in conjunction with contemporary narratives regarding the behavior of complex systems (Montroll and Shlesinger, 1982; West and Deering, 1995).

To be sure, the methods we describe reveal less complete dynamic information than the methods customarily used in conjunction with observable dynamics, such as phase-space reconstruction. Nevertheless, they do yield enough information to categorize systems in terms of a straightforward taxonomy that distinguishes between *component-dominant dynamics* and *interaction-dominant dynamics*. The event-distributions of component-dominant systems reflect the activity of isolable system components, their time-course, functional details, plus unsystematic additive sources of noise (e.g., Sternberg, 1969; Simon, 1973; Lewontin, 1974). By contrast, the event distributions of interaction-dominant systems reflect emergent, irreducible coordination and coupling among the processes that govern the system (e.g., Pattee, 1973; Jensen, 1998). Dynamics are determined by the category of component interactions in the sense that if a given category of system dynamics is in place then particular categories of outcome distributions are a necessary consequence.

Over the course of this article, we present several methods for analyzing and interpreting distributions of observations in terms of their implications for a measured system's dynamic properties. Our entry point is a fractal perspective on distributions that augments the traditional Euclidean geometry that underpins conventional approaches to distribution fitting and parameter estimation. We illustrate how to compute the fractal dimension of an empirical distribution, how to estimate the scaling exponent of an inverse power-law distribution, and finally discuss how to apply maximum likelihood techniques to fit a promising "cocktail" mixture model of response time distributions from cognitive performances.

FRACTAL DISTRIBUTION METHODS

The traditional approach to the characterization of distributions is framed within the context of Euclidian geometry and the standard "signal *plus* noise" theory of measurement error that was largely perfected by the mid-20th century (Stigler, 1986). It is a powerful and useful framework. Arguably, however, many natural systems live on the boundary of its assumptions, or sometimes simply fail to conform to its assumptions. The present goal is to illustrate how distribution analysis can be broadened and enhanced by the inclusion of concepts from fractal geometry. We begin by reviewing the concept of dimension, and generalize the intuitions of the standard Euclidian integer dimension to include the fractal concept of non-integer dimension.

FRACTAL DIMENSION

Regular objects, conforming to classical Euclidean geometry, can be characterized by their Euclidean dimension. A punctate observation is a zero-dimensional point; a dimensionless location on a one-dimensional line of measurement. A line is a one-dimensional object; a smooth surface has a dimension of two, and a cube three. Euclidian objects are homogeneous and uniform, breaking them into scaled-down but geometrically identical pieces, reveals their dimension.

If the sides of a cubic decimeter are measured in cubic centimeters; that is, if they are scaled down by a factor of 10, then exactly 1000 cubic centimeters will fit in the original cubic decimeter because $1000 = 10^3$. Thus the Euclidean dimension of the original cube is exactly three. In the same vein, if the sides of a squared decimeter are measured in squared centimeters, $100 = 10^2$ squared centimeters fit in the original squared decimeter, and the Euclidean dimension of the original surface is two. Finally, if a line of one decimeter length is measured in centimeters, $10 = 10^1$ centimeters fit in the original line and the Euclidean dimension is one (see **Figure 1**). This mapping even works for points, $1 = 10^0$, a point cannot be rescaled or divided, and is therefore a zero-dimensional object.

Another way to measure an object's dimension is by determining its topological dimension. Topological dimension in rooted in the idea of connectedness among points in a set. It is computed by determining the dimension of the object required to separate any part of the original set from the rest, plus one. For instance, a line has a topological dimension of one because it can be segmented by a single point that has zero dimension. In fact, regular objects such as curves, surfaces, and solids each have an integer topological dimension of 1, 2, and 3, respectively—values that equal their Euclidean dimension (Bassingthwaighte et al., 1994; Falconer, 2003). Both the Euclidean and the topological dimension take only integer values.

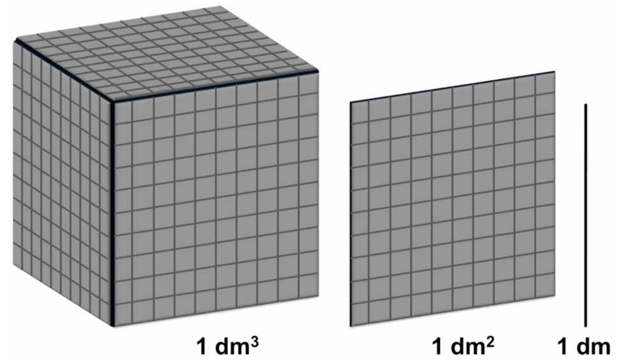

FIGURE 1 | Depicts the rescaling relationships of a cube, surface, and a line that determine a regular object's Euclidean dimension.

Euclidean geometry, while characteristic of many human artifacts, is an exception to the rule for natural objects. The geometry of most natural objects is highly irregular. Idealized fractal objects are typically comprised of nested copies of the whole object. Their dimension may fall *in between* the integer Euclidean values. The fractal dimension of an object effectively indexes the relative irregularity or space-filling properties of an object. Imagine a piece of thread held taught between two hands, the thread resembles a straight line with Euclidean (and topological) dimension of one. The thread begins to occupy space when it is weaved back and forth, as in a loom, for instance, and the tighter the weave, the more closely it approximates a two dimensional object, cloth. It can be said to "leak" into the next higher, 2nd Euclidean dimension, and thus corresponds to a non-integer *fractal dimension*.

Ours is an admittedly intuitive treatment of fractal dimension. It is a complex mathematical topic and the most formal definition of a fractal concerns a comparison of an object's topological dimension with its space filling properties, as indexed by yet another measure of dimension called the Hausdorff–Besicovitch (H–B) dimension. A set for which the H–B dimension strictly exceeds its topological dimension is a fractal (Mandelbrot, 1977). A more inclusive proposal, also put forward by Benoit Mandelbrot, is that "*a fractal is a shape that is made of parts similar to the whole in some way*" (Feder, 1988).

The take-home point is that objects can be fractal, and are characterized by a non-integer fractal dimension. These facts apply to sets of repeated observations of the self-same process. If repeated measurements of the same object or process always yield exactly the same result, then the measurement converges to a zero-dimensional point—a value commensurate with any observation's Euclidean or topological dimension. However, repeated measurements of natural systems rarely yield sets of identical outcomes. Instead, they almost inevitably vary from observation to observation.

It is this variability or uncertainty in repeated but categorically identical measurements that yields dispersion over the *x*-axis of a dependent measure in an experiment. In this way, the set of measured points begins to "fill" an interval and approximate the one-dimensional x-axis of measurement. Just as a more tightly woven piece of thread better approximates a plane, a variable collection of zero-dimensional points roughly approximates a line. Other things equal, such as sample size, a more dispersed distribution will occupy a broader interval and leak further into the domain of the line than a less variable distribution. As such, a distribution's interval-filling properties are indexed by its fractal dimension.

One way to estimate the fractal dimension of a distribution is entailed in the common *relative entropy* statistic. First, generate a histogram of the observations across a fixed interval on the x-axis of measurement. The maximum potential range of the observations should define the interval. Once the interval is divided into a convenient number of smaller intervals or bins, the observed frequency in each bin is transformed into a probability, by dividing each bin count by the total number of observations. Next the *Shannon information* (Shannon and Weaver, 1949) is computed across all bins, and divided by the maximum possible entropy—the negative base-2 log of one divided by the total number of bins B.

$$FD_{re} = \frac{-\sum p_i \log_2 p_i}{-\log_2(1/B)} \tag{1}$$

Equation 1. The fractal dimension based on the relative entropy statistic (FD_{re}) as a function of the probability p_i of finding observations in bin i, and B, the total number of bins.

Equation 1 computes the fractal dimension based on the relative entropy statistic, the probability of finding observations in each bin, and the number of bins. The relative entropy statistic measures the relative "evenness" of the distribution; a value of one indicates a uniform distribution where the probability weights evenly cover the measurement interval. Values progressively less than one indicate progressively more "clumpiness" (Seuront, 2010). It can be directly interpreted as a fractal dimension, the degree to which the collection of zero-dimensional points representing the observations leaks into the next higher first Euclidean dimension. Effectively, increases in the variability of the measurements equate with increases in the fractal dimension of the measurements. **Figure 2** displays the FD_{re} and probability densities of four probability distributions that will be discussed in this article, alongside the uniform distribution, which marks the maximum relative entropy, and FD_{re} of one.

On one hand, using relative entropy as a measure of the fractal dimension is a fairly course grained method for assessing or comparing the dispersion among distributions. Parametric variability statistics are more sensitive. On the other hand, it is largely assumption free. It is most useful for empirical distributions that are not particularly orderly. For instance, distributions that do not appear to conform to a shape that might indicate a standard probability density function could be reasonably adopted as a model. We now consider the more specialized cases where empirical distributions conform to familiar, idealized shapes of defined probability density functions. We provide an introduction to a general taxonomy of random variables that distinguishes the characteristic mode of interactions that give rise to observables. Again, the key focus is characteristic patterns of variability.

SUPERPOSITION vs. INTERDEPENDENCE

The central theme of statistical physics is that the macroscopic behavior of a system reflects the microscopic arrangements of its constituent parts (Bruce and Wallace, 1989). Characteristic system dynamics originate in the relationships among the processes that comprise a system. Our introduction briefly distinguished two broad taxonomies of characteristic system dynamics: *component-dominant dynamics* and *interaction-dominant dynamics*. They each entail distinct system transactions, superposition, and interdependence, respectively. We now explain how component-dominant dynamics arise.

The term applies to systems that are governed by the activity of largely isolable processes, themselves, their time-course, and their functional details (plus unsystematic noise). Relatively weak interactions among causal processes insure that perturbations affect components locally, unsystematically, and individually. As such, the effects of systematic perturbations can be localized to individual components—that is a consequence and a benefit of encapsulated design. Weak and additive cross-process transactions insure that the *components*, themselves, dominate system output. Systems that express component-dominant dynamics are consistent with Simon's (1973) *nearly decomposable* systems, since they entail minimal linkages across time-scales and minimal within-timescale feedback. Component-dominant dynamics represent a key prerequisite for a successful reductive analysis of a system. They are presumed in the application of standard linear Gaussian statistical techniques such as ANOVA and regression.

COMPONENT-DOMINANT DYNAMICS

The standard *Gaussian* distribution represents an archetypal outcome or end state for systems that are comprised of components whose effects dominate their time evolution. The dispersion or variability around the mean of a Gaussian distribution emerges from the combined, additive influence of innumerable weak, accidental, and mutually independent factors (Gnedenko and Khinchin, 1962; Hays, 1994). Each influence or perturbation affects the outcome, if ever so slightly. Since the factor's effects are independent and unsystematic they cancel each other's influence as often as they reinforce each other, in the long run. Thus, Gaussian distributions emerge from systems whose observables are subject to vast arrays of relatively weak, additive, and independently acting perturbations: component-dominant systems. In effect, the dynamics of superposition simply restate Laplace's Central Limit Theorem. If the assumptions of the theorem are met, then a Gaussian distribution will result. In that case, the distribution's mean is the only real piece of information imparted by the entire distribution.

The standard *exponential* distribution represents a different expression of component-dominant dynamics. Its probability density is $p(x) = (1/\lambda)e^{-x}$ where x is the axis of measurement. An exponential distribution often signifies processes that conform to stochastic "counting" or a bottlenecked queuing process. It represents a steady, reliable accrual process that is characterized by the mean (λ) of the distribution. The exponential distribution is thus

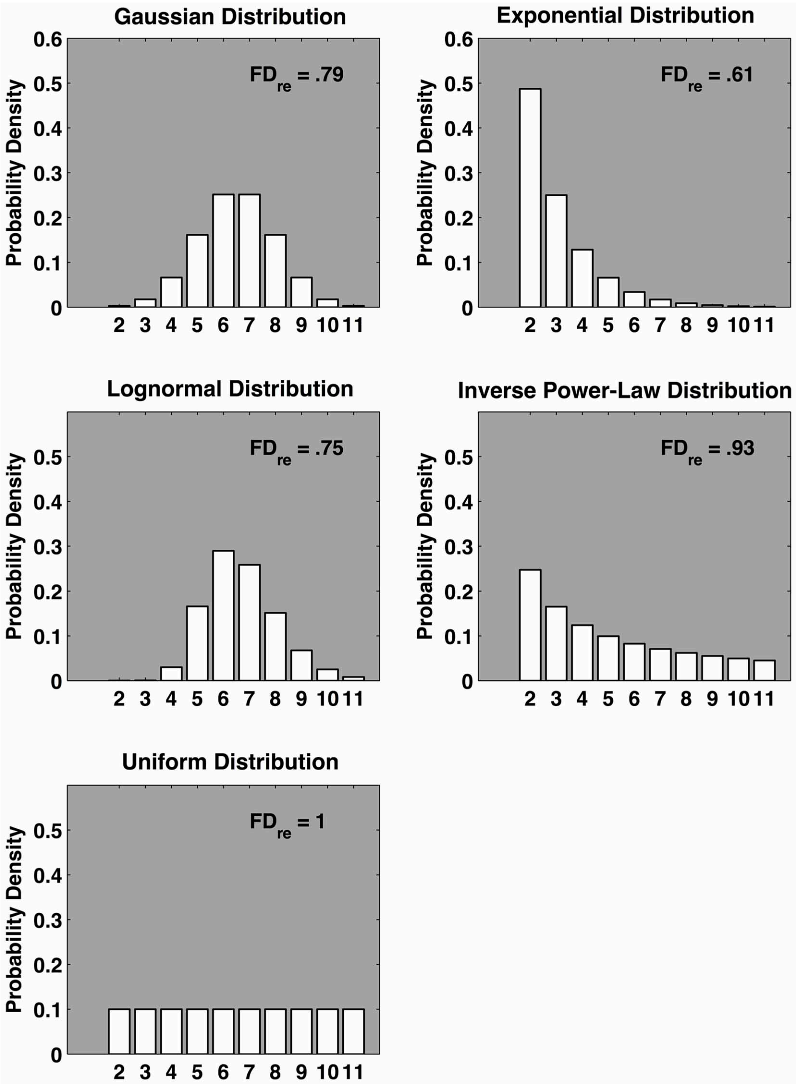

FIGURE 2 | Five model distributions with approximately equal mean and variance and the corresponding fractal dimension *FD_{re}* based on the relative entropy computed using 10 bins. The top four distributions (Gaussian, exponential, lognormal, and inverse power-law) are ordered according to two broad taxonomies of characteristic system dynamics: component-dominant dynamics and interaction-dominant dynamics (see text for details). The uniform distribution is included to define the upper boundary for FD_{re}. The fractal dimension gauges the relative variability of the respective distributions; the more evenly dispersed, the larger the FD_{re}.

a typical example of a distribution resulting from a component-dominant process; its properties are fully described by the average rate $1/\lambda$. The exponential is an expression of additive perturbation in time, as the exponential arises when events have a constant average rate per interval of time, and conform to a Poisson distribution, which, in turn, can be approximated by a Gaussian distribution. As with the Gaussian, exponential variability arises from unsystematic additive influences and its mean is the key piece of information imparted by the distribution.

If an exponential rate parameter is sufficient to characterize a process then it could, in principle, be identified and discriminated from other processes with different characteristic rate parameters or distribution functions. System outputs that conform to an exponential support a hypothesis that component processes themselves, dominate a system's transactions and observed variability. Next, we introduce an alternative case, in which the system dynamics are dominated by reciprocal, interdependent, and multiplicative transactions among processes.

INTERACTION-DOMINANT DYNAMICS

Understanding how a system's components interact takes priority over identifying the components themselves. This is because one must first determine whether the components can, in principle, be recovered before one goes looking for their signatures in event-distributions, for example (Uttal, 1990; Van Orden et al., 2003, 2005). *Interaction-dominant dynamics* are associated with systems that entail tightly coupled processes spanning a wide range of temporal or spatial scales, including fractal systems.

They refer to systems that entail multiplicative and/or interdependent feedback transactions among the processes that govern the system's dynamics. Just as component-dominant dynamics are associated with additivity, and the Gaussian distribution, interaction-dominant dynamics are also consistent with specific categories of distributions.

An *inverse power-law* distribution is a so-called *heavy-tailed* distribution; the heavy tail represents large magnitude, but rare events (Clauset et al., 2009). Thus, it expresses a salient positive skew. If the extreme right tail of an event distribution decays as a power function, then the probability of observing a particular event magnitude, $p(x)$, is the inverse of the x value itself, raised to the *scaling exponent* α (alpha) that is $p(x) \approx x^{-\alpha}$. The formal mathematical equation of the inverse power-law probability density function is $p(x) = b \cdot x^{-\alpha}$, where b is a positive constant. The scaling exponent α quantifies the rate of decay of the distribution's tail. In scientific papers, α is normally reported as a positive number, derived from the equivalence of $x^{-\alpha}$ and $1/x^{\alpha}$. It is crucial to understand that it indexes a completely different property of data than the scaling exponent α of $1/f^{\alpha}$ or *1/f* noise (e.g., Holden, 2005); the former characterizes the shape of a distribution, the latter describes long-range fractal patterns of correlation across successive observations. They are statistically independent patterns.

Inverse power-law distributions describe phenomena that range from the distribution of online music sales to earthquake magnitudes and citations of scientific publications (Anderson, 2006; Bak, 1996; Redner, 1998). Neurophysiological processes also express power law behavior. For instance, the distribution of endogenous EEG and MEG oscillations are inversely power-law distributed (Linkenkaer-Hansen et al., 2001). Similarly, fMRI measurements of human brains, under untasked conditions, reveal scale-free power-law coordination—correlated relational networks of a given average size, that span approximately three orders of magnitude in their observed frequency (Fraiman et al., 2009). Circular, interdependent feedback transactions likely govern systems that express inverse power-law scaling.

Power law behavior is symptomatic of self-organizing physical systems poised near a critical point (Bak, 1996; Jensen, 1998). One of several model systems for studying the behavior of self-organized and critical systems is a simple rice pile. Actual rice pile experiments use an apparatus that makes detailed measurements of rice grain activity, as kernels are continuously added to and exit the pile (see **Figure 3**). Initially, small, localized piles emerge within the larger pile. As the local piles grow, avalanches unfold. At a critical point, a *holistic coordinative balance* emerges throughout the system. The balance is governed by two competing sources of constraint: friction and inertia (Jensen, 1998). From that point on, the rice pile maintains a time-invariant organization, even in the face of the constant perturbation induced by the intermittent clusters of inflowing and avalanching rice. Notably, while the classic lore surrounding this phenomenon concerned *sand* piles, it is in fact long-grain rice rather than sand that entails the proper ratio between friction and inertia to express the characteristic behaviors associated with self-organized criticality (cf. Frette et al., 1996).

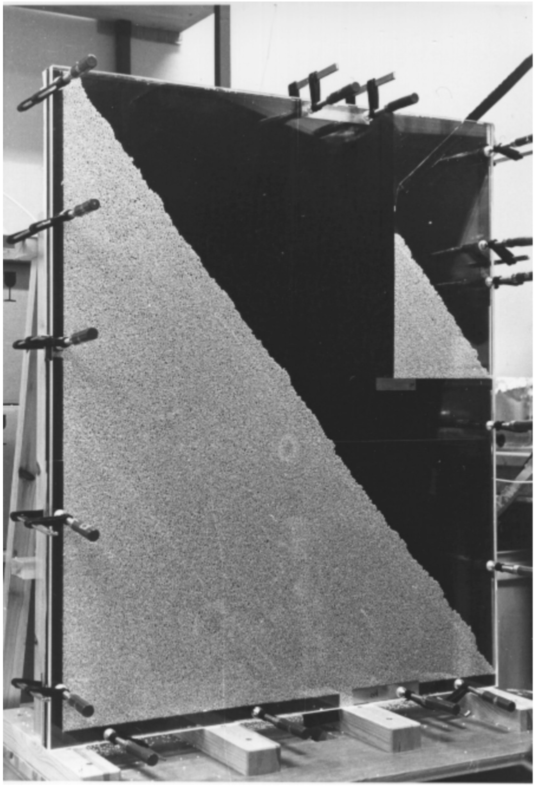

FIGURE 3 | An example experimental setup used to study the dynamics of one-dimensional rice piles. The first experimental confirmation that self-organized criticality occurs in granular systems was reported by the Cooperative Phenomena Group at the University of Oslo (Frette et al., 1996). Rice kernels were slowly fed into the pictured device. High-resolution photographs and tracer grains were used to track grain transport. As predicted, the distribution of avalanche magnitudes was consistent with an inverse power-law distribution (Image reprinted with permission from the Cooperative Phenomena Group, University of Oslo).

When a rice pile is in a critical regime the effects of perturbation are no longer proportional to the size of the perturbation—adding one new grain might result in no change, a tiny avalanche, or a large avalanche, affecting the entire pile. In the long run, small avalanches occur frequently and occasional very large avalanches unfold, all the while the pile maintains a time-invariant average height and slope. An inverse power-law distribution neatly summarizes the relationship between the avalanche magnitudes (indexed by grain counts) and their frequency of occurrence.

More generally, *scale-invariance*, as indicated by power law scaling, is characteristic of many complex systems near a critical point. Scale-invariance may be observed with respect to temporal or spatial variables (or both), but in each case similar changes unfold at all time (or length) scales of the system. Of course, power law scaling alone is not sufficient to establish criticality. For instance, mathematical fractals routinely yield scaling relations, but they are fully deterministic systems of equations. So, while they are iterative systems and exploit feedback, they are not open physical or biological systems. Formally established self-organized critical systems entail nonlinear, far-from equilibrium dynamics, with identified system control parameters that govern qualitative state changes (phase transitions) in the system's observables (order parameters, e.g., see Bruce and Wallace, 1989; Nicolis, 1989). That said, self-organization and critical behavior are generally accepted as plausible working hypotheses with the observation of non-trivial scaling in complex biological systems (e.g., Bak and Paczuski, 1995; Bak, 1996).

A striking outcome of research on critical phenomena is the concept of *universality*—while the physical details of various critical systems vary widely, their behavior near their respective critical points is highly similar. Model rice piles are *dynamic critical phenomena* and express scale invariance and time-invariant organization. *Equilibrium critical phenomena*, such as a superconducting phase transition, arise in certain conductive materials and express scale invariant coordination near the critical temperature at which electrical resistance vanishes in a superconducting phase transition. The physical details of rice piles and superconductive materials could hardly be more distinct. Nevertheless, member systems of both categories of critical phenomena exhibit universalities, such as critical exponents, characteristic fractal dimensions, and scale-free spatial and temporal correlation functions.

By way of summary, the model rice pile system only reaches a critical state when certain grain size and smoothness requirements are met. For instance, if one adds a constraint that changes the balance between inertia and friction so that one or the other term dominates the interactions, the empirical consequences of feedback are minimized, and the rice pile converges on a characteristic relaxation time. Systems in which the effects of feedback are negligible but that are still governed by multiplicative interactions exhibit *lognormal* instead of power law dispersion (Farmer, 1990; Holden and Rajaraman, 2012).

Lognormal distributions are found in various systems in chemistry, biology, ecology, and economics. In biology and ecology, multiplicative processes describe population and organism growth (Preston, 1948, 1962; Koch, 1966; May, 1981; Magurran, 1988). Proportional amplification yields accelerating growth. Thus, Nishiura (2007) discussed the lognormal distribution as a model for the incubation times of viral infections. Similarly, normally distributed economic growth rates yield a lognormal distribution of future investment values because growth operators are multiplicative.

A lognormal distribution arises from pure multiplicative interactions among independent random variables. The Central Limit Theorem established that the sum of many independent random variables yields a Gaussian distribution. A lognormal distribution becomes Gaussian after a logarithmic transform of the measured variable. Summing the logarithms of two or more numbers and then taking the antilog of the sum, yields their cumulative product. This fact offers a route to generalize the Central Limit Theorem to multiplicative interactions among independent random variables. Processes that generate a lognormal distribution directly are analogue to processes that generate a normal distribution. Just as the *sum* of many independent random variables yields a Gaussian distribution, the *product* of many independent random variables yields a lognormal distribution (Koch, 1966; Ulrich and Miller, 1993).

One may envision a loose continuum of ideal distributions spanning the general taxonomy of component-dominant and interaction-dominant dynamics (e.g., Montroll and Shlesinger, 1982; West and Deering, 1995). At one extreme, there is the Gaussian distribution, a signature of weak unsystematic additive interactions among independent, random variables. At the other extreme, there is the heavy-tailed inverse power-law, the signature distribution of interdependent feedback dynamics. The moderately skewed lognormal stands between these two extremes; it arises from multiplicative interactions among independent variables.

Admittedly, the distributions we discuss, depicted in **Figure 4**, represent a tiny subset of the full catalogue of ideal statistical distributions available to scientists. However, no matter their original form, variables conforming to the majority of common statistical distributions are attracted to the Gaussian shape in the case of unsystematic summation, the lognormal in the case of unsystematic multiplication, and the power law in the case of amplification contingent on interdependent feedback operations. Since complex systems likely entail many processes, operating across many time scales, the subset of distributions discussed here represent a plausible entry point for scientific investigation.

We illustrated how the characteristic shapes of ideal distributions supply clues about the dynamics governing a complex system. Dynamics governing a system are determined by the transactions among the processes that compose the system. The shapes of distributions of repeated measurements from a system reveal information about the nature of those transactions. Note that inferences regarding the relation between signature dynamics and a distribution's shape are not necessarily invertible. If the said

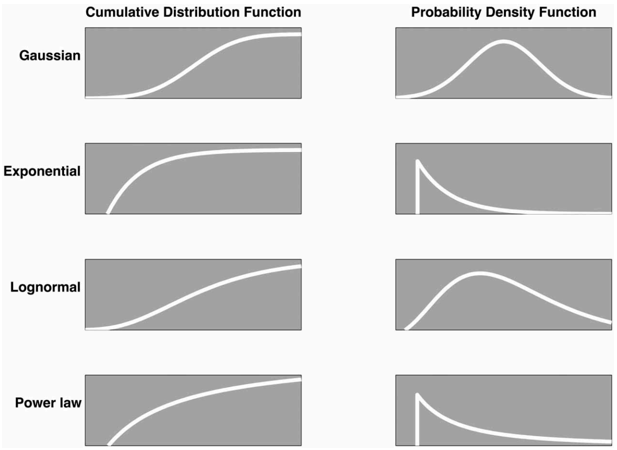

FIGURE 4 | The plots depict the cumulative distributions (left), and probability density (right) functions of four ideal distributions that signal either component-dominant or interaction-dominant dynamics. The Gaussian and exponential distributions are symptomatic of component-dominant dynamics while the lognormal and inverse power-law distributions are symptomatic of interaction-dominant dynamics. To the extent that the shapes of *empirical distributions* resemble these various ideal shapes, they likely reveal information about the governing dynamics of the system that gave rise to the distribution.

dynamics govern the interactions of the underlying processes, the various shapes are an unavoidable consequence. However, there are any number of *ad-hoc* ways to contrive the shapes of these distributions. Fortunately, few natural systems represent ad-hoc contrivances.

EXAMPLE STATISTICAL TECHNIQUES

This section intersperses example distribution analyses with a bit of practical advice for conducting and using distribution analyses, especially for response time data. We emphasize a complex systems perspective on the phenomena we discuss. We do not claim that a complexity perspective is the only legitimate perspective one could take on these topics. There are, however, many sources that one may consult for conventional narratives on these topics. Complexity theory is a relative newcomer to the physiological, behavioral, and social sciences and offers a promising new perspective on human cognition.

HISTOGRAM METHODS

This section overviews histogram-based techniques for characterizing power law distributions. The details and relative strengths of these techniques are well characterized in extant references. We strongly encourage readers to consult Newman (2005), Perline (2005), Clauset et al. (2009), and Brown and Liebovitch (2010), for more complete treatments of rank-frequency, histogram, and related methods for characterizing power laws.

The rank-frequency plot is among the earliest techniques routinely used to identify and characterize power law distributions (e.g., Zipf, 1935/1972). The relation between rank and word frequency is the method's namesake, but variables other than frequency can be depicted instead. These plots sort items in terms of their use, or popularity, a *ranking* measure, in conjunction with a measure of *magnitude*. For instance, one could rank items in a retail store in terms of best to worst sellers, and also record their price or how often each item is sold (e.g., see Anderson, 2006). **Figure 5** depicts English words with respect to how often they appear in printed text, according to the word frequency counts of Brysbaert and New (2009). The plot illustrates Zipf's Law, an inverse power-law relation between usage rank and frequency of words in written text (Zipf, 1935/1972). The plot's x-axis tracks the relative ranking of the words on a logarithmic scale and the y-axis similarly represents a logarithmic transform of frequency. When the points in a double-logarithmic rank-frequency plot lie on a straight line, the density is likely a power law (Perline, 2005; Brown and Liebovitch, 2010).

The mathematical properties of logarithms allow a bivariate linear regression analysis to be used to estimate the distribution's scaling exponent. Recall that the general form of the tail of an inverse power-law rank-frequency plot is $p(x) = bx^{-\alpha}$, where b is a positive constant and α the scaling exponent. Taking the natural logarithm of both sides of this equation yields $ln(p(x)) = ln(b) - \alpha ln(x)$. This denotes a linear relation on double logarithmic axes with slope $-\alpha$, and scaling exponent α. Thus, a scaling exponent can be roughly estimated from the slope of the distribution's heavy tail on double-logarithmic scales. A fractal dimension FD_{rf}, related but not isomorphic to FD_{re}, can be estimated as $1/\alpha$ (Mandelbrot, 1977; Seuront, 2010).

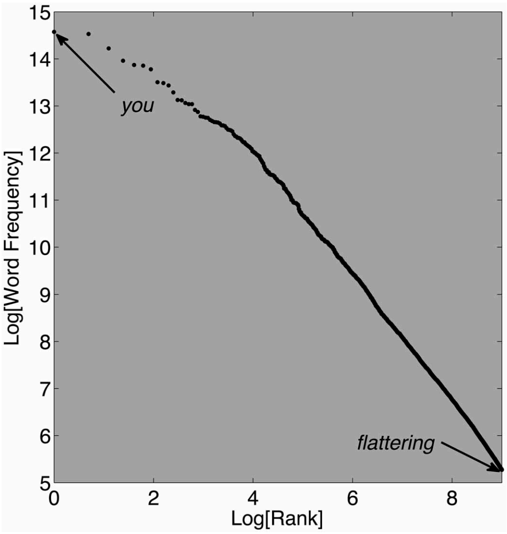

FIGURE 5 | This plot depicts the Zipf's Law relation between the frequency of occurrence of words in the SUBTLEX$_{US}$ database and the usage rank for approximately 8000 of the most common words (Brysbaert and New, 2009). The SUBTLEX$_{US}$ database is based on a total of 51 million words that were made available as part of the Elexicon project (http://elexicon.wustl.edu/). Displayed on log-log axes, the rank-frequency relation approximates a straight line, indicating a power law.

Real languages, whether sampled from specific texts, whole languages, and even translated ancient texts, express Zipf's law (Seuront, 2010). Some authors speculated the pattern is inevitable and claimed it even emerged in randomly assembled letter strings or meaningless text (Miller and Chomsky, 1963). Despite these historical claims, randomly assembled letter strings do not express Zipf's Law. In fact, careful recent simulations and statistical analyses revealed that random texts do not accurately correspond to the expected power law, but real texts do express power laws (Ferrer-i-Cancho and Elvevåg, 2010). Ferrer-i-Cancho and colleagues observed that real texts are constrained by context and meaning, not just by prior character probabilities. They conjectured that the law-like relation between usage rank and frequency results from these competing constraints. Zipf himself speculated that the pattern in language emerges as a consequence of the competing requirements to facilitate a diversity of expressions while preserving simplicity of use. In any case, Zipf's Law appears to reflect the expression of a universal principle of natural language.

Rank-frequency plots are useful tools for computing scaling exponents and estimating a fractal dimension from a distribution of measurements. However, they lack many statistical advantages offered by continuous distribution functions. For example, empty histogram bins become problematic under a logarithmic transform because the log of zero is undefined.

One way to address the empty bin issue, especially with smaller sample sizes, while maintaining the histogram approach, is to adopt logarithmically spaced histogram bins. **Figure 6** depicts the outcome of a free-recall semantic memory experiment (Nash, 2012). Participants were asked to recall as many animals as

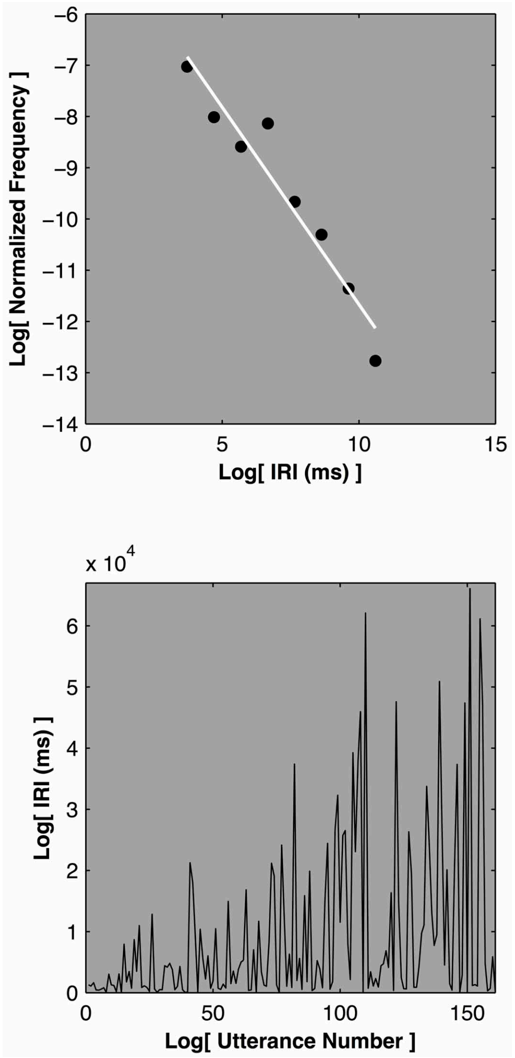

FIGURE 6 | Depicts the outcome of a free-recall semantic memory session for a single participant from Nash (2012). The upper plot displays the normalized frequency as a function of the inter-recall interval on log-log axes. The relationship is approximately linear, indicating a power law. The lower plot displays the inter-recall-intervals as a function of the utterance number, the raw data used to generate the histogram.

possible in a 20-min time span. The key dependent measure was the inter-recall-interval (IRI), the elapsed time between the participants successive recall utterances. This paradigm yields data sets that are comprised of perhaps 150–250 observations—a relatively small sample in the domain of power law distributions. Increasing the histogram bin widths logarithmically renders even these relatively small datasets open to statistical characterization (Sims et al., 2007). Measurements can then be characterized and contrasted with alternative distributions, such as an exponential. The IRI distributions are consistent with a power law description and often yield scaling exponent values between 1 and 3 (Rhodes and Turvey, 2007; Nash, 2012). As such they are commensurate with a particular subtype of power law distribution called a Lévy distribution that is implicated in animal foraging activity (Sims et al., 2012, see also Edwards et al., 2012).

PROBABILITY DENSITY METHODS

We now discuss techniques that use kernel density smoothing and maximum likelihood estimation rather than histogram binning and regression fits to characterize empirical distributions. **Textbox 1** provides the basics on the Gaussian kernel density estimator; it is a common technique and we adopt it in the examples that follow. The goal is to characterize distributions in terms of standard probability density functions. Our particular focus is on a parametric lognormal and inverse power-law mixture density function, designed to approximate pronunciation and response time distributions that arise from standard laboratory-based cognitive tasks.

As such, our example analyses focus on one particular category of measurements: human response time distributions derived from cognitive tasks. There are many types of response time tasks. Different tasks seek to uncover the functional details of various categories of perceptual and cognitive activities; examples include word recognition, reading, decision-making, perceptual categorization, and many others. Despite this variety of cognitive activity, most tasks similarly impose discrete trials, and each trial presents a single stimulus. Participants are timed as they perform each elementary cognitive act. Once they respond, often with a button press signaling a specific response, the timer stops. Thus, response time is the interval of time that elapses between the onset of a stimulus and the collection of a response in a laboratory-based cognitive task.

We focus on response time data from a mental rotation task. On each trial of the task, a single character from the set 2, 5, 7, G, J, and R was presented. The characters' rotation ranged from 0° to 180° in 60° increments. The stimuli were presented in random order, on half the trials in a normal orientation, and on the other half, mirror-reversed. Participants pressed one key if the character was presented in its normal orientation and another when mirror-reversed, as quickly and accurately as possible.

Broadly speaking, for this and related paradigms, statistical analyses reveal approximately constant increases in mean response time, as a function of both the rotation and orientation factors. This outcome was originally put forward as evidence that an analogue cognitive process literally rotates a mental representation of each character back to the normal orientation, at a constant rate, to accomplish the orientation judgment (e.g., Cooper and Shepard, 1973; Cooper, 1975; Shepard and Metzler, 1988).

Next, we present novel analyses, conducted on a subset of response time data collected as part of a Master's thesis project (Ruzicka, 2005). **Figure 9** depicts kernel smoothed response time probability densities for the normally oriented, 60° and 120° rotated characters as straight, dashes and dotted black lines, respectively. The plotted distributions represent correct individual response times, aggregated across 17 of 27 total participants. The 17 participants were selected because they each achieved overall error rates of 10% or less. The density function shapes make it clear that mean response time increases as a function of rotation. However, the density functions express complex

Textbox 1 | Characterizing empirical distributions with Gaussian kernel density estimators.

Kernel density estimation is an empirical distribution smoothing technique. The bars of a histogram are comprised of small rectangular "kernels" that each represents an individual data point. A kernel density uses the same logic, but in place of the standard rectangle, it substitutes a small probability density curve to represent each point. A Gaussian kernel is perhaps the most common kernel, but any continuous and smooth density function can be used. The value of each data point is defined as the mean of each kernel. The standard deviation around the kernel's mean is used for smoothing, it can be set arbitrarily, but is usually set automatically in reference to the variability of the data set. Large kernel standard deviations yield wide kernels and lots of smoothing; small standard deviations yield narrow kernels and very little smoothing. At each point on the *x*-axis the values resulting from the kernel function are summed. Clustered regions of data contribute to larger sums, while sparse regions contribute little to the sums across the *x*-axis. The outcome is then normalized to occupy unit area and yields a continuous and smooth empirical density function. Notably, the density function inherits the properties of the kernels, such as differentiability (see Silverman, 1986; Van Zandt, 2000, 2002). The basic steps for generating a Gaussian kernel density function are as follows:

Step 1. Let $x_1, x_2, \ldots, x_n$ be a set of data points perhaps a sample drawn from a population with unknown density *f*. The kernel density estimate, *f-hat* is given by Equation 2, where the kernel, *K*, is the function of a continuous distribution.

$$\hat{f}_h(x) = \frac{1}{nh}\sum_{i=1}^{n} K\left(\frac{x - x_i}{h}\right) \tag{2}$$

Equation 2. Kernel density estimate of a sample $x_1, x_2, \ldots, x_n$, drawn from an unknown distribution *f*.

$$K(x) = \frac{1}{\sqrt{2\pi}} e^{-\frac{1}{2}x^2} \tag{3}$$

Equation 3. The standard Gaussian probability density function.

Step 2. Equation 3 is the standard Gaussian density function, substituting this function for *K* in Equation 2 results in the *Gaussian* kernel density estimator:

$$\hat{f}_h(x) = \frac{1}{nh}\sum_{i=1}^{n} \frac{1}{\sqrt{2\pi}} e^{-\frac{1}{2}\left(\frac{x - x_i}{h}\right)^2} \tag{4}$$

Equation 4. Gaussian kernel density estimation for a sample $x_1, x_2, \ldots, x_n$, drawn from an unknown distribution *f*. In this equation, the *x* variable refers to the location on the *x*-axis of measurement, and x_i refers to an individual data point and *h* is the smoothing parameter. It is worth noting that FD_{re} can be computed from a kernel density function. In this case the *B* in Equation 1 is simply the number of points on the *x*-axis for which the kernel density was computed.

changes in shape: increasing rotation results in more variable and skewed distributions, as if they were progressively stretched. Now we introduce a distribution function that describes these response time distributions in terms of a probabilistic mixture of lognormal and power law samples.

THE COCKTAIL MODEL

The cocktail model was originally conceived as a description of individual participant's pronunciation times derived from the speeded naming task (see Holden et al., 2009; Holden and Rajaraman, 2012). Pronunciation time is the elapsed time required to begin speaking a word into a microphone, once a printed target word is presented on a computer screen in a speeded naming task. As such, pronunciation time is a subtype of response time.

Stochastic systems yield distributions of measurements and in any reasonably complex biological system innumerable immediate and historical constraints attenuate measurement variability. In a cognitive act, constraints arise from a participant's idiosyncratic personal history, their present state of body and mind, and task-imposed (environmental) constraints (Hollis et al., 2009; Van Orden et al., 2012). On any given trial in an experiment the laboratory protocol delineates task constraints, but a vast array of additional idiosyncratic constraints are also sampled. Relevant constraints serve to cohere and stabilize a given cognitive activity. Most important, if the system is governed by interaction-dominant dynamics, at minimum, probabilistically sampled constraints are expected to influence the observable multiplicatively, yielding lognormal behavior. Competing constraints or the absence of sufficient constraints may amplify variability in interdependent feedback dynamics, yielding power law behavior. The end result is likely to be a mixture of samples that indicate a continuum of relative dynamic stability.

Since lognormal patterns of variability arise from relatively homogenous multiplicative interactions, lognormal samples represent more stable interactions among the processes and constraints governing a given act. By contrast, power law distributions emerge in the context of more balanced competition among constraints, or more weakly constrained transactions among governing processes. For instance, interdependence and power law behavior is associated with highly context sensitive near-critical physical systems. The cocktail model attempts to capture this continuum as straightforward mixtures of lognormal and inverse power-law samples. Thus, for any given fit to empirical data, the lognormal and power law samples are mixed in fixed proportions, just as the various liquids in a cocktail are mixed in fixed proportions.

The shape and location of the cocktail distribution are controlled by four free parameters: a lognormal *mean* and *standard deviation* (Ω_{LN} and σ), a power law *scaling exponent* (α) and a *power law weight* parameter (ρ_{PL}), see **Table 1**. Three additional parameters refer to the relative proportions of lognormal samples in the front and back-end of the distribution (ρ_{FLN} and ρ_{BLN}), and the onset threshold of the power law (Ω_{PL}). Their values, however, are fully determined by the free parameters to insure a smooth, continuous, and legitimate density and distribution function. Some of the relationships among the cocktail model parameters are described in **Table 1**. Additional details regarding the model's parameters and its full derivation can be found in Holden and Rajaraman (2012).

There are several ways to approximate or fit a model distribution to an empirical distribution. For instance, one could compute a nonparametric Gaussian kernel estimate of the sample distribution and then use non-linear least squares to approximate the distribution's parameters. A more common approach is to use search algorithms that compute maximum likelihood estimates of the model's parameters. Van Zandt (2000; 2002) provides an accessible introduction to both the methods and the statistical properties of a number of standard response time models.

The goal of maximum likelihood estimation is to adjust a model's parameters, such as the cocktail distribution, so that the overall probabilities under the density curve are maximized. The essentials of the algorithm are straightforward. First, a guess is made for each parameter. There are numerous ways to make an initial guess, ranging from "eyeballing" the distribution to generating quantitative estimates based on special transformations of empirical statistics. Next, the probability density is computed at each point on the *x*-axis of measurement representing all observations. A point-estimate of the probability is returned for each observation. The sum of the natural logarithm of each probability is computed, yielding a summed log-likelihood value. The bigger this number, the more likely it is to observe the sample, given the model and its specific parameter settings. Computerized search algorithms are then used to iteratively explore the parameter space for even larger log-likelihood values, until an apparent maximum value is reached. The search stage of the process represents an entire statistical sub-discipline, and we do not discuss it here (see Press et al., 1992). Some search algorithms, instead of maximizing the summed log-likelihood, minimize the negative summed log-likelihood. Matlab scripts that accomplish this procedure for the cocktail model can be downloaded from: http://homepages.uc.edu/~holdenjn/.

The left column of plots in **Figure 7** display kernel density estimates of the same empirical mental rotation distributions depicted in **Figure 9**, now as solid black lines on three separate plots. Maximum likelihood fits of the cocktail mixture are depicted as white lines plotted behind the empirical density functions. The model reasonably captures the empirical distributions. All three distributions generated reliable fits (based on the 2-step bootstrapped K–S test described in **Textbox 3**). Given that the cocktail model was developed to describe the shapes of individual participant's pronunciation time distributions, its apparent success at describing response time distributions aggregated across different individuals is encouraging.

Nevertheless, an aggregation approach requires that individuals contribute relatively homogeneous distributions to the aggregate or omnibus distribution. Otherwise, one risks either successfully fitting a statistical artifact, a set of individual distributions that are not individually consistent with cocktail mixtures, but when combined appear as such. The alternative risk is unsuccessfully approximating an idiosyncratic aggregate of distributions despite the fact that individually, they can be legitimately

Table 1 | Parameters of the cocktail distribution.

Parameter	Description	Details
Ω_{LN}	The mean of the lognormal portion of the cocktail mixture distribution.	Ω_{LN} tracks the location of the lognormal portion of the cocktail distribution along the *x*-axis of measurement. It is expressed in natural-log units. (See details in **Textbox 2** on transformation to linear units).
σ	The standard deviation of the lognormal portion of the cocktail distribution.	σ describes the dispersion of the lognormal portion of the cocktail mixture distribution and is depicted on a natural-log scale (see also **Textbox 2**).
α	The scaling exponent of the inverse power-law portion of the cocktail distribution.	α characterizes the dispersion of the power law portion of the cocktail distribution. It describes the decay in the slow tail of the distribution. Plausible values of α range from 1 to about 10, values outside this range are suspect, and likely indicate a poor fit.
ρ_{PL}	The relative weight of the power law distribution in the tail of the cocktail distribution.	ρ_{PL} indicates the portion of the mixture attributed to the power law portion of the cocktail distribution. ρ_{FLN}, ρ_{BLN} together indicate the portion of the distribution attributable to the lognormal. ρ_{FLN} corresponds to the portion of the lognormal that falls to the left of Ω_{LN} and ρ_{BLN} captures the portion right of the Ω_{LN}. All together, the three portions must sum to 1, the area under the density curve.
ρ_{FLN}, ρ_{BLN}, Ω_{PL}	The relative weight proportions of the lognormal distribution in the front (FLN) and back end (BLN) of the distribution, and the onset threshold of the power law.	The values of these three parameters are constrained by the values of the four free parameters to ensure a smooth and continuous legitimate probability density function.

Textbox 2 | Transforming Ω_{LN} and σ to a linear-unit mean and standard deviation.

The lognormal mean Ω_{LN} and standard deviation σ parameters of the cocktail distribution characterize the lognormal portion of the mixture distribution. They are both defined in natural log units, however. Typically, distributions are characterized by their mean (M) and standard deviation (*SD*) in linear units, and it is useful the transform Ω_{LN} and σ values into the linear domain. Equations 5 and 6 specify the relation between the M and *SD* on linear scales and the parameters μ and σ of a lognormal distribution, as specified in the logarithmic domain. They transform the lognormal cocktail parameters into measured units, such as response time. For example, $\Omega_{LN} = 6.2$ and $\sigma = 0.15$ corresponds to a mean response time of 498 ms ($SD = 75$ ms). Note these values will differ from the empirical mean and standard deviation. Empirical statistics include all the data, and will likely be larger than the Ω_{LN}, and σ that describe only the lognormal portion of the distribution.

$$M = e^{\mu + \left(\frac{\sigma^2}{2}\right)} \tag{5}$$

$$SD = e^{\mu + \left(\frac{\sigma^2}{2}\right)} \sqrt{e^{\sigma^2} - 1} \tag{6}$$

Equations 5 and 6. The mean and standard deviation on linear scales, as a function of the logarithmic parameters μ and σ of a lognormal distribution.

described as cocktail mixtures. For instance, when the participants that generated error rates greater than 10% were included in the aggregate distribution, the cocktail model failed to fit all but the 0° condition. Quite often, there are many ways to perform a task poorly, and very few ways to perform it well. Thus, including all the participants' responses in the empirical distribution likely introduced multiple categories of performance, and the omnibus distribution became too heterogeneous to be successfully approximated by a single cocktail distribution. Similarly, neither of the two aggregate 180° distributions (normal and mirror-reversed) was successfully approximated by the cocktail model. Naturally, these potential pitfalls apply to all model distributions, not just the cocktail distribution (Estes and Maddox, 2005).

In any case, the cocktail distribution is a statistically reasonable description of the three example rotation response time distributions. Examining how the cocktail parameters tend to change across conditions offers insight into how a given manipulation affects performance dynamics. For instance, if the power law proportion increases at the expense of the lognormal proportions, then the manipulation plausibly increases the likelihood of interdependent dynamics. Conversely, if the proportion parameters controlling the power law tend to decrease, and/or the alpha parameter increases, the manipulation may stabilize cognitive dynamics.

Of course, more complex and idiosyncratic patterns of change are possible as well. Several parameters might change as a function of differences across individuals or across conditions. Effectively, the cocktail parameters fall into two broad categories: parameters that control location (Ω_{LN} and Ω_{PL}) and parameters that control variability and skew (σ, α, ρ_{FLN}, ρ_{BLN}, and ρ_{PL}). This is important to keep in mind when interpreting parameter changes. Occasionally, a fitting operation will return an extremely large power law threshold (Ω_{PL}) or scaling exponent (α). A large discrepancy between this threshold and the lognormal mean may indicate a gap in the empirical distribution, possibly resulting in a spurious local likelihood minimum. Similarly, scaling exponent values greater than 10 or so are an indication that the power law is likely superfluous to the fit. In that case, a pure lognormal or another model may be more appropriate. Excepting wishful thinking, we know of no viable rationale that identifies the model's individual parameters with specific cognitive functions or activities.

It is important to recognize that the cocktail model is descriptive, and that it relies on a reverse inference regarding the relation between dynamics and their expression in measurements. This reverse inference is common in scientific enterprises, an identical logic yields the routine conclusion that if a Gaussian is observed, the system's dynamics are additive. Given that scientists lack *a-priori* knowledge about how any given cognitive manipulation actually impacts neurophysiological dynamics, there really is no guarantee that one can make sense of observed parameter changes for the cocktail model, or other models.

RESCALING

One specific empirical pattern the cocktail model is capable of elucidating is a rescaling relation. All the location and variability parameters are defined in the logarithmic domain (an exception is the power law threshold, but one can simply compute its natural log for a rescaling test). Rescaling is indicated if location changes, in the logarithmic domain, are the only reliable differences that appear among the model's parameters in contrasts across a given set of conditions. These contrasts can be conducted with the help of bootstrap resampling techniques (Efron and Tibshirani, 1991).

Figure 8 depicts the outcome of a rescaling test completed for the normally oriented 0°, 60°, and 120° rotations. Each density function represents 300 bootstrapped (resampled) replications of the cocktail fit. The bootstrapped parameter distributions can be treated as standard errors for each corresponding parameter. Parameter distributions that overlap within each other's lower 2.5 and upper 97.5 percentiles are not likely different, distributions that are segregated beyond these thresholds are likely different. The plots for each parameter illustrate that only the lognormal mean and the power law threshold are reliably segregated. (Arguably, σ trended up slightly, as did the 120° ρ_{PL} parameter). Progressive increases that exclusively affect the location parameters are consistent with a rescaling of the distributions. The bootstrap analyses indicate that the 60° distribution is a near

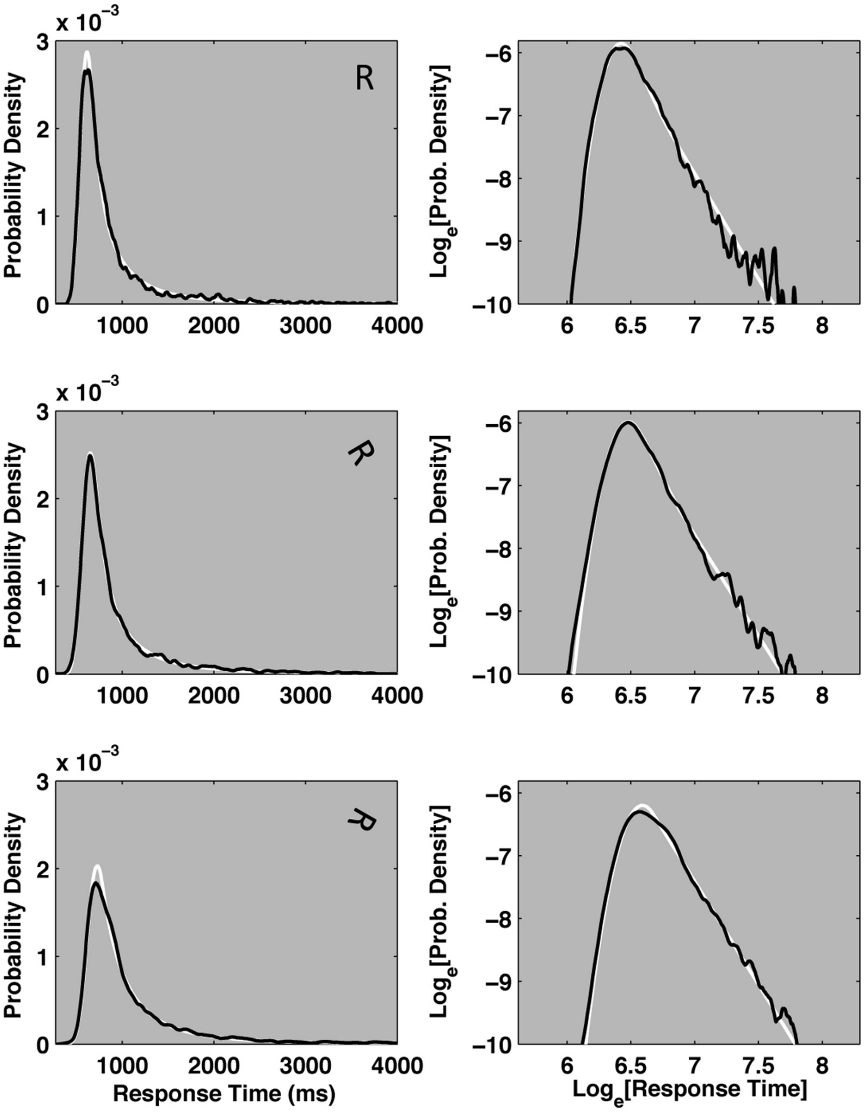

FIGURE 7 | The plots depict three example empirical response time distributions taken from a mental rotation task presented in Ruzicka (2005). Each plot depicts the probability density function of an empirical pronunciation time distribution aggregated over 17 participants. In each plot, the black line represents a kernel-smoothed empirical probability density function. Maximum likelihood fits of the Cocktail model are depicted in white, behind the empirical density functions. The three left-hand plots represent the response time distributions for normally oriented and 0°, 60°, and 120° rotated characters on linear axes. The three right-hand plots depict the same empirical and ideal cocktail distributions on double logarithmic axes, and make the power law decay of the distributions' tails more apparent. All three conditions can be reasonably approximated by the cocktail distribution.

exact rescaled copy of the baseline 0° distribution. This implies multiplying the 0° distribution by a constant will approximate the shape of the 60° distribution.

One interpretation of rescaling is that an increase in the rotation angle yields a less stable incarnation of the same basic dynamic organization that governs the orientation judgment in the normal condition. In a sense, increasing the rotation effectively weakens the constraints that enable participants to make the orientation judgment, leading to a proportional weakening in the dynamic interdependencies supporting the performance. Thus, increasing the rotation angle dilates the dynamics that support the act in a manner that resembles "zooming in" on a self-similar fractal object by requiring additional dynamic flow to disambiguate normal and mirror-reversed orientations, relative to the 0° baseline.

An accurate description of the 120° distribution required slight increases in Ω_{PL} and the proportion of power law samples, over and above a pure rescaling operation. If one assumes that discriminating orientations is more difficult when characters are increasingly rotated, then a plausible working hypothesis is that rotation progressively destabilizes this cognitive activity. Multiplicative compensation is sufficient to overcome the perturbations induced by the 60° rotation. However, less constrained interdependent power law dynamics become more

Textbox 3 | Goodness of fit.

The cocktail distribution-fitting code returns four free cocktail parameters and three additional determined parameters. However, goodness of fit must then be assessed in some manner. There are many procedures available to complete these tests. One technique is the so-called Kolmogorov–Smirnov test for comparing a sample distribution with a reference probability distribution. For each point on the *x*-axis, the difference (*D*) is computed as the absolute value of the difference between the empirical and the model distribution. The *maximum* of those differences is the *D* statistic. If the best-fitting parameters were used to define the model distribution, then a Monte Carlo technique is recommended to evaluate the plausibility of the fit. Clauset et al. (2009), described one such method: First, a synthetic dataset is generated using the best-fit model parameters. Second, the synthetic dataset is itself fitted with the model, and then *D* is computed with respect to the synthetic dataset and its own best-fit parameters. The resulting *D* value is then retained. This 3-step procedure is repeated 2500 times, resulting in a distribution of 2500 *D* values. Significance (a *p*-value) is computed as the proportion of synthetic datasets with *D* larger than the *D* resulting from a contrast to the empirical dataset and its own best-fit model. If the significance value is *small* (e.g., $p < 0.1$), few synthetic datasets yielded a larger *D* than the empirical dataset, and the empirical distribution *is not* likely a member of the population described by the model. If the significance value is *large* (e.g., $p > 0.1$), many synthetic datasets yielded a larger *D* than the empirical dataset and the empirical distribution is a plausible, but not necessary candidate member of the population described by the model.

This resampling procedure is very sensitive, and one must carefully evaluate the impact of routine statistical procedures and other artifacts, such as data censoring and measurement noise, on the outcome of any goodness of fit procedure. For example, simulations that added Gaussian noise with *SD* equal to 1% (5 ms) of the average variability of a true synthetic cocktail distribution revealed that the Clauset et al. (2009) 3-step Monte Carlo method ruled out the cocktail as a plausible model 66% of the time. By contrast, a 2-step version of the procedure, that omitted a best-fit of the synthetic data (step 2), ruled out the cocktail model as plausible 20% of the time with the addition of 5% (32 ms) Gaussian noise. Cognitive activity is known to entail intrinsic and extrinsic sources of noise (Diependaele et al., 2012). On the other hand, the 2-step procedure is recognized as biased in favor of a fitted model, relative to the Clauset et al. 3-step approach. One potential safeguard is to focus on relative goodness of fit judgments, by using identical techniques on a few candidate models. Then each model is subject to the same procedures. Statistical mimicking and over-fitting are long recognized issues in the modeling literature and, so far, no one-size-fits-all solution has emerged. Nevertheless, this issue can be ameliorated somewhat by focusing on candidate models that are motivated theoretically and corroborated by independent sources of evidence (Van Zandt and Ratcliff, 1995).

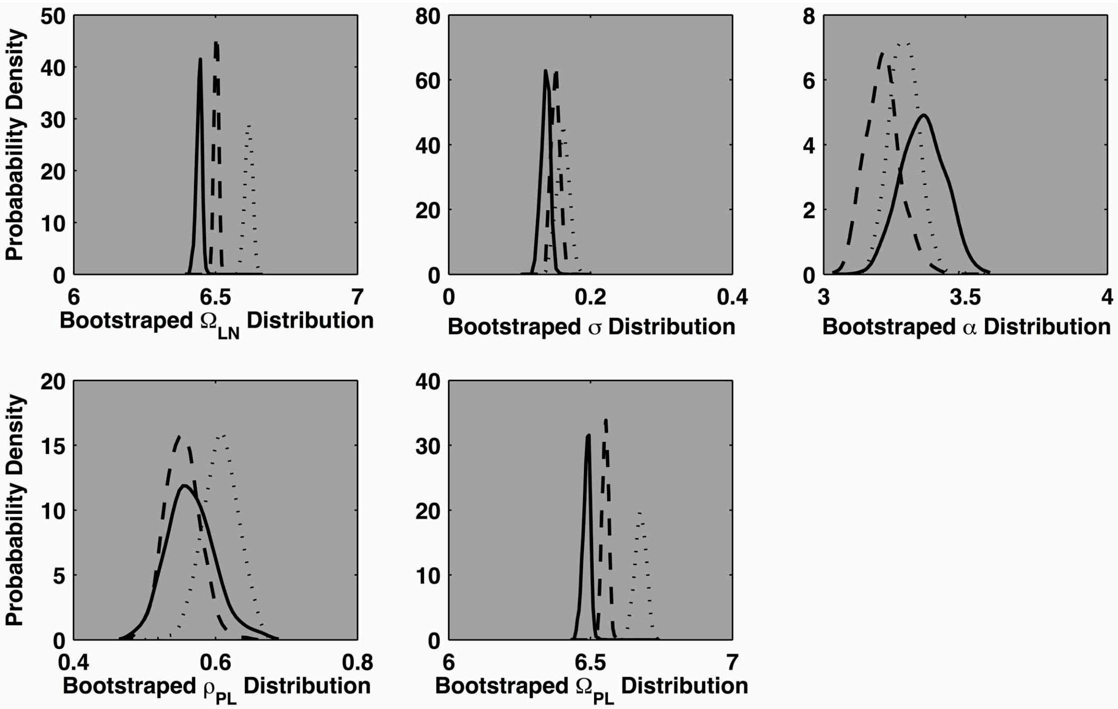

FIGURE 8 | Each plot depicts the bootstrapped distribution for each of five parameters of the cocktail model. The outcomes for the 0°, 60°, and 120° conditions are depicted as solid, dashed, and dotted lines, respectively. The bootstrapping procedure randomly resamples the empirical response time distributions 300 times, with replacement. The model is fit to each resampled data set and the resulting distribution of parameter values for each of the three mental rotation conditions are depicted in plots. Identical analyses of the mirror-reversed conditions indicated the 120° distribution as a rescaled version of the 0° and 60° distribution which, themselves were nearly identical.

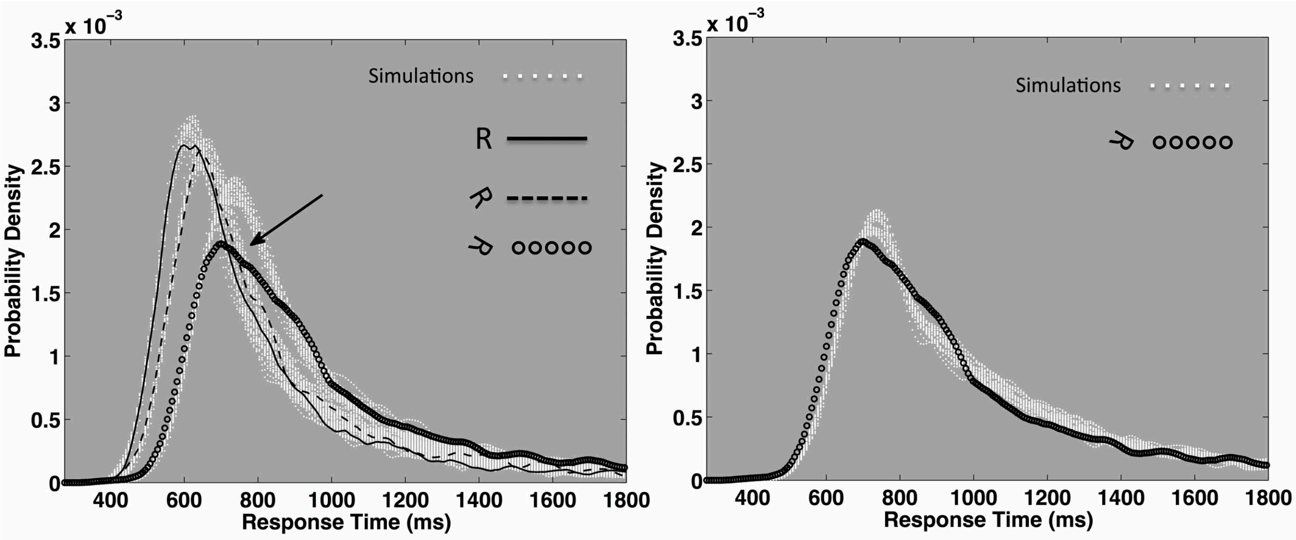

FIGURE 9 | The left-hand plot depicts the outcome of three rescaling simulations. Synthetic cocktail response times were generated based on the fitted parameters for the baseline 0° condition (solid black line). Kernel smoothed densities for 22 replications of the synthetic distribution are depicted as white points, plotted behind the empirical 0° density. Rescaled synthetic 60° distributions were generated by first computing the natural logarithm for each synthetic baseline 0° distribution, after which, a constant of 0.061 was added to each value. Likewise a constant of 0.173 was added to duplicate the baseline synthetic data and mimic the 120° distribution. These two values represent the difference between the 0° Ω_{LN} parameter and the same parameter for the 60° and 120° distributions (see **Table 2**). The antilog of each synthetic distribution was then computed, thus yielding a rescaled model for both the empirical 60° and 120° distributions. The rescaled synthetic 60° and 120° distributions are both plotted as white points behind the empirical distributions (dashed line, and open circles, respectively). In this case, the pure multiplicative operation properly located the synthetic distributions, but the synthetic 120° distribution was more peaked at the mode than the empirical distribution (see arrow). Additional simulations revealed that a larger Ω_{PL} and proportion of power law samples, in addition to the multiplicative operation, were required to approximate the empirical 120° distribution, as depicted in the right-hand plot.

Table 2 | Cocktail parameters corresponding to the three example empirical response time distributions taken from a letter rotation task in Figure 7.

	Ω_{LN}	σ	α	ρ_{PL}	Ω_{PL}	*p*-value
Normal Rotation	6.44	0.14	3.35	0.56	657	0.27
60 Degrees	6.50	0.15	3.21	0.55	702	0.39
120 Degrees	6.62	0.16	3.29	0.61	793	0.24

The lognormal location parameter, (Ω_{LN}) was used to capture the bulk of the observed shape changes across the three conditions, in a rescaling test. Goodness of fit was computed using the 2-step bootstrap procedure described in ***Textbox 3****.*

likely with increased character rotation. Apparently, in this case, cognitive dynamics unfold near a point of qualitative change.

The dynamic patterns observed in these conditions unfold in a manner that is reminiscent of near-critical systems that are approaching critical points. As such, we speculate that rescaling may represent a minimum boundary of change as task difficulty, broadly construed, increases in the face of a relatively skilled performance. At some point the manipulation overwhelms the key constraints supporting the performance, and a cognitive system must either make do with ambiguous, unreliable, or strongly competing constraints, or perhaps it must reorganize and entrain with alternative reliable sources of constraint. Clearly additional research on this topic is needed, and we continue to pursue these issues in our laboratory.

CONCLUSION

In a sense, this article has now come full circle. It began with an overview of the fractal geometry. The crux concept of a fractal is the notion of nesting and self-similarity—fractal objects are said to be composed of rescaled copies of the whole object. We now see that, at least for the narrowly circumscribed mental rotation data, the response time distributions can be plausibly described as rescaled copies of each other. Not all cognitive effects can be expected to fit into such a neat package. One more typically observes changes in shape representing variability increases that are larger and well beyond the limits circumscribed by a rescaling hypothesis.

Ideal mathematical fractals are typically generated through iteration—the repeated application of the same rule. This is an example of a single process that extends across multiple scales.

Additional paths to scaling are available to physical and biological systems. Short-range interactions facilitate the emergence of multi-scale entrainment among rice grains in a rice pile and in so-called dynamic critical systems (e.g., Bruce and Wallace, 1989; Bak, 1996; Jensen, 1998). Model self-organizing physical systems, such as rice piles, tend to be comprised of many relatively simple homogenous elements. By contrast, complex organisms, such as human beings, entail heterogeneous physiochemical and neurophysiological processes and constraints that span a range of temporal and spatial scales. Nevertheless, these processes must somehow coordinate to support and sustain an organism across space and time. As we explained, the fractal scaling expressed in event distributions derived from biological systems, and related empirical patterns, are likely symptomatic of the dynamics governing this multiscale coordinative activity (Bassingthwaighte et al., 1994; Turvey, 2007; Holden and Rajaraman, 2012).

ACKNOWLEDGMENTS

We acknowledge financial support from the National Science Foundation Grants BCS-0446813 and BCS-0843133 to John G. Holden and BCS-0642718 to John G. Holden and Guy van Orden.

REFERENCES

Anderson, C. (2006). *The Long Tail: Why the Future of Business is Selling Less of More.* New York, NY: Hyperion.

Bak, P. (1996). *How Nature Works.* New York, NY: Springer-Verlag.

Bak, P., and Paczuski, M. (1995). Complexity, contingency, and criticality. *Proc. Natl. Acad. Sci. U.S.A.* 92, 6689–6696.

Bassingthwaighte, J. B., Liebovitch, L. S., and West, B. J. (1994). *Fractal Physiology.* New York, NY: Oxford University Press.

Brown, C. T., and Liebovitch, L. S. (2010). *Fractal Analysis.* Thousand Oaks, CA: Sage.

Bruce, A. D., and Wallace, D. J. (1989). "Critical point phenomena: universal physics at large length scales," in *The New Physics,* ed P. Davies (Cambridge, MA: Cambridge University Press), 236–267.

Brysbaert, M., and New, B. (2009). Moving beyond Kučera and Francis: a critical evaluation of current word frequency norms and the introduction of a new and improved word frequency measure for American English. *Behav. Res. Methods* 41, 977–990.

Clauset, A., Shalizi, C. R., and Newman, M. E. J. (2009). Power-law distributions in empirical data. *SIAM Rev.* 51, 661–703.

Cooper, L. A. (1975). Mental rotation of random two-dimensional shapes. *Cogn. Psychol.* 7, 20–43.

Cooper, L. A., and Shepard, R. N. (1973). The time required to prepare for a rotated stimulus. *Mem. Cogn.* 1, 246–250.

Diependaele, K., Brysbaert, M., and Neri, P. (2012). How noisy is lexical decision? *Front. Psycho.* 3:348. doi: 10.3389/fpsyg.2012.00348

Edwards, A. M., Freeman, M. P., Breed, G. A., and Jonson, I. D. (2012). Incorrect likelihood methods were used to infer scaling laws of marine predator search behavior. *PLoS ONE* 7:e45174. doi: 10.1371/journal.pone.0045174

Efron, B., and Tibshirani, R. (1991). Statistical data analysis in the computer age. *Science* 253, 390–395.

Estes, W. K., and Maddox, W. T. (2005). Risks of drawing inferences about cognitive processes from model fits to individual versus average performance. *Psychon. Bull. Rev.* 12, 403–408.

Falconer, K. J. (2003). *Fractal Geometry: Mathematical Foundations and Applications, 2nd Edn.* New York, NY: Wiley.

Farmer, J. D. (1990). A Rosetta stone for connectionism. *Physica D: Nonlinear Phenomena.* 42, 153–187.

Feder, J. (1988). *Fractals.* New York, NY: Plenum Press.

Ferrer-i-Cancho, R., and Elvevåg, B. (2010). Random texts do not exhibit the real Zipf's law-like rank distribution. *PLoS ONE* 5:e9411. doi: 10.1371/journal.pone.0009411

Fraiman, D., Balenzuela, P., Foss, J., and Chialvo, D. R. (2009). Ising-like dynamics in large-scale functional brain networks. *Phys. Rev. E Stat. Nonlin. Soft. Matter Phys.* 79:061922. doi: 10.1103/PhysRevE.79.061922

Frette, V., Christensen, K., Malthe-Sorenssen, A., Feder, J., Jossang, T., and Meakin, P. (1996). Avalanche dynamics in a pile of rice. *Nature* 379, 49–52.

Gnedenko, R. V., and Khinchin, A. Ya. (1962). *An Elementary Introduction to the Theory of Probability,* Trans. L. Boron, New York, NY: Dover.

Haken, H., Kelso, J. A. S., and Bunz, H. (1985). A theoretical model of phase transitions in human hand movements. *Biol. Cybern.* 51, 347–356.

Hays, W. L. (1994). *Statistics.* 5th Edn. Fort Worth, TX: Harcourt Brace College Publisher.

Holden, J. G. (2005). "Gauging the fractal dimension of response times from cognitive tasks," in *Contemporary Nonlinear Methods for Behavioral Scientists: A Webbook Tutorial*, eds M. A. Riley and G. C. Van Orden, 267–318. Available online at: http://www.nsf.gov/sbe/bcs/pac/nmbs/nmbs.jsp

Holden, J. G., and Rajaraman, S. (2012). The self-organization of a spoken word. *Front. Psychol.* 3:209. doi: 10.3389/fpsyg.2012.00209

Holden, J. G., Van Orden, G. C., and Turvey, M. T. (2009). Dispersion of response times reveals cognitive dynamics. *Psychol. Rev.* 116, 318–342.

Hollis, J., Kloos, H., and Van Orden, G. C. (2009). "Origins of order in cognitive activity," in *Chaos and Complexity in Psychology: The Theory of Nonlinear Dynamical Systems,* eds S. J. Guastello, M. Koopmans, and D. Pincus (Cambridge, MA: Cambridge University Press), 206–241.

Huygens, C. (1986). *The Pendulum Clock or Geometrical Demonstrations Concerning the Motion of Pendula as Applied to Clocks,* Trans. R. J. Blackwell, Ames, IA: Iowa State University Press. (Original work published 1673).

Jensen, H. J. (1998). *Self-Organized Criticality.* Cambridge, MA: Cambridge University Press.

Koch, A. L. (1966). The logarithm in biology. I. Mechanisms generating the log-normal distribution exactly. *J. Theor. Biol.* 23, 276–290.

Kugler, P. N., and Turvey, M. T. (1987). *Information, Natural Law and the Self-Assembly of Rhythmic Movement.* Hillsdale, NJ: Erlbaum.

Lewontin, R. C. (1974). The analysis of variance and the analysis of causes. *Am. J. Hum. Genet.* 26, 400–411.

Linkenkaer-Hansen, K., Nikouline, V. V., Palva, J. M., and Ilmoniemi, R. J. (2001). Long-range temporal correlations and scaling behavior in human brain oscillations. *J. Neurosci.* 21, 1370–1377.

Magurran, A. E. (1988). *Ecological Diversity and its Measurement.* London: Croom Helm.

Mandelbrot, B. B. (1977). *The Fractal Geometry of Nature.* San Francisco, CA: W.H. Freeman.

May, R. M. (1981). "Patterns in multi-species communities," in *Theoretical Ecology: Principles and Applications,* ed R. M. May (Oxford: Blackwell), 197–227

Miller, G. A., and Chomsky, N. (1963). "Finitary models of language users," in *Handbook of Mathematical Psychology, Vol. 2.* eds R. D. Luce, R. Bush, and E. Galanter (New York, NY: Wiley), 419–491

Montroll, E. W., and Shlesinger, M. F. (1982). On 1/f noise and other distributions with long tails. *Proc. Natl. Acad. Sci. U.S.A.* 79, 3380–3383.

Nash, B. A. (2012). *Environmental Constraints on Human Memory.* Unpublished Master's thesis, University of Cincinnati, Ohio.

Newman, M. E. J. (2005). Power laws, pareto distributions and Zipf's law. *Contemp. Phys.* 46, 323–351.

Nicolis, G. (1989). "Physics of far-from-equilibrium systems and self-organisation." in *The New Physics*, ed P. Davies, (Cambridge, MA: Cambridge University Press), 316–347.

Nishiura, H. (2007). Early efforts in modeling incubation period of infectious diseases with an acute course of illness. *Emerg. Themes Epidemiol.* 4:2 doi:10.1186/1742-7622-4-2

Pattee, H. H. (ed.). (1973). *Hierarchy Theory: The Challenge of Complex Systems.* New York, NY: George Braziller, Inc.

Perline, R. (2005). Strong, weak and false inverse power Laws. *Stat. Sci.* 20, 68–88.

Press, W. H., Flannery, B. P., Teukolsky, S. A., and Vetterling, W. T. (1992). *Numerical Recipes in C: The Art of Scientific Computing. 2nd Edn,* Cambridge, MA: Cambridge University Press.

Preston, F. W. (1948). The commonness, and rarity of species. *Ecology* 29, 254–283.

Preston, F. W. (1962). The canonical distribution of commonness and Rarity. *Ecology* 43, 185–215.

Redner, S. (1998). How popular is your paper? An empirical study of the citation distribution. *Eur. Phys. J.* 4, 131–134.

Rhodes, T., and Turvey, M. T. (2007). Human memory retrieval as lévy foraging. *Phys. A Stat. Mech. Appl.* 385, 255–260.

Ruzicka, A. L. (2005). *Performance Limitations in Cogntive Workload: Does Task Difficulty Impact Response time Variability?* Unpublished Master's thesis, California state university, Northridge.

Seuront, L. (2010). *Fractals and Multifractals in Ecology and Aquatic Science.* Boca Raton, FL: CRC Press.

Shannon, C. E., and Weaver, W. (1949). *The Mathematical Theory of Communication.* Urbana, IL: University of Illinois Press.

Shepard, S., and Metzler, D. (1988). Mental rotation: Effects of dimensionality of objects and type of task. *J. Exp. Psychol. Hum. Percept. Perform.* 14, 3–11.

Silverman, B. W. (1986). *Estimation for Statistics and Data Analysis.* New York, NY: Chapman and Hall.

Simon, H. A. (1973). "The organization of complex systems," in *Hierarchy Theory: The Challenge of Complex Systems,* ed H. H. Pattee (New York, NY: George Braziller, Inc), 1–27.

Sims, D. W., Humphries, N. E., Bradford, R. W., and Bruce, B. D. (2012). Lévy flight and Brownian search patterns of a free-ranging predator reflect different prey field characteristics. *J. Anim. Ecol.* 81, 432–442.

Sims, D. W., Righton, D., and Pitchford, J. W. (2007). Minimizing errors in identifying Lévy flight behavior of organisms. *J. Anim. Ecol.* 76, 222–229.

Sternberg, S. (1969). The discovery of processing stages: extensions of Donders' method. *Acta Psychol.* 30, 276–315.

Stigler, S. M. (1986). *The History of Statistics: The Measurement of Uncertainty Before 1900.* Cambridge, MA: Harvard University Press.

Ulrich, R., and Miller, J. (1993). Information processing models generating lognormally distributed reaction times. *J. Math. Psychol.* 37, 513–525.

Turvey, M. T. (2007). Action and perception at the level of synergies. *Hum. Mov. Sci.* 26, 657–697.

Uttal, W. R. (1990). On some two-way barriers between models and mechanisms. *Percept. Psychophys.* 48, 188–203.

Van Orden, G., Hollis, G., and Wallot, S. (2012). The blue collar brain. *Front. Physiol.* 3:207. doi: 10.3389/fphys.2012.00207

Van Orden, G. C., Holden, J. G., and Turvey, M. T. (2003). Self-organization of cognitive performance. *J. Exp. Psychol. Gen.* 132, 331–350.

Van Orden, G. C., Holden, J. G., and Turvey, M. T. (2005). Human cognition and 1/f scaling. *J. Exp. Psychol. Gen.* 134, 117–123.

Van Zandt, T. (2000). How to fit a response time distribution. *Psychon. Bull. Rev.* 7, 424–465.

Van Zandt, T. (2002). "Analysis of response time distributions," in *Stevens' Handbook of Experimental Psychology, 3rd Edn. Vol 4: Methodology in Experimental Psychology*, (Vol. ed.) J. T. Wixted and (Series ed.) H. Pashler (New York, NY: Wiley Press), 461–516.

Van Zandt, T., and Ratcliff, R. (1995). Statistical mimicking of reaction time data: single process models, parameter variability, and mixtures. *Psychon. Bull. Rev.* 2, 20–54.

von Holst, E. (1973). "Relative coordination as a phenomenon and as a method of analysis of central nervous system function," in *The Collected Papers of Erich von Holst: Vol. 1. The Behavioral Physiology of Animal and Man,* (Ed and Trans) R. Martin (Coral Gables, FL: University of Miami Press), 33–135. (Original work published 1939).

West, B. J., and Deering, B. (1995). *The Lure of Modern science: Fractal Thinking.* River Edge, NJ: World Scientific.

Zipf, G. K. (1972). *Human Behaviour and the Principle of Least Effort. An Introduction to Human Ecology.* 1st Edn. New York, NY: Hafner reprint. Cambridge, MA: Addison-Wesley, 1949.

Conflict of Interest Statement: The authors declare that the research was conducted in the absence of any commercial or financial relationships that could be construed as a potential conflict of interest.

Received: 29 June 2012; accepted: 01 January 2013; published online: 29 January 2013.

Citation: van Rooij MMJW, Nash BA, Rajaraman S and Holden JG (2013) A fractal approach to dynamic inference and distribution analysis. Front. Physio. ***4****:1. doi: 10.3389/fphys.2013.00001*

This article was submitted to Frontiers in Fractal Physiology, a specialty of Frontiers in Physiology.

frontiers in
PHYSIOLOGY

METHODS ARTICLE
published: 07 May 2012
doi: 10.3389/fphys.2012.00127

Measuring fractality

Tatjana Stadnitski *

Psychological Methods, Institute of Psychology and Education, University of Ulm, Ulm, Germany

Edited by:
Kjerstin Torre, Montpellier-1 University, France

Reviewed by:
Didier Delignieres, University Montpellier 1, France
Nick Stergiou, University of Nebraska at Omahah, USA

Correspondence:
Tatjana Stadnitski, Psychological Methods, Institute of Psychology and Education, University of Ulm, 89069 Ulm, Germany.
e-mail: tatjana.stadnitski@uni-ulm.de

When investigating fractal phenomena, the following questions are fundamental for the applied researcher: (1) What are essential statistical properties of 1/*f* noise? (2) Which estimators are available for measuring fractality? (3) Which measurement instruments are appropriate and how are they applied? The purpose of this article is to give clear and comprehensible answers to these questions. First, theoretical characteristics of a fractal pattern (self-similarity, long memory, power law) and the related fractal parameters (the Hurst coefficient, the scaling exponent α, the fractional differencing parameter *d* of the autoregressive fractionally integrated moving average methodology, the power exponent β of the spectral analysis) are discussed. Then, estimators of fractal parameters from different software packages commonly used by applied researchers (R, SAS, SPSS) are introduced and evaluated. Advantages, disadvantages, and constrains of the popular estimators ($\hat{d}_{\mathrm{ML}}$, power spectral density, detrended fluctuation analysis, signal summation conversion) are illustrated by elaborate examples. Finally, crucial steps of fractal analysis (plotting time series data, autocorrelation, and spectral functions; performing stationarity tests; choosing an adequate estimator; estimating fractal parameters; distinguishing fractal processes from short-memory patterns) are demonstrated with empirical time series.

Keywords: fractal, 1/*f* noise, ARFIMA, long memory

MEASURING FRACTALITY

Fractal patterns have been observed in numerous scientific areas including biology, physiology, and psychology. A specific structure known as *pink* or 1/*f noise* represents the most prominent fractal phenomenon. Because it is intermediate between white noise and red or Brown noise, it exhibits both stability and adaptability, thus properties typical for healthy complex systems (Bak et al., 1987). Consequently, pink noise serves as an adequate model for many biological systems and psychological states. For instance, pink noise was found in human gait (Hausdorf et al., 1999), rhythmic movements like tapping (Chen et al., 1997, 2001; Ding et al., 2002; Delignières et al., 2004; Torre and Wagenmakers, 2009), visual perception (Aks and Sprott, 2003), brain activity (Linkenkaer-Hansen, 2002), heart rate fluctuations, and DNA sequences (Hausdorf and Peng, 1996; Eke et al., 2002; Norris et al., 2006). Hence, one of the main objectives for measuring fractality is to distinguish reliably between fractal (healthy) and non-fractal (unhealthy) patterns for diagnostic purposes. For instance, many diseases result from dysfunctional connections between organs, which can be viewed as loss of adaptive behavior of the body as a complex system. Therefore, deviations from the 1/*f* structure can serve as indicators for disease severity.

Additionally, Gilden et al. (1995), Van Orden et al. (2003, 2005) discovered fractality in controlled cognitive performances and other mental activities. The most striking feature of the observed patterns was their long memory. Serial correlations were not necessarily large in absolute magnitude but very persistent, which is typical for 1/*f* noise. Since memory characteristics are decisive for the development of a process, an accurate measurement of fractality is indispensible for correct statistical inference concerning the properties of empirical data and precise forecasting. Therefore, further important goals of fractal analyses are to test for the effective presence of genuine long-range correlations and provide an accurate estimation of their strength.

There are different methodological approaches, and their respective statistical parameters, to capture fractality. For each parameter, numerous estimators have been developed, but there is no clear winner among them (Stroe-Kunold et al., 2009; Stadnytska et al., 2010; Stadnitski, 2012). Furthermore, statistical characteristics of some non-fractal empirical structures can resemble those of 1/*f* noise, which may cause erroneous classifications (Wagenmakers et al., 2004; Thornton and Gilden, 2005). Therefore, proper measurement of fractality and reliable discrimination of pink noise from other fractal or non-fractal patterns represent crucial challenges for applied researchers. The main purposes of this paper are to introduce appropriate measurement strategies to practitioners and to show how to use them in applied settings. The article intends to outline the basics of fractal analysis by providing insight into its concepts and algorithms. Detailed descriptions of the methods are beyond the scope of this paper and can be found in Beran (1994), Brockwell and Davis (2002), Delignières et al. (2006), Eke et al. (2002), Jensen (1998), and Warner (1998).

THEORETICAL CHARACTERISTICS OF FRACTAL PATTERNS

What are essential attributes of 1/*f* noise? The answer is *long memory* and *self-similarity*. Fractals are self-similar structures where the whole has the same shape as its parts (e.g., broccoli or the Koch snowflake). Hence, characteristics of a 1/*f* noise process remain similar when viewed at different scales of time or space. This implies the following statistical properties: (1) a hyperbolically (i.e., very slow) decaying autocorrelation function (ACF) and (2) a specific relation between frequency (f) and size of process variation (S): $S(f) \propto 1/f$. This so-called *power low* means that the power (variance or amplitude) of the $1/f$ noise process is inversely proportional to the frequency.

The ACF describes the correlation of a signal with itself at different lags. In other words, it reflects the similarity between observations in reference to the amount of time between them. Hyperbolically decaying autocorrelations imply statistical dependence between observations separated by a large number of time units or a long memory of the process. In contrast, if a process has a short-memory and can be predicted by its immediate past, the autocorrelations decay quickly (e.g., exponentially) as the number of intervening observations increases. *White noise* is a sequence of time-ordered uncorrelated random variables, sometimes called random shocks or innovations, and therefore has no memory. *Brown noise* or a *random walk* evolves from integrating white noise, and thus can also be represented as the sum of random shocks. As a result, the impact of a particular innovation does not dissipate and a random walk remembers the shock forever, which implies an infinite memory and no decay in ACF. The upper section of **Figure 1** compares the ACF of processes with different memory characteristics.

Granger and Joyeux (1980) and Hosking (1981, 1984) demonstrated that hyperbolically decaying autocorrelations of pink noise can be parsimoniously modeled by means of the differencing parameter d of the Box–Jenkins autoregressive integrated moving average (ARIMA) methodology, allowing it to take on continuous values (Box and Jenkins, 1970). The ARIMA method describes processes through the three parameters p, d, and q. For example, the following process

$$Y_t = \phi_1 Y_{t-1} + u_t + \theta_1 u_{t-1}, \quad u_t \sim \mathrm{IIDN}\left(0, \sigma^2\right).$$

is called ARMA (1, 1) because it contains one autoregressive (Y_{t-1}) and one moving average term (u_{t-1}). Therefore, the value of the autoregressive parameter p reflects how many preceding observations influence the current observation. The value of the moving average term q describes how many previous random shocks must be taken into account when describing the dependency present in the time series. ϕ is the autoregressive prediction weight and θ is the proportion of the previous random component that still affects the observation at a time T. Within the Box–Jenkins ARIMA framework, d is whole number and refers to the order of differencing that is necessary to make a process *stationary* ($d = 0$). Statistical characteristics of a stationary process do not change over time or position, i.e., mean, variance, and autocorrelation remain stable. Thus the ARMA (1, 1) process can also be written as ARIMA (1, 0, 1). White noise is ARIMA (0, 0, 0). Models with $d = 1$ correspond to a process with an *infinite* persistence of random shocks and are called integrated of order 1. Brown noise is ARIMA (0, 1, 0). Autoregressive fractionally integrated moving average (ARFIMA) modeling extends the traditional Box–Jenkins approach by allowing the differencing parameter d to take on non-integer values. This enables ARFIMA-models to give parsimonious descriptions of any long-range dependencies in time series. Pink noise has d of 0.5. Stationary fractal processes with finite long memory can be modeled with $0 < d < 0.5$. For $0.5 \leq d \leq 1$, the process is non-stationary. Consult Beran (1994) and Brockwell and Davis (2002) for more background on long memory and ARFIMA modeling.

The so-called *power spectrum* determines how much power (i.e., variance or amplitude) is accounted for by each frequency in the series. The term frequency describes how rapidly things repeat themselves. Thus, there exist fast and slow frequencies. For instance, a time series with $T = 100$ observations can be reconstructed in 50 periodic or cyclic components ($T/1$, $T/2$, $T/3$,. . ., 2). The frequency is the reciprocal of the period and can be expressed in terms of number of cycles per observation. Therefore, $f = 0$ implies no repetition, $f = 1/T$ the slowest, and $f = 0.5$ the fastest frequency. *Spectral density function* gives the amount of variance accounted for by each frequency we can measure. The analysis of power distribution can be seen as a type of ANOVA where the

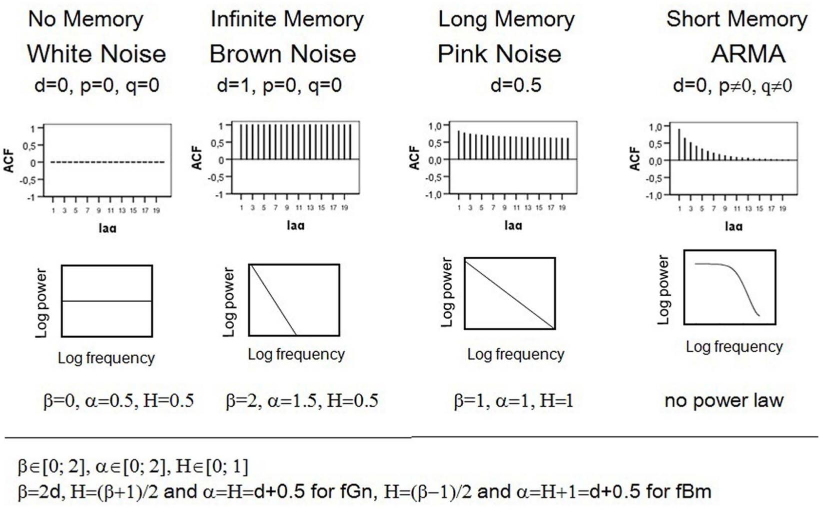

FIGURE 1 | Autocorrelation functions, logarithmic power spectra and parameter values of different fractal and non-fractal patterns.

overall process variance is divided into variance components due to independent cycles of different length. If the data are cyclic, there are a few so-called major frequencies that explain a great amount of the series' variance (i.e., all of the series' power is concentrated at one or a few frequencies). For non-periodic processes like white noise, the variance is equally distributed across all possible frequencies. For pink noise, there is a special kind of relationship between frequency and variance, which is expressed by the following power low: $S(f) \propto 1/f$. Self-similarity of this process implies that its variance is inversely proportional to its frequency. This property becomes more vivid if the power spectrum is plotted on a log–log scale, showing that the logarithmic power function of $1/f$ noise follows a straight line with slope –1. In contrast, the power of Brown noise falls off rapidly with increasing frequency, which means that low frequency components predominate. As a result, the log–log power function of Brown noise is a line with a slope of -2. The logarithmic power spectrum of white noise has a slope of 0. Denoting the power spectrum function $1/f^{\beta}$, where β is called the *power exponent*, we obtain $\beta = 0$ for white noise, $\beta = 2$ for Brown noise, and $\beta = 1$ for pink noise. For short-memory (e.g., autoregressive) processes, the log–log power spectrum in *not* a straight line because the linear relation between the power and the frequency breaks down at the low frequencies where random variation appears. As a result, a flat plateau (the zero slope of white noise) dominates low frequencies in spectral plots. The bottom section of **Figure 1** shows the power spectra of the discussed processes. For more details on spectral analyses, consult Warner (1998).

Self-similarity of pink noise can also be expressed by the following power low: $F(n) \propto n^{\alpha}$ with $\alpha = 1$. Dividing a process in intervals of equal length n allows viewing it on different scales. Fluctuations (F) of pink noise are proportional to n, i.e., they increase with growing interval length. The *scaling exponent* α of Brown noise is 1.5; white noise has α of 0.5.

The so-called Hurst phenomenon represents a further manifestation of self-similarity (Hurst, 1965). It expresses the probability that an event in a process is followed by a similar event. This probability, expressed as the *Hurst coefficient* (H), is 0.5 for both white and Brown noises, which is not surprising because white noise is a sequence of independent innovations and Brown noise consists of uncorrelated increments. The Hurst coefficient of self-similar processes deviates from 0.5. For pink noise, $H = 1$. In general, we distinguish two different classes of fractal signals: *fractional Brownian motions* (fBm) and *fractional Gaussian noises* (fGn; Mandelbrot and van Ness, 1968; Mandelbrot and Wallis, 1969). Gaussian noises are stationary processes with constant mean and variance, whereas Brownian motions are non-stationary with stationary increments. Differencing Brownian motion creates Gaussian noise and summing Gaussian noise produces Brownian motion. The related processes are characterized by the same Hurst coefficient.

To summarize, long memory and self-similarity are specific characteristics of $1/f$ noise. These properties become manifest in the hyperbolically decaying ACF and power lows. The differencing statistic d, the power exponent β, the scaling exponent α, and the Hurst coefficient H are parameters that reflect fractality. The expected theoretical parameter values of the pink noise are $d = 0.5$, $\beta = 1$, $\alpha = 1$, $H = 1$. **Figure 1** outlines relations between parameters and contrasts the autocorrelation and spectral density functions of $1/f$ noise with those of other processes.

To understand subsequent explanations, it is important to conceive the difference between the following concepts: *parameter*, *estimator*, and *estimate*. A parameter is a quantity that defines a particular system, e.g., the mean μ of the normal distribution. H, β, α, and d are fractal parameters that express exactly the same statistical characteristics. The formulas presented in **Figure 1** allow for unequivocal transformations from one quantity into the other. For instance, a stationary process with the scaling exponent $\alpha = 0.8$ can be alternatively specified by $H = 0.8$, $d = \alpha - 0.5 = 0.3$, or $\beta = 2$, $d = 0.6$. An estimator is a rule or formula that is used to infer the value of an unknown parameter from the sample information. For each parameter, there are usually different estimators with diverse statistical properties. In contrast to parameters, estimators are not numbers but functions characterized by their distributions, expectancy values, and variances. For example, μ can be estimated using the arithmetic mean $\hat{\mu} = \bar{X} = \frac{1}{T}\Sigma_{i=1}^{T} X_i$ or the median $\hat{\mu} = X_{0.5}$. Both methods are unbiased, which implies that their expected values match $\mu : E(\bar{X}) = E(X_{0.5}) = \mu$. However, $\bar{X}$ is the better estimator of μ because of its smaller variance ensuring narrower confidence intervals and thus more precise inference. The superiority of $\bar{X}$ is determined mathematically. Unfortunately, it is not always possible to find out the best estimator this way. In such cases, Monte Carlo simulations represent adequate tools to determine the best method to use under the given circumstances. For instance, computational algorithms can generate a population with a known parameter value, e.g., a process with $\alpha = 1$. Repeated samples of the same size can be drawn from this population, e.g., 1000 time series with $T = 500$, and different estimators can be applied to the series. As a result one gets 1000 estimates of the parameter per method. Estimate is a particular numerical value obtained by the estimator in an application. Good estimators are unbiased, i.e., their means equal the true parameter value, and have small variability, i.e., their estimates do not differ strongly. Considering that just one estimate per method is available in a typical research situation, an estimator with the narrow range, e.g., $[\hat{\alpha}(1)_{\min} = 0.9; \hat{\alpha}(1)_{\max} = 1.1]$ for $\alpha = 1$, is obviously better that the one with the broad range, e.g., $[\hat{\alpha}(2)_{\min} = 0.5; \hat{\alpha}(2)_{\max} = 1.5]$.

ESTIMATORS OF FRACTAL PARAMETERS

Numerous procedures for measuring the fractal parameters β, α, H, and d have been developed in recent years. **Table 1** includes estimators that are available in software packages traditionally used by psychologists (R, SPSS, and SAS). The methods can be assigned to three categories: (1) exact or approximate maximum likelihood (EML or AML) ARFIMA estimation of d with the corresponding conditional sum of squares (CSS) algorithm; (2) detrended fluctuation analysis (DFA) and signal summation conversion (SSC), fractal methods predicated on the relationship $F(n) \propto n^{\alpha}$; (3) periodogram based procedures like power spectral density (PSD), Whittle (FDWhittle), Sperio (fdSperio), and Geweke–Porter-Hudak (fdGPH). The periodogram is an estimate of the spectral density function.

Autoregressive fractionally integrated moving average algorithms were described and evaluated by Stadnytska and Werner (2006) and Torre et al. (2007). Eke et al. (2000), Delignières

Table 1 | Estimators of fractal parameters from statistical packages R, SAS, and SPSS.

Method	Outputs	Available	Command
ARFIMA			
EML	$\hat{d}$, $\hat{\phi}$, $\hat{\theta}$	SAS: IML subroutine FARMAFIT	Fitting ARFIMA (1, *d*, 1): `call farmafit(d, ar, ma, sigma, x, opt=1) p=1 q=1; print d ar ma sigma;`
CSS	$\hat{d}, \hat{\phi}, \hat{\theta}$	SAS: IML subroutine FARMAFIT	`call farmafit(d, ar, ma, sigma, x, opt=0) p=1 q=1; print d ar ma sigma;`
AML	$\hat{d}, \hat{\phi}, \hat{\theta}$	R: library *fracdiff*	`summary(fracdiff(x, nar=1, nma=1))`
FRACTAL			
DFA	$\hat{\alpha}$	R: library *fractal*	DFA(x, detrend="bridge", sum.order=1)
SSC	$\hat{\alpha}$	R-Code *SSC.R*	Download the file SSC.R from http://www.psychologie.uni-heidelberg.de/projekte/zeitreihen/R_Code_Data_Files.html then click *"read R-code"* from the *data* menu and start the test via command SSC(x)
PERIODOGRAM			
$^{\text{low}}$PSD	$\hat{\beta}$	SPSS, SAS, R	SPSS-, SAS-, and R-Codes in Appendix
$^{\text{low}}$PSD$_{\text{we}}$	$\hat{\beta}$	R-Code lowPSDwe.R	Download the file lowPSDwe.R from http://www.psychologie.uni-heidelberg.de/projekte/zeitreihen/R_Code_Data_Files.html then click "read R-code" from the data menu and start the test via command PSD(x)
hurstSpec	$\hat{\alpha}$	R: library *fractal*	hurstSpec(x)
fdGPH	$\hat{d}$	R: library *fracdiff*	fdGPH(x)
fdSperio	$\hat{d}$	R: library *fracdiff*	fdSperio(x)
FDWhittle	$\hat{d}$	R: library *fractal*	FDWhittle(x)

x is the time series name. For further details, consult Stadnytska et al. (2010) and Stadnitski (2012).

et al. (2006), Stroe-Kunold et al. (2009), Stadnytska et al. (2010), Stadnitski (2012) systematically analyzed different fractal and periodogram based methods. What are the key findings of these studies? First, all estimators require at least 500 observations for acceptable measurement accuracy. Further, for researchers studying fractality, it is essential to know that there exist different procedures with diverging characteristics. Unfortunately for the researcher, none of the procedures is superior to the other. The central difficulty is that there is no clear winner among them. Simulation studies on this topic demonstrated that the performance of the methods strongly depends on aspects like the complexity of the underlying process or parameterizations. As a result, elaborated strategies to estimate the fractality parameters are necessary. Thornton and Gilden (2005) developed a spectral classifier procedure that estimates the likelihood of a time series by comparing its power spectrum with spectra of the competing memory models. Stadnytska et al. (2010) proposed a method to estimate the long memory parameter *d* that combines different techniques and incorporates ARFIMA approaches from Wagenmakers et al. (2004). The application of this strategy to an empirical time series will be presented later. A brief overview of procedures summarized in **Table 1** precedes the empirical demonstration.

ARFIMA METHODS

The most popular estimators of the fractional differencing parameter *d* are the EML method proposed by Sowell (1992a), the CSS approach introduced by Chung (1996) and the *approximate method* (AML) of Haslett and Raftery (1989). The main advantage of the ARFIMA methods is the possibility of the joint estimation of the short-memory and long memory parameters. This solves a potential finite-sample problem of biased overestimation of fractality in time series which contain both long-range and short-range components (see Sowell, 1992b, for details). Moreover, goodness of fit statistics based on the likelihood function, like the Akaike information criterion (AIC) or the Bayesian information criterion (BIC), allow to determine the amount of "short-term contamination" and enable a reliable discrimination between short- and long memory processes.

The greatest problem with ARFIMA estimators is that they work only for stationary series, because their range is confined to (0; 0.5). This entails erroneous classifications of non-stationary processes with $d > 0.5$ as $1/f$ noise. Recall that the theoretical parameter values of pink noise are $d = 0.5$, $\beta = 1$, $\alpha = 1$, $H = 1$. To illustrate this problem, a Brown noise series [ARIMA (0, 1, 0) with $d = 1$, $\beta = 2$, $\alpha = 1.5$, $H = 0.5$] of length $T = 500$ was simulated. The upper section of **Figure 2** shows the series with its ACF and logarithmic power spectrum. Applying ARFIMA methods to this data provided estimates of *d* close to 0.5 : $\hat{d}_{\text{AML}} = 0.499$, $\hat{d}_{\text{EML}} = 0.5$, $\hat{d}_{\text{CSS}} = 0.49$. Hence, checking for stationarity is a necessary precondition for ARFIMA estimation.

Special procedures called *unit root tests* were developed to prove stationarity (see Stadnytska, 2010, for a comprehensive overview). The augmented Dickey–Fuller (ADF) test, the most popular method available in statistical packages R or SAS, checks the null hypothesis $d = 1$ against $d = 0$. Hence, an empirical series with *d* close to 0.5 will probably be misclassified as non-stationary. In contrast, the Kwiatkowski–Phillips–Schmidt–Shin (KPSS) test acts on the assumption that process is stationary (H_0: $d = 0$). Therefore the combination of both procedures allows to determine the properties of the series under study: (1) if the ADF is significant

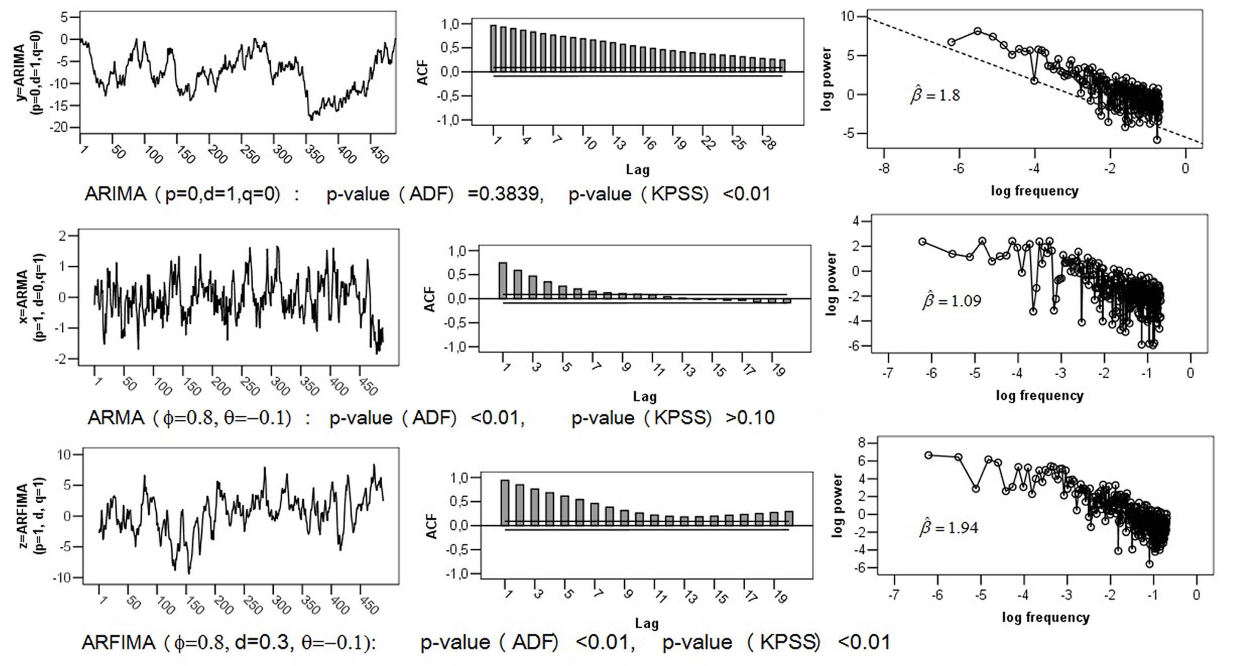

FIGURE 2 | Comparison of ACF and power spectra of empirical Series: (1) Brown Noise or ARIMA (0, 1, 0); Short-Memory Series ARIMA (1, 0, 1); (3) Fractal Series ARFIMA (1, *d*, 1) with $d = 0.3$.

and the KPSS is not, then the data are probably stationary with $d \in (0; 0.5)$; (2) in the Brown noise case, an insignificant ADF and a significant KPSS results are expected; (3) $d \in (0; 1)$, if both tests are significant. Applying the unit root tests to the simulated Brown noise series showed the following *p*-values: $p_{\text{ADF}} = 0.3839$ and $p_{\text{KPSS}} < 0.01$ (see **Figure 3**). According to this outcome, the series is probably non-stationary, and estimating fractal parameters with the ARFIMA methods is inappropriate.

FRACTAL AND PERIODOGRAM BASED METHODS

In contrast to ARFIMA procedures, methods like PSD (Eke et al., 2002), DFA (Peng et al., 1993), or SSC (Eke et al., 2000) can be applied directly to different classes of time series. Consequently, they represent adequate tools for distinguishing fGn and fBm signals. For the simulated Brown noise series the following results were obtained: $\hat{d}_{\text{DFA}} = 1.1$, $\hat{d}_{\text{SSC}} = 0.8$, $\hat{d}_{\text{PSD}} = 0.83$, $\hat{d}_{\text{hurstSpec}} = 1.1$, $\hat{d}_{\text{fdGPH}} = 0.88$, $\hat{d}_{\text{fdSperio}} = 0.79$, $\hat{d}_{\text{FDWhittle}} = 1$ (see **Figure 3**). All estimates were converted to $\hat{d}$ using the formulas in **Figure 1** to make the comparison more convenient. For instance, DFA outputs $\hat{\alpha}_{\text{DFA}} = 1.595 \approx 1.6$ (see **Table 1**; **Figure 3**), thus $\hat{d}_{\text{DFA}} = \hat{\alpha}_{\text{DFA}} - 0.5 = 1.1$. The estimate of β presented in **Figure 3** is $\hat{\beta}_{\text{PSD}} = 1.66$, hence $\hat{d}_{\text{PSD}} = \hat{\beta}_{\text{PSD}}/2 = 0.83$. Recall that the true *d*-value of Brown noise is 1, therefore, compared to the ARFIMA algorithms, the most estimates reflect the parameter rather accurate.

However, due to considerably larger biases and more pronounced SEs, the precision of fractal and periodogram based methods is distinctly inferior to that of the ARFIMA approaches. Moreover, algorithms like PSD, DFA, or SSC use different data transformations like detrending or filtering. As a result, the performance of estimators strongly depends on the manipulations employed. For instance, numerous modifications have been suggested to improve the PSD estimation. The method designated as $^{\text{low}}\text{PSD}_{\text{we}}$ consists of the following operations: (1) subtracting the mean of the series from each value, (2) applying a parabolic window to the data (*w*), (3) performing a bridge detrending (*e*), (4) estimating β excluding 7/8 of high-frequency power estimates (*low*). The estimator $^{\text{low}}\text{PSD}$ is constructed without transformations 2 and 3. Simulation studies demonstrated that $^{\text{low}}\text{PSD}$ were more accurate for fGn noises whereas $^{\text{low}}\text{PSD}_{\text{we}}$ were accurate for fBm signals (Delignières et al., 2006; Stadnitski, 2012).

The greatest disadvantage of fractal and periodogram based methods is their poor performance for complex processes that combine long- and short-term components. Stadnitski (2012) demonstrated that FDWhittle, the best procedure for pure noises, showed the worst accuracy in complex cases. To illustrate this problem, the following two series with $T = 500$ observations were simulated: a short-memory ARIMA (1, 0, 1) model with $d = 0$, $\phi = 0.8$, and $\theta = -0.1$; a long memory ARFIMA (1, *d*, 1) model with $d = 0.3$, $\phi = 0.8$, and $\theta = -0.1$ (see **Figure 2**). Recall that within the scope of the ARFIMA methodology the short-memory components of a time series can be captured through the autoregressive terms weighted with ϕ and the moving average terms weighted with θ. The following estimates were obtained for the short-memory series with the true *d*-value of 0 : $\hat{d}_{\text{DFA}} = 0.53$, $\hat{d}_{\text{SSC}} = 0.22$, $\hat{d}_{\text{PSD}} = 0.55$, $\hat{d}_{\text{hurstSpec}} = 0.62$, $\hat{d}_{\text{fdGPH}} = 0.38$, $\hat{d}_{\text{fdSperio}} = 0.12$, $\hat{d}_{\text{FDWhittle}} = 0.67$ (see **Figure 4**). Hence, most estimators erroneously indicate a $1/f$

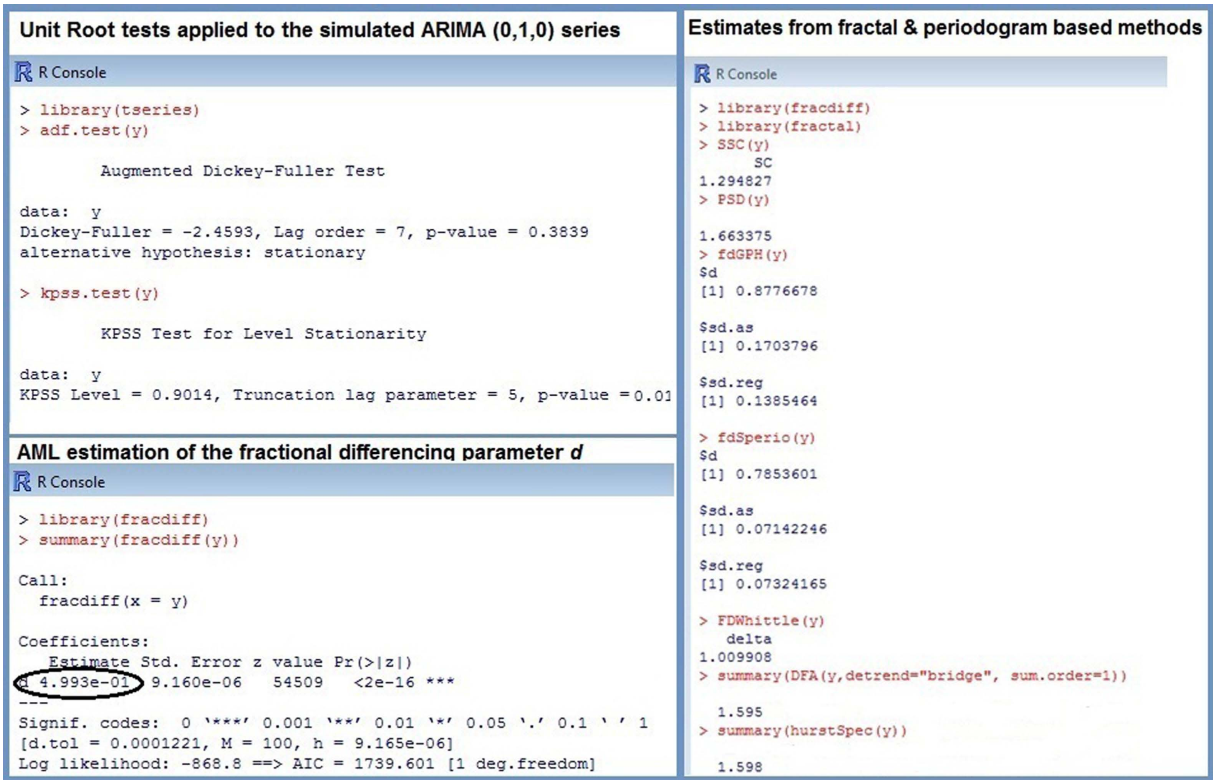

```
> library(tseries)
> adf.test(y)

        Augmented Dickey-Fuller Test

data:  y
Dickey-Fuller = -2.4593, Lag order = 7, p-value = 0.3839
alternative hypothesis: stationary

> kpss.test(y)

        KPSS Test for Level Stationarity

data:  y
KPSS Level = 0.9014, Truncation lag parameter = 5, p-value =0.01
```

```
> library(fracdiff)
> summary(fracdiff(y))

Call:
  fracdiff(x = y)

Coefficients:
   Estimate Std. Error z value Pr(>|z|)
d 4.993e-01 9.160e-06   54509   <2e-16 ***
---
Signif. codes:  0 '***' 0.001 '**' 0.01 '*' 0.05 '.' 0.1 ' ' 1
[d.tol = 0.0001221, M = 100, h = 9.165e-06]
Log likelihood: -868.8 ==> AIC = 1739.601 [1 deg.freedom]
```

```
> library(fracdiff)
> library(fractal)
> SSC(y)
      SC
1.294827
> PSD(y)

1.663375
> fdGPH(y)
$d
[1] 0.8776678

$sd.as
[1] 0.1703796

$sd.reg
[1] 0.1385464

> fdSperio(y)
$d
[1] 0.7853601

$sd.as
[1] 0.07142246

$sd.reg
[1] 0.07324165

> FDWhittle(y)
   delta
1.009908
> summary(DFA(y,detrend="bridge", sum.order=1))

  1.595
> summary(hurstSpec(y))

  1.598
```

FIGURE 3 | R commands and results for the simulated Brown noise ARIMA (0, 1, 0) series.

pattern for this non-fractal series. For the long memory series with the true *d*-value of 0.3, we obtained $\hat{d}_{\text{DFA}} = 0.85$, $\hat{d}_{\text{SSC}} = 0.49$, $\hat{d}_{\text{PSD}} = 0.97$, $\hat{d}_{\text{hurstSpec}} = 0.91$, $\hat{d}_{\text{fdGPH}} = 0.2$, $\hat{d}_{\text{fdSperio}} = 0.28$, $\hat{d}_{\text{FDWhittle}} = 1.16$. Except for fdGPH and fdSperio, we observed here a pronounced positive bias. As a result, this stationary fGn series could be misclassified as a non-stationary fBm signal.

The following example demonstrates the advantages of ARFIMA methodology for complex cases. Since not every data generating process can adequately be represented by a simple (0, *d*, 0)-structure, information Criteria AIC and BIC of different ARFIMA-models were compared first. Recall that the smallest AIC or BIC indicate the best model. The results summarized in **Table 2** clearly favored the (1, *d*, 1)-pattern for the simulated long memory ARFIMA (1, *d*, 1) with $d = 0.3$, $\phi = 0.8$, and $\theta = -0.1$. The AML estimates for this structure were $\hat{d}_{\text{AML}} = 0.2$, $\hat{\phi}_{\text{AML}} = 0.83$, $\hat{\theta}_{\text{AML}} = -0.23$. The point estimate of *d* is comparable to those of fdGPH and fdSperio, but AML has a distinctly smaller SE ($\text{SE}_{\text{AML}} = 0.007$ vs. $\text{SE}_{\text{fdGPH}} = 0.17$, $\text{SE}_{\text{fdSperio}} = 0.07$) assuring smaller confidence intervals, i.e., a more precise measurement. For the short-memory series with $d = 0$, $\phi = 0.8$, and $\theta = -0.1$, there were two plausible models: (1, 0, 1) according to the AIC and (1, *d*, 0) according to the BIC. Fitting the (1, *d*, 0) model to the data provided $\hat{d}_{\text{AML}} \approx 0$, $\hat{\phi}_{\text{AML}} = 0.75$ (see **Figure 4**). Therefore, in both cases the series was correctly identified as non-fractal short-memory structure.

FRACTAL ANALYSIS WITH EMPIRICAL DATA

As demonstrated previously, strategic approach is necessary for a proper measurement of fractal parameters. In the following we show how to apply the estimation methodology proposed by Stadnytska et al. (2010) to empirical data by employing the R software.

R can be downloaded free of charge from http://www.r-project.org/. To perform fractal analyses, we need three packages (*fracdiff*, *fractal*, *tseries*) that do not come with the standard installation. Click *install packages* under the *packages* menu, select these packages and confirm with *ok*. Now the packages will be available for use in the future. Since every command of R is a function that is stored in one of the packages (libraries), you have to load the libraries *fracdiff*, *fractal*, *tseries* each R session before performing fractal analyses. To do so, click *load packages* under the *packages* menu then choose the package and confirm with *ok*.

R is able to read data in many different formats. An easy way to get an *excel file* into R is to save it in the *csv* format, and read it using the command like

```
data=read.csv2 ("C:/ /data.csv")
```

Now *data* is a data frame with named columns ready for analysis. If *data* contains three variables *x*, *y*, and *z*, you can analyze them with the commands like

```
mean(data$x)
```

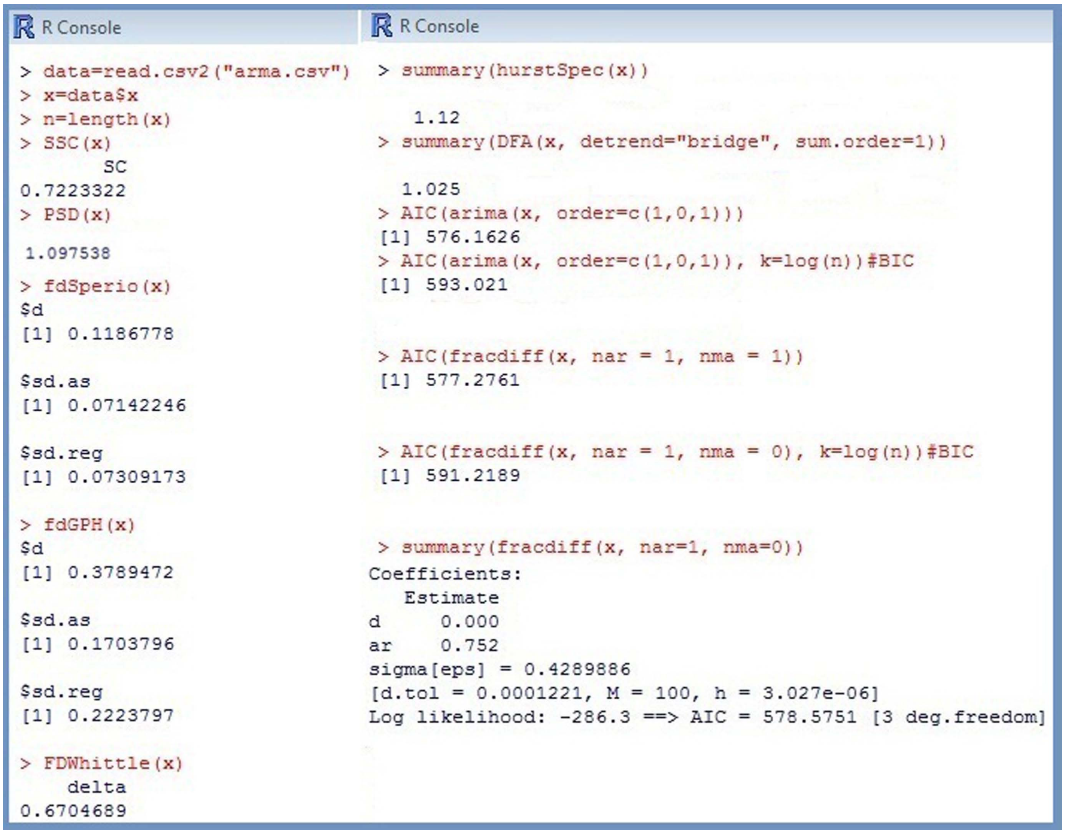

```
> data=read.csv2("arma.csv")
> x=data$x
> n=length(x)
> SSC(x)
       SC
0.7223322
> PSD(x)

 1.097538
> fdSperio(x)
$d
[1] 0.1186778

$sd.as
[1] 0.07142246

$sd.reg
[1] 0.07309173

> fdGPH(x)
$d
[1] 0.3789472

$sd.as
[1] 0.1703796

$sd.reg
[1] 0.2223797

> FDWhittle(x)
    delta
0.6704689
```

```
> summary(hurstSpec(x))

   1.12
> summary(DFA(x, detrend="bridge", sum.order=1))

  1.025
> AIC(arima(x, order=c(1,0,1)))
[1] 576.1626
> AIC(arima(x, order=c(1,0,1)), k=log(n))#BIC
[1] 593.021


> AIC(fracdiff(x, nar = 1, nma = 1))
[1] 577.2761


> AIC(fracdiff(x, nar = 1, nma = 0), k=log(n))#BIC
[1] 591.2189


> summary(fracdiff(x, nar=1, nma=0))
Coefficients:
   Estimate
d     0.000
ar    0.752
sigma[eps] = 0.4289886
[d.tol = 0.0001221, M = 100, h = 3.027e-06]
Log likelihood: -286.3 ==> AIC = 578.5751 [3 deg.freedom]
```

FIGURE 4 | R output for the simulated short-memory ARIMA (1, 0, 1) series.

```
summary(data$y)
cor(data$x,data$z)
```

You can easily rename variables using the following command **x=data$x**.

The empirical series of length $T = 512$ that is analyzed below was generated in the context of a *reaction time task* experiment described by Stadnitski (2012). Response time between stimulus presentation and reaction served as dependent measurement (**Figure 5A**).

The first step of the analysis is to plot a series and examine its ACF and logarithmic power spectrum. Recall that for 1/*f* noise we expect a slower hyperbolic decaying autocorrelations and a straight line with a slope of −1 in the log plot. If the autocorrelations decline quickly or exponentially, the series is definitely non-fractal.

```
plot(x, ty=''l'')
acf(x)
PSD-Code of R (see Appendix)
```

Satisfactory stability in level and variability of the series as well as a slow decay of its ACF, depicted in **Figure 5A**, signalized a finite long memory typical for fractal noises. The negative slope $\hat{\beta}_{\text{PSD}} = 0.347$ is, however, distinctly smaller than 1. It is important to know that the original PSD procedure is not always the best method. Simulation studies demonstrated that excluding the high-frequency spectral estimates from fitting for the spectral slope may improve estimation (Taqqu and Teverovsky, 1997; Eke et al., 2000). Applying the $^{\text{low}}$PSD method (see Appendix) provided $\hat{\beta}_{\text{lowPSD}} = 1.11$. Thus, the logarithmic power spectrum of the series seems to be compatible with the pink noise pattern. The problem is that the log–log power spectrum of short-memory ARMA (p, q) processes can resemble the spectrum of 1/*f* noise (see, for example, the log plot of the ARMA (1,1) structure in **Figure 2**).

Unit root tests may help to find out more about the statistical properties of the series.

```
adf.test(x)
kpss.test(x)
```

The following p-values were observed for the analyzed series: $p_{\text{ADF}} < 0.01$ and $p_{\text{KPSS}} < 0.01$. According to these results, the data under study is probably not Brown noise but it can be both fGn and fBm. Thus, ARFIMA as well as fractal and periodogram based method are appropriate here (see commands in **Table 1**). To make the comparison of results more convenient, the fractal, and periodogram based estimators were converted to $\hat{d}$ and presented in **Figure 5A**. The estimates ranged from 0.248 to 0.577 indicating a fractal pattern. We know, however, that these methods overestimate fractality in time series that contain both long-range and short-range components. Since the obtained values were all smaller than 0.6, the ARFIMA analysis appeared appropriate.

Table 2 | Values of the information criteria AIC and BIC for the simulated short-memory ARMA and long memory ARFIMA series in dependence of the fitted model.

Fitted model	ARMA ($\phi = 0.8$, $d = 0$. $\theta = -0.1$)		ARFIMA ($\phi = 0.8$, $d = 0.3$, $\phi = -0.1$)	
	AIC	BIC	AIC	BIC
(2, 0, 2)	579.9649	605.2525	1439.242	1464.530
(2, 0, 1)	578.1632	599.2363	1439.540	1460.613
(1, 0, 2)	578.1626	599.2356	1438.977	1460.050
(2, 0, 0)	576.2489	593.1073	1439.350	1456.209
(0, 0, 2)	576.2489	678.1116	1763.675	1780.533
(1, 0, 1)	**576.1626**	**593.0210**	1439.625	1456.483
(1, 0, 0)	577.5258	590.1697	1489.436	1502.080
(0, 0, 1)	738.9594	751.6032	2059.512	2072.156
(0, 0, 0)	984.6744	993.0052	2573.536	2581.965
(2, *d*, 2)	580.3508	605.6384	1440.078	1465.366
(2, *d*, 1)	578.3731	599.4461	1438.590	1459.663
(1, *d*, 2)	578.3752	599.4482	1438.261	1459.334
(2, *d*, 0)	576.5114	593.3699	1437.906	1454.764
(0, *d*, 2)	588.8440	605.7024	1465.847	1482.706
(1, *d*, 1)	577.2761	594.1346	**1436.262**	**1453.121**
(1, *d*, 0)	578.5751	**591.2189**	1447.913	1460.557
(0, *d*, 1)	592.3358	604.9797	1526.298	1538.942
(0, *d*, 0)	612.2110	620.5418	1761.094	1769.523

Bold are estimates from the models with the smallest Akaike information criterion (AIC) or Bayesian information criterion (BIC).

The preceding analyses do not allow rejecting the hypothesis of non-fractality of the analyzed series. Therefore AIC and BIC of different short- and long memory models were compared. The following commands compute AIC of the (1, *d*, 1) and (1, 0, 1) models:

```
AIC(fracdiff(x, nar = 1, nma = 1))
AIC(arima(x, order=c(1,0,1)))
```

To obtain BIC instead of AIC, use

```
AIC(fracdiff(x, nar = 1, nma = 1), k=log(n))
AIC(arima(x, order=c(1,0,1)), k=log(n)),
```

n is the number of observations (see **Figure 4**).

The results summarized in **Table 3** indicated either the long memory model (1, *d*, 2; the smallest AIC) or the short-memory

Table 3 | Values of the information criteria AIC and BIC for the empirical time series.

Model ARMA	AIC	BIC	Model ARFIMA	AIC	BIC
(0, 0, 0)	5308.030	5316.506	(0, *d*, 0)	5181.524	5190.001
(1, 0, 0)	5256.566	5269.281	(1, *d*, 0)	5170.354	5183.069
(0, 0, 1)	5274.145	5286.860	(0, *d*, 1)	5163.365	5176.080
(1, 0, 1)	5158.735	**5175.688**	(1, *d*, 1)	5161.513	5178.466
(2, 0, 1)	5160.726	5181.917	(2, *d*, 1)	5156.040	5177.208
(1, 0, 2)	5160.729	5181.920	**(1, *d*, 2)**	**5156.016**	5177.232
(2, 0, 0)	5226.219	5243.172	(2, *d*, 0)	5165.411	5182.365
(0, 0, 2)	5256.336	5273.29	(0, *d*, 2)	5162.237	5179.190
(2, 0, 2)	5162.699	5188.129	(2, *d*, 2)	5158.016	5183.446

Bold are estimates from the models with the smallest AIC or BIC.

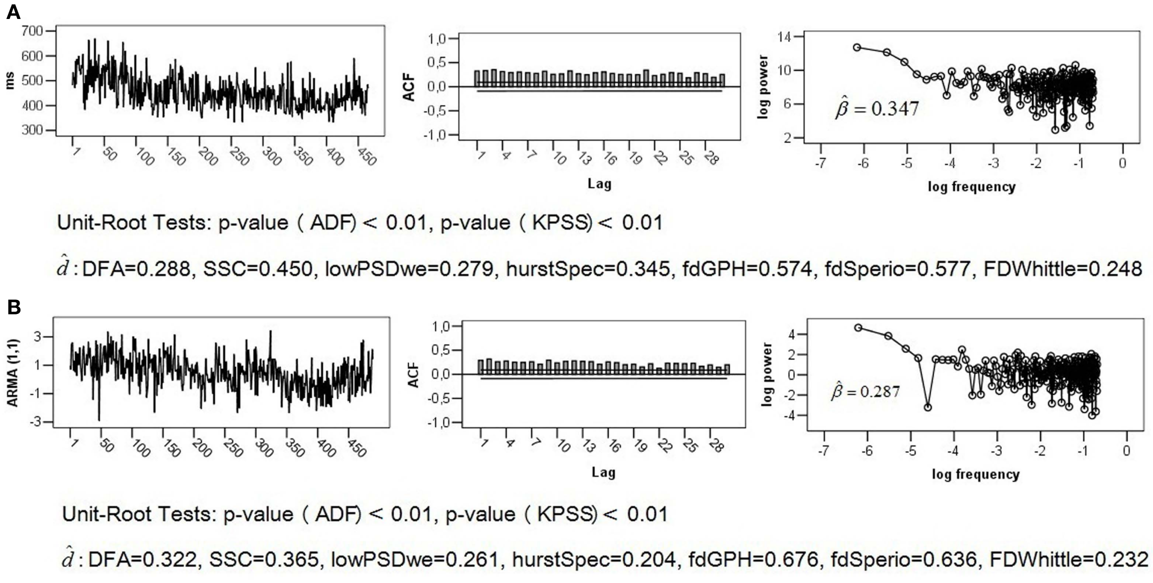

Unit-Root Tests: p-value (ADF) < 0.01, p-value (KPSS) < 0.01

$\hat{d}$: DFA=0.288, SSC=0.450, lowPSDwe=0.279, hurstSpec=0.345, fdGPH=0.574, fdSperio=0.577, FDWhittle=0.248

Unit-Root Tests: p-value (ADF) < 0.01, p-value (KPSS) < 0.01

$\hat{d}$: DFA=0.322, SSC=0.365, lowPSDwe=0.261, hurstSpec=0.204, fdGPH=0.676, fdSperio=0.636, FDWhittle=0.232

FIGURE 5 | ADF and log–log plot of (A) empirical series obtained from temporal estimation task; (B) simulated ARIMA (1, 0, 1) series with $\phi = 0.99$, and $\theta = -0.92$.

model (1, 0, 1; the smallest BIC). Fitting the (1, *d*, 2) pattern to the data with the command "**summary(fracdiff(x, nar=1, nma=2))**," provided the d estimate very close to 0 : $\hat{d}_{\text{AML}} = 0.06$, $\text{SE}_{\text{AML}} = 0.026$, $\text{KI}_{0.95} = (0.009; 0.111)$. Therefore, the series is probably *not* generated from the 1/*f* noise process.

Fitting the (1, 0, 1) model to the data using "**arima(x, order=c(1,0,1))**," resulted in $\hat{\phi}_{\text{AML}} = 0.99$, $\text{SE}_{\phi} = 0.005$ and $\hat{\theta}_{\text{AML}} = -0.92$, $\text{SE}_{\theta} = 0.021$. To demonstrate that short-memory series with such parameter values can mimic the statistical properties of the pink noise, we simulated the ARIMA (1, 0, 1) models of length $T = 512$ with the true values $d = 0$, $\phi = 0.99$, and $\theta = -0.92$. **Figure 5B** shows that its ACF, log plot, and estimates obtained from fractal and periodogram based methods are very similar to those of the analyzed empirical series. For explanations of this phenomenon, consult Thornton and Gilden (2005), Wagenmakers et al. (2004), and Stadnitski (2012). Detailed descriptions of R analyses are presented in Appendix.

CONCLUDING REMARKS

Self-similarity and long memory are essential characteristics of a fractal pattern. Slow hyperbolically decaying autocorrelations and power lows reflect these properties, which can be expressed with the correspondent parameters d, β, α, and H. The fractal parameters express exactly the same statistical characteristics, thus each quantity can be converted to the other. The expected theoretical values of pink noise are $d = 0.5$, $\beta = 1$, $\alpha = 1$, $H = 1$. There are two major types of estimators for these parameters: ARFIMA algorithms and procedures searching for power laws. The former are very accurate methods capable of measuring both long- and short-term dependencies, but they can handle only stationary processes. The latter are adequate procedures for stationary and non-stationary data, their precision, however, is distinctly inferior to that of the ARFIMA methods. Moreover, they tend to overrate fractal parameters in series containing short-memory components. The greatest problem is that no estimator is superior for a majority of theoretical series. Moreover, in a typical research situation it is usually unclear what kind of process generated empirical data. Consequently, the estimation of fractality requires elaborate strategies. The spectral classifier procedure by Thornton and Gilden (2005) and the ARFIMA estimation proposed by Stadnytska et al. (2010) are examples of such strategic approaches. Furthermore, depending of the hypotheses of the research, diverse key objectives of fractal analyses can be distinguished: discriminate between fractal and non-fractal patterns for diagnostic purposes, test for the effective presence of genuine persistent correlations in the series, provide an accurate estimation of the strength of these long-range dependencies, or identify the short-term process that accompanies a fractal pattern. Delignières et al. (2005) point out that different objectives require distinct strategies. This paper demonstrated how to distinguish between fractal and non-fractal empirical time series employing the open source software R.

REFERENCES

Aks, D. J., and Sprott, J. C. (2003). The role of depth and 1/f dynamics in perceiving reversible figures. *Nonlinear Dynamics Psychol. Life Sci.* 7, 161–180.

Bak, P., Tang, C., and Wiesenfeld, K. (1987). Self-organized criticality: an explanation of 1/f noise. *Phys. Rev. Lett.* 59, 381–384.

Beran, J. (1994). *Statistics for Long-Memory Processes.* New York: Chapman & Hall.

Box, G. E. P., and Jenkins, G. M. (1970). *Time Series Analysis, Forecasting and Control.* San Francisco: Holden Day.

Brockwell, P. J., and Davis, R. A. (2002). *Introduction to Time Series and Forecasting.* New York: Springer.

Chen, Y., Ding, M., and Kelso, J. A. S. (1997). Long memory processes (1/fa type) in human coordination. *Phys. Rev. Lett.* 79, 4501–4504.

Chen, Y., Ding, M., and Kelso, J. A. S. (2001). Origins of time errors in human sensorimotor coordination. *J. Mot. Behav.* 33, 3–8.

Chung, C. F. (1996). A generalized fractionally integrated ARMA process. *J. Time Ser. Anal.* 2, 111–140.

Delignières, D., Lemoine, L., and Torre, K. (2004). Time intervals production in tapping oscillatory motion. *Hum. Mov. Sci.* 23, 87–103.

Delignières, D., Ramdani, S., Lemoine, L., and Torre, K. (2006). Fractal analyses for short time series: a re-assessment of classical methods. *J. Math. Psychol.* 50, 525–544.

Delignières, D., Torre, K., and Lemoine, L. (2005). Methodological issues in the application of monofractal analyses in psychological and behavioral research. *Nonlinear Dynamics Psychol. Life Sci.* 9, 435–462.

Ding, M., Chen, Y., and Kelso, J. A. S. (2002). Statistical analysis of timing errors. *Brain Cogn.* 48, 98–106.

Eke, A., Herman, P., Bassingthwaighte, J. B., Raymond, G., Percival, D., Cannon, M. J., Balla, I., and Ikenyi, C. (2000). Physiological time series: distinguishing fractal noises from motions. *Pflügers Arch.* 439, 403–415.

Eke, A., Herman, P., Kocsis, L., and Kozak, L. R. (2002). Fractal characterization of complexity in temporal physiological signals. *Physiol. Meas.* 23, R1–R38.

Gilden, D. L., Thornton, T., and Mallon, M. W. (1995). 1/f noise in human cognition. *Science* 267, 1837–1839.

Granger, C. W. J., and Joyeux, R. (1980). An introduction to long-range time series models and fractional differencing. *J. Time Ser. Anal.* 1, 15–30.

Haslett, J., and Raftery, A. E. (1989). Space-time modelling with long-memory dependence: assessing Ireland's wind power resource. *Appl. Stat.* 38, 1–50.

Hausdorf, J. M., and Peng, C. K. (1996). Multiscaled randomness: a possible source of 1/f noise in biology. *Phys. Rev. E. Stat. Phys. Plasmas Fluids Relat. Interdiscip. Topics* 54, 2154–2157.

Hausdorf, J. M., Zemany, L., Peng, C. K., and Goldberger, A. L. (1999). Maturation of gait dynamics: Stride-to-stride variability and its temporal organization in children. *J. Appl. Physiol.* 86, 1040–1047.

Hosking, J. R. M. (1981). Fractional differencing. *Biometrika* 68, 165–176.

Hosking, J. R. M. (1984). Modelling persistence in hydrological time series using fractional differencing. *Water Resour. Res.* 20, 1898–1908.

Hurst, H. E. (1965). *Long-Term Storage: An Experimental Study.* London: Constable.

Jensen, H. J. (1998). *Self-Organized Criticality.* Cambridge: University Press.

Linkenkaer-Hansen, K. (2002). *Self-Organized Criticality and Stochastic Resonance in the Human Brain.* Dissertation, Helsinki University of Technology Laboratory of Biomedical Engineering.

Mandelbrot, B. B., and van Ness, J. W. (1968). Fractional Brownian motions, fractional noises and applications. *SIAM Rev.* 10, 422–437.

Mandelbrot, B. B., and Wallis, J. R. (1969). Computer experiments with fractional Gaussian noises. *Water Resour. Res.* 5, 228–267.

Norris, P. R., Stein, P. K., Cao, H., and Morris, J. J. Jr. ((2006)). Heart rate multiscale entropy reflects reduced complexity and mortality in 285 patients with trauma. *J. Crit. Care* 21, 343.

Peng, C.-K., Mietus, J., Hausdorff, J. M., Havlin, S., Stanley, H. E., and Goldberger, A. L. (1993). Long-range anticorrelations and non-Gaussian behavior of the heartbeat. *Phys. Rev. Lett.* 70, 1343–1346.

Sowell, F. (1992a). Maximum likelihood estimation of stationary univariate fractionally integrated time series models. *J. Econom.* 53, 165–188.

Sowell, F. (1992b). Modeling long-run behavior with the fractional ARFIMA model. *J. Monet. Econ.* 29, 277–302.

Stadnitski, T. (2012). Some critical aspects of fractality research. *Nonlinear Dynamics Psychol. Life Sci.* 16, 137–158.

Stadnytska, T. (2010). Deterministic or stochastic trend: decision on the basis of the augmented Dickey-Fuller Test. *Methodology* 6, 83–92.

Stadnytska, T., Braun, S., and Werner, J. (2010). Analyzing fractal dynamics employing R. *Nonlinear Dynamics Psychol. Life Sci.* 14, 117–144.

Stadnytska, T., and Werner, J. (2006). Sample size and accuracy of estimation of the fractional differencing parameter. *Methodology* 4, 135–144.

Stroe-Kunold, E., Stadnytska, T., Werner, J., and Braun, S. (2009). Estimating long -range dependence in time series: An evaluation of estimators implemented in R. *Behav. Res. Methods* 41, 909–923.

Taqqu, M. S., and Teverovsky, V. (1997). Robustness of Whittle-type estimators for time series with long range dependence. *Stochastic Models* 13, 723–757.

Thornton, T. L., and Gilden, D. L. (2005). Provenance of correlation in psychological data. *Psychon. Bull. Rev.* 12, 409–441.

Torre, K., Delignières, D., and Lemoine, L. (2007). Detection of long-range dependence and estimation of fractal exponents through ARFIMA modeling. *Br. J. Math. Stat. Psychol.* 60, 85–106.

Torre, K., and Wagenmakers, E.-J. (2009). Theories and models for 1/f$^{\beta}$ noise in human movement science. *Hum. Mov. Sci.* 28, 297–318.

Van Orden, G. C., Holden, J. G., and Turvey, M. T. (2003). Self-organization of cognitive performance. *J. Exp. Psychol.* 3, 331–350.

Van Orden, G. C., Holden, J. G., and Turvey, M. T. (2005). Human cognition and 1/f scaling. *J. Exp. Psychol. Gen.* 134, 117–123.

Wagenmakers, E.-J., Farrell, S., and Ratcliff, R. (2004). Estimation and interpretation of 1/fa noise in human cognition. *Psychon. Bull. Rev.* 11, 579–615.

Warner, R. M. (1998). *Spectral Analysis of Time-Series Data*. New York: Guilford.

Conflict of Interest Statement: The author declares that the research was conducted in the absence of any commercial or financial relationships that could be construed as a potential conflict of interest.

Received: 06 March 2012; accepted: 16 April 2012; published online: 07 May 2012.

Citation: Stadnitski T (2012) Measuring fractality. Front. Physio. ***3****:127. doi: 10.3389/fphys.2012.00127*

This article was submitted to Frontiers in Fractal Physiology, a specialty of Frontiers in Physiology.

APPENDIX

^{low}**PSD SPSS**-Code for series X with $T = 512$ to obtain a PSD-estimate of β.
$\hat{\beta}$ is the negative slope of the regression $\ln\_p = b_0 + b_1 \ln\_f\ (\hat{\beta} = -b_1)$.

```
SPECTRA
/VARIABLES=X
/CENTER
/SAVE FREQ(f) P(SS).

COMPUTE ln_f = LN(f).
EXECUTE.
COMPUTE ln_p = LN(SS_1).
EXECUTE.
COMPUTE filter_$=(T>1 and T<(512/2*1/8+2)).
FILTER BY filter_$.

REGRESSION
/STATISTICS COEFF
/DEPENDENT ln_p
/METHOD=ENTER ln_f .
```

^{low}**PSD SAS**-Code for series X with $T = 512$ to obtain a PSD-estimate of β.

```
proc spectra data=data out=spec p s center;
var X;
run;

data spec;
set spec;
T+1;
run;

data loglog;
set spec;
if FREQ=0 then delete;
if T>(512/2*(1/8)+1) then delete;
ln_f=log(FREQ);
ln_p=log(S_01);
keep ln_f ln_p;
run;

proc reg data=loglog;
model ln_p=ln_f;
run;
```

^{low}**PSD R-Code** for series X to obtain a PSD-estimate of β.

```
n <- length(x)
spec <- spectrum(x, detrend=FALSE, demean=TRUE, taper=0)
nr <- (n/2) * (1/8)
specfreq <- spec$freq[1:nr]
specspec <- spec$spec[1:nr]
logfreq <- log(specfreq)
logspec <- log(specspec)
lmb <- lm(logspec ~ logfreq)
b <- coef(lmb)
beta=-b[2]
```

```
plot (logfreq, logspec, type="l")
abline(lmb)
print(beta)
```

PSD R-Code for series X to obtain a PSD-estimate of β.

```
spec <- spectrum(x, detrend=FALSE, demean=TRUE, taper=0)
specfreq <- spec$freq
specspec <- spec$spec
logfreq <- log(specfreq)
logspec <- log(specspec)
lmb <- lm(logspec ~ logfreq)
b <- coef(lmb)
beta=-b[2]
plot (logfreq, logspec, type="l")
abline(lmb)
print(beta)
```

FRACTAL ANALYSES WITH R

1. Step "Preparation"
   - Install R from http://www.r-project.org/
   - Install the packages *fracdiff*, *fractal*, *tseries* [Click *install packages* under the *packages* menu, select these packages and confirm with *ok*].

   Some tips for comfortably working with R:
   - R commands can be typed directly in the R console after the symbol ">" (see **Figures 3** and **4**). To obtain the R output, just press [ENTER].
   - The easiest way to administer R commands is to open a new script [click *data – new script*] and write the commands there. You can enter one or more commands in the R console by selecting them and pressing [CTRL + R].
2. Step "Data Import in R"
   - Create an *excel file* (e.g., for one time series of length $T = 500$, type the name "x" in the first row of the first column, then type 500 observations in the subsequent rows of the column).
   - Save data in *csv* format [Excel: click *save as*, then activate *save as type* and choose *CSV* (*Comma delimited*)]. As a result, you obtain an excel file ***name.csv***.
   - Open R and *click data – change directory* and choose the directory where you saved the file ***name.csv***. Typing the command **getwd**() shows the current working directory of R.
   - Get the excel file ***name.csv*** into R by writing in the R console the command **data**=**read.csv2(“name.csv”)** (see **Figure 4**).
   - Choose the variable *x* from the frame ***data*** by typing **x=data$x.** Because the file ***name.csv*** and accordingly the R frame ***data*** consist of one variable saved in the first column, you can alternatively get the variable *x* using the command **x=data[,1].** Note that the command **data[2,]** outputs the second row of the frame ***data***.
3. Step "Performing fractal analyses"
   - Load the packages *fracdiff*, *fractal*, *tseries* [type the commands **library (fracdiff)**, **library (fractal)**, **library(tseries)**].
   - Load SSC and $^{low}PSD_{we}$ (download the files *SSC.R* and *lowPSDwe.R* from http://www.psychologie.uni-heidelberg.de/projekte/zeitreihen/R_Code_Data_Files.html, then click *read R-code* from the *data* menu).
   - Type the following commands in the R console (see **Figures 3** and **4**) or write them in a script and submit by pressing [CTRL + R].

```
plot(x, ty=’’l’’)
acf(x)
adf.test(x)
kpss.test(x)
PSD(x)
SSC(x)
DFA(x, detrend="bridge", sum.order=1)
fdSperio(x)
fdGPH(x)
FDWhittle(x)
hurstSpec(x)
fracdiff(x)
```

4. Step "ARFIMA analyses"
   - Compute AIC and BIC of different long and short-memory models (see **Tables 2** and **3**). The command **AIC(fracdiff(x, nar = 2, nma = 2))** outputs the AIC of the ARFIMA (2, *d*, 2) model. The command **AIC(arima(x, order=c(2,0,1)))** calculates the AIC of the ARIMA (2, 0, 1) structure.
   - Estimate *d* of the model with the smallest AIC or BIC using the command **summary(fracdiff(x, nar=0, nma=2))**.
   - Compute a 0.95-confidence interval using the estimate of d ($\hat{d}$) and its SE: $[\hat{d} - 1.96 \cdot SE;\ \hat{d} + 1.96\text{SE}]$.

frontiers in
PHYSIOLOGY

METHODS ARTICLE
published: 28 September 2012
doi: 10.3389/fphys.2012.00371

A tutorial introduction to adaptive fractal analysis

***Michael A. Riley*[1]*, *Scott Bonnette*[1], *Nikita Kuznetsov*[1], *Sebastian Wallot*[2] *and Jianbo Gao*[3,4]**

[1] *Department of Psychology, Center for Cognition, Action, and Perception, University of Cincinnati, Cincinnati, OH, USA*
[2] *MINDLab, Aarhus University, Aarhus, Denmark*
[3] *PMB Intelligence, LLC, West Lafayette, IN, USA*
[4] *BME, School of Life Sciences and Technology, Xi An Jiao Tong University, Xian, PR China*

Edited by:
John G. Holden, University of Cincinnati, USA

Reviewed by:
Andras Eke, Semmelweis University, Hungary
Dranreb E. Juanico, Ateneo de Manila University, Philippines

****Correspondence:***
Michael A. Riley, Department of Psychology, Center for Cognition, Action, and Perception, University of Cincinnati, Cincinnati, OH 45221-0376, USA.
e-mail: michael.riley@uc.edu

The authors present a tutorial description of adaptive fractal analysis (AFA). AFA utilizes an adaptive detrending algorithm to extract globally smooth trend signals from the data and then analyzes the scaling of the residuals to the fit as a function of the time scale at which the fit is computed. The authors present applications to synthetic mathematical signals to verify the accuracy of AFA and demonstrate the basic steps of the analysis. The authors then present results from applying AFA to time series from a cognitive psychology experiment on repeated estimation of durations of time to illustrate some of the complexities of real-world data. AFA shows promise in dealing with many types of signals, but like any fractal analysis method there are special challenges and considerations to take into account, such as determining the presence of linear scaling regions.

Keywords: adaptive fractal analysis, time series analysis, fractal physiology, biosignal processing, non-linear analysis

INTRODUCTION

Adaptive fractal analysis (AFA; Hu et al., 2009; Gao et al., 2010, 2011) is a relatively new fractal analysis method that may hold promise in dealing with many types of real-world data. In this paper we present a step-by-step tutorial approach to using AFA. We begin by reviewing some basic principles of fractal processes that will be helpful for our presentation of AFA. We then discuss AFA and provide a guide for implementing it. We conclude with an analysis of some synthetic signals and of some real data from an experiment in human cognition.

FRACTAL PROCESSES

Many physiological and behavioral processes exhibit fractal dynamics. This means the measured patterns of change over time—the behavioral time series—exhibit certain properties, including *self-similarity* and *scaling* (Lebovitch and Shehadeh, 2005). Self-similarity means that the patterns of fluctuations at faster time scales mimics the patterns of fluctuations at slower time scales. Scaling means that measures of the patterns (such as the amount of variability present) depend on the resolution or the time scale at which the measurements have been taken. Many fractal analyses, including AFA, focus explicitly on how a measure of variability scales with the size of a time window over which the measure is calculated. Gao et al. (2007) provided a succinct and comprehensive treatment of various fractal analysis methods.

When conducting fractal analysis of a time series it is important to understand the concepts of *fractional Gaussian noise* (fGn) and *fractional Brownian motion* (fBm), and the differences between the two. fGn is a stationary, long-memory process, whereas fBm is a non-stationary, long-memory process (Mandelbrot and van Ness, 1968; Beran, 1994; Mandelbrot, 1997). Roughly speaking, stationary processes fluctuate by a relatively constant degree around a mean value that remains relatively constant over time, whereas for a non-stationary process the statistical moments of the process (e.g., mean and variance) are time-dependent. "Long-memory" means that the processes exhibit statistical dependencies (correlations) over very long time scales, as opposed to a process for which only adjacent or nearly adjacent data points are correlated with each other. **Figure 1** depicts sample time series of fBm and fGn processes.

fGn and fBm are, nominally, dichotomous types of signals. While this is true in an important sense, fGn and fBm are nonetheless related. The increments of a fBm process (created by differencing the signal, i.e., subtracting each value in the time series from the prior value) form a fGn signal [see Eke et al. (2000), for a detailed description of the fGn-fBm dichotomy]. Stated differently, successively summing the data points in a fGn time series will produce a fBm time series. As described below, fGn and fBm require different treatment when using fractal methods to analyze their temporal structure, and the results of a fractal analysis on these two different types of signals will necessarily have different interpretations.

A parameter called the Hurst exponent, H, provides a way to quantify the "memory" or serial correlation in a time series. The exact meaning of H depends on whether a signal is fGn or fBm. H values indicate the correlation structure of a fGn signal, but for a fBm signal the H values refer to the correlation structure of the increments obtained by differencing the time series (Cannon et al., 1997). It is therefore necessary to carefully classify a signal as fGn or fBm (or some other kind of signal) before proceeding with fractal analysis of the signal.

With that caveat noted, different H values indicate different types of long-memory. Actually, $H = 0.5$ indicates the absence of long-memory (i.e., the process is random—it possesses no memory meaning that data points are uncorrelated with each other) or possesses only short-memory (correlations across very

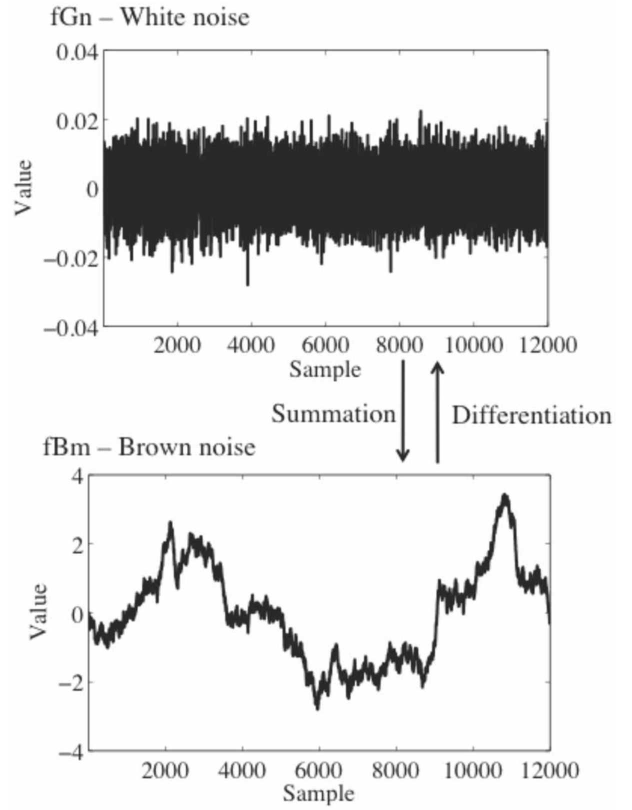

FIGURE 1 | Top: A time series of white noise, a fGn process. **Bottom**: a time series of brown noise, a fBm process. A brown noise process can be obtained by successively summing data points in the white noise process.

small scales only). This can be considered a null hypothesis of sorts when conducting a fractal analysis; one is often interested in determining whether the data possess some sort of temporal structure rather than being just a truly random, uncorrelated process.

A finding of $0 < H < 0.5$ indicates an anti-correlated or *anti-persistent* process for cases of fGn and fBm, respectively. This means that increases in the signal (for fGn) or in the increments of the signal (for fBm) are likely to be followed by decreases (and decreases are likely to be followed by increases)—a negative long-range correlation. In contrast, $0.5 < H < 1$ indicates a correlated process for fGn or what is termed a *persistent* process for fBm. In this case, increases in the signal (for fGn) or in the increments of the signal (for fBm) are likely to be followed by further increases, and decreases are likely to be followed by decreases (i.e., a positive long-range correlation). Anti-persistent and persistent processes contain structure that distinguishes them from truly random sequences of data.

To reiterate the point made earlier, and as Eke et al. (2000) carefully explained, an important first step in any type of fractal analysis is to determine the basic type of signal one has measured, i.e., whether the signal is fGn or fBm (see also Cannon et al., 1997). Simply plotting the time series can sometimes help the user make a first-pass determination about whether a pre-processing stage of integrating the data is required. Integration is required only if the data are a stationary, noisy increment process (such as fGn; **Figure 1**). Integration is not advised if the data are a non-stationary random-walk process (such as fBm; **Figure 1**). The consequences of this choice are important; H estimates can be artificially inflated by integration of a signal which should not be integrated, for example, whereas a lack of integration when it should be performed could suggest the appearance of multiple scaling regions separated by a cross-over point when only one scaling region actually exists (see Delignieères et al., 2003).

Of course, it is often the case that a plot of the time series cannot be easily classified as an increment or random-walk process based on its appearance alone. Eke et al. (2000) presented a strategy for determining the signal type, termed the signal summation conversion (SSC) method, in the context of a broader approach to analyzing physiological signals that might exhibit fractal dynamics. The method essentially involves comparison of results obtained when the signal is integrated versus not integrated. If H values for the non-integrated data approach or exceed a value of 1, then integration of the signal is generally not recommended. H values for non-integrated and integrated time series generated by an ideal fBm process should differ by a value of 1; if the difference is considerably greater or less than 1 further scrutiny of the data is required, because in that case the data may not fit within the fBm-fGn framework (Gao et al., 2006; Kuznetsov et al., 2012).

ADAPTIVE FRACTAL ANALYSIS

AFA is similar in some regards to detrended fluctuation analysis (DFA; Peng et al., 1994), and many aspects of AFA will be familiar for readers who already understand DFA. We point out some of these similarities in our presentation of AFA to help those readers, although familiarity with DFA is not required. Because of these similarities, AFA shares many of the same advantages as DFA over other fractal methods, such as the fact that H estimated by DFA and AFA do not saturate at 1 as is the case for other methods (Gao et al., 2006).

But despite the similarities between the methods, there are important differences which provide AFA with some advantages over DFA. For example, AFA can deal with arbitrary, strong non-linear trends while DFA cannot (Hu et al., 2009; Gao et al., 2011), AFA has better resolution of fractal scaling behavior for short time series (Gao et al., 2012), AFA has a direct interpretation in terms of spectral energy while DFA does not (Gao et al., 2011), and there is a simple proof of why AFA yields the correct H while such a proof is not available for DFA [see Equations 6 and 7 in Gao et al. (2011)].

It is important to note that like many other analyses used to quantify fractal scaling AFA cannot be used independently to assert that a process is or is not a fractal process. Because there are non-fractal processes that can falsely give the appearance of fractal scaling and long-range correlations, it is desirable to use other methods for this purpose (e.g., Wagenmakers et al., 2004; Delignieères et al., 2005; Farrell et al., 2006; Torre et al., 2007).

The first step in AFA is to identify a globally smooth trend signal that is created by patching together local polynomial fits to the time series. This is one of the primary differences between DFA and AFA; DFA does not involve the creation of this globally smooth trend, and instead relies on discontinuous, piece-wise linear fits. Basically, creating a globally smooth trend signal means that one tries to recreate local features of the data using simple polynomial functions. An example is shown in **Figure 2**. Small segments of the time series can be approximated reasonably well by adjusting the parameters of a polynomial regression model.

We can now express these ideas in more precise terms [see also Tung et al. (2011), who provided a thorough description of the detrending scheme that forms the basis of AFA]. The goal of this step of the analysis is to create a global trend—a synthetic time series $v(i)$, $i = 1, 2, \ldots, N$, where N is the length of the original time series. We denote the original time series as $u(i)$. Determination of the global trend is achieved by partitioning the original data $u(i)$ into windows of length $w = 2n + 1$, with the windows overlapping by $n + 1$ points. Since setting w (a process we describe below) determines the value of n [i.e., $n = (w - 1)/2$], n is not a free parameter that must be chosen.

Within each window the best fitting polynomial of order M is identified. This is done through standard least-squares regression—the coefficients of the polynomial model are adjusted until the polynomial fits the data with the least amount of residual error. Increasing the order M can usually enhance the quality of the fit, but one must be cautious about over-fitting the data. Typically M should be 1 or 2—i.e., a linear or quadratic function. The goal is not to fit every squiggle or variation in $u(i)$ with the polynomial model, but simply to capture any relatively global trends in the data while leaving enough residual variability to analyze further. Presently, there are no validated, objective criteria for selecting M, so careful exploration of different M values may be required when analyzing a given time series.

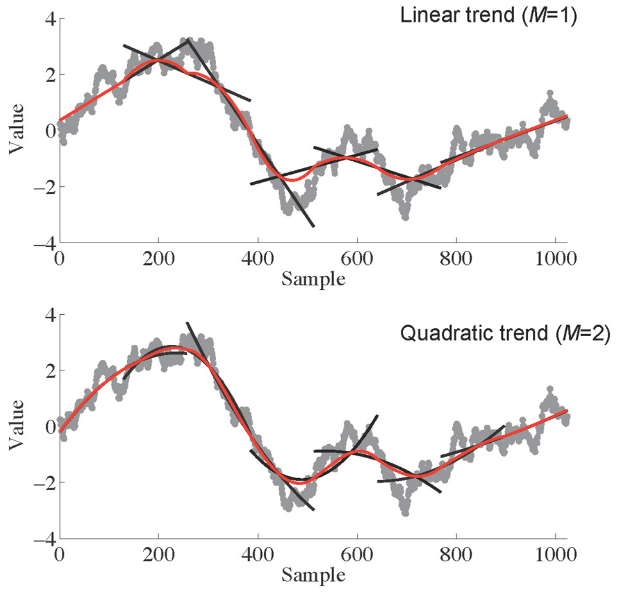

FIGURE 2 | An illustration of the process of identifying a globally smooth trend signal. Linear (**Top**; $M = 1$) or polynomial (**Bottom**; $M = 2$) trends are fit to pieces of the signal of length w (257 in this case). These fits are shown as black lines superimposed on the original data series (gray curves). The local fits are then stitched together (see Equation 1) to create a smooth global trend signal, depicted in red. Notice that when the end of the series is encountered only half of the data points in that window are used for the trend without smoothing.

The local fits then have to be "stitched" together in such a way that they provide a smooth global fit to the time series. Without this stitching, the local polynomial fits would be disconnected with each other, as is the case for DFA. The stitching and the resulting smooth trend signal thus represents a major distinction between DFA and AFA. The fit to overlapping regions is created by taking a weighted combination of the fits of two adjacent regions to ensure that the concatenation of the local fits is smooth [mathematically, this means that $v(i)$ is continuous and differentiable], according to

$$y^{(c)}(l) = w_1 y^{(i)}(l + n) + w_2 y^{(i+1)}(l), \quad l = 1, 2, \ldots, n + 1 \quad (1)$$

where $w_1 = \left(1 - \frac{l-1}{n}\right)$ and $w_2 = \frac{l-1}{n}$. According to this scheme, the weights decrease linearly with the distance between the point and the center of the segment. This ensures symmetry and effectively eliminates any jumps or discontinuities around the boundaries of neighboring regions. In fact, the scheme ensures that the fitting is continuous everywhere, is smooth at the non-boundary points, and has the right- and left-derivatives at the boundary. By choosing the parameters of each local fit to maximize the goodness of fit in each case, and then applying Equation 1 to stitch the local fits together, the global fit will be the best (smoothest) fit to the overall time series. Furthermore, this fitting scheme will work with any arbitrary signal without any a priori knowledge of the trends in the data.

The next step is to detrend the data by removing the global trend signal that was just created. We remove the trend because are interested in how the variance of the residuals of the fit—the more fine-grained fluctuations in the original time series $u(i)$—scale with w, as described below. This type of detrending is very different than simply removing a linear (or higher-order) fit to the original time series prior to data analysis (cf. Di Matteo et al., 2003); the detrending method in AFA (and DFA) is done locally over windows of varying length w but not to the entire time series as a whole. The residuals of the fit of the data to the trend signal are identified by subtracting the global trend from the original time series—we compute $u(i) - v(i)$. (This is similar to the detrending step performed in DFA, except that as noted for DFA the local linear fits are not smoothly stitched together to create a globally smooth trend signal, but rather are discontinuous with respect to one another.)

These steps that have been described are then repeated for a range of w values (i.e., for a range of time scales). Thus, one must choose a minimum and maximum w, as well as the size of the time steps (i.e., increases in w) used for the analysis. It is perhaps best to begin with the smallest and largest possible w values, i.e., $w = 3$ samples and $w = N/2$ samples (or $N/2 + 1$ if the time series has an even number of samples) where N is the length of the time series. However, as discussed by Cannon et al. (1997), exclusion of some of the smaller and larger window sizes can increase the reliability of H estimates. This may be a helpful step when analyzing signals that show a single scaling region over some intermediate range of time scales, and where issues such as measurement noise or insufficient time series length could cause an apparent breakdown of scaling at smaller and larger time scales, respectively. However, one should first ensure that the regions under consideration for exclusion do not themselves contain distinct types of fractal scaling (i.e., that the signal contains multiple scaling regions) to avoid loss of information about the signal. In light of such considerations, we used a w range of 3 to $(2^9 + 1 \;=)$ 513 samples for the analyses reported here. Any further adjustments to the w range can be determined after the next step in the analysis, when one plots $\log_2 F(w)$ as a function of $\log_2 w$, as we describe below in our analyses of sample data (and see Kuznetsov et al., 2012). Typically it is sufficient to use a step size of 1, although there may be occasions when a smaller step size is desired to obtain better resolution for identifying linear scaling relations in the plot. In our experience, a step size of less than 0.5 typically does not provide useful new information, but this is an issue that should be explored for each unique data set.

The next step is to examine the relation between the variance of the magnitude of the residuals, $F(w)$, and the window size, w. For a fractal process, the variance of the residuals scales with w (i.e., is proportional to w raised to the power H) according to

$$F(w) = \left[\frac{1}{N}\sum_{i=1}^{N}(u(i) - v(i))^2\right]^{1/2} \sim w^H. \qquad (2)$$

Fractal scaling can be quantified through the slope (obtained using simple linear regression) of a linear relation in a plot of $\log_2 F(w)$ as a function of $\log_2 w$ (**Figure 3**). This slope provides an estimate of the Hurst exponent, H.

It should be noted that two qualitatively different signals (one fGn, the other fBm) could have the same H value. For example, a white noise signal (fGn, so it is integrated prior to analysis) and a brown noise signal (fBm, so it would not be integrated prior to analysis) would both yield $H = 0.5$. Because of this one should use caution performing statistical comparisons of H for signals that may differ in regard to being fGn or fBm, and it is partly for this reason that Eke et al. (2000) emphasize the need to report signal classification along with H values. For clarity, here we distinguish between H for these two processes using the labels H_{fGn} and H_{fBm}.

The above steps constitute the basic process of applying AFA. Often one would perform AFA on each time series in an experimental data set to obtain an H value(s) for each, and then submit the set of H values to standard statistical analyses (e.g., t-test or analysis of variance) to determine if H changes across experimental conditions or between groups of subjects. That is, H becomes a dependent variable that is analyzed to determine if it changes across levels of some factor.

In the next sections, we apply AFA to known, mathematical fractal processes and then to real-world data obtained from an experiment on human cognition (repeated estimation of the duration of a time interval). The application to known fractal signals demonstrates how AFA is capable of classifying signals in terms of H. The application to real-world data reveals the complexities and challenges of using fractal analysis methods to signals that are not idealized fractal processes, like most real signals in the biological, behavioral, and physical sciences. One of these challenges is the matter of deciding how to identify linear scaling regions for AFA (and this challenge applies to other fractal methods, including DFA).

APPLICATIONS OF AFA

APPLICATION TO KNOWN FRACTAL PROCESSES

Here we present applications of AFA to artificially created time series including some well-studied fractal processes. The advantage of doing so is that we can compare the results of AFA to what should be the "right" answers based on a priori, mathematical knowledge of the artificial time series. Consistent with the goal of this paper to serve as a tutorial for using AFA, we do not mean for this to represent a fully comprehensive test of the method, but rather a straightforward, minimal demonstration that the method correctly identifies these simple "toy" signals. We present results of AFA applied to time series of random, white noise, and two idealized fractal processes known as pink noise and brown noise.

Synthetic time series properties

The artificial time series were generated using MATLAB (The MathWorks, Inc.; Natick, MA). Ten time series of length $N = 10{,}000$ were generated for each of three categories of signals using an inverse Fourier transform (Lennon, 2000): White, pink, and brown noise (see **Figure 4**). Initially, DFA was used to verify that the synthetic time series we created indeed had the desired mathematical characteristics. The integrated white, integrated pink, and non-integrated brown series were found to have mean (± 1 SD) H values of $H_{\mathrm{fGn}} = 0.49 \pm 0.01$, $H_{\mathrm{fGn}} = 0.97 \pm 0.01$, and $H_{\mathrm{fBm}} = 0.51 \pm 0.01$, respectively. The close correspondence between those results and the theoretical values of $H_{\mathrm{fGn}} = 0.5$, $H_{\mathrm{fGn}} = 1.0$, and $H_{\mathrm{fBm}} = 0.5$, respectively, indicates that the simulations produced accurate simulations of fractal processes. Based on our a priori knowledge of the signals, confirmed by visual inspection of stationarity of the time series and these preliminary checks using DFA, only the white and pink noise time series were integrated prior to AFA. The brown noise time series were not integrated.

Data reduction and analysis

The AFA steps described above were implemented on the set of 30 synthetic time series. Parameters of window size $w = 0.5$ and polynomial orders of $M = 1$ and $M = 2$ were chosen for the analyses (AFA was performed once with each polynomial order). Sample AFA plots are shown in **Figure 5**.

Results

For the white noise time series, using polynomial orders of $M = 1$ and $M = 2$, AFA returned mean H values of $H_{\mathrm{fGn}} = 0.49 \pm 0.01$ and $H_{\mathrm{fGn}} = 0.50 \pm 0.01$, respectively. The pink noise time series

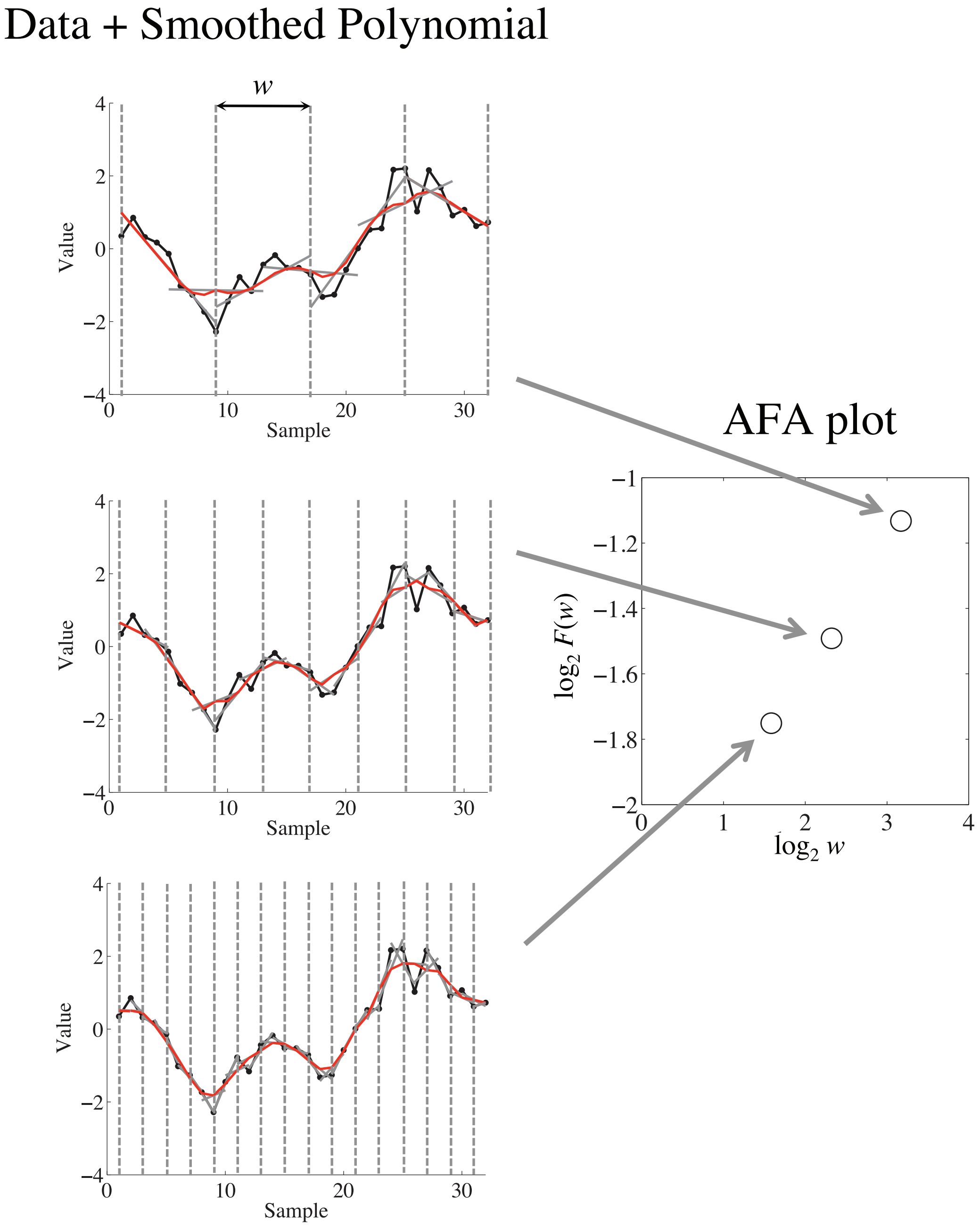

FIGURE 3 | On the left is depicted a demonstrations of how the fits to different window sizes *w* relate to the AFA plot, shown on the right. The AFA plot is a plot of $\log_2 F(w)$ (i.e., variance of the residual to the globally smooth trend signal) as a function of $\log_2 w$ (i.e., time scale or window size). A linear relation in this plot captures fractal scaling, and the slope of the line of best fit provides an estimate of the Hurst exponent H. For visual simplicity we only depicted non-overlapping window edges with the dotted gray line, while the analysis uses overlapping windows.

were also effectively categorized by AFA in the original time series. A mean H value of $H_{\mathrm{fGn}} = 0.98 \pm 0.01$ was obtained using a polynomial order $M = 1$ and a mean value of $H_{\mathrm{fGn}} = 0.99 \pm 0.02$ was found using a polynomial order $M = 2$. Lastly, AFA successfully characterized the non-integrated synthetic brown noise time series. Using polynomial orders of $M = 1$ and $M = 2$, AFA returned mean H_{fBm} values of 0.51 ± 0.02 and 0.52 ± 0.01, respectively.

Discussion

The application of AFA to the synthetic time series indicated that AFA is able to characterize the types of noise with a similar accuracy as DFA. The obtained H values corresponded very closely to the theoretically expected values and to the values obtained by DFA (presented earlier). The estimates also exhibited high reliability (low SD values). Changing the polynomial order M had very small consequences for these synthetic data; $M = 2$ resulted

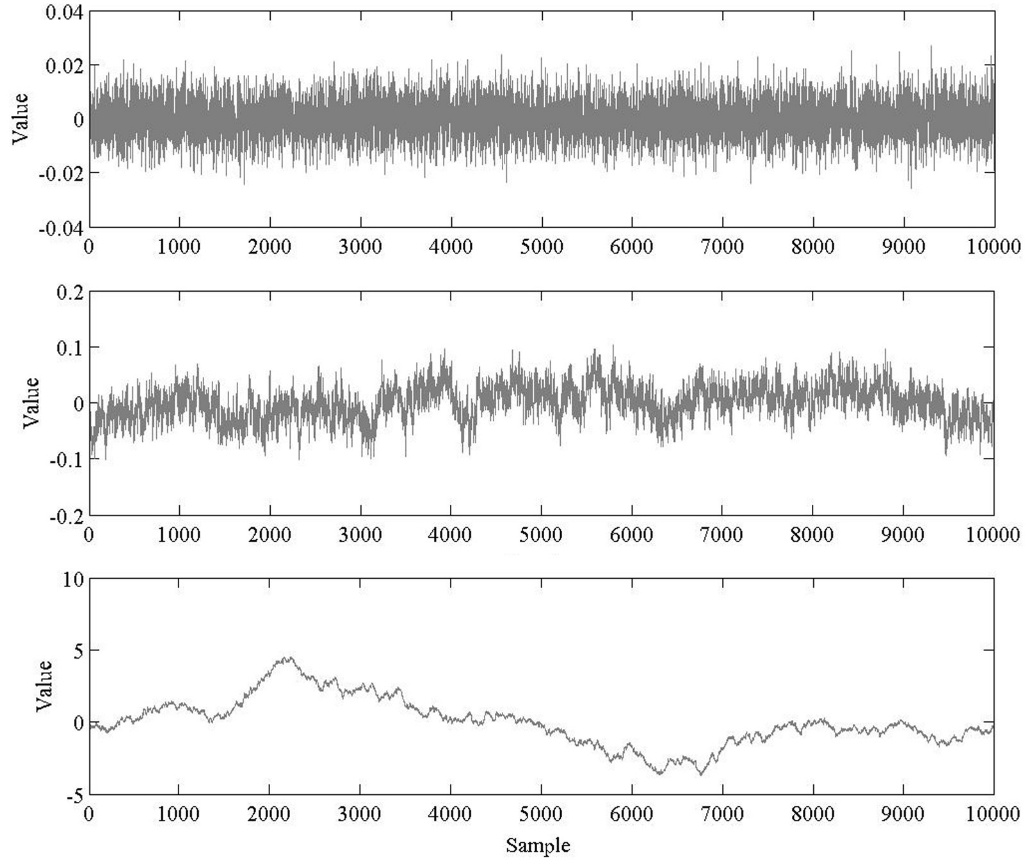

FIGURE 4 | Sample time series of white (top), pink (middle), and brown (bottom) noise.

in slightly better estimates for white and pink noise (and for this polynomial order AFA produced slightly more accurate estimates than did DFA), but slightly worse estimates for brown noise.

APPLICATION TO REAL-WORLD DATA FROM A COGNITIVE PSYCHOLOGY EXPERIMENT

We analyzed time series produced by a single participant who repeatedly performed a cognitive task (estimating the duration of a temporal interval) over the course of multiple experimental sessions. The task of repeated temporal estimation is frequently used to study the variability of human time estimation (Delignières and Torre, 2011) and was one of the first reported cases of 1/*f* noise in human cognitive behavior (Gilden et al., 1995).

Experimental methods

A single female undergraduate student who gave informed consent participated voluntarily in the study which was approved by the Institutional Review Board at the University of Cincinnati. She was paid $10 per session. The task required the participant to provide repeated estimates of a 1-s time interval. Time estimates were recorded from the presses of the spacebar of a millisecond-accurate keyboard (Apple A1048, Empirisoft). Response times were recorded using the *Psychophysics Toolbox for Matlab* (Brainard, 1997), which recorded the time of each key press during the experiment. We defined one time interval estimate as the time from the beginning of one space bar press to the next one.

At the beginning of each experimental session the participant listened to 20 metronome beats of the 1-s interval to be estimated. The metronome was then turned off, and the participant then immediately began performing the time estimation task. A total of 1050 estimates were produced consecutively in each experimental session, and each session lasted approximately 20 min. There were two experimental conditions that varied with regard to the presence or absence of feedback about the accuracy of the estimates. In the no-feedback condition the participant did not receive any explicit feedback about timing performance. This condition was similar to tasks used previously in continuation tapping experiments (Gilden et al., 1995; Chen et al., 2002; Wagenmakers et al., 2004; Torre and Delignières, 2008). In the feedback condition a computer monitor was used to present feedback specifying the error (in ms) of the most recent estimate on every trial. For example, if the participant hit the space bar 250 ms after 1 s had passed since the previous press, the feedback on the screen would read “250 ms late.” The participant first completed 10 no-feedback trials, one per day on consecutive days, and then completed 10 feedback trials (again one per day on consecutive days). For present purposes we focus

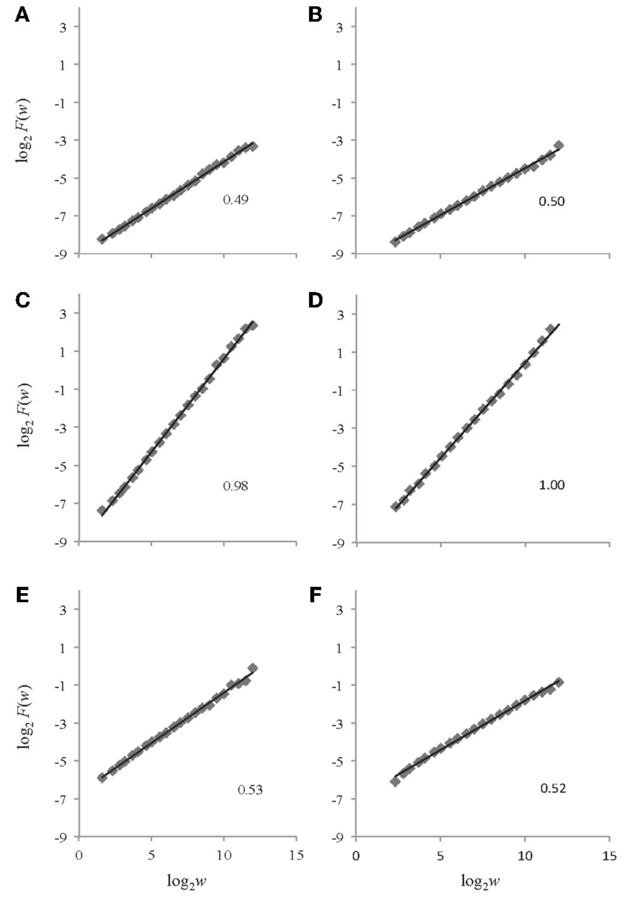

FIGURE 5 | Example $\log_2 F(w)$ vs. $\log_2 w$ plots returned by AFA for the time series depicted in Figure 4. The plots on the left side (panels **A, C,** and **E**) are from AFA using a polynomial order of $M = 1$ while those on the right side (panels **B, D,** and **F**) are from AFA using a polynomial order of $M = 2$. Plots **A** and **B** are for white noise, plots **C** and **D** are for pink noise, and plots **E** and **F** are for brown noise. The respective H_{fGn} (**A, B, C,** and **D**) and H_{fBm} (**E** and **F**) values are shown for each signal.

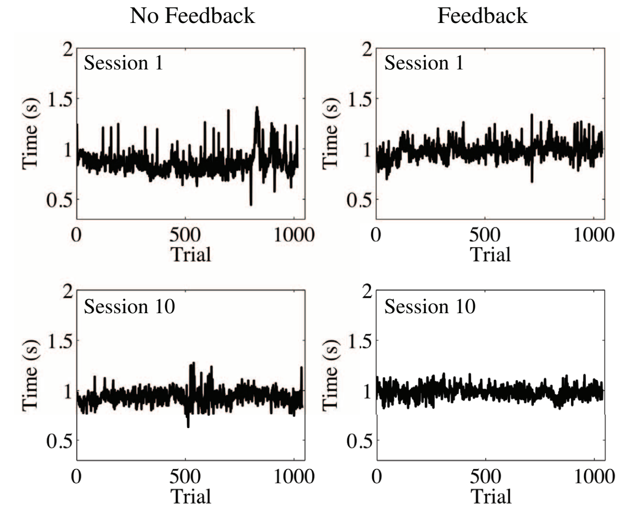

FIGURE 6 | Trial series of continuous time estimates with and without accuracy feedback after removing observations faster than 300 ms and beyond 3 SD from the mean. The participant performed the task 10 times in each feedback condition.

on just the first and the last trial in each of the two feedback conditions.

Data processing and results

We followed the standard procedure in the literature on temporal estimation to remove all observations less than 300 ms and any observations falling beyond 3 SD from the mean. Such values are likely to originate from accidents such as double-tapping the space bar or not initially pressing the bar hard enough, and a significant number of these kinds of outlying values can have detrimental results. From looking at plots of the data processed in this way (**Figure 6**), it was clear that the time series of temporal estimates were more similar to fGn than fBm (compare to **Figure 1**)[1]. Therefore, we integrated our data prior to performing AFA. Then, the same basic steps for AFA described previously were again implemented, but with the following additional considerations taken into account. We used $M = 1$ (given that using $M = 2$ did not show consistently better results in our analysis of the sample time series) and $\log_2 w$ step sizes of 0.5 (because we wanted to enhance the resolution of the AFA plots to facilitate the identification of linear scaling regions).

When dealing with real-world data, if fractal scaling is present it may be limited to a range of time scales (i.e., w values). If this is not taken into account, it may lead to inaccuracies in the estimation of H. Before estimating H, then, it was important to visually inspect the plots of $\log_2 F(w)$ as a function of $\log_2 w$ to identify regions where linear scaling might be present. If fractal scaling appears limited, it may be necessary to restrict the range of the linear fit to the plot to exclude regions where linear scaling does not occur. Inclusion of regions where fractal scaling is actually absent can lead to inaccuracies and reduce the reliability of H estimates (Cannon et al., 1997), and may present an unrealistic picture of the degree to which fractal scaling really is a major feature of the signal being analyzed. In practice, it is desirable to make this process as objective and automated as possible to avoid bias. Elsewhere (Kuznetsov et al., 2012) we have described this issue in more detail, and presented a quantitative procedure designed for this process. For the sake of this tutorial, however, we chose the linear regions visually after inspecting the AFA plots for each trial without the linear fits imposed to examine the possibility of linear scaling.

As often occurs with empirical data (as opposed to pure mathematical fractals), some of our time series yielded slightly curved $\log_2 F(w)$ functions (cf. Di Matteo et al., 2003) and had cut-off edge effects especially at larger time scales ($w > 8$ or 256 estimates). Visual inspection of the AFA plots (see **Figure 7**) suggested two distinct regions of linear scaling, one for low w

---

[1] Following suggestions by Cannon et al. (1997) and Eke et al. (2000), we performed spectral analyses on the data to provide a more objective classification of our time series as fGn or fBm. The spectral exponents ranged from 0.48 to 0.75, indicating the signals were consistent with fGn.

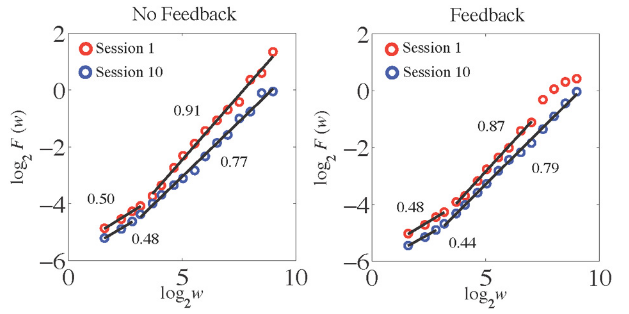

FIGURE 7 | AFA plots for the time series of time estimates presented in Figure 6. The H_{fGn} values are indicated for each scaling region.

(i.e., fast time scales) and a longer region for higher w (i.e., slower time scales), for both feedback conditions and for both the first and last experimental sessions. Such a finding was expected based on previous studies that revealed $H_{\mathrm{fGn}} < 0.5$ over the faster scales and $H_{\mathrm{fGn}} > 0.5$ at the slower scales (Lemoine et al., 2006; Delignieìres et al., 2008).

In the first experimental session the fast scaling region for the no-feedback condition spanned windows $\log_2 w$ from 1.58 to 3.17 (in terms of actual number of time estimates this corresponded to a range of 3–9). The H_{fGn} value associated with this region was 0.50, indicating the presence of uncorrelated white noise. The slower scaling region for the no-feedback condition had an H_{fGn} value of 0.91 (indicating a positive correlation at this scale) and spanned windows $\log_2 w$ from 3.17 to 9 (13–513 estimates). On the last trial, after a period of practice, the fast scaling region showed a tendency to become slightly anti-correlated but was still very close to white noise ($H_{\mathrm{fGn}} = 0.48$) and its length decreased compared to the first session (it now spanned 1.58–2.81 $\log_2 w$, or 3–7 estimates). The slow scaling region increased in length (it now spanned from $\log_2 w = 3.17$ to 9; 9 to 513 estimates) and became more uncorrelated because its H_{fGn} value decreased to 0.77.

A similar pattern of results was found for performance in the feedback condition (see **Figure 6**, right panel). The fast scaling region during the first session spanned windows from 1.58 to 3.17 $\log_2 w$ (in terms of actual number of time estimates this corresponded to a range of 3–9) and had a $H_{\mathrm{fGn}} = 0.48$, indicating uncorrelated white noise dynamics on this scale. One major difference compared to the no-feedback condition was the shorter length of the slow scaling region in the first session, which now spanned values of $\log_2 w$ from 3.17 to 8 (9–257 estimates). Similar to the no-feedback condition, the dynamics at this scale exhibited positive correlation as indexed by $H_{\mathrm{fGn}} = 0.87$. The breakdown at larger $\log_2 w$ is likely due to an initial transient evident in the time series plot for this session—for about the first 100 estimates the participant consistently underestimated the 1-s interval, but then began to estimate it more accurately. Because this only happened during one part of the trial, this affected the slowest scaling region of the AFA plot. At trial number 10, similarly to the no-feedback condition, the fast scaling region showed a tendency to become slightly more anti-correlated but was still very close to white noise ($H_{\mathrm{fGn}} = 0.44$) and its length decreased compared to the first session (it now spanned 1.58–2.81 $\log_2 w$, or 3–7 estimates). The slow scaling region increased in length (it now spanned $\log_2 w = 3.17$–9; 9–513 estimates) and became less correlated because its H_{fGn} value decreased to 0.79.

Discussion

Finite, real-world time series are typically more complex than the ideal simulated noises of mathematics. For example, as was apparent in these time series, experimental data can contain multiple scaling regions. Partly, this may be because experimental data contain both the intrinsic dynamics of the process that generated the signal plus the measurement noise inherent in any recording device. Apart from that, the intrinsic dynamics of real-world signals may have singular events and non-stationarities that if severe enough often can complicate many analyses (including AFA). Because of this it is very important to carefully examine the raw data and the corresponding scaling plots before conducing any quantitative analyses.

With regard to the dynamics of cognitive performance in this temporal estimation task, these results provide preliminary evidence of the presence of practice effects in the continuous time estimation task. Practice led to a decrease in the H exponent of the slow scaling region, suggesting that the responses became somewhat more uncorrelated at this scale with practice. Of course our preliminary results have to be interpreted with caution because they are based on single participant and there are individual differences in the slow scaling region H values in this task (Torre et al., 2011). The differences between feedback conditions at the fast time scales were not expected because previous literature reported anti-correlated dynamics at this scale (Lemoine et al., 2006; Delignieìres et al., 2008). Feedback clearly resulted in an increased tendency for anti-correlated, corrective dynamics at faster time scales because participants were displayed their performance with regard to the benchmark 1 s time. They appeared to use that information to correct performance on a trial-by trial-basis. In the no-feedback condition, this information was not readily available, which led to essentially random performance at the fast time scales.

GENERAL DISCUSSION

We applied AFA to known fractal signals and to real-world data from an experiment in human cognitive psychology that involved the repeated reproduction of a time interval. AFA recovered the H values of the known mathematical signals with high accuracy. This was generally true for both $M = 1$ and $M = 2$. The choice of polynomial order did not have a very large effect, although $M = 2$ yielded slightly better results for the white and pink noise signals but slightly worse results for the brown noise signal. Linear scaling was well defined over a single region for these signals.

Application of AFA to the experimental data revealed some of the complexities in applying fractal analyses to real data, particularly the issue of identification of linear scaling regions. We determined the scaling regions visually and then fit lines to them to obtain estimates of H. Often this is sufficient, but it is not an objective process and it could be subject to bias in an experiment that involves testing a particular hypothesis or an initial effort to classify a previously unanalyzed type of signal. If visual selection of the scaling region is used, it should be done by multiple observers (so that inter-rater reliability can be computed) who are blind to the experimental conditions and study hypotheses (to avoid bias). In Kuznetsov et al. (2012) we present an objective, quantitative technique based on model-selection methods that could be used to identify scaling regions, but more work remains to be done on this issue.

For the experimental time series we analyzed two linear scaling regions were apparent rather than one. Consistent with previous results using other analysis methods including spectral analysis (Lemoine et al., 2006; Delignières et al., 2008), these regions showed distinct slopes. The faster time scale yielded lower H_{fGn} and were basically random white noise processes (especially for the no-feedback condition) with a slight tendency toward exhibiting anti-correlated fluctuations. The longer time scale yielded higher H_{fGn} values consistent with a correlated process that was close to idealized pink-noise. The presence of feedback had some influence on the structure of the fluctuations of the repeated temporal estimates, as did the practice afforded by performance on consecutive experimental sessions. One of these effects was that linear scaling for the slower time scale broke down at larger w for the first session in the no-feedback condition, but spanned the entire upper range of w for the last session. These results show that AFA may be sensitive to experimental manipulations that affect the temporal structure of data series both with regard to the estimated H values and the range of w over which fractal scaling occurs.

Besides the issue of identifying linear scaling region, AFA requires several other choices such as the step size for the window size w. Typically 0.5 or 1 $\log_2 w$ are used, with smaller values providing greater resolution in the AFA plot. In principle this choice should have little impact on H estimates, and would not seriously impact computation time except perhaps for extremely long time series. It could, however, have a strong impact on the ability to identify linear scaling regions, especially with regard to resolving the existence of linear scaling regions at faster time scales. The choice of polynomial order M for the local fits is also important, especially for signals that may have oscillatory or nonlinear trends as higher-order polynomials may be more effective at extracting those trends. Typical choices of 1 or 2 seemed to provide about the same accuracy in estimates of H for the known signals we analyzed.

Other factors that impact the ability to identify linear scaling include the sampling rate and the trial length, which, respectively, will affect the ability to resolve faster and slower time scales. These are important choices. A very high sampling rate might indicate the appearance of scaling at very fast time scales, but if those time scales are not physically realistic, one should be cautious about interpreting them. Increasing trial length may help reveal or resolve scaling over very long time scales, which may be very important when dealing with apparently non-stationary time series.

Ideally, AFA should be used in conjunction with other methods, and converging results should be sought. But because AFA but has several advantages over similar methods such as DFA (Gao et al., 2011) the results may not always agree, so care should be taken in interpreting the results. Like all fractal analysis methods, AFA requires careful consideration of signal properties, parameter settings, and interpretation of results, and should not be applied blindly to unfamiliar signals. It is particularly important to plot and carefully inspect the time series and the AFA plots to ensure that the apparent signal properties match with the obtained results. In addition, as we noted previously the appearance of linear scaling regions in an AFA plot is not a definitive test for fractal scaling. When used carefully AFA may provide another useful tool for analyzing signals that may exhibit fractal dynamics.

ACKNOWLEDGMENTS

Supported by NSF grants CMMI 1031958 (Jianbo Gao) and BCS 0926662 (Michael A. Riley).

REFERENCES

Beran, J. (1994). *Statistics for Long-Memory Processes.* Boca Raton, FL: CRC Press.

Brainard, D. H. (1997). The psychophysics toolbox. *Spat. Vis.* 10, 433–436.

Cannon, M. J., Percival, D. B., Caccia, D. C., Raymond, G. M., and Bassingthwaighte, J. B. (1997). Evaluating scaled windowed variance methods for estimating the Hurst coefficient of time series. *Physica A* 241, 606–626.

Chen, Y., Repp, B., and Patel, A. (2002). Spectral decomposition of variability in synchronization and continuation tapping: comparisons between auditory and visual pacing and feedback coditions. *Hum. Mov. Sci.* 21, 515–532.

Delignières, D., Deschamps, T., Legros, A, and Caillou, N. (2003). A methodological note on non-linear time series analysis: is Collins and De Luca (1993)'s open- and closed-loop model a statistical artifact? *J. Mot. Behav.* 35, 86–96.

Delignières, D., and Torre, K. (2011): Event-based and emergent timing: dichotomy or continuum? A reply to Repp and Steinman (2010). *J. Mot. Behav.* 43, 311–318.

Delignières, D., Torre, K., and Lemoine, L. (2005). Methodological issues in the application of monofractal analyses in psychological and behavioral research. *Nonlinear Dynamics Psychol. Life Sci.* 9, 451–477.

Delignières, D., Torre, K., and Lemoine, L. (2008). Fractal models for event-based and dynamical timer. *Acta Psychol.* 127, 382–397.

Di Matteo, T., Aste, T., and Dacorogna, M. M. (2003). Scaling behaviors in differently developed markets. *Physica A* 324, 183–188.

Eke, H. A., Bassingthwaighte, P. J., Raymond, G., Percival, D., Cannon, M., Balla, I., and Ikrényi, C. (2000). Physiological time series: distinguishing fractal noises from motions. *Pflügers Arch.* 439, 403–415.

Farrell, S., Wagenmakers, E.-J., and Ratcliff, R. (2006). 1/*f* noise in human cognition: is it ubiquitous, and what does it mean? *Psychon. Bull. Rev.* 13, 737–741.

Gao, J. B., Cao, Y. H., Tung, W. W., and Hu, J. (2007). *Multiscale Analysis of Complex Time Series: Integration of Chaos and Random Fractal Theory, and Beyond.* Hoboken, NJ: Wiley Interscience.

Gao, J. B., Hu, J., Mao, X., and Perc, M. (2012). Culturomics meets random fractal theory: insights into long-range correlations of social and natural phenomena over the past two centuries. *J. R. Soc. Interface* 9, 1956–1964.

Gao, J. B., Hu, J., and Tung, W. W. (2011). Facilitating joint chaos and fractal analysis of biosignals through nonlinear adaptive filtering. *PLoS ONE* 6:e24331. doi: 10.1371/journal.pone.0024331

Gao, J. B., Hu, J., Tung, W. W., Cao, Y. H., Sarshar, N., and Roychowdhury, V. P. (2006). Assessment of long range correlation in time series: how to avoid pitfalls. *Phys. Rev. E* 73, 016117.

Gao, J. B., Sultan, H., Hu, J., and Tung, W. W. (2010). Denoising nonlinear time series by adaptive filtering and wavelet shrinkage: a comparison. *IEEE Signal Process. Lett.* 17, 237–240.

Gilden, D. L., Thornton, T., and Mallon, M. (1995). 1/f noise in human cognition. *Science* 267, 1837–1839.

Hu, J., Gao, J. B., and Wang, X. S. (2009). Multifractal analysis of sunspot time series: the effects of the 11-year cycle and Fourier truncation. *J. Stat. Mech*. P02066.

Kuznetsov, N., Bonnette, S., Gao, J., and Riley, M. A. (2012). Adaptive fractal analysis reveals limits to fractal scaling in center of pressure trajectories. *Ann. Biomed. Eng.* doi: 10.1007/s10439-012-0646-9. [Epub ahead of print].

Lebovitch, L. S., and Shehadeh, L. A. (2005). "Introduction to fractals," in *Tutorials in contemporary nonlinear methods for the behavioral sciences,* eds M. A. Riley and G. C. Van Orden 178–266. Retrieved June 28 2012, from http://www.nsf.gov/sbe/bcs/pac/nmbs/nmbs.jsp

Lemoine, L., Torre, K., and Delignières, D. (2006). Testing for the presence of 1/f noise in continuation tapping data. *Can. J. Exp. Psychol.* 60, 247–257.

Lennon, J. L. (2000). Red-shifts and red herrings in geographical ecology. *Ecography* 23, 101–113.

Mandelbrot, B. B. (1997). *Fractals and Scaling in Finance.* New York, NY: Springer-Verlag.

Mandelbrot, B. B., and van Ness, J. W. (1968). Fractional Brownian motions, fractional noises and applications. *SIAM Rev.* 10, 422–437.

Peng, C. K., Buldyrev, S. V., Havlin, S., Simons, S. M., Stanley, H. E., and Goldberger, A. L. (1994). Mosaic organization of DNA nucleotides. *Phys. Rev. E* 49, 1685–1689.

Torre, K., Balasubramaniam, R., Rheaume, N., Lemoine, L., and Zelaznik, H. (2011). Long-range correlation properties in motor timing are individual and task specific. *Psychon. Bull. Rev.* 18, 339–346.

Torre, K., and Delignières, D. (2008). Unraveling the finding of 1/f noise in self-paced and synchronized tapping: a unifying mechanistic model. *Biol. Cybern.* 99, 159–170.

Torre, K., Delignières, D., and Lemoine, L. (2007). $1/f^{\beta}$ fluctuations in bimanual coordination: an additional challenge for modeling. *Exp. Brain Res.* 183, 225–234.

Tung, W. W., Gao, J. B., Hu, J., and Yang, L. (2011). Recovering chaotic signals in heavy noise environments. *Phys. Rev. E* 83, 046210.

Wagenmakers, E. J., Farrel, S., and Ratcliff, R. (2004). Estimation and interpretation of 1/f-noise in human cognition. *Psychon. Bull. Rev.* 11, 579–615.

Conflict of Interest Statement: The authors declare that the research was conducted in the absence of any commercial or financial relationships that could be construed as a potential conflict of interest.

Received: 29 June 2012; paper pending published: 03 August 2012; accepted: 29 August 2012; published online: 28 September 2012.

Citation: Riley MA, Bonnette S, Kuznetsov N, Wallot S and Gao J (2012) A tutorial introduction to adaptive fractal analysis. Front. Physio. ***3****:371. doi: 10.3389/fphys.2012.00371*

This article was submitted to Frontiers in Fractal Physiology, a specialty of Frontiers in Physiology.

frontiers in
PHYSIOLOGY

METHODS ARTICLE
published: 18 June 2012
doi: 10.3389/fphys.2012.00208

Relative roughness: an index for testing the suitability of the monofractal model

Vivien Marmelat, Kjerstin Torre and Didier Delignières*

Movement to Health, University Montpellier 1, Montpellier, France

Edited by:
John G. Holden, University of Cincinnati, USA

Reviewed by:
Maarten Wijnants, Radboud University Nijmegen, Belgium
Theo Rhodes, University of California Merced, USA

Correspondence:
Didier Delignières, EA 2991 Movement to Health, University Montpellier 1, Euromov, 700 Avenue du Pic Saint Loup, 34090 Montpellier, France.
e-mail: didier.delignieres@univ-montp1.fr

Fractal analyses have become very popular and have been applied on a wide variety of empirical time series. The application of these methods supposes that the monofractal framework can offer a suitable model for the analyzed series. However, this model takes into account a quite specific kind of fluctuations, and we consider that fractal analyses have been often applied to series that were completely outside of its relevance. The problem is that fractal methods can be applied to all types of series, and they always give a result, that one can then erroneously interpret in the context of the monofractal framework. We propose in this paper an easily computable index, the *relative roughness* (RR), defined as the ratio between local and global variances, that allows to test for the applicability of fractal analyses. We show that RR is confined within a limited range (between 1.21 and 0.12, approximately) for long-range correlated series. We propose some examples of empirical series that have been recently analyzed using fractal methods, but, with respect to their RR, should not have been considered in the monofractal model. An acceptable level of RR, however, is a necessary but not sufficient condition for considering series as long-range correlated. Specific methods should be used in complement for testing for the effective presence of long-range correlations in empirical series.

Keywords: monofractal model, long-range correlations, relative roughness

INTRODUCTION

Long-range correlations (LRC) represent a very special kind of fluctuation in time series. In a long-range correlated series, the current value is related to a large set of previous values, often hundreds. Intuitively, the concept of short-term correlation is easily conceivable: the current value can, for example, keep a memory of the just previous value, as in one-order auto-regressive processes. The concept of LRC is less intuitive: correlations appear simultaneously among all time scales, and are not confined on the short-term: the current value seems to possess the memory of the whole previous history of the series.

Long-range correlations have been discovered in the dynamics of a number of natural and physical systems, including for example the series of discharges of the Nile River (Hurst, 1951), the series of magnitudes of earthquakes (Matsuzaki, 1994), the evolution of traffic in Ethernet networks (Leland et al., 1994), or the dynamics of self-esteem over time (Delignières et al., 2004). In the domain of human movement, LRC have been evidenced in serial reaction time (Gilden, 1997; van Orden et al., 2003), in finger tapping (Gilden et al., 1995; Lemoine et al., 2006), in stride duration during walking (Hausdorff et al., 1995), or in relative phase in a bimanual coordination task (Torre et al., 2007a).

Long-range correlations appear as a ubiquitous phenomenon, and this is one of the reasons that motivated its scientific appealing. However, LRC should not be considered only a mathematical curiosity: a number of authors suggested that LRC in a time series is the hallmark of the complexity of the system that produced the series. Complexity, in this theoretical context, is conceived as the rich set of interactions between the multiple components that compose the system. LRC have been particularly studied in physiology and movement sciences, and have been recurrently evidenced in the series produced by young and healthy organisms. In contrast, LRC disappeared in the series produced by aged of diseased systems (Hausdorff et al., 1997; Goldberger et al., 2002). This result has been interpreted as the hallmark of a loss of complexity, induced by aging or disease.

Long-range correlations analyses are based on the monofractal model, initially introduced by Mandelbrot and van Ness (1968). This model is supported by a number of basic assumptions that should be satisfied for a proper use of the analysis methods and for sustaining consistent interpretations. In general, statistical models allow the use of formal statistical properties for analyzing the properties of empirical data, but this is only possible if there is a kind of analogy between the formal properties of the model and those of the analyzed data.

This principle was at the origin of the Stevens' theory of scales of measurement (Stevens, 1951). As stated by Stevens, measure is acceptable from the moment where there is a correspondence between the empirical properties of the observed phenomenon and the formal properties of numbers. In that case, the latter can serve as a model for the former. Stevens described four levels of measurement (nominal, ordinal, interval, and ratio scales), each level being characterized by distinctive properties, and especially by the set of mathematical operations that it allows. Each empirical phenomenon has properties that limit to a specific level of measurement, and any reference to a higher level causes erroneous uses numbers and inadequate statistical descriptions.

A similar reasoning can be sustained for normality. The suitability of parametric statistical tests depends on the adequacy of the normal distribution for accounting for the actual distribution of the analyzed samples. This assumption, basically, suggests that each value x_i in the sample is composed of the additive combination of a "true" value (μ) and a random, normally distributed noise (Eq. 1).

$$x_i = \mu + \varepsilon_i \tag{1}$$

This model supposes that the random term accounts for the multiple uncontrolled factors that affect the measure (individual characteristics, experimental errors, etc.). Considering that this random term is centered on zero, averaging the sample converges toward μ. The distribution of the sample is supposed to be normal, thanks to the normality of the random term, and the statistical properties of the normal distribution can be applied.

Note, however, that it is possible to use forbidden operations, with regards to the level of measurement, or to apply parametric statistics to non-normal samples. These operations will give absurd results, and statistic tests will yield erroneous conclusions, but in both cases one will obtain a "result." A similar problem can occur with the monofractal model. Fractal methods can be applied to all types of series, in absolute terms, and they always give a result, that one can then erroneously interpret in the context of the monofractal framework.

Our aim in the present paper is to provide researchers with some indications for assessing the suitability of the monofractal framework for serving as a model for a given time series. In a first step it seems necessary to present in more details the monofractal model.

THE MONOFRACTAL MODEL

This model has been introduced by Mandelbrot and van Ness (1968), and is composed of to distinct families of processes, *fractional Gaussian noises* (fGn) and *fractional Brownian motions* (fBm). These two families represent extensions of two well-known stochastic processes, white noise and Brownian motion. Brownian motion represents the displacement obtained by the iterative summation of uncorrelated, normally distributed increments. In other words, Brownian motion is the integration of a white noise process. An important property of Brownian motion is that its expected displacement is proportional to the square root of the expended time.

Fractional Brownian motions extends the concept of Brownian motion by allowing the successive increments to be correlated over time. A positive or persistent correlation signifies that an increasing trend in the past is likely to be followed by an increasing trend in the future. Conversely, a negative or anti-persistent correlation signifies that an increasing trend in the past is likely to be followed by a decreasing trend.

Mathematically, a fBm series is characterized by the following scaling law:

$$\mathrm{SD}(x) \propto \Delta t^{H} \tag{2}$$

which signifies that the standard deviation of the process is a power function of the time interval (Δt) over which it was computed. H is the Hurst exponent and can be any real number in the range $0 < H < 1$. Anti-persistent series are characterized by $H < 0.5$, and persistent series by $H > 0.5$. Brownian motion corresponds to the special case $H = 0.5$ and constitutes the frontier between anti-persistent and persistent fBm. Eq. 2 expressed the so-called *diffusion property* of fBm processes. With respect to the standard diffusion of Brownian motion (standard deviation is proportional to the square root of time), anti-persistent fBm are said to be under-diffusive, and persistent fBm over-diffusive. We present in **Figure 1** (top row) three example fBm series, for three contrasted H exponents.

Fractional Gaussian noise is defined as the series of successive increments in a fBm. In other words a fGn is the differentiation of a fBm, and conversely the integration of a fGn gives a fBm. Each fBm is then related to a specific fGn, and both are characterized by the same H exponent. We present in the bottom row of **Figure 1** the fGn series corresponding to the just above fBm series. The fGn family is centered around white noise ($H = 0.5$), which represents the frontier between anti-persistent and persistent fGn.

These two families of processes possess fundamentally different properties: fBm series are non-stationary with time-dependent variance (diffusion property), while fGn are stationary with constant expected mean and variance over time. As previously explained, fGn and fBm can be conceived as two superimposed families, invertible in terms of differentiation and integration.

Another useful conception is to conceive these two families as representing a continuum, ranging from the most anti-persistent fGn to the most persistent fBm. This fGn/fBm continuum is characterized by the presence of scaling laws that could be expressed in the frequency or in the time domain. In the frequency domain, a scaling law relates power (i.e., squared amplitude) to frequency according to an inverse power function, with an exponent β:

$$S(f) \propto \frac{1}{f^{\beta}} \tag{3}$$

This scaling law is exploited by the Power Spectral Density (PSD) method that reveals β as the negative of the slope of the

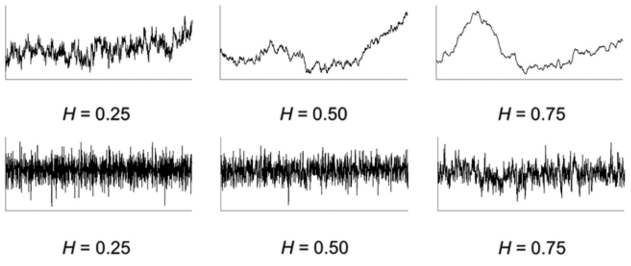

FIGURE 1 | Top row: example series of fractional Brownian motions (fBm) for three typical values of the scaling exponent. The central graph represents an ordinary Brownian motion ($H = 0.5$). The left graph shows an anti-persistent fBm ($H = 0.25$) and the right graph a persistent fBm ($H = 0.75$). The corresponding fractional Gaussian noises series (fGn) are displayed in the bottom row.

log–log representation of the power spectrum (**Figure 2**). The fGn/fBm continuum is then characterized by exponents β ranging from −1 to 3 (see **Figure 4**).

In the time domain, the typical scaling law states that the standard deviation of the integrated series is a power function of the time over which it is computed, with an exponent α. Considering a time series $x(i)$:

$$\begin{cases} y(i) = \sum_{k=0}^{i} x(k) \\ \mathrm{SD}(y) \propto n^{\alpha} \end{cases} \tag{4}$$

This scaling law is exploited by the Detrended Fluctuation Analysis (DFA) that reveals α as the slope of the log–log diffusion plot (**Figure 3**). The fGn/fBm continuum is characterized by exponents α ranging from 0 to 2 (see **Figure 4**). Note that the scaling law expressed in Eq. 4 just derives from the original definition of fBm (Eq. 1). If the series $x(i)$ is a fGn, $y(i)$ is the corresponding fBm and α is the Hurst exponent. If $x(i)$ is a fBm, $y(i)$ belongs to another family of over-diffusive processes, characterized by exponents α ranging from 1 to 3, and in that case $\alpha = H + 1$.

The different exponents that characterize these scaling laws are mutually linked by very simple equations:

For fGn series:

$$\beta = 2H - 1 \quad \text{and} \quad \alpha = H \tag{5}$$

For fBm series:

$$\beta = 2H + 1 \quad \text{and} \quad \alpha = H + 1 \tag{6}$$

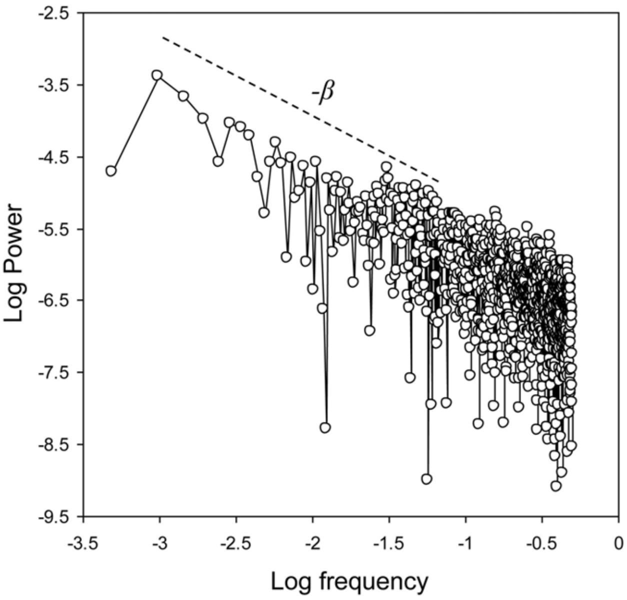

FIGURE 2 | Power Spectral Density analysis. The exponent β is given by the negative of the slope of the log–log representation of the power spectrum.

For fGn and fBm series:

$$\beta = 2\alpha - 1 \quad \text{or} \quad \alpha = \frac{(\beta + 1)}{2} \tag{7}$$

The exponents provided by PSD and DFA (β and α, respectively), are useful because they allow to unambiguously distinguish between fGn and fBm series, which could be characterized by the same H exponents.

In this fGn/fBm continuum, LRC are generally considered to appear in a narrow range, between $\beta = 0.5$ and $\beta = 1.5$ (i.e., between $\alpha = 0.75$ and $\alpha = 1.25$, see Wagenmakers et al., 2004). This range is centered on $\beta = \alpha = 1$, corresponding to the ideal $1/f$ noise. Long-range correlated series present typical fluctuations, often referred to as $1/f$ fluctuations, characterized by multiple interpenetrated waves. As can be seen in **Figure 4**, with the increase of the scaling exponent (α or β), the series becomes smoother and less stationary. Within this continuum, LRC series are characterized by a weak stationarity, and a median level of roughness.

A INDEX OF RELATIVE ROUGHNESS

As previously stated, our aim in this paper is to provide researchers with some indications for assessing the suitability of the monofractal model for a given time series. A number of procedures can be proposed, often complex and time-consuming. We think, however, that the property of roughness, previously evoked, could support a very simple and easily computable index for testing this suitability.

Roughness has been extensively used for characterizing the texture of surfaces (Thomas, 1999). In this context, roughness can be quantified by the deviations of a real surface from its ideal form. If deviations are large, the surface is rough, and the surface is smooth if deviations are small. A number of roughness parameters have been proposed, for example the *Mean Roughness*, defined as the arithmetic average of the absolute values of the deviations from the ideal surface, or the *Root Mean Square Roughness*, defined as the root mean square average of these deviations.

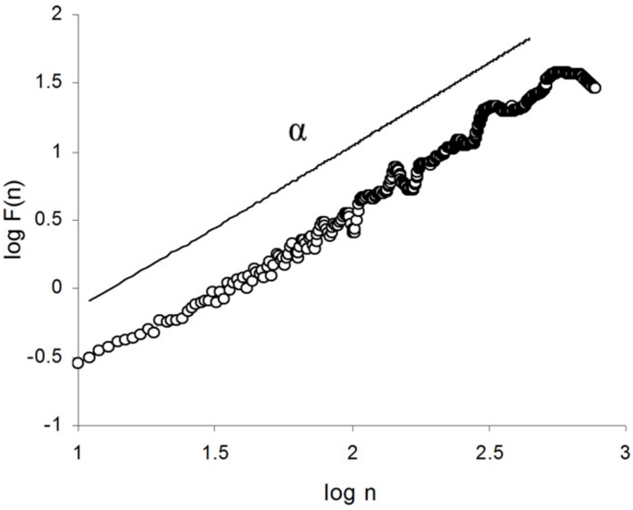

FIGURE 3 | Detrended Fluctuation Analysis. The exponent α is determined as the slope of the log–log diffusion plot.

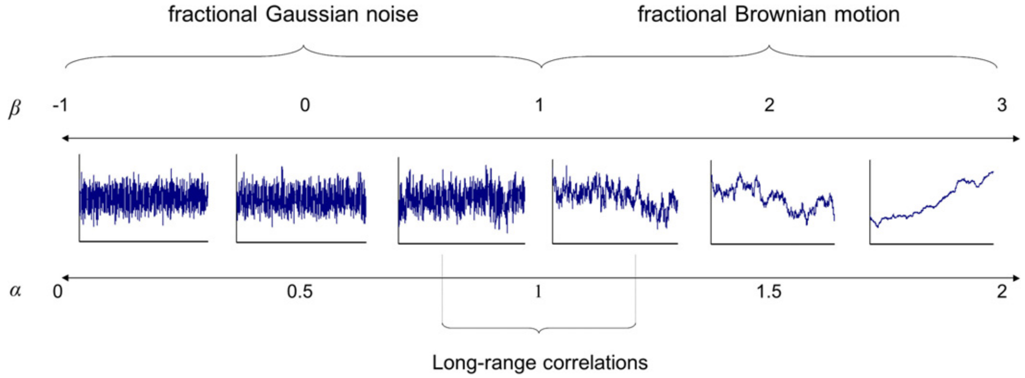

FIGURE 4 | Representation of the fGn/fBm continuum. The continuum is characterized by exponents β ranging from −1 to 3, and by exponents α ranging from 0 to 2. White noise corresponds to β = 0 and α = 0.5, and Brownian motion to β = 2 and α = 1.5. Long-range correlations are considered to appear between β = 0.5 and β = 1.5. β = α = 1 corresponds to ideal 1/*f* noise.

In the domain of time series analysis, roughness refers to the level of short-term irregularity in the evolution of the series. As previously proposed, roughness appears as a typical property of 1/*f* fluctuations, and we think that it could be useful for assessing the suitability of the monofractal model for a given series.

Roughness in a series can be assessed by the computation of local variance (Madison et al., 2009). Local variance can be defined as the variability between adjacent points in the series. This source of variance in a series is independent on others typical sources, such as long-term drifts (Madison et al., 2009), or more local trends induced by serial correlations (Torre and Balasubramaniam, 2011).

An easy way for estimating local variance is to compute the variance of the series of increments in the original series (Torre and Balasubramaniam, 2011). Some other estimates have been proposed: for example Ogden and Collier (2002) and Madison et al. (2009) assessed local variance through the average of the squared differences between adjacent values, and Delignières et al. (2004) used the average of the absolute differences between adjacent values. Despite some algorithmic divergences, all these measures provide equivalent measures of local variability, in terms of variance or standard deviation.

Local variance, however, cannot in isolation provide a relevant indication for the suitability of the monofractal model. As previously stated, local variance is independent on the strength of serial correlations in the series: similar patterns of correlation can be obtained with different levels of local variance, and conversely identical levels of local variance could appear in series possessing different levels of serial correlation (Torre and Balasubramaniam, 2011). The problem is to assess the relative contribution of local variance to the global variance of the series. In this aim, we propose an index of *relative roughness* (RR), defined as the ratio between local variance and global variance.

Consider a series (x_i). Local variance ($LVar$) can be expressed as:

$$\mathrm{LVar}\,(x_i) = \mathrm{Var}\,(x_i - x_{i-1}) = 2\,[\mathrm{Var}\,(x_i) - \gamma_1\,(x_i)] \tag{8}$$

$\gamma_1(x_i)$ representing the lag-one autocovariance. One can then obtain the following expression for RR:

$$\mathrm{RR} = 2\left[1 - \frac{\gamma_1\,(x_i)}{\mathrm{Var}\,(x_i)}\right] \tag{9}$$

This equation suggests that for a white noise process, local variance should be twice the global variance, and RR should equal 2. One could also expect a progressive decrease of RR with the increase of serial correlations in the series. Finally, the diffusion property suggests that for fBm series global variance increases with series length. As a consequence, for fBm series RR should decrease as series length increases.

In order to analyze the evolution of RR according to the strength of serial correlations in the series, we generated exact fractal series with α exponents ranging from 0.1 (highly anti-persistent fGn) to 1.9 (highly persistent fBm), by steps of 0.1, using the algorithm proposed by Davies and Harte (1987). In order to check the effect of series length on RR, we worked on series of 512, 1024, and 2048 data points, which correspond to the series lengths mostly used in the literature. One-hundred series was generated for each α level and each series length. The results are illustrated in **Figure 5**. As expected RR decreased as correlations increased in the series. RR was about 2.0 for white noise, and anti-persistent fGn series were characterized by values greater than 2.0, up to 2.9 for the most negatively correlated series ($\alpha = 0.1$). For fBm series RR presented an asymptotical trend toward zero as α increased. As expected, series length affects RR, but this effect is located in a narrow range of anti-persistent fBm (between $\alpha = 1.0$ and $\alpha = 1.4$).

We present in **Table 1** the details of the results for the range 0.5–1.5. We obtained for 1/*f* series ($\alpha = 1.0$) a mean RR ranging from 0.4 to 0.5, depending of series length. On the basis of these results, it is possible to roughly estimate the limits of the range of RR values that corresponds to the series that are usually considered as long-range correlated ($0.75 < \alpha < 1.25$). For series of 512 points, RR should be approximately comprised between 1.24 and 0.28, for series of 1024 points between 1.24 and 0.17, and for series of 2048 points between 1.21 and 0.12. Note that these values

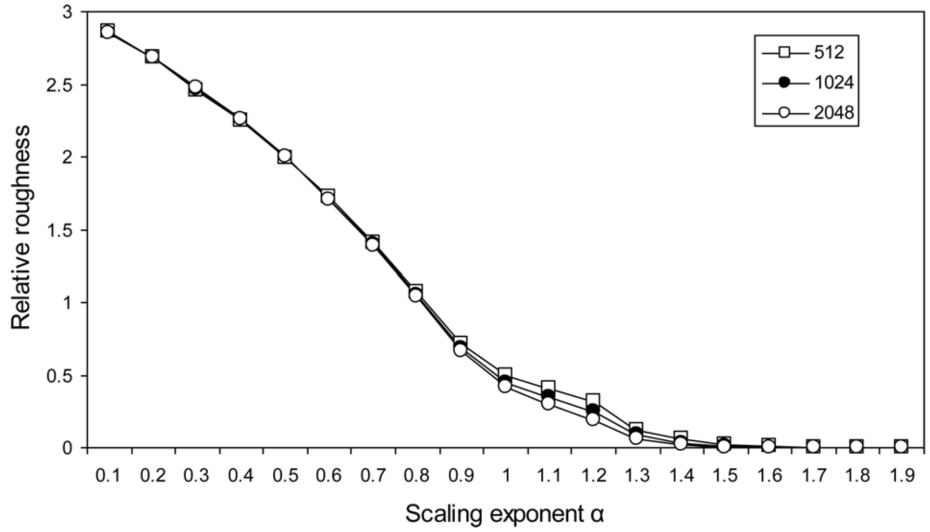

FIGURE 5 | Relative roughness as a function of the scaling exponent α in simulated fGn and fBm series. Results are given for series lengths of 512, 1024, and 2048 data points.

Table 1 | Mean relative roughness (RR), computed for exact fractal series with α exponents ranging from 0.5 to 1.5.

α	Relative roughness (RR)		
	512	**1024**	**2048**
0.5	1.990	2.005	2.004
0.6	1.722	1.705	1.705
0.7	1.410	1.397	1.388
0.8	**1.074**	**1.052**	**1.037**
0.9	**0.718**	**0.688**	**0.662**
1.0	**0.496**	**0.449**	**0.417**
1.1	**0.407**	**0.349**	**0.301**
1.2	**0.318**	**0.248**	**0.186**
1.3	0.116	0.087	0.057
1.4	0.056	0.031	0.017
1.5	0.018	0.010	0.005

Results are given for series lengths of 512, 1024, and 2048 data points. Forty series have been generated for each α level and each series length. Series that correspond to the LRC range are indicated in bold.

should certainly not be considered as strict and absolute boundaries. The present results are dependent on the method we used to generate series, and another method would have given slightly different values.

RELEVANT SERIES FOR FRACTAL ANALYSIS: RELATIVE PHASE IN BIMANUAL COORDINATION TASKS

The aim of RR is to provide an easily computable index for testing the *a priori* suitability of the monofractal model. We think that this index could be useful for distinguishing the variables that could be relevant for the application of fractal analyses, and those that clearly fall out of the scope of the monofractal model.

An interesting example can be proposed on the basis of studies that analyzed the fractal properties of series collected in bimanual coordination tasks. In the bimanual coordination paradigm, participants are requested to perform simultaneous rhythmical oscillations with the two hands, according to a prescribed phase relationship between the two effectors (Kelso, 1984). Two modes of coordination have been shown to be particularly stable: the in-phase coordination, in which homologous muscles perform simultaneous contractions, and the anti-phase coordination, in which homologous muscles perform alternate contractions. The relevant variable for analyzing such coordination is the relative phase, i.e., the difference between the instantaneous phases of each oscillator. Relative phase equals 0° for the in-phase mode, and 180° for the anti-phase mode.

Two measures of relative phase are used in the literature, and are generally considered as interchangeable. Continuous relative phase (CRP) is derived from the position (x_t) and velocity (x_t) time series of each oscillator. The phase angle is determined for each oscillator using the following equation:

$$\phi_t = \tan^{-1}\left(\frac{\dot{x}_t}{x_t}\right), \tag{10}$$

and the relative phase is determined as the instantaneous difference between the phase of each oscillator.

Discrete relative phase (DRP) is punctually computed, as the temporal difference between similar inflection points in the oscillation of the two oscillators, reported to the period of one of the oscillators. CRP has often been interpreted as a higher resolution form of DRP. Nevertheless, Peters et al. (2003) showed that these two measures essentially differ in nature: DRP yields information regarding the relative dispersion of events in oscillatory signals, while CRP described their relationship in a higher order phase space.

Torre et al. (2007a) analyzed the fractal properties of both DRP and CRP series. Two example series, collected in trials performed in in-phase mode, are presented in **Figure 6** (top row). At first glance, the two series look similar, presenting a weak stationarity around a mean value of 0°. However, the DRP series (left graph) contains only 1044 data points, while the CRP series is composed of 32,000 data points (sampled at 100 Hz, representing approximately 96 consecutive cycles). The graphs in the second row highlight the differences between the two series, by focusing on 200 points for DRP and 2000 points for CRP. The DRP series is composed of discrete points, and differences between adjacent values provide the series with a marked level of roughness. In contrast the CRP series appears as a very smooth motion, with slow oscillations around the mean value.

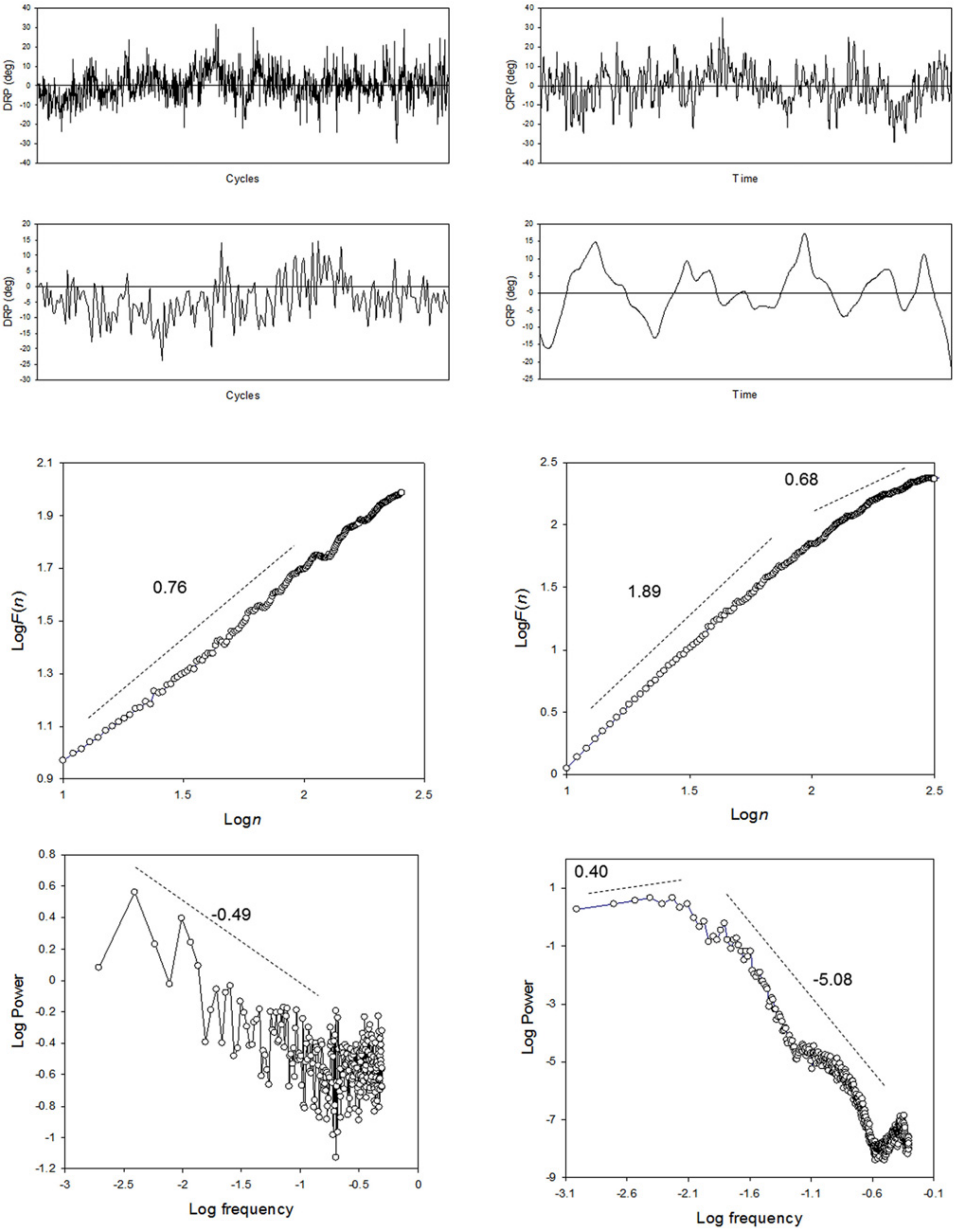

FIGURE 6 | Top Row: relative phase series collected during a bimanual coordination task. The task was performed following an in-phase mode. The left graph represents a series of discrete relative phases (DRP, 1044 data points, computed by the point estimate method at the time of maximal pronation of the right hand). The right graph is a series of continuous relative phase (CRP, 32,000 data points, sampled at 100 Hz, representing approximately 96 consecutive cycles). Second row: DRP (left) and CRP (right) series. These graphs focus on 200 points for DRP and 2000 points for CRP. Third row: average DFA diffusion plots obtained for DRP (left), and CRP (right) series. Bottom row: average log–log power spectra obtained for DRP (left), and CRP (right) series.

Relative roughness, averaged over 12 series composed of the 2048 first points of the experimental data, was about 1.22 (±0.44) for DRP, and 0.0015 (±0.000) for CRP. These results suggest that DRP series could be reasonable candidates for being modeled as fGn processes, while CRP series appear clearly out of the range of RR values expected for LRC processes.

These results are confirmed by the application of DFA and PSD. DRP series yielded a mean α exponent of 0.76 (±0.12). The mean β was 0.49 (±0.15), corresponding according to Eq. 7 to a α value of about 0.75. These values converge toward the characterization of DRP series as weakly persistent fGn series. The analysis of CRP series provided completely different results. When computed over the whole range of intervals, the mean α was of about 1.25 (±0.11). However, a close examination of the diffusion plot (see **Figure 6**) revealed a clear inflection, with a steeper slope of about 1.89 (±0.03) for short time intervals, and a flattened slope (0.69 ± 0.41) for long intervals. PSD yielded a mean log–log power spectrum that also presented an inflection, with a positive mean slope of about 0.40 (±1.58) in the very low frequency region, and a highly negative slope (-5.08 ± 0.28) in the medium to high-frequency region. This last result was consistent with that reported by Schmidt et al. (1991), which obtained very high β exponents for CRP series. One could question, however, the relevancy of computing an exponent on the basis on the average slope of this kind of spectrum. An interesting point here is the discrepancy between the results obtained in the time domain (DFA) and the frequency domain (PSD). According to Rangarajan and Ding (2000), such a discrepancy should lead researchers to doubt of the genuine presence of LRC in the analyzed series.

THE SPECIAL CASE OF BOUNDED SERIES

Another problem that could prevent the application of the monofractal model is the fact that series could appear bounded within physiological or biomechanical limits. The monofractal model suggests that fBm series are typically unbounded. The diffusion over time of a pure fBm is theoretically unlimited: fluctuations grow as a power function of time, and the expected displacement of the process from a given origin is likely to increase indefinitely.

When a series is bounded within physiological boundaries, the diffusion process is obviously limited and variance cannot exceed a ceiling value. In other words, variance is likely to become independent on time beyond a critical time interval necessary for reaching this ceiling value.

This problem was recently considered by Delignières et al. (2011a), in the domain of postural control. Research on postural control focuses on the analysis of center-of-pressure (COP) trajectory, easily recorded with force platforms. A number of authors, during the last decade, have proposed to apply to these data diverse non-linear methods, including fractal analyses. Delignières et al. (2011a) formulated strong reserves about the suitability of the fractal framework for modeling COP data, which appear clearly bounded within functional limits. Interestingly, they showed that bounding affected primarily COP velocity, rather than COP position series, as generally accepted in the literature (Collins and De Luca, 1993). This result suggested that bounding could be due to motor control limitations, rather than by biomechanical constraints as commonly assumed. We present in **Figure 7** (top row) an example COP velocity series, sampled at 40 Hz, that illustrates this bounding phenomenon: COP velocity presents highly persistent trends on the short-term, but these trends tend to reverse in direction when velocity reaches the upper or the lower limits represented by the dashed lines.

The presence of persistent trends on the short-term suggests a rather low roughness, similar to that observed for persistent fBm series. However, the ceiling effect on global variance yields surprising results: The computation of RR for 26 experimental series of COP velocity of 2048 data points gave a mean value of about 1.64 (±0.66), corresponding the value expected for weakly persistent fGn series (see **Figure 5**).

Liebovitch and Yang (1997) analyzed the effect of bounding on the results produced by fractal analyses. Especially, the diffusion plot obtained with the application of DFA is supposed in that case to present a typical inflection, with a steep slope for short time intervals revealing the persistence of the process on the short-term, and a flattening of the slope for long time intervals, due to the limitation of diffusion. The application of DFA on the series of COP velocity clearly illustrate this crossover (see **Figure 7**): the diffusion plot presents a slope of about 1.0 for short time intervals, and a slope of 0.43 for long intervals. Note that the crossover can also be revealed by PSD: the log–log power spectrum presents a marked inflection, with a positive slope in the low frequency region revealing negative correlations on the long-term, and a negative slope in the high-frequency region, due to the persistent trends on the short-term (**Figure 7**, bottom row, right column).

The application of fractal-like methods to bounded series has sometimes lead to interpretations in terms of dual fractal regime, with a persistent behavior on the short-term and an anti-persistent behavior on the long-term (e.g., Collins and De Luca, 1993; Treffner and Kelso, 1995, 1999). In the present case a simpler hypothesis related to the effect of bounding on the dynamics of the variable under study, offers a more interesting and useful interpretation.

DISCREPANCIES BETWEEN RELATIVE ROUGHNESS AND SCALING EXPONENTS

The previous examples showed how the measure of RR could allow to *a priori* assessing the plausibility of the fractal hypothesis. When RR is clearly out of the range expected for LRC, the reference to the monofractal framework can be abandoned.

Relative roughness, however, is not sufficient for unambiguously characterizing a given series as long-range correlated. In others words, a series can present a level of RR located in the range expected for LRC processes, without being actually long-range correlated.

In order to illustrate this problem, we simulated three sets of time series, possessing different correlation properties. The first set was generated by a one-order auto-regressive model:

$$y_i = \varphi y_{i-1} + \varepsilon_i \qquad (11)$$

In this equation φ is the auto-regressive parameter and was set to 0.85. ε_i is a white noise process with zero mean and unit variance. The second set was generated by an integrated one-order moving average model:

$$y_i = y_{i-1} - \theta\varepsilon_{i-1} + \varepsilon_i \qquad (12)$$

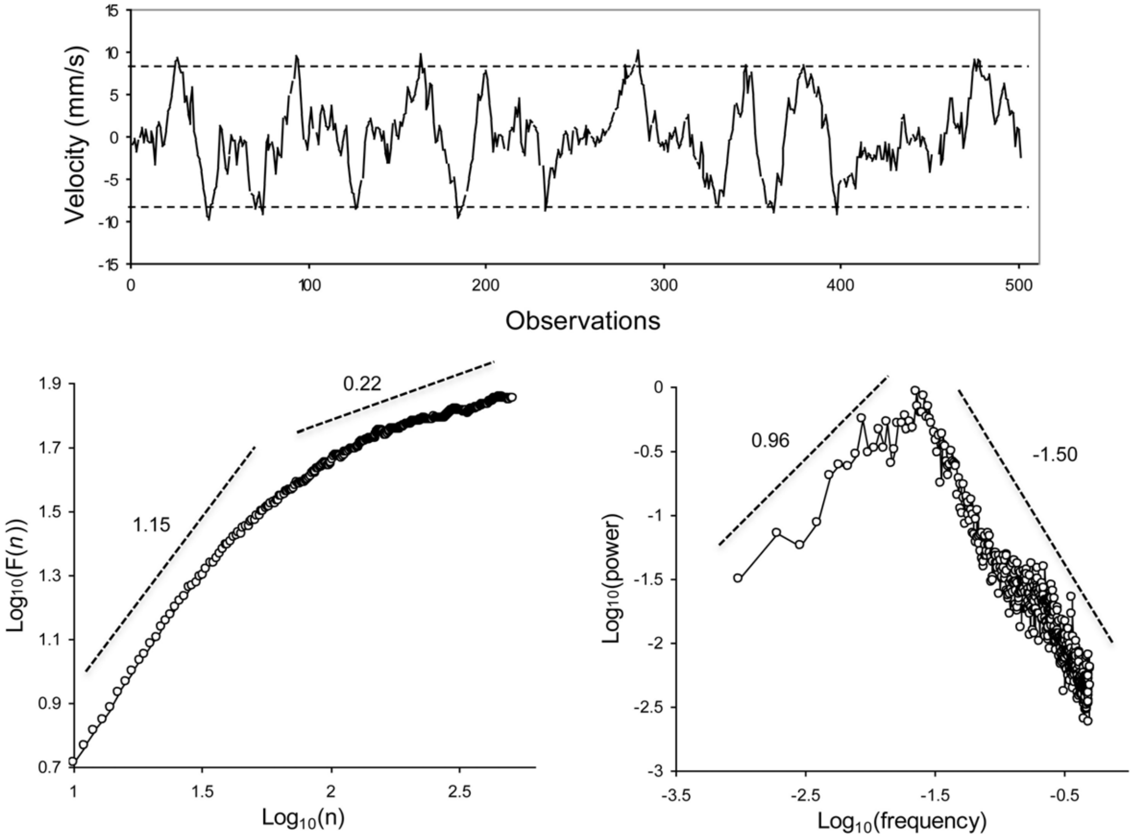

FIGURE 7 | Top: an example series of center-of-pressure velocity, during the maintenance of upright posture (sampling frequency: 40 Hz). The dashed lines represent the upper and lower limits that bound the evolution of the series. Bottom: average DFA diffusion plot (left) and average log–log power spectrum (right). From Delignières et al. (2011a).

In this equation θ is the first-order moving average parameter and was set to 0.8. ε_i is a white noise process with zero mean and unit variance. Finally we used the Davies–Harte algorithm for simulating a set of fractional Gaussian noise series, with $H = 0.9$ (Davies and Harte, 1987). Each set was composed of 100 series of 1024 points. By construction, the two first sets of series present only short-term correlations, while the third one possesses LRC properties.

We choose these ARMA models and their parameters values because the application of DFA on the series generated by these models yields diffusion plots similar to those obtained with fGn series. We present in **Figure 8** one example series of each set, and the corresponding diffusion plots: in all cases a linear slope close to 0.9 is obtained. Obviously the best linear fit is observed for the fGn series, which contains genuine LRC. For the AR series, the diffusion plot presents a slight flattening for long intervals, and conversely the slope tends to increase for long intervals for the MA series. However the diffusion plots obtained the AR and MA series roughly mimic the typical shape expected from long-range correlated series, and could easily lead to erroneous interpretations.

More precisely, considering the 100 series of each set, the mean α exponent was 0.92 ± 0.06 for AR series, 0.92 ± 0.08 for MA series, and 0.90 ± 0.07 for fGn series. In contrast, the computation of RR gave different values in the three sets: the mean RR was 0.30 ± 0.03 for AR series, 0.87 ± 0.36 for MA series, and 0.69 ± 0.09 for fGn series. For fGn series, the mean RR corresponded exactly to the expected value (see **Table 1**). With respect to the obtained α exponent, AR series were characterized by a mean RR value lower than expected, and conversely for MA series RR was slightly higher than expected.

Such discrepancies between the expected and obtained RR values could represent an interesting test for the suitability of the monofractal model. Note, however, that these differences between expected and obtained values should be considered with some caution. The mean RR value of 0.30 obtained for AR series corresponds to the expected value for fBm series with $\alpha = 1.1$, and the mean value of 0.83 obtained for MA series to the expected value for fGn series with $\alpha = 0.8$. Considering the possible error in the estimation of α, especially for relatively short series (see Delignières et al., 2006), the discrepancy between α and RR should be only considered one indicator, among others, for characterizing the series.

Some methods have been especially developed for distinguishing between short-term and LRC. Wagenmakers et al. (2005) and Torre et al. (2007b) have proposed a method based on ARMA and

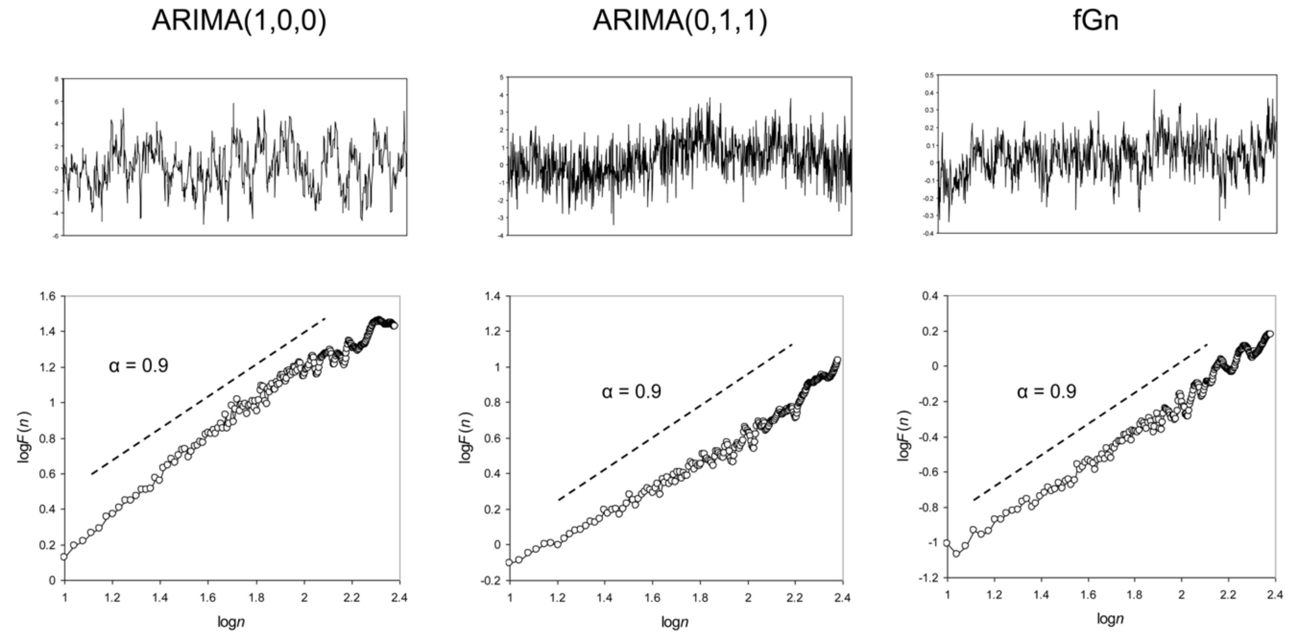

FIGURE 8 | Top row: example series simulated with a one-order auto-regressive model ($y_i = 0.85y_{i-1} + \varepsilon_i$, left column), a one-order moving average model ($y_i = y_{i-1} - 0.8\varepsilon_{i-1} + \varepsilon_i$, central column), and the Davies–Harte algorithm (fGn with $H = 0.9$, right column). The corresponding DFA diffusion plots are presented in the bottom row.

ARFIMA modeling. This method consists in fitting 18 models to the series. Nine of these models are ARMA (p, q) models, p and q varying systematically from 0 to 2. These ARMA models do not contain any long-range serial correlations. The other nine models are the corresponding ARFIMA (p, d, q) models, differing from the previous ARMA models by the inclusion of the fractional integration parameter d representing persistent serial correlations. One supposes that if the analyzed series contains LRC, ARFIMA models should present a better fit than their ARMA counterparts. We applied the ARMA/ARFIMA modeling to the three sets of series: as expected, all series in the fGn set were recognized as long-range correlated. In contrast, only 10% of the AR series and 14% of the MA series were best fitted by ARFIMA models.

Note that Gilden (2009) has issued severe reservations against methods based on goodness-of-fit criteria, such as the ARMA/ARFIMA procedure proposed by Wagenmakers et al. (2004). As an alternative, the author proposed global analyses that evaluate models on the basis of their capacity of generalization. The models are examined in terms of cross-validity, flexibility, and representativeness.

One could wonder about the added value of the proposed RR index, with regard to these methods that allow to detect the genuine presence of LRC in data sets. RR just provides an *a priori* indication about the possible relevancy of the monofractal model, but is unable to attest for the genuine presence of LRC. One could propose to systematize the application the aforementioned methods before any consideration of the fractal approaches. However it is clear that these methods are rarely used in the litterature. These methods remain complex to implement, and their theoretical backgrounds are sometimes difficult. Often authors prefer to directly apply fractal methods such as PSD or DFA, and to interpret *a posteriori* the obtained results. The RR index presents the advantage to be very easy to compute, and can allow avoiding superfluous investigations.

TIME SERIES AND EVENT SERIES

The two first examples we evoked in this paper (relative phase series and COP velocity) open an interesting line of discussion about the relevancy of fractal analyses. One could note that in both cases the series that appear unsuitable for being modeled through the monofractal framework were genuine time series, i.e., series of successive values spaced by equal time intervals.

In contrast, DRP series correspond to a cycle-to-cycle measurement, and the time interval between two successive values depends on the local period used as denominator in the calculation of relative phase. DRP series are just *event series*, composed of temporally ordered measures, but cannot be considered genuine time series. It is important to note that in most cases, experiments that clearly evidenced the presence of fractal fluctuations did not consider time series but event series. This was the case, for example, for the inter-tap intervals series in finger tapping experiments (Gilden et al., 1995; Lemoine et al., 2006), or for the stride intervals series analyzed in walking experiments (Hausdorff et al., 1995, 1997). In the set of experiments proposed by Gilden (2001), all analyzed series were as well composed of ordered successive performances.

At a methodological level, this could be considered an obstacle for the application of time series analyses such as those previously presented. Is it possible to apply analyses dealing with notions such as frequency or time intervals with data series where time is not effectively present? The application of time series analyses to event series is generally accepted pending some theoretical adaptations. Obviously, when dealing with an event series, time cannot be considered in its absolute sense. When applying PSD, "frequency" should not be read in Hertz units, but rather in terms of inverse trial number (Gilden, 2001), or in number of cycles for N trials or observations (Musha et al., 1985; Yamada, 1996). As well, the "intervals" taken into account by DFA are not genuine time intervals, but rather lengths of samples of successive observations.

This distinction between time series and event series is a key point in fractal analyses. Researchers aiming at undertaking a fractal approach to a given system could be naturally inclined to opt for time series, considering the nature of the statistical procedures commonly used in this domain. However, we think that the key variable in fractal analysis is not fluctuation in time, but rather cycle-to-cycle or trial-to-trial fluctuation. As argued by Kello et al. (2007), $1/f$ fluctuations are likely to occur when a system is repeatedly exposed to the same set of constraints. Gilden (2001) developed a similar idea, suggesting that the emergence of $1/f$ fluctuations is dependent on the consistency of the mental set, i.e., the reproducibility of constraints over successive trials. When a system has to repeatedly produce the same performance in the same situation, fluctuations in performance are likely to reveal its constitutive complexity. Essential properties of complex systems, such as degeneracy, suggest that the neural networks that are in charge of the production of performance are never identical from one trial to the other, but are never completely different. This capacity to mobilize softly assembled and evolving networks over successive trials could be considered the essential origin of LRC in the series of performances produced by complex systems (Delignières et al., 2011b).

Note, however, that the collection of event series is often difficult and time-consuming. The successive performance of hundreds of trials on a given task raises evident methodological problems and experimental biases, related to fatigue, or motivation. In contrast, the collection of time series, especially with high-frequency recording devices, could appear easier. Obviously, we do not argue that fractal analyses cannot be applied on genuine time series. Some convincing experiments have been published that were based on the analysis of time series, for example in the study of force production (Sosnoff and Newell, 2005), or electroencephalographic data (Nikulin and Brismar, 2004). In these examples, however, series were recorded from systems in steady state condition, and the successive measurements are likely to represent ordered assessments of a more or less stationary variable. In contrast, in a number of situations time series represent a kind of displacement in a given physical environment (for example COP trajectories) or in a more formal space (for example CRP series). Obviously, such series tend to present strong persistent correlations between successive positions, and this kind of motion falls clearly out of the scope of LRC processes. A solution in this case can be to seek for LRC properties in the series of successive increments, rather than in the original series (see, for example, Stephen et al., 2010).

CONCLUSION

Long-range correlations remain a very intriguing phenomenon, and the recent theoretical advances in this domain suggest that these fluctuations could represent a key entry in the study of the functional complexity of living systems. However, if the presence of serial correlations in series of data collected on such systems is surely more the rule than the exception (Slifkin and Newell, 1998), this does not imply that these correlations possess long-range properties. The RR index we discussed in this paper represents a simple tool allowing an easy prior assessment of the plausibility of the LRC hypothesis for a given series. We showed, however, that additional precautions are necessary in order to avoid erroneous conclusions or interpretations.

Note, however, that if the RR index can serve as an *a priori* warning light, some options can be considered before the definitive abandon of the monofractal framework. As previously suggested, one can often choose alternative variables that are better suitable for fractal analyses (e.g., DRP rather than CRP). Series transformations, by means of differentiation or integration, can also be used for obtaining more relevant data sets. Finally series are often contaminated by trends, caused by external effects, that could spuriously increase global variance, with respect to the amplitude of local fluctuations. In those cases RR could appear very low and lead to rejection of the monofractal hypothesis. Modified versions of the DFA, including polynomial detrending of various orders, have been proposed for controlling this kind of non-stationarities (Kantelhardt et al., 2001). When series are definitively too smooth for being accounted for by the monofractal model, one could consider other methods, based on phase space reconstruction, and especially Recurrence Analysis that allows revealing hidden regularities in apparently unpredictable signals (Webber and Zbilut, 2005).

Long-range correlations have recently become a very popular theme of research. A number of researchers have tried to check whether their usual objects of research could present LRC properties. However, we think that evidencing the presence of LRC in a given system cannot represent *per se* an interesting research goal. The problem is not to seek everywhere for LRC, but to determine, theoretically, where it could be important, and empirically where it could be plausible to find such long-term persistent serial correlations.

REFERENCES

Collins, J. J., and De Luca, C. J. (1993). Open-loop and closed-loop control of posture: a random-walk analysis of center-of-pressure trajectories. *Exp. Brain Res.* 95, 308–318.

Davies, R. B., and Harte, D. S. (1987). Tests for Hurst effect. *Biometrika* 74, 95–101.

Delignières, D., Fortes, M., and Ninot, G. (2004). The fractal dynamics of self-esteem and physical self. *Nonlinear Dynamics Psychol. Life Sci.* 8, 479–510.

Delignières, D., Ramdani, S., Lemoine, L., Torre, K., Fortes, M., and Ninot, G. (2006). Fractal analysis for short time series: a reassessment of classical methods. *J. Math. Psychol.* 50, 525–544.

Delignières, D., Torre, K., and Bernard, P. L. (2011a). Transition from persistent to anti-persistent correlations in postural sway indicates velocity based control. *PLoS Comput. Biol.* 7, e1001089. doi:10.1371/journal.pcbi.1001089

Delignières, D., Marmelat, V., and Torre, K. (2011b). "Degeneracy and long-range correlation: a simulation study," *in Proceeding BIO Web of Conferences* 1, Montpellier, 00020.

Gilden, D. L. (1997). Fluctuations in the time required for elementary decisions. *Psychol. Sci.* 8, 296–301.

Gilden, D. L. (2001). Cognitive emissions of 1/f noise. *Psychol. Rev.* 108, 33–56.

Gilden, D. L. (2009). Global model analysis of cognitive variability. *Cogn. Sci.* 33, 1441–1467.

Gilden, D. L., Thornton, T., and Mallon, M. W. (1995). 1/f noise in human cognition. *Science* 267, 1837–1839.

Goldberger, A. L., Amaral, L. A. N., Hausdorff, J. M., Ivanov, P. Ch., Peng, C.-K., and Stanley, H. E. (2002). Fractal dynamics in physiology: alterations with disease and aging. *Proc. Natl. Acad. Sci. U.S.A.* 99, 2466–2472.

Hausdorff, J. M., Mitchell, S. L., Firtion, R., Peng, C. K., Cudkowicz, M. E., Wei, J. Y., and Goldberger, A. L. (1997). Altered fractal dynamics of gait: reduced stride-interval correlations with aging and Huntington's disease. *J. Appl. Physiol.* 82, 262–269.

Hausdorff, J. M., Peng, C.-K., Ladin, Z., Wei, J. Y., and Goldberger, A. L. (1995). Is walking a random walk? Evidence for long-range correlations in stride interval of human gait. *J. Appl. Physiol.* 78, 349.

Hurst, H. E. (1951). Long-term storage capacity of reservoirs. *Trans. Am. Soc. Civil Eng.* 116, 770–799.

Kantelhardt, J. W., Koscielny-Bunde, E., Rego, H. H. A., Havlin, S., and Bunde, A. (2001). Detecting long-range correlations with detrended fluctuation analysis. *Physica A* 295, 441–454.

Kello, C. T., Beltz, B. C., Holden, J. G., and Van Orden, G. C. (2007). The emergent coordination of cognitive function. *J. Exp. Psychol. Gen.* 136, 551–568.

Kelso, J. A. S. (1984). Phase transition and critical behaviour in human bimanual coordination. *Am. J. Physiol.* 15, R1000–R1004.

Leland, W. E., Taqqu, M. S., Willinger, W., and Wilson, D. V. (1994). On the self-similar nature of ethernet traffic (extended version). *IEEE/ACM Trans. Netw.* 2, 1–15.

Lemoine, L., Torre, K., and Delignières, D. (2006). Testing for the presence of 1/f noise in continuation tapping data. *Can. J. Exp. Psychol.* 60, 247–257.

Liebovitch, L. S., and Yang, W. (1997). Transition from persistent to antipersistent correlation in biological systems. *Phys. Rev. E* 56, 4557–4566.

Madison, G., Forsman, L., Blom, Ö., Karabanov, A., and Ullén, F. (2009). Correlations between intelligence and components of serial timing variability. *Intelligence* 37, 68–75.

Mandelbrot, B. B., and van Ness, J. W. (1968). Fractional Brownian motions, fractional noises and applications. *SIAM Rev.* 10, 422–437.

Matsuzaki, M. (1994). Fractals in earthquakes. *Philos. Trans. R. Soc. Lond. A* 348, 449–457.

Musha, T., Katsurai, K., and Teramachi, Y. (1985). Fluctuations of human tapping intervals. *IEEE Trans. Biomed. Eng.* 32, 578–582.

Nikulin, V. V., and Brismar, T. (2004). Long-range temporal correlations in alpha and beta oscillations: effect of arousal level and test–retest reliability. *Clin. Neurophysiol.* 115, 1896–1908.

Ogden, R. T., and Collier, G. L. (2002). Inference on variance components of autocorrelated sequences in the presence of drift. *J. Nonparamet. Stat.* 14, 409–420.

Peters, B. T., Haddad, J. M., Heiderscheit, B. C., van Emmerik, R. E. A., and Hamill, J. (2003). Limitation in the use and interpretation of continuous relative phase. *J. Biomech.* 36, 271–274.

Rangarajan, G., and Ding, M. (2000). Integrated approach to the assessment of long range correlation in time series data. *Phys. Rev. E Stat. Phys. Plasmas Fluids Relat. Interdiscip. Topics* 61, 4991–5001.

Schmidt, R. C., Beek, P. J., Treffner, P. J., and Turvey, M. T. (1991). Dynamical substructure of coordinated rhythmic movements. *J. Exp. Psychol. Hum. Percept. Perform.* 17, 635–651.

Slifkin, A. B., and Newell, K. M. (1998). Is variability in human performance a reflection of system noise? *Curr. Dir. Psychol. Sci.* 7, 170–177.

Sosnoff, J. J., and Newell, K. M. (2005). Intermittent visual information and the multiple timescales of visual motor control of continuous isometric force production. *Percept. Psychophys.* 67, 335–344.

Stephen, D. G., Arzamarski, R., and Michaels, C. F. (2010). The role of fractality in perceptual learning: exploration in dynamic touch. *J. Exp. Psychol. Hum. Percept. Perform.* 36, 1161–1173.

Stevens, S. S. (1951). "Mathematics, measurement and psychophysics," in *Handbook of Experimental Psychology*, ed. S. S. Stevens (New York: Wiley), 1–49.

Thomas, T. R. (1999). *Rough Surfaces*. London: Imperial College Press.

Torre, K., and Balasubramaniam, R. (2011). Disentangling stability, variability and adaptability in human performance: focus on the interplay between local variance and serial correlation. *J. Exp. Psychol. Hum. Percept. Perform.* 37, 539–550.

Torre, K., Delignières, D., and Lemoine, L. (2007a). $1/f^{\beta}$ fluctuations in bimanual coordination: an additional challenge for modeling. *Exp. Brain Res.* 183, 225–234.

Torre, K., Delignières, D., and Lemoine, L. (2007b). Detection of long-range dependence and estimation of fractal exponents through ARFIMA modelling. *Br. J. Math. Stat. Psychol.* 60, 85–106.

Treffner, P. J., and Kelso, J. A. S. (1999). Dynamic encounters: long-memory during functional stabilization. *Ecol. Psychol.* 11, 103–137.

Treffner, P. J. and Kelso, J. A. S. (1995). "Functional stabilization on unstable fixed-points," in *Studies in Perception and Action III*, eds B. G. Bardy, R. J. Bootsma, and Y. Guiard (Hillsdale, NJ: Laurence Erlbaum Associates), 83–86.

van Orden, G. C., Holden, J. G., and Turvey, M. T. (2003). Self-organization of cognitive performance. *J. Exp. Psychol. Gen.* 132, 331–350.

Wagenmakers, E.-J., Farrell, S., and Ratcliff, R. (2004). Estimation and interpretation of $1/f^{\alpha}$ noise in human cognition. *Psychon. Bull. Rev.* 11, 579–615.

Wagenmakers, E.-J., Farrell, S., and Ratcliff, R. (2005). Human cognition and a pile of sand: a discussion on serial correlations and self-organized criticality. *J. Exp. Psychol. Gen.* 134, 108–116.

Webber, C. L. Jr., and Zbilut, J. P. (2005). "Recurrence quantification analysis of nonlinear dynamical systems," in *Tutorials in Contemporary Nonlinear Methods for the Behavioral Sciences*, eds M. A. Riley and G. C. Van Orden, 26–94. Available at: http://www.nsf.gov/sbe/bcs/pac/nmbs/nmbs.jsp (Retrieved March 2, 2011).

Yamada, M. (1996). Temporal control mechanism in equalled interval tapping. *Appl. Human Sci.* 15, 105–110.

Conflict of Interest Statement: The authors declare that the research was conducted in the absence of any commercial or financial relationships that could be construed as a potential conflict of interest.

Received: 14 March 2012; paper pending published: 18 April 2012; accepted: 25 May 2012; published online: 18 June 2012.

Citation: Marmelat V, Torre K and Delignières D (2012) Relative roughness: an index for testing the suitability of the monofractal model. Front. Physio. ***3****:208. doi: 10.3389/fphys.2012.00208*

This article was submitted to Frontiers in Fractal Physiology, a specialty of Frontiers in Physiology.

frontiers in
PHYSIOLOGY

METHODS ARTICLE
published: 21 January 2013
doi: 10.3389/fphys.2012.00495

Does sample rate introduce an artifact in spectral analysis of continuous processes?

Maarten L. Wijnants[1]*, R. F. A. Cox[2], F. Hasselman[1], A. M. T. Bosman[1] and Guy Van Orden[3]

[1] *Behavioural Science Institute, Radboud University Nijmegen, Nijmegen, Netherlands*
[2] *Department of Developmental Psychology, Heymans Institute, University of Groningen, Netherlands*
[3] *Cap Center for Cognition and Action, University of Cincinnati, Cincinnati, OH, USA*

Edited by:
John G. Holden, University of Cincinnati, USA

Reviewed by:
Christopher Kello, University of California, USA
John G. Holden, University of Cincinnati, USA

****Correspondence:***
Maarten L. Wijnants, Behavioural Science Institute, Radboud University Nijmegen, PO Box 9104 6500 HE Nijmegen, Netherlands.
e-mail: m.wijnants@pwo.ru.nl

Spectral analysis is a widely used method to estimate $1/f^{\alpha}$ noise in behavioral and physiological data series. The aim of this paper is to achieve a more solid appreciation for the effects of periodic sampling on the outcomes of spectral analysis. It is shown that spectral analysis is biased by the choice of sample rate because denser sampling comes with lower amplitude fluctuations at the highest frequencies. Here we introduce an analytical strategy that compensates for this effect by focusing on a fixed amount, rather than a fixed percentage of the lowest frequencies in a power spectrum. Using this strategy, estimates of the degree of $1/f^{\alpha}$ noise become robust against sample rate conversion and more sensitive overall. Altogether, the present contribution may shed new light on known discrepancies in the psychological literature on $1/f^{\alpha}$ noise, and may provide a means to achieve a more solid framework for $1/f^{\alpha}$ noise in continuous processes.

Keywords: 1/*f* noise, 1/*f* scaling, spectral analysis, periodic sampling, sample rate

Over recent decades, there has been an increasing interest in the time-evolutionary properties of psychological data series, and the number of methods to quantify the *degree-of-randomness* in time series data is rapidly expanding. It is becoming increasingly acknowledged that the variation from one measurement to the next rarely fluctuates randomly, as traditionally assumed in most standard statistical methods (Gilden et al., 1995; Gilden, 2001; Van Orden et al., 2003). Especially the presence of $1/f$ noise (also called $1/f$ scaling or pink noise) in repeated performances is a robust finding. The presence of $1/f$ noise implies that a data signal may not be accurately described without incorporating time at the level of analysis. We will first explain the workings of spectral analysis through a fictive example, and then we explain how spectral analysis can be used to estimate the presence of $1/f$ noise.

Consider a participant, performing a 500-trial simple response task. The task instruction is, for instance, to press a button whenever a stimulus is presented. The dependent variable of interest for the researcher is response time to the stimulus. This participant's average response time turns out to be 500 ms with a standard deviation of 35 ms. However, this participant's task performance constitutes the unrealistic case where the pattern of response variability over time looks exactly like a sine wave (see **Figure 1A**). Now, imagine another participant, who received the same task instruction, and showed exactly the same response times but in a different trial order (see **Figure 1C**). While both response series have an identical mean and standard deviation, they show a distinct pattern of responses over time.

Statistics based on central tendency measures are not sensitive to the different pattern of variability observed in both participants. If in one experimental group all participants were like participant 1, and in another experimental group all participants were like participant 2, a t-test for instance, would not differentiate among both groups because the groups would yield equal means and standard deviations. Yet, a different inherent process likely produced the responses. Thus, a researcher may wonder whether trial-to-trial fluctuations observed in an experiment occur randomly or not, and ask whether there is anything systematic about the observed temporal patterns of variation.

Spectral analysis is one of the available methods to estimate the degree of randomness in a pattern of responses over trials. Spectral analysis translates dependencies in the time domain (i.e., a pattern of change in response time over trials) as simple features in the frequency domain using an operation called a Fourier transform, which decomposes the data series containing changes in response over trials into its constituent frequencies. Next, the power (the square of the amplitude) at each frequency in the decomposed signal is plotted in a so-called a power spectrum (also called power spectral density function). For instance, a power spectrum of participant 1′ s response series (shown in **Figure 1B**) reveals one peak at the dominant frequency of the sine wave. Participant 2′ s responses do not yield a dominant frequency in the time domain, and consequently a spectral analysis does not reveal any peaks in the power spectrum (see **Figure 1D**). Thus, while the performances of both participants are indistinguishable using central tendency measures, the two different temporal arrangements of the same responses are distinct in the frequency domain. The power spectrum thus provides information which effectively complements information from t-tests, ANOVA's, etc. (see Slifkin and Newell, 1998; Riley and Turvey, 2002, for more examples).

Spectral analysis can not only be used to detect simple periodicities as in the example above, but can also be used to quantify more complex and realistic patterns of variation in psychological

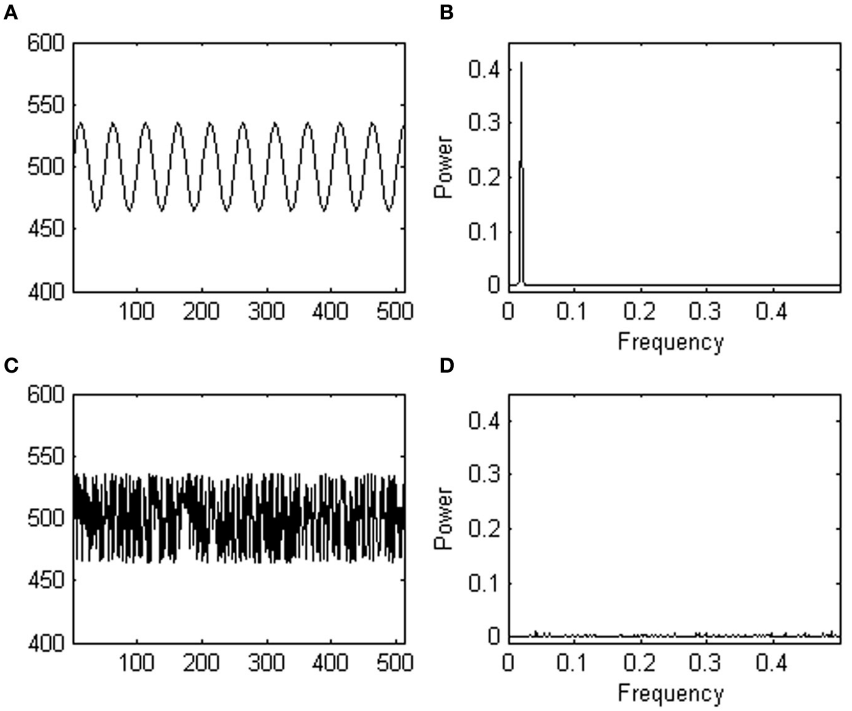

FIGURE 1 | (A) Shows a fictive data series yielding response times oscillating as a sine wave (in milliseconds, y-axis) over trials (x-axis). **(B)** Shows a power spectrum of the fictive data series shown in **(A)**; note the peak. **(C)** Shows the same data series as in **(A)** after randomization. **(D)** Shows a power spectrum of the randomized data series shown in **(C)**; note the absence of a peak.

data series. Consider, for instance, another participant in the simple reaction task whose response times show a pattern of variability called 1/*f* noise, as shown in **Figure 2A**. 1/*f* noise is a complex sequence effect spanning over the entire time course of an experiment, and comprises undulating "waves" of relatively longer and then shorter response times that travel across the series. In a 1/*f* signal, faster (high-frequent) changes in response time are typically small, and embedded in overarching, slower (lower-frequent) changes of higher amplitude. In only a few simple steps, this characteristic pattern of response variability can be observed through spectral analysis. First, a Fourier transform translates the data series into the sum of sines and cosines that best fits the data series. This is schematically represented in **Figure 2B**. Next, the frequency and power (amplitude^2) of each of the fitted waveforms are plotted against each other in a power spectrum (see **Figure 2C**). **Figure 2D** shows the power spectrum on log-scales, which makes the 1/*f* noise pattern even more visible; power is in inverse proportion to frequency. The log–log power spectrum in **Figure 2D** yields a slope of -1 (hence, $1/f^1$ noise).

Observing 1/*f* noise may run against standard statistical intuitions because the variability in psychological data is usually assumed to fluctuate randomly from trial to trial. A data series with random background noise (also called white noise, see **Figure 3A**), however, does not yield a relationship among frequency (f) and a particular change of amplitude $S(f)$ in the signal (see **Figure 3B**). A power spectrum of white noise variability has a flat slope on log scales (yielding $1/f^0$ noise).

A third category of noise is called Brownian noise (see **Figure 3C**), and can be described as $1/f^2$ noise (see **Figure 3D**; the slope is -2). Brownian noise is also called a random walk, because it can be produced by adding a random increment to each sample to obtain the next. In contrast to white noise, which can be produced by randomly choosing each sample independently, Brownian noise yields persistence or memory in the data series.

1/f NOISE IN HUMAN PERFORMANCE

1/*f* noise has been observed in repeated responses in many cognitive tasks. Examples include simple and choice reaction (Kello et al., 2007), mental rotation (Gilden, 1997), visual search (Aks et al., 2002), lexical decision (Gilden, 1997), word naming (Van Orden et al., 2003), color and shape discrimination (Gilden, 2001), implicit associations (Correll, 2008), and self-reports of self-esteem (Delignières et al., 2004), to name a few examples. Apart from the ubiquitous presence of 1/*f*-like noise in cognitive performances (Kello et al., 2007), 1/*f* noise has been observed in temporal patterns of variation at all levels of neural (Werner, 2010) and physiological organization (West, 2010).

The origins of 1/*f* noise in human cognition remain a theoretical topic of debate, however, (Van Orden et al., 2003, 2005; Wagenmakers et al., 2005; Torre and Wagenmakers, 2009; Diniz et al., 2010). Nonetheless, the relative presence of 1/*f* noise (hence, the slope $-\alpha$) has empirically been shown to distinguish among experimental conditions (Kello et al., 2007; Diniz et al., 2010; Van Orden et al., 2011, are reviews). Therefore, the slope of a power spectrum is an informative measure in psychological research.

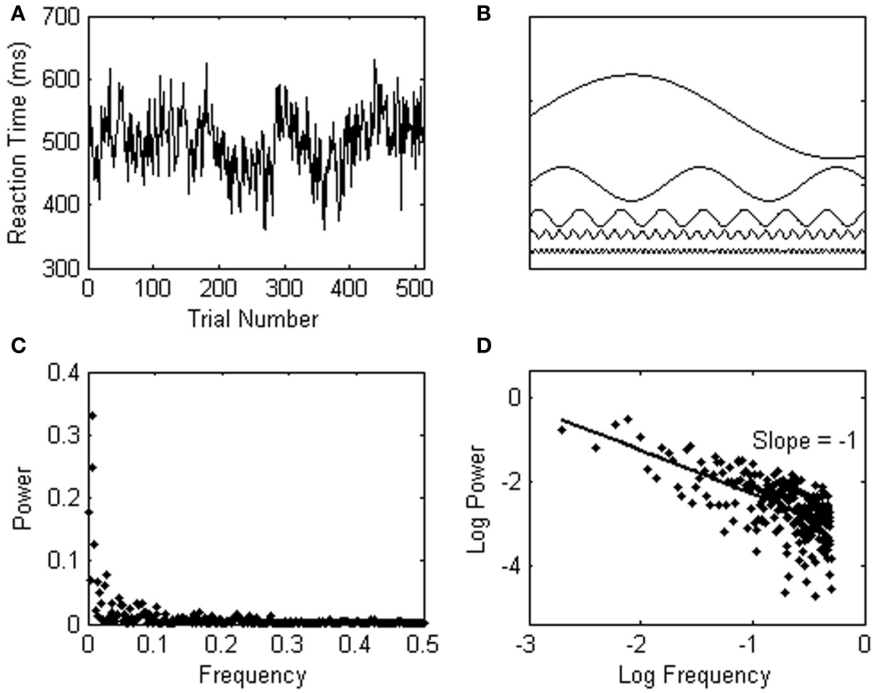

FIGURE 2 | (A) Shows a response series yielding 1/*f* noise. **(B)** Schematically represents a number of sine waves which are fitted to the data series through a Fourier transform. **(C)** Shows the 1/*f* noise pattern in a power spectrum, which is shown on logarithmic scales in **(D)**.

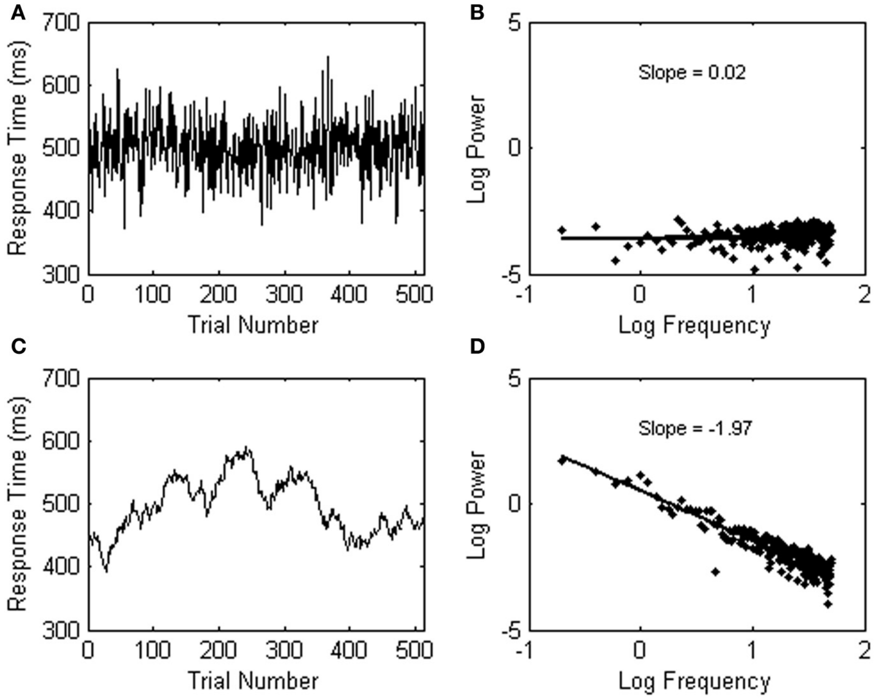

FIGURE 3 | (A) Shows an example of white (random) noise. The power spectrum of the white noise series is shown in **(B)**. **(C)** Shows an example of Brownian noise. The power spectrum of the Brownian noise series is shown in **(D)**.

The scaling exponent α in $1/f^{\alpha}$ noise usually varies between white noise and 1/*f* noise ($0 < \alpha < 1$), but sometimes also between 1/*f* noise and Brownian noise ($1 < \alpha < 2$).

Intriguingly, empirical evidence has accumulated suggesting that the relative presence of 1/*f* noise is related to the coordination of cognitive and physiological processes. For instance, deviations from 1/*f* noise (either toward white noise or toward Brownian noise) have been found with epilepsy (Ramon et al., 2008), heart failure (Goldberger et al., 2002), fetal distress syndrome (Goldberger, 1996), major-depressive disorder (Linkenkaer-Hansen et al., 2005), mania (Bahrami et al., 2005), attention-deficit-hyperactivity-disorder (Gilden and Hancock, 2007), developmental dyslexia (Wijnants et al., 2012b), autism (Lai et al., 2010), Alzheimer's disease (Abásolo et al., 2006), Huntington's disease (West, 2006), and Parkinson's disease (Hausdorff, 2007). In addition, the presence of 1/*f* noise correlates, for instance, with the severity of depression symptoms (Linkenkaer-Hansen et al., 2005), the success rate of recovery from traumatic brain injury (Burr et al., 2008), and falling risk in elderly (Hausdorff, 2007). Also, the presence of 1/*f* noise increases with learning (Wijnants et al., 2009) and may decrease as task demands increase (Clayton and Frey, 1997; Correll, 2008). In each case the overly random or overly rigid behaviors showed a value of α further from 1, compared to conditions allowing for more flexibly stable and adaptive performances.

These studies confirm the importance of time series methods like spectral analysis in psychological research. Interestingly, however, all of the examples above are based on the analysis of *trial series* or interval series. In a trial series, each sampled data value represents a measure of a discrete response or response interval, as in the example of the simple reaction task mentioned earlier. Many variables in psychological research, however, are continuous in nature, rather than discrete. Continuous processes are represented as a *time series* through periodic sampling. Periodic sampling means that the continuous process $x \rightarrow (t)$ is digitized as a sequence of discrete data values $t_1, t_2, t_3, t_n \ldots$, where the total number of data points depends on the chosen sampling rate. Interestingly, however, the clear framework suggested by the role of $1/f^{\alpha}$ noise in trial series has not (yet) found a univocal parallel in the analysis of psychological time series.

Here, we investigate whether differences in sample rate constitute an artifact which obscures comparisons across studies and experimental conditions. The paper is organized as follows. First, a number of details pertaining to analytical choices for spectral analysis are discussed. Then, it is discussed in which way sample rate affects the frequency content of a time series, and it is explained how this artifact is usually dealt with in psychological studies of $1/f^{\alpha}$ noise relying on continuous processes. Next, we show how this approach renders heterogeneous estimates of the slope $-\alpha$, and offer an alternative solution that circumvents the artifact.

1/*f* NOISE AND PERIODIC SAMPLING

Psychologists are in general well-aware of the characteristics of a desired sampling regime. That is, any signal that has been periodically sampled can only be perfectly reconstructed if the sampling rate corresponds to a frequency that is minimally twice the highest frequency in the original signal (this is known as the Shannon–Nyquist sampling theorem; Shannon, 1949). When sampling more sparsely, a phenomenon called aliasing is likely to occur. Aliasing means that fluctuations outside of the measured frequency range are misinterpreted as different frequencies that fall within the measured range of frequencies, yielding distorted results (see Holden, 2005). Therefore, sample rate is an important input parameter when applying spectral analysis to periodically sampled data series. The estimated frequencies should not be faster than half the sample rate. For example, when a given time series is sampled at 100 Hz, the frequencies estimated in spectral analysis (the x-axis in the power spectrum) should fall in the range of 0–50 Hz to avoid aliasing.

The next input parameter for spectral analysis is the number of frequencies to be estimated within the non-aliased frequency range. This parameter will determine the number of data points in the power spectrum. A spectral analysis with maximum frequency resolution will estimate half as many frequencies as there are data points, because the highest resolvable frequency oscillates back and forth every other data point. In order to understand why the regression fit over the 25% lowest frequencies covers such a substantial portion of the power spectrum (as can be seen in **Figures 2D** and **3C**,**D**), note that a Fourier transform evaluates the power of each frequency within the signal equidistantly within the desired frequency range. After the log transformation, however, the frequencies are no longer equidistant, and exponentially more frequencies are observed in the high-frequency range than in the low-frequency range of the power spectrum.

When the goal of the spectral analysis is to estimate the α scaling exponent (thus, the negative slope of the logarithmic power spectrum, or the presence of 1/*f* noise), another choice concerns the number of frequencies in the power spectrum over which the slope is fitted. That is, the slope $-\alpha$ is rarely fitted over all frequencies, because it is known that a power spectrum often gives unreliable results in the highest frequency range. Specifically, the right-hand side of a power spectrum often presents a flattening (or whitening) of the slope (Holden, 2005; Holden et al., 2011). Therefore, excluding the highest frequencies in the log–log regression is generally recommended (Beran, 1994; Eke et al., 2000, 2002; Holden, 2005). The linear fit is often limited to the 25% lowest frequencies that compose the spectral slope (Eke et al., 2000, 2002) or even 10% (Taqqu et al., 1995), to achieve more reliable scaling estimates of the scaling exponent α.

THE ARTIFACT OF SAMPLE RATE

The aim of this study is to achieve a more solid appreciation for the effects of periodic sampling on the outcomes of spectral analysis. Specifically, a researcher's choice of sample rate is known to change the estimated α exponents in a particular way (Carlini et al., 2002; Eke et al., 2002), and this bias is usually not anticipated. This is especially problematic when different studies are compared, which employ a different sampling regime of similar performances (i.e., comparing the outcomes of spectral analysis of trial series with outcomes of spectral analysis of time series), or which rely on periodic sampling but employ different sample rates.

Carlini et al. (2002) point out that higher sample rates yield steeper spectral slopes, hence larger α scaling exponents, compared with more sparsely sampled processes. "The amplitude of the (*highest frequency*) oscillations themselves decreases sharply (*when sample rate increases*)" (Carlini et al., 2002, p. 246, emphasis added for terminological consistency). Eke et al. (2002) add: "Increasing f_s [*sample rate*], …cannot continue beyond some upper limit for exceeding it would increase the chance that high-frequency estimates in the power spectrum would not reflect physiology (*or more generally, the process of interest*)" (Eke et al., 2002, p. 27, emphasis added).

These observations constitute the core measurement problem raised in this paper: the outcomes of spectral analysis hinge on sample rate. This artifact is visually presented in **Figures 4A** and **B**, which shows the relative roughness of two different time series (Goldberger et al., 2000) that were downsampled so that they yield different sampling rates. Relative roughness can be conceived as an index of the suitability of the monofractal framework (cf. Marmelat et al., 2012), and describes the relative contribution of local variance to the global variance of a time series. **Figures 4A** and **B** reveal that the relative roughness of a time series is reduced when sampled more densely. Specifically, **Figures 4A** and **B** suggest that faster sampling comes with lower amplitude at the higher frequencies (making the series more smooth, thus reducing local variance), which may result in overall steeper slopes in the power spectrum compared with processes that are sampled more sparsely.

This line of reasoning so far is straightforward, but can make a world of difference nonetheless concerning the utility of spectral analysis when confronted with periodically sampled, continuous processes. That is, the highest-frequency range in the spectrum has lower amplitude when higher sample rates are employed, and this artifact likely protrudes gradually into lower frequencies as sample rate further increases. Correctly, some authors have assumed that such an artifact does not affect the estimate of α, given that the biased frequencies are not used to fit the slope −α: "This would not be much of a problem if the upper 75% of the spectral estimates were to be discarded as recommended and if these irrelevant estimates would fall into the discarded range" (Eke et al., 2002, pp. 27–28). In other words, the challenge is to focus on the range of frequencies that is not contaminated by the artifact. If, however, the biased frequencies exceed the highest 75% frequency range, the assumption cited above would not be valid, and different values of α would be obtained with different sample rates. Thus, the question is whether the non-contaminated frequency range converges on the 25% lowest-frequency range.

To answer the question, we evaluated a Galvanic Skin Response (GSR) time series that was sampled at either 200 Hz (yielding a time series of 2^{16} data points), 100 Hz (2^{15} data points), 50 Hz (2^{14} data points), or 25 Hz (2^{13} data points). For each sample rate of the same time series, the frequencies in the power spectrum range between 0 Hz and half the sample rate to avoid aliasing. Then, following Eke et al. (2002), the linear regression fit was plotted over the 25% lowest frequency range, to estimate α (see **Figures 5A–D**; the discarded 75% frequency range is represented as a horizontal line). Remarkably, **Figures 5A**,**B** show rather variable estimates of the spectral slope −α for the same measured process; α ranged between 1.56 and 2.57 depending on sample rate. In other words, even with all precautions in place, sample rate still distorts the estimate of α.

Here, we introduce an alternative solution to the problem that outcomes of spectral analysis can hinge on sample rate. The logic is to fit the slope −α over a fixed amount, rather than over a fixed percentage, of lowest frequencies. This solution takes advantage of, rather than being contaminated by, inherent differences in sample rate. Since more frequencies are estimated overall from more densely sampled time series, fitting the slope −α over a fixed number of low-frequencies implies a fit over a lower percentage of low frequencies when a time series is sampled more densely. Thus, while the bias leaks into more of the lower frequencies for higher sample rates, a lower percentage of low-frequencies is used

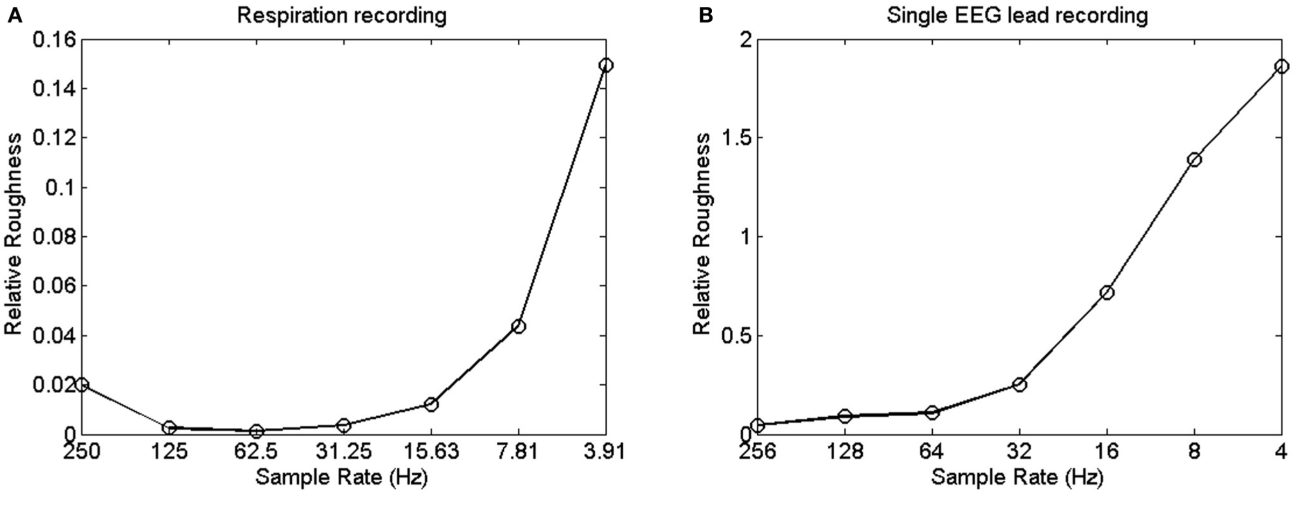

FIGURE 4 | (A) Shows the relative roughness of a respiration time series at various sampling rates. **(B)** Shows the change in relative roughness of an EEG time series at various sampling rates.

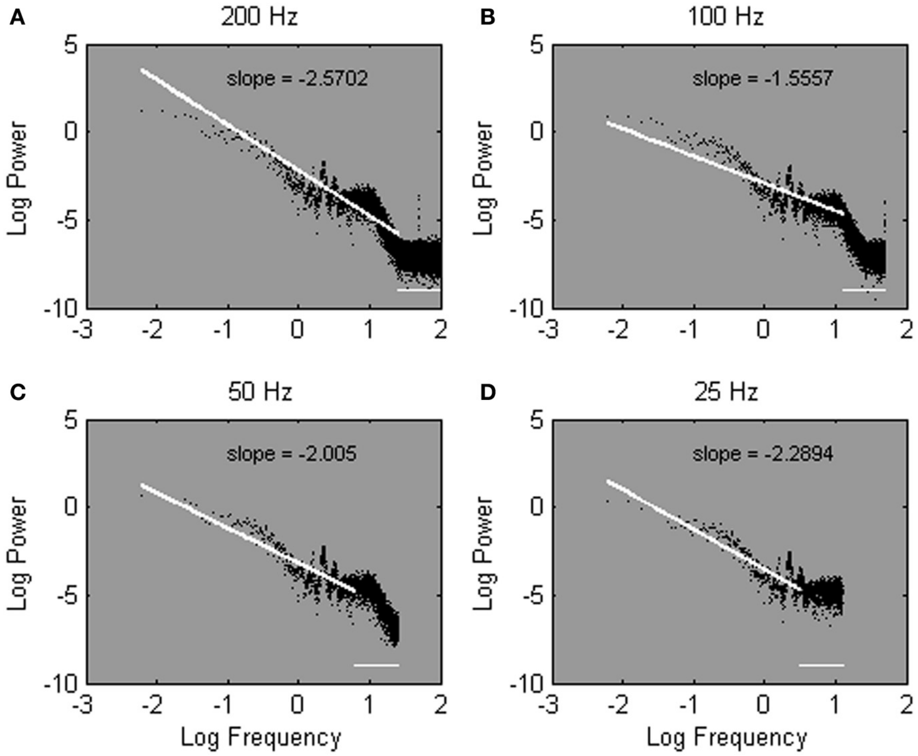

FIGURE 5 | Power spectra estimated from one Galvanic Skin Response time series sampled at 200 Hz (A), 100 Hz (B), 50 Hz (C), and 25 Hz (D). Spectral slopes are fitted over the lowest 25% of 2^{15} **(A)**, 2^{14} **(B)**, 2^{13} **(C)**, and 2^{12} **(D)** estimated frequencies. Note that most of the estimated frequencies fall in the high-frequency range of the spectrum.

to fit the slope −α. At sparser sample rates, the bias extends over a smaller portion of the low frequencies, and a larger portion of estimated frequencies is used to fit the slope −α. The advantages of the introduced strategy can be seen in **Figures 6A–D**, which shows the same power spectra as shown in **Figures 5A–D**, but with the spectral slope −α now fitted over a set number of frequencies. In contrast to **Figures 5A–D**, robust estimates of α are obtained regardless of sample rate.

Fitting over a fixed number of frequencies is notably different from fitting over a fixed percentage of frequencies. With regard to the high-frequency range, when the slope −α is fitted over the 25% of lowest frequencies, the high-frequency range of a power spectrum is treated equally regardless of the relative presence of spurious high-frequencies, and thus, regardless of sample rate. Specifically, the range of discarded high frequencies remains equals across different sample rates. When the slope −α is fitted over a fixed number of low frequencies, as proposed here, the discarded frequency range changes as a function of sample rate. Specifically, as sample rate increases the range of discarded high-frequencies increases as well (hence, the horizontal line in **Figures 6A–D**). As a result, the range of discarded frequencies converges much more closely with the range of spurious frequencies.

With regard to the low-frequency range, fitting over the 25% of lowest frequencies implies fitting over a different low-frequency range for different sample rates. Specifically, relatively higher frequencies (hence, more biased frequencies) are incorporated in the fit as sample rate increases. For instance, in **Figures 5A–D**, the fitted frequencies range between 0 and 25 Hz, 0 and 12.5 Hz, 0 and 6.25 Hz, and 0 and 3.13 Hz for sample rates of 200, 100, 50, and 25 Hz, respectively. Fitting over a fixed amount of low frequencies (50 frequencies in this example), in contrast, implies a fit over a stable low-frequency range, regardless of sample rate. Hence, in **Figures 6A–D**, the cut-off frequency is the same; the slope −α is fitted between 0 and 0.31 Hz regardless of sample rate.

DOWNSAMPLING

This paper examines the artifact in the estimation of $1/f$ noise parameters introduced by the choice of sample rate. We expect, based on previous observations (e.g., Carlini et al., 2002; Eke et al., 2002), that low-amplitude fluctuations are introduced in the high-frequency range of the power spectrum as sample rate increases. We examine this artifact by comparing α exponent over a range of different sample rates using a variety of simulated and empirical time series. That is, we compare empirical or simulated data signals with their downsampled copies. In essence, downsampling is simply a *post-hoc* reduction in sampling rate by an integer factor. For a time series $x(n)$, when downsampling by the constant factor M, the downsampled copy $y(m)$ may be represented as $y(m) = x(nM)$, where $y(m)$ is the downsampled sequence, obtained by taking every Mth sample from the original data sequence $x(n)$, thereby discarding $M - 1$ samples for every

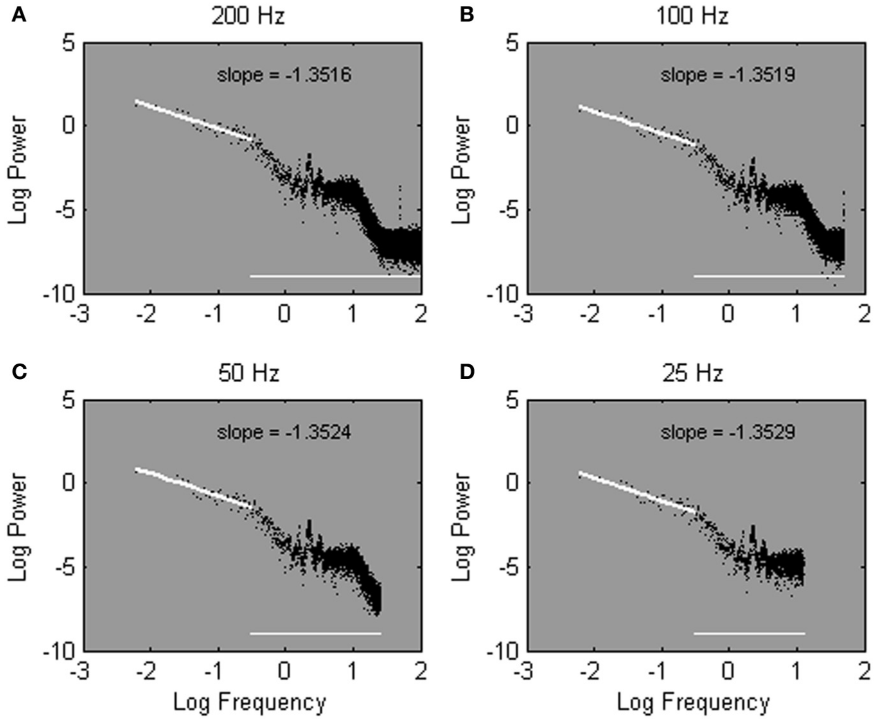

FIGURE 6 | The same power spectra as shown in Figure 5, estimated from one Galvanic Skin Response time series sampled at 200 Hz (A), 100 Hz (B), 50 Hz (C), and 25 Hz (D). Spectral slopes are fitted over the lowest 50 of 2^{15} **(A)**, 2^{14} **(B)**, 2^{13} **(C)**, and 2^{12} **(D)** estimated frequencies.

M samples. It is to be expected that this *post-hoc* reduction in sample rate will effectively alter the spectral estimates for sampled data signals.

If increasing the sample rate has indeed the effect of reducing the amplitude of the signal at the highest frequencies, the overall estimated α exponent should increase as sample rate increases. This bias should not affect the low-frequency range of the power spectrum, and should become more pronounced when the spectral slope −α is fitted over a wider frequency range. This is investigated by fitting the spectral slope over 10, 25, or 100% of the lowest frequencies in the power spectrum. The outcomes are expected to be biased more strongly when the slope is fitted over 100% of the spectrum, and gradually become less biased as the slope is fitted over 25% (cf. Eke et al., 2002) and 10% (cf. Taqqu et al., 1995) of the lowest frequencies only. In contrast, when the slope is fitted over the lowest 50 frequencies only, and is thus fitted over a stable low-frequency range, with a stable cut-off frequency, it would be natural to expect the bias to be absent.

THE RELIABILITY OF α

The empirical data series have been collected in a precision aiming study. In the study, 15 participants were invited to draw lines back and forth between two visual targets with a stylus, as fast and as accurately as possible. Participants received no instruction concerning pen pressure or pen tilt strategies. The targets were presented on a printed sheet of paper, one at the left side of the paper and one at the right side. The target width was 0.4 cm and the distance between targets was 24 cm. One block of 1100 trials was completed with the dominant hand. When the last trial was reached, a tone signaled the end of the experiment.

Pen pressure (in grams) and pen tilt (absolute deviation from the center of the stylus, in cm) coordinates were recorded using a digitizer tablet connected to a regular PC. The tablet samples at a temporal rate of 171 Hz. In addition, a GSR signal was recorded on the fingertips of the non-moving hand at 200 Hz. Also, artificial 15 white noise signals ($1/f^0$), 15 $1/f$ noise signals ($1/f^1$), and 15 Brownian noise signals ($1/f^2$) were generated with a series length of 2^{16} data points, using an Inverse Fourier transform algorithm described by Lennon (2000).

After data collection, each time series was prepared to fit the needs for the spectral analysis (cf. Holden, 2005). First, outliers outside 3 × the standard deviation from the mean were removed. Next, because the Fourier transform fits stationary sines and cosines to the data series, simple drifts or long-term trends may distort the results. Linear and quadratic detrending ensures that the analyzed data series is in line with the idealized mathematics of spectral analysis. Thus, linear and quadratic trends were removed for all data series (cf. Holden, 2005). Then, the original time series were normalized, and truncated by removing the data points at the beginning of the data series until 2^{16} data points were left. None of the empirical data series contained fewer than 2^{16} data values.

Next, the original data series (2^{16} data points) were downsampled by removing every next data point from the analysis, so that the new data series length was 2^{15}. This procedure was iterated until only 2^{10} data points were left, thereby reducing sample rate by a factor of 2^6. Then, for each of the resulting series, the spectral slope was either fitted over 10, 25, or 100% of the lowest frequencies, or over the 50 lowest frequencies.

RESULTS AND DISCUSSION

The results from the pen pressure, pen tilt, and GSR data are shown in **Figures 7A–C**, which represents the fitted slope $-\alpha$ over a range of different sample rates for each data set. The different choices of fit are shown as separate lines in each Figure. It can be seen that regardless of the percentage of low frequencies used to fit the slope $-\alpha$ (10, 25, or 100%), the observed α values effectively change in function of sample rate. As predicted, α exponents are higher at high sample rates. The artifact is most apparent when fitting the slope over the entire power spectrum and gradually becomes somewhat less dramatic as smaller portions of the low-frequencies are used to fit the spectral slope $-\alpha$. When fitting over the 50 lowest frequencies, however (shown as 50Low in **Figures 7A–D**), the slope $-\alpha$ remains robust against sample rate conversion.

Only the pen tilt data do not entirely confirm the expected artifact. At the highest sample rates, α values derived from a fit over the entire spectrum appear more robust than α values derived from a fit over the 10 or 25% lowest frequencies. But also in this example, α values derived from a fit over the 50 lowest frequencies constituted the most robust solution.

The simulated noise patterns, however, reveal a very distinct (hence, absent) effect of sample rate. The four choices of fit that were evaluated are shown in **Figure 7D** for each category of noise simultaneously. The random ($\alpha = 0$), $1/f$ ($\alpha = 1$) and Brownian ($\alpha = 2$) noise simulations reveal robust values of α, regardless the choice of fit. This result confirms that the change in α arises from differences in sample density rather than from the differences in series length *per se* (with the 100% fit somewhat less reliable than the other choices of fit, however).

These results demonstrate that the relatively arbitrary choice of a sample rate dramatically alters the value of the α exponent if the spectral slope $-\alpha$ is fitted over a fixed percentage of low-frequencies. The bias is so strong that sample rate appears to be more influential on the estimated exponents than the process under scrutiny itself. This artifact is obviously problematic and leaves researchers with difficult decisions concerning the reliability of their analysis. The strategy of spectral analysis introduced here results in scaling exponents that are robust against artifacts that come with dense sampling, and thus may solve those questions.

THE SENSITIVITY OF α

A final confirmation of the introduced strategy for spectral analysis would require an evaluation of the sensitivity of the estimated exponents, in addition to their robustness against sample rate conversion. Sensitive exponents are more likely to differentiate

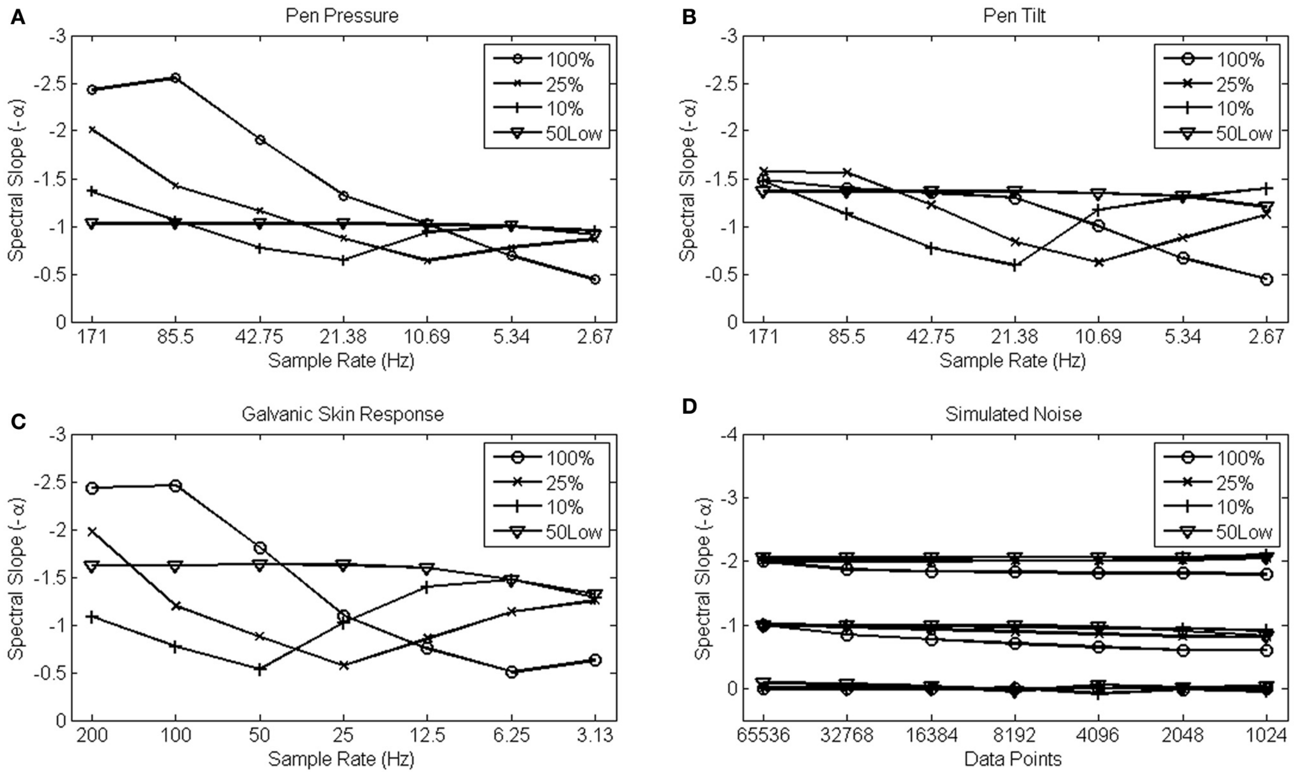

FIGURE 7 | Average α scaling exponents from 15 pen pressure (A), pen tilt (B), Galvanic Skin Response (C), and simultated $1/f^0$, $1/f^1$, and $1/f^2$ data series (D) are shown on the y-axis. The x-axis shows sample rate for the empirical data series, and series length for the simulated series that also were downsampled by a factor of 2 in each step on the x-axis.

among experimental conditions, and more clearly reveal the relation among different variables, given that such relations are present. In this case, we evaluate the correlation among different streams of 1/*f* noise (pen pressure and pen tilt) that were collected simultaneously in the previously introduced motor task.

The pattern of correlations between both streams of 1/*f* noise (pen pressure and pen tilt) shown in **Figure 8** is remarkably heterogeneous over different sample rates, except for the strategy introduced here. α exponents estimated from the original, non-down-sampled data appear uncorrelated when relying on conventional spectral strategies. The correlations among pen pressure and pen tilt scaling exponents tend to grow stronger as sample rate decreases (hence, when fewer "smoothed" high-frequencies are introduced in the analysis). The introduced method for spectral analysis (shown as 50Low in **Figure 8**), in contrast, indicates strongly correlated streams of 1/*f* noise, regardless of sample rate.

THE VALIDITY OF α

The results presented above suggest that if one follows the exact same procedure in an experimental set-up, but uses a different measurement device or device setting, one may end up with vastly deviant outcomes if sampling artifacts are not anticipated. Anticipating sampling artifacts can be as simple as fitting the power spectrum over a set number of low frequencies (i.e., fitting over a stable low-frequency range), rather than fitting the regression line over a set percentage of frequency (i.e., fitting over a variable low frequency range). This practice results in more reliable and more sensitive scaling exponents. Nonetheless, the goal should not be to fit over a prescribed amount of low frequencies (e.g., 50) *per se*. Importantly, as long as the slope does not change in function of sample rate (i.e., after downsampling), any set number will do reliability-wise. For instance; an idealized 1/*f* process would reveal a linear slope regardless of the fitted frequency range (hence **Figure 7D**).

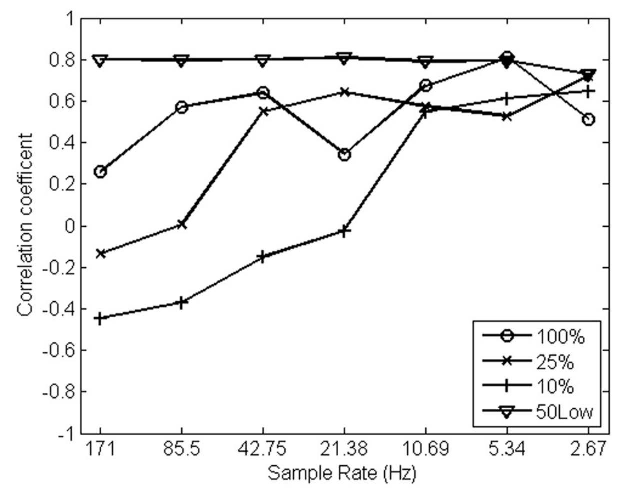

FIGURE 8 | Correlation coefficients among α exponents estimated from pen pressure and pen tilt data (y-axis, *N* = 15) over a range of sample rates (in Hz; x-axis) using different strategies for spectral analysis.

Empirical data often show scale-invariance in a restricted range only, however. In these cases an optimal number of frequencies can be determined by performing a simple downsampling test (i.e., **Figure 7**). When the scaling outcomes do not change in function of sample rate the chosen frequency range to fit is reliable. If the outcomes do change, the number of low frequencies in the fit should be reduced until the outcomes remain robust against sample rate conversion. In this process, one should obviously be aware of two final criteria: (1) the amount of frequencies should be sufficient to yield reliable regression outcomes, and (2) a linear range of the power spectrum is preferred given the nature of the regression analysis.

With these less idealized examples of 1/*f* scaling, changing the frequency range used for slope fitting may reveal ever changing slopes over different frequency ranges, however. This would mean one would want to ascertain the validity of an estimate in addition to its reliability over different sample rates, leading to the question whether the scaling exponents derived using the suggested fitting approach are representative for the process under scrutiny.

To inquire the validity of the suggested fitting approach, we simulated artificial series using the fBmW model (Thornton and Gilden, 2005). This procedure produces series that compose a scaling part α (i.e., a fractional Brownian motion with a known exponent α) with white noise β (whose variance is β^2) added to it. Given that relative roughness decreases at higher sampling rates (cf. **Figure 4**), it is fair to assume that the high-frequency range of the spectrum is an artifact of sampling, and that the valid information is to be found in the low-frequency range i.e., the alpha put in the model. In addition, faster sampling arguably is more susceptible to instrument noise that may distort spectral outcomes at the higher frequencies. Thus, power spectra produced by the fBmW-model present examples in analogy with the sampling rate artifact, producing a well-defined elbow in the power spectrum.

Four example power spectra produced by the model, with $\alpha = 1.5$ and $\beta = 1.5$, 1, 0.5, and 0, respectively, are shown in **Figure 9**. We know from these parameters that a valid scaling estimate should approximate 1.5; a reference point against which different fitting strategies can be assessed. The x-axis in **Figure 10** shows the number of low frequencies included in the regression fit. The pentagram-shaped markers indicate the exponents estimated when the spectra where fitted over 25% of lowest frequencies. The inset reveals a region of convergence around roughly 50 frequencies, after which a point of expansion reveals the white noise process added to varying degrees. This observation supports the suggestion that a fit over the lowest 50 frequencies provides valid estimates of the "true" scaling exponent α (i.e., 1.5), and questions the validity of estimates over the 25% of lowest frequencies.

This simple simulation confirms the validity of the proposed fitting strategy, but a better analogy to the empirical data is possible, however. The produced series keep a number of variables stable that vary in the empirical series (e.g., series length, number of frequencies in the spectrum, relative roughness). Also, the resulting spectra are simple in the sense that they reveal a single elbow, rather than the more complex staircase-like shape of

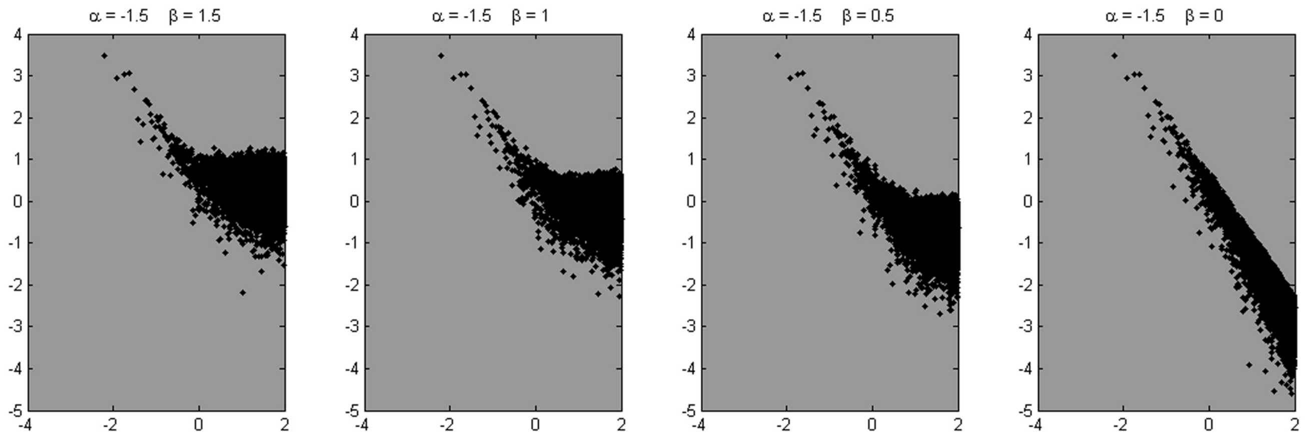

FIGURE 9 | Four example spectra are shown, derived from the signals simulated using the fBmW-model.

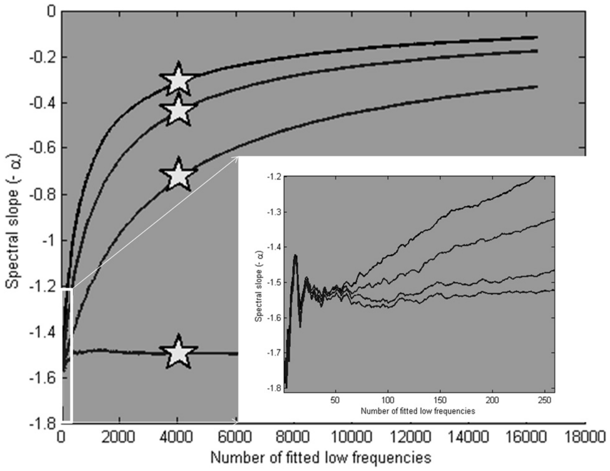

FIGURE 10 | Average scaling estimates of ten simulated signals (length is 2^{16} data points), with α is 1.5, and β is 1.5, 1, 0.5, and 0, respectively, fitted over a varying number of low frequencies. The pentagram markers indicate the scaling estimates for a fit over the 25% lowest frequencies. In the inset, it is shown that the estimates converge closely on the modeled α parameter at around 50 low frequencies.

the empirical spectra seen in **Figures 5** and **6**. We therefore determined empirically the parameters that resemble the empirical power spectra more closely.

In search for a more realistic representation, we constructed 10 series with $\alpha = 1.35$ with a series length of 2^{16}, with white noise added to it ($\beta = 1.6$). The series were smoothed with a moving average filter with a span of 14 data points, to mimic the decrease in relative roughness at higher sample rates. This procedure added a steeper slope (i.e., lower amplitudes) at the high frequencies in addition to the initial flattening due to the added white noise. Then a portion of white noise was added again, to complete the staircase-shape of the empirical power spectra (i.e., white noise at the high-end of the power spectrum). Next, three times 10 series were produced, reducing in each case the series length and the number of overall estimated frequencies by a factor of two. Also the β parameter and the span of the moving average filter were reduced at each step. Examples of the resulting power spectra are shown in **Figure 11**.

When fitted over a varying number of frequencies, the average estimate of 10 simulated series for each set of parameters converged on the "true" α of 1.35 at around 50 low frequencies. This can be seen in **Figure 12** (see inset), which also shows the scaling estimates (as pentagram-shaped markers) when the lowest 25% of frequencies were used to fit the slope. Note that **Figure 12** is restricted to 25% of low frequencies.

GENERAL DISCUSSION

When spectral scaling exponents are estimated without anticipating artifacts introduced by sample rate, the exponent values themselves may fluctuate widely. The order of magnitude of these discrepancies is dramatic: scaling exponents may differ in magnitude by 1 or 2 depending on sample rate, while the order of magnitude of reliable differences in exponents between experimental groups and conditions are often in the range of 0.05–0.25 (e.g., Chen et al., 2001; Kello et al., 2007; Wijnants et al., 2009). These discrepancies may account for known inconsistencies in the psychological literature on 1/*f* noise, and perhaps, for the lack of a comprehensive framework of 1/*f* noise in continuous performance measures. Here we have introduced an empirical solution to this problem. The proposed strategy for spectral analysis is robust against changes in sample rate and renders more sensitive and valid α exponents compared with more conventional strategies of analysis.

The artifact introduced in the high-frequency range of a power spectrum by differences in sample rate is not due to the inherent difference in data series length (hence, **Figure 7D**) but is rather a natural consequence of the resulting differences in sample density. That is, denser sampling implies a decrease in relative roughness (i.e., because the highest frequencies in a measured signal have lower amplitude) compared with more sparsely sampled data. This artifact is important because it is implied that subtle methodological choices, often choices of convenience, may

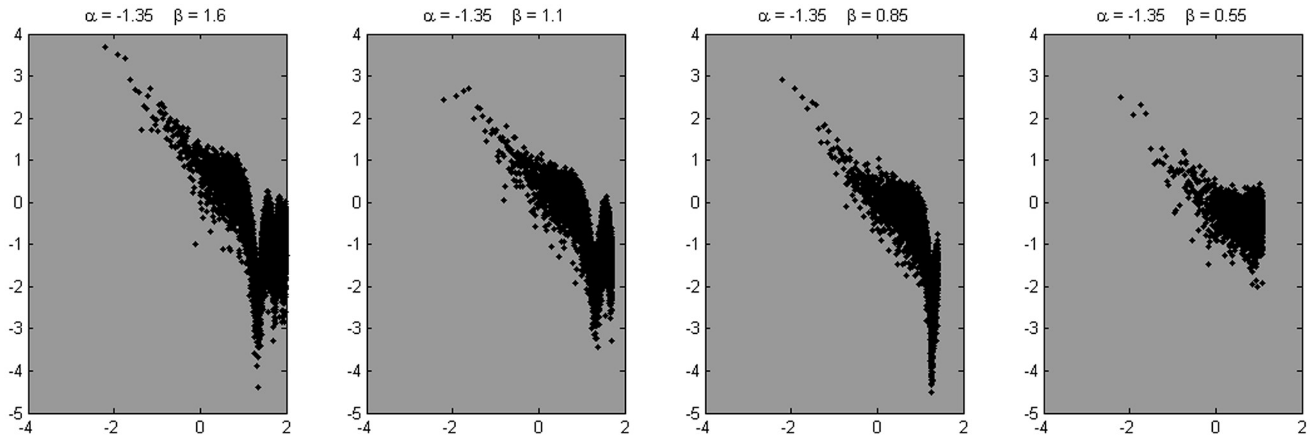

FIGURE 11 | Four example spectra are shown, derived from the signals simulated using the fBmW-model. These signals were subjected to a moving average filter with a span of 14, 7, 4, and 2 data points, respectively, to mimic the reduced relative roughness at high sample rates. To these composites, another portion of white noise was added to mimic the flattening at the high-end of the power spectrum, as in **Figures 5** and **6**.

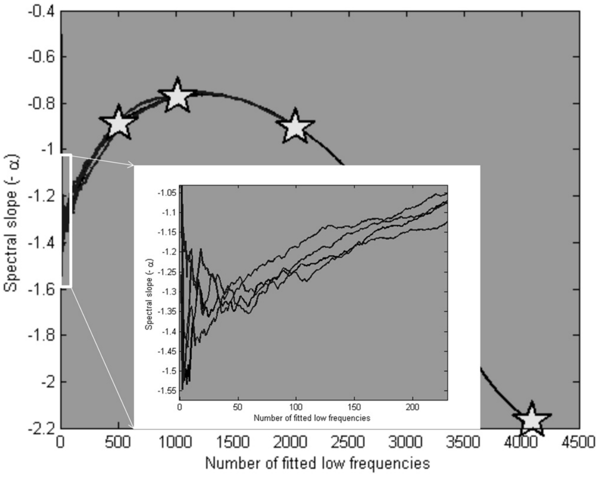

FIGURE 12 | Average scaling estimates of four times 10 simulated signals, with parameters presented in Figure 11, fitted over a varying number of low frequencies. The pentagram markers indicate the scaling estimates for a fit over the 25% lowest frequencies. In the inset, it is shown that the estimates converge closely of the modeled α parameter (1.35) at around 50 low frequencies.

radically alter the outcome of spectral analysis when sampling artifacts are not adequately anticipated.

The proposed strategy for spectral analysis of continuous processes is to determine the spectral slope −α over a fixed number, rather than a fixed percentage of low-frequencies in a power spectrum. Fitting the slope over a set number of low frequencies implies a fit over a different high-frequency range for different sample rates, but over a stable low-frequency range. Fitting the slope over a fixed percentage of lowest frequencies, however, implies a fit over a stable high-frequency range, but over a different low-frequency range. Given that the artifact introduced by sample rate specifically concerns the high-frequency range of a power spectrum, it is obvious that the former strategy is to be preferred. That said, the aim of the present suggestion is not to exclude high-frequency range of a power spectrum *per se*, but rather to exclude comparisons that are unreliable in terms of frequency content (i.e., when a range of low frequencies quiescently varies in function of sample rate). While this may not solve the actual measurement problem (i.e., the outcomes change in function of measurement procedure and choices of data analysis), it does define the relation between observer and observable more clearly than before (i.e., outcomes should be independent of sample rate).

This suggestion follows the logic of Eke et al.'s (2002) recommendation to discard the highest frequencies and to focus on the lower frequencies, a recommendation that is consistent with all example studies cited in the section "1/*f* noise in human performance." In the section "1/*f* noise and periodic sampling," we acknowledged nonetheless that 1/*f* scaling relations often are observed within a finite range of scales only. The 1/*f* scaling relation may thus break down at specific frequency ranges, and usually at the highest frequencies. Interestingly, this basic fact about power spectra of psychological data series has led some scientists to inquire whether low- and high-frequency ranges in a power spectrum may represent the variability of different component mechanisms (Gilden, 2001; Delignières et al., 2008; Torre and Delignières, 2008). The scope of the present paper did not include an in depth discussion of that potential of spectral analysis. The present evaluation of spectral analysis reveals no reason to believe that such uses of spectral analysis are problematic in any way when dealing with trial series or simulated data series. Yet, the cautious implication is that estimating high-frequency slopes is a rather delicate enterprise when confronted with time series sampled at arbitrary sample rates.

The present investigation may shed new light on known discrepancies in the literature on 1/*f* noise in psychological data. For instance, an explicit demonstration of such a discrepancy is described by Delignières et al. (2005) in the context of a study of relative phase in bimanual coordination. These authors estimated the scaling properties of *discrete* relative phase, corresponding to a cycle-to-cycle measurement yielding a trial series. The mean values of the estimated scaling exponent α ranged from 0.72 to 0.78, while *continuous* relative phase (hence, the same performance when treated as a time series), results in scaling exponents with an average value of about 2.52 (Schmidt et al., 1991), far from the scaling range typically observed in trial series. This example confirms that different sampling regimes may effectively lead to appreciably different conclusions about the nature of the observed patterns of variability.

Also within a similar sampling regime (i.e., when an across-study comparison yields only time series, rather than comparing time series with trial series) different results may be obtained with different choices of sampling. An example is provided by studies of postural sway. "Postural sway typically exhibits fractal scaling with exponents characteristic of fractional Brownian motion (cf. Collins and De Luca, 1993), although prolonged, unconstrained standing has suggested a pink [*1/f*] noise structure (Duarte and Zatsiorsky, 2001)" (Bonnet et al., 2006, p. 806). These different results are methodologically interesting as well, if one notes that Collins and De Luca (1993) sampled their data at 100 Hz, while Duarte and Zatsiorsky (2001) sampled at 20 Hz. Here, we have shown that a comparison of these studies is only meaningful when the different sample rates of both experiments are taken into account, hence, when the scaling parameters are determined over an equivalent low-frequency range.

The ability to reliably and sensitively estimate valid scaling exponents, regardless of sample rate, and to compare these exponents (whether among different streams of 1/*f* noise, across experimental conditions or across studies) is undoubtedly a requisite to achieve a coherent and comprehensive framework of 1/*f* noise in continuous processes. The present contribution might motivate an extension of the coherent framework of 1/*f* noise that has emerged for trial series of repeated discrete responses (e.g., Diniz et al., 2010; Van Orden et al., 2011; Wijnants et al., 2012a,b) to continuous performance measures.

REFERENCES

Abásolo, D., Hornero, R., Gómez, C., García, M., and López, M. (2006). Analysis of EEG background activity in Alzheimer's disease patients with Lempel-Ziv complexity and central tendency measure. *Med. Eng. Phys.* 28, 315–322.

Aks, D. J., Zelinsky, G. J., and Sprott, J. C. (2002). Memory across eye-movements: 1/f dynamic in visual search. *Nonlinear Dynamics Psychol. Life Sci.* 6, 1–25.

Bahrami, B., Seyedsadjadi, R., Babadi, B., and Noroozian, M. (2005). Brain complexity increases in mania. *Neuroreport* 16, 187–191.

Beran, J. (1994). *Statistics for Long-Memory Processes.* New York, NY: Chapman and Hall.

Bonnet, C. T., Faugloire, E. M., Riley, M. A., Bardy, B. G., and Stoffregen, T. A. (2006). Motion sickness preceded by unstable kinematics of the center of pressure. *Hum. Mov. Sci.* 25, 800–820.

Burr, R. L., Kirkness, C. J., and Mitchell, P. H. (2008). Detrended fluctuation analysis of intracranial pressure predicts outcome following traumatic brain injury. *IEEE Trans. Biomed. Eng.* 55, 2509–2518.

Carlini, P., Bizzarri, A. R., and Cannistraro, S. (2002). Temporal fluctuations in the potential energy of proteins: $1/f^{\alpha}$ noise and diffusion. *Physica D* 165, 242–250.

Chen, Y., Ding, M., and Kelso, J. A. S. (2001). Origins of time errors in human sensorimotor coordination. *J. Mot. Behav.* 33, 3–8.

Clayton, K., and Frey, B. B. (1997). Studies of mental "noise." *Nonlinear Dynamics Psychol. Life Sci.* 1, 173–180.

Collins, J. J., and De Luca, C. J. (1993). Open-loop and closed-loop control of posture: a random-walk analysis of center-of-pressure trajectories. *Exp. Brain Res.* 95, 308–318.

Correll, J. (2008). 1/f noise and effort on implicit measures of racial bias. *J. Pers. Soc. Psychol.* 94, 48–59.

Delignières, D., Fortes, M., and Ninot, G. (2004). The fractal dynamics of self-esteem and physical self. *Nonlinear Dynamics Psychol. Life Sci.* 8, 479–510.

Delignières, D., Torre, K., and Lemoine, L. (2005). Methodological issues in the application of monofractal analyses in psychological and behavioral research. *Nonlinear Dynamics Psychol. Life Sci.* 9, 435–462.

Delignières, D., Torre, K., and Lemoine, L. (2008). Fractal models for event-based and dynamical timers. *Acta Psychol.* 127, 382–397.

Diniz, A., Wijnants, M. L., Torre, K., Barreiros, J., Crato, N., Bosman, A. M. T., et al. (2010). Contemporary theories of 1/f noise in motor control. *Hum. Mov. Sci.* 30, 889–905.

Duarte, M., and Zatsiorsky, V. M. (2001). Long-range correlations in human standing. *Phys. Lett. A* 283, 124–128.

Eke, A., Hermán, P., Bassingthwaighte, J. B., Raymond, G. M., Percival, D. B., Cannon, M., et al. (2000). Physiological time series: distinguishing fractal noises from motions. *Pflugers Arch.* 439, 403–415.

Eke, A., Hermán, P., Kocsis, L., and Kozak, L. R. (2002). Fractal characterization of complexity in temporal physiological signals. *Physiol. Meas.* 23, 1–38.

Gilden, D. L. (1997). Fluctuations in the time required for elementary decisions. *Psychol. Sci.* 8, 296–301.

Gilden, D. L. (2001). Cognitive emissions of 1/f noise. *Psychol. Rev.* 108, 33–56.

Gilden, D. L., and Hancock, H. (2007). Response variability in attention deficit disorders. *Psychol. Sci.* 18, 796–802.

Gilden, D. L., Thornton, T., and Mallon, M. W. (1995). 1/f noise in human cognition. *Science* 267, 1837–1839.

Goldberger, A. L. (1996). Non-linear dynamics for clinicians: Chaos theory, fractals and complexity at the bedside. *Lancet* 347, 1312–1314.

Goldberger, A. L., Amaral, L. A. N., Glass, L., Hausdorff, J. M., Ivanov, P. C., Mark, R. G., et al. (2000). PhysioBank, PhysioToolkit, and PhysioNet: components of a new research resource for complex physiologic signals. *Circulation* 101, e215–e220.

Goldberger, A. L., Amaral, L. A. N., Hausdorff, J. M., Ivanov, P. Ch., Peng, C.-K., and Stanley, H. E. (2002). Fractal dynamics in physiology: alterations with disease and aging. *Proc. Natl. Acad. Sci. U.S.A.* 99, 2466–2472.

Hausdorff, J. M. (2007). Gait dynamics, fractals and falls: finding meaning in the stride-to-stride fluctuations of human walking. *Hum. Mov. Sci.* 26, 555–589.

Holden, J. G. (2005). "Gauging the fractal dimension of response times from cognitive tasks," in *Contemporary Nonlinear Methods for Behavioral Scientists: A Webbook Tutorial,* eds M. A. Riley and G. C. Van Orden, 267–318. Available online at: http://www.nsf.gov/sbe/bcs/pac/nmbs/nmbs.jsp

Holden, J. G., Choi, I., Amazeen, P. G., and Van Orden, G. (2011). Fractal 1/f dynamics suggest entanglement of measurement and human performance. *J. Exp. Psychol. Hum. Percept. Perform.* 37, 935–948.

Kello, C. T., Beltz, B. C., Holden, J. G., and Van Orden, G. C. (2007). The emergent coordination of cognitive function. *J. Exp. Psychol. Gen.* 136, 551–568.

Lai, M. C., Lombardo, M. V., Chakrabarti, B., Sadek, S. A., Pasco, G., Wheelwright, S. J., et al. (2010). A shift to randomness of brain oscillations in people with autism. *Biol. Psychiatry* 68, 1092–1099.

Lennon, J. L. (2000). Red-shifts and red herrings in geographical ecology. *Ecography* 23, 101–113.

Linkenkaer-Hansen, K., Monto, S., Rytsälä, H., Suominen, K., Isometsä, E., and Kähkönen, S. (2005). Breakdown of long-range temporal correlations in theta oscillations in patients with major depressive disorder. *J. Neurosci.* 25, 10131–10137.

Marmelat, V., Torre, K., and Delignières, D. (2012). Relative roughness: an index for testing the suitability of the monofractal model. *Front. Physio.* 3:208. doi: 10.3389/fphys.2012.00208

Ramon, C., Holmes, M. D., Freeman, W. J., McElroy, R., and Rezvanian, E. (2008). Comparative analysis of temporal dynamics of EEG and phase synchronization of EEG to localize epileptic sites from high density scalp EEG interictal recordings. *Conf. Proc. IEEE Eng. Med. Biol. Soc.* 2008, 4548–4550.

Riley, M. A., and Turvey, M. T. (2002). Variability and determinism in motor behavior. *J. Mot. Behav.* 34, 99–125.

Schmidt, R. C., Beek, P. J., Treffner, P. J., and Turvey, M. T. (1991). Dynamical substructure of coordinated rhythmic movements. *J. Exp. Psychol. Hum. Percept. Perform.* 17, 635–651.

Shannon, C. E. (1949). Communication in the presence of noise. *Proc. Inst. Radio Eng.* 37, 10–21.

Slifkin, A. B., and Newell, K. M. (1998). Is variability in human performance a reflection of system noise? *Curr. Dir. Psychol. Sci.* 7, 170–177.

Taqqu, M. S., Teverovsky, V., and Willinger, W. (1995). Estimators for long-range dependence. an empirical study. *Fractals* 3, 785–798.

Thornton, T. L., and Gilden, D. L. (2005). Provenance of correlations in psychological data. *Psychon. Bull. Rev.* 12, 409–441.

Torre, K., and Delignières, D. (2008). Unraveling the finding of 1/fb noise in self-paced and synchronized tapping: a unifying mechanistic model. *Biol. Cybern.* 99, 159–170.

Torre, K., and Wagenmakers, E. J. (2009). Theories and models for $1/f^{b}$ noise in human movement science. *Hum. Mov. Sci.* 28, 297–318.

Van Orden, G. C., Holden, J. G., and Turvey, M. T. (2003). Self-organization of cognitive performance. *J. Exp. Psychol. Gen.* 132, 331–350.

Van Orden, G. C., Holden, J. G., and Turvey, M. T. (2005). Human cognition and 1/f scaling. *J. Exp. Psychol. Gen.* 134, 117–123.

Van Orden, G., Kloos, H., and Wallot, S. (2011). "Living in the pink: intentionality, wellbeing, and complexity," in *Philosophy of Complex Systems: Handbook of the Philosophy of Science, Vol. 10,* ed C. A. Hooker (Amsterdam: Elsevier), 639–683.

Wagenmakers, E.-J., Farrell, S., and Ratcliff, R. (2005). Human cognition and a pile of sand: a discussion on serial correlations and self-organized criticality. *J. Exp. Psychol. Gen.* 135, 108–116.

Werner, G. (2010). Fractals in the nervous system: conceptual implications for theoretical neuroscience. *Front. Physio.* 1:15. doi: 10.3389/fphys.2010.00015

West, B. J. (2006). *Where Medicine Went Wrong: Rediscovering the Path to Complexity.* Hackensack, NJ: World Scientific.

West, B. J. (2010). Fractal physiology and the fractional calculus: a perspective. *Front. Physio.* 1:12. doi: 10.3389/fphys.2010.00012

Wijnants, M. L., Bosman, A. M. T., Hasselman, F., Cox, R. F. A., and Van Orden, G. (2009). 1/f scaling in movement time changes with practice in precision aiming. *Nonlinear Dynamics Psychol. Life Sci.* 13, 75–94.

Wijnants, M. L., Cox, R. F. A., Hasselman, F., Bosman, A. M. T., and Van Orden, G. (2012a). A trade-off study revealing nested timescales of constraint. *Front. Physio.* 3:116. doi: 10.3389/fphys.2012.00116

Wijnants, M. L., Hasselman, F., Cox, R. F. A., Bosman, A. M. T., and Van Orden, G. (2012b). An interaction-dominant perspective on reading fluency and dyslexia. *Ann. Dyslexia* 62, 100–119.

Conflict of Interest Statement: The authors declare that the research was conducted in the absence of any commercial or financial relationships that could be construed as a potential conflict of interest.

Received: 29 June 2012; paper pending published: 03 August 2012; accepted: 27 December 2012; published online: 21 January 2013.

Citation: Wijnants ML, Cox RFA, Hasselman F, Bosman AMT and Van Orden G (2013) Does sample rate introduce an artifact in spectral analysis of continuous processes? Front. Physio. ***3****:495. doi: 10.3389/fphys.2012.00495*

This article was submitted to Frontiers in Fractal Physiology, a specialty of Frontiers in Physiology.

frontiers in
PHYSIOLOGY

OPINION ARTICLE
published: 08 April 2013
doi: 10.3389/fphys.2013.00075

When the blind curve is finite: dimension estimation and model inference based on empirical waveforms

Fred Hasselman*

Learning and Plasticity, Behavioural Science Institute, Radboud University Nijmegen, Nijmegen, Netherlands
**Correspondence: f.hasselman@bsi.ru.nl*

Edited by:
Michael A. Riley, University of Cincinnati, USA

Reviewed by:
Michael A. Riley, University of Cincinnati, USA
John G. Holden, University of Cincinnati, USA
Sebastian Wallot, Aarhus University, Denmark

A PLEA FOR STRONG INFERENCE

The recent research topic "*Fractal Analyses: Statistical and Methodological Innovations and Best Practices*" reveals there is no consensus among experts about the best procedure to estimate self-affine structure in trial and time series data. One of the recurring issues pertains to the validity of inferences based on analysis results about the physical change processes that generated the empirical waveforms. In this paper I argue that none of these approaches can be used to validate such inferences outside of the context of theory evaluation by strong inference (e.g., Platt, 1964). Two arguments warrant this claim: (1) All procedures make an assumption about the physics of the system under scrutiny. This is arguably most prominent in ARFIMA modeling, but associating an estimated scaling exponent to a fractal dimension is also based on assumptions (e.g., fGn vs. fBm; Mandelbrot and Van Ness, 1968); (2) given infinitesimal measurement resolution and infinite observation time, properties like dimension and self-affinity are not unique descriptors of a process, pattern or object (cf. Vicsek, 2001). Multiple mathematical models of physical processes can be constructed to generate a waveform with exactly the dynamical and invariant properties as observed in the finite sample (e.g., Mandelbrot, 2001; Kantz and Schreiber, 2003; Thornton and Gilden, 2005; Morrison, 2008).

The second issue pertains to a general problem of model-based inference: a good fit to a finite sample of measurement outcomes can never be conclusive in the evaluation of predictions by theories (cf. Roberts and Pashler, 2000, 2002; Fiedler et al., 2012). Using results of (fractal) analyses to answer questions about the physics of the observed system is an attempt to evaluate the ontology of a theory, ex post facto; let's leave ontology evaluation to the metaphysicians (cf. Poincaré, 1905, p. 211). The scientific method is not a competition for *mathematical models* constructed to produce the best fit to measurement outcomes; instead, *theoretical predictions* about the observed system compete for highest empirical precision and accuracy in order to gain scientific credibility.

In what follows I evaluate to what extent fractal analyses are used in the context of strong inference given the current empirical record of human physiology and performance. Subsequently I will explore what may be gained when implicit ontology falsification is removed from fractal analyses by introducing the concepts of intuitive dimension and informed dimension estimates.

ON FRACTAL SCALING AND PLANETARY ORBITS

Why should an accurate prediction by a theory be preferred over a good retrospective model fit? Models proposed to explain the orbit of Mercury (which displays a perihelion advance) present an interesting historical analogy. The orbit was accurately modeled by the classical geocentric models based on Ptolemy's Almagest (used from around 100–3500 CE; Toomer, 1984). These models assumed celestial objects moved around the earth on a celestial sphere that could host one or more local orbits or epicycles. The number of nested epicycles was simply varied until the predicted trajectory was sufficiently in accordance with the empirical record. Curiously, to the heliocentric models replacing Ptolemaic astronomy like Newton's theory of celestial mechanics, Mercury's orbit was an anomaly! No wonder that Einstein considered the accurate prediction of this anomaly the most important empirical test of his theory of general relativity (Einstein, 1916; Will, 2005).

This brief history of orbit modeling reveals that the theoretical perspective used to observe the empirical record changes one and the same reliably measured pattern from a good model fit, into an anomalous phenomenon into a critical benchmark for theory evaluation. Ptolemy's solution of adding epicycles to reconstruct the shape of a trajectory is essentially the same as adding weighted autoregressive, moving average, seasonally changing, or (fractionally) integrating components in a time series model. Those components are constructed into the model in order to create a better fit with a pattern in the data. This is allowed by mathematics, but their presence is not predicted by a theory of principles about physical change processes in living systems and this renders its scientific evaluation invulnerable to the presence of anomalies. Compare to Newton's closed theory of principles: "*In Ptolemy's case, if the orbit didn't fit, he could add other epicycles. But if an experiment does not fit in Newtonian physics, you don't know what you mean by the words.*" (Heisenberg interviewed by Kuhn, 1963, p. 24, February 27th).

In order to advance scientific knowledge about scaling phenomena in living systems a program of strong inference that aims to produce closed theories of principles is needed. In order to reach this goal, empirical inquiries need to go beyond describing scaling phenomena in different populations in the context of impaired performance or pathology (e.g., Goldberger et al., 2002; Gilden and Hancock, 2007; West, 2010; Wijnants et al., 2012a). Several recent studies reveal scaling phenomena can be brought under experimental control, which is essential for a program of strong inference (e.g., Kello et al., 2007; Wijnants et al., 2009; Van Orden et al., 2010; Correll, 2011; Holden et al., 2011; Kuznetsov et al., 2011; Stephen et al., 2012). The diverging theoretical predictions examined in most studies reveal that the observed waveforms are more likely to originate from interaction-dominant complexity than from component-dominant mechanics (also see Turvey, 2007; Kello et al., 2010; Diniz et al., 2011).

A closed theory should account for most phenomena in the existing empirical record. A first step was recently made in which it was shown that the well-known speed-accuracy tradeoff in human performance is meaningfully related to the emergence of self-affine structure via nested timescales (Wijnants et al., 2012b). At the current level of scientific understanding it seems reasonable to ask of those who insist models based on AR-processes provide a parsimonious explanation of fractal scaling (e.g., Wagenmakers et al., 2005; Torre and Wagenmakers, 2009; Stadnitski, 2012), to provide experimental evidence that can validate their claims.

As stated above however, most claims about scaling phenomena based on fractal analyses are prone to implicit ontology falsification. In what follows, I will suggest an approach to dimension estimation that is based on intuitions about the geometry of a curve rather than on known mathematical models of change processes. I will focus on the mono-fractal case and show that a consistent conversion scheme for common estimates of self-affine structure is possible when using this notion of dimension.

FINITE SELF-AFFINITY: THE BLIND CURVE AND THE PERIMETER WALK

Dimension is an intrinsic property of a mathematical object that indicates to what extent it occupies the topological space in which it is embedded. A dimension estimate that is based on the properties of an empirical waveform can be defined as a finite walk in the plane that never forms a perimeter. Formally, this is a self-avoiding open curve dividing a bounded plane in two unconnected regions (i.e., it is not a Jordan Curve). Note that the properties of the curve have a physical origin: it is self-avoiding and open due to the arrow of time and because observation duration and measurement outcomes are finite, the planar topology is bounded.

Estimation procedures derived from formal definitions of dimension respect an intuitive geometric notion of a scaling of bulk with size (Theiler, 1990). Using the definition above, the intuitive concept to quantify would be a characterization of the waveform as line-like or plane-like, hence *planar extent* (e.g., Higuchi, 1988; Katz, 1988; Raghavendra and Dutt, 2010). Sevcik (1998) introduced such a dimension estimate based on the Hausdorff-Besicovitch dimension (Hausdorff, 1919; Xiao, 2008). It involves a double linear transformation of the axes embedding the waveform in a unit square of size N by N. Its length can be calculated as the sum of the Euclidean distance between points on the normalized curve. The graph entitled "Sevcik method" in **Figure 1** shows the equation used to approximate D based on number of observation intervals (N–1) and curve length L (for details see Sevcik, 1998, 2006). Across the top of **Figure 1**, twelve different waveforms are shown that were analyzed for self-affine structure (see caption for details). The waveforms were generated using freely available Matlab scripts[1].

INTUITIVE DIMENSION

The dimension estimates for the 12 waveforms based on Sevcik's mehod are numerically different from D_{uBC}, as well as from known exact values, the goal however is to achieve relative consistency. Processes that generated waveform 9 and 10 have known $D = 1.5$, which is equal to a sequence of random numbers drawn from a Normal distribution (i.e., waveform 5, waveform 10 is its cumulative sum). Using Sevcick's method however, both waveforms are classified as a Brownian noise. If this waveform were known to be physiological and medical in nature, the constrained dynamics associated with Brownian noise would lead to profoundly different conclusions about the health and well-being of the patient in question compared to blindly interpreting the limit values $D = 1.5$ and $H = 0.5$ (e.g., Goldberger et al., 2002; Van Orden et al., 2009). The gray-scale areas represent Sevcik's estimate for 12100 simulated series with ideal spectral slopes ranging from −3 to 3. Note that at 25% of the data length (first set of markers) the relative ordering according to D_{uBC} is recovered for almost all waveforms.

INFORMED DIMENSION ESTIMATES

The other graphs represent self-affinity exponents estimated using the power spectrum (PSD), detrended fluctuation analysis (DFA), standardized dispersion analysis (SDA), and ARFIMA (modeling strategy: Reisen and Lopes, 1999; Silva et al., 2006). The informed estimates of D refer to conversions of the self-affinity indices obtained for the 12 waveforms. ARFIMA modeling did not provide a consistent conversion scheme therefore the differencing parameter was plotted against the PSD based estimates. The gray-scale coded regions in these plots refer to the PSD slope estimates for the 12100 simulated series. These areas thus display the relation between the DFA, SDA, and ARFIMA self-affinity indices and the PSD slope based estimate.

The equations suggested for PSD and DFA indices produce approximations of well-known (H, D) pairs and should not be confused with an analytic solution. For SDA the known formula *1-Slope* yields relatively consistent results, a problem is that for some ranges of PSD slopes, the SDA indices are the same. ARFIMA modeling by the AIC selection criterion preferred models without self-affine structure ($d = 0$) of varying order ($p = 0$–2, $q = 0$–2) for the majority of simulated PSD slope series (ARIMA 42.8% vs. ARFIMA 20.6%). The remaining series produced fit errors (see Supplementary Materials for details).

Most waveforms in **Figure 1** get assigned a value for D that is in accordance with their planar extent as indicated by D_{uBC}. Waveform 11 is more line-like than waveform 9 and 10, which both map

---

[1] The scripts are available at http://fredhasselman.com in the section Supplementary Materials.

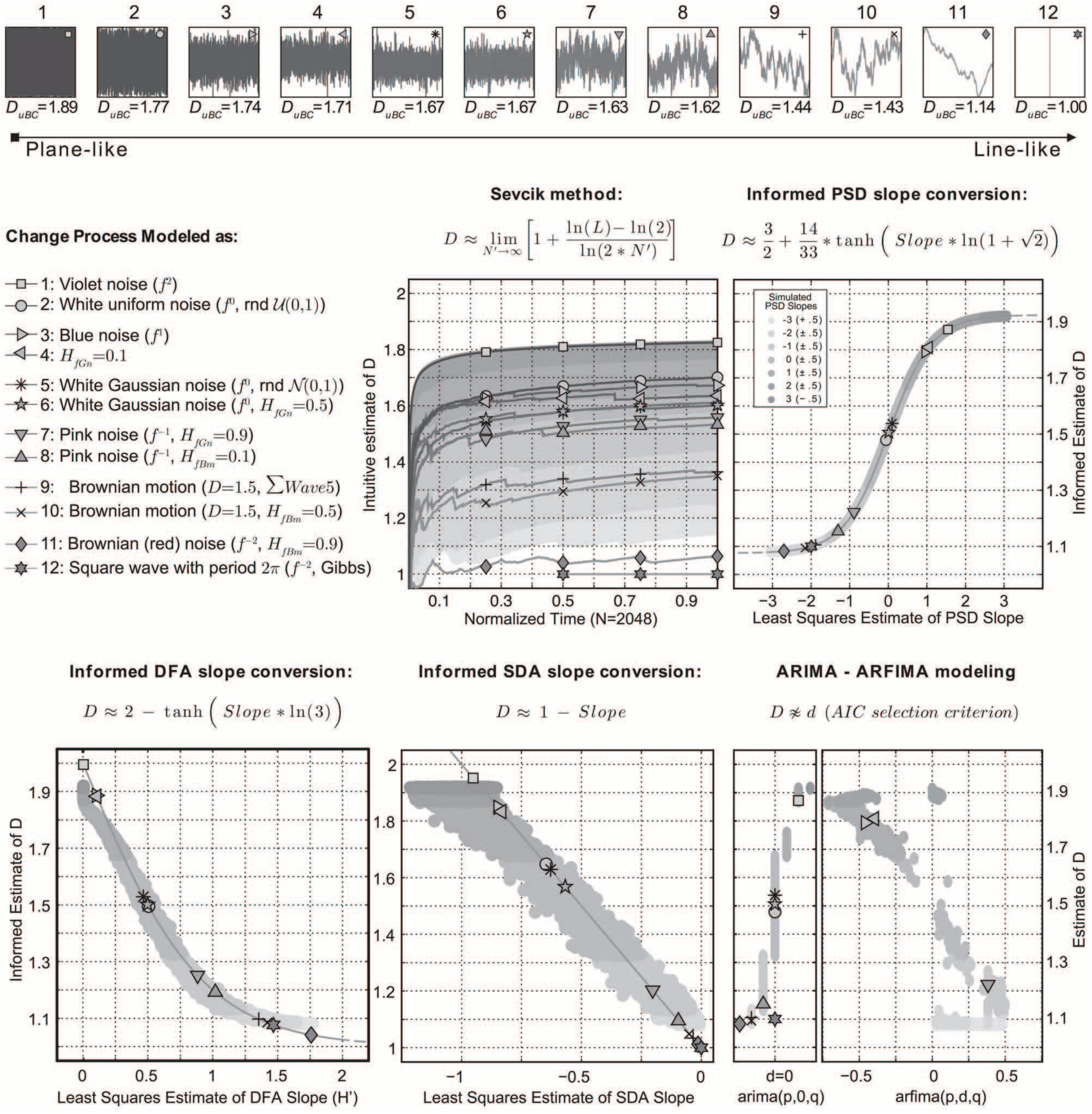

FIGURE 1 | The top row shows 12 waveforms of 2^{11} data points embedded in a unit square and ordered according to their planar extent estimated by D_{uBC}. This is a 2D box-counting dimension estimate calculated from a binary image (2×N by 2×N logical matrix) of the graph of the waveform. The same relative order was recovered using Sevcik's method, which estimates *D* from the waveform based on curve length *L* and data length *N* – 1 (*N'*). The gray-scale coded areas refer to Sevcik's estimate for 12100 simulated series with PSD slopes varying from −3 to 3. In the other graphs, the gray areas show the estimate of *D* based on PSD slope. The conversion formulas relate self-affinity exponents to *D* informed by known values of these exponents for power laws in spectral density. No conversion could be found for ARFIMA modeling. See text for details.

closely to known *D* of Brownian noise. Expected exceptions are waveforms 2 and 12. A sequence of random numbers drawn from a uniform distribution (waveform 2) has a PSD slope of zero. Taking the Fourier transform of a square wave (waveform 12) gives a frequency spectrum of odd harmonics only, with a slope of exactly −2 (the Gibbs phenomenon). Another expected result is that ARFIMA is preferred for series produced as H_{fGn} (except $H_{fGn} = 0.5$).

TO SELF-AFFINITY … AND BEYOND!

It seems possible to remove implicit assumptions about system ontology from fractal analysis by defining dimension as the planar extent of a finite curve. Direct estimates based on curve length and 2D box-counting provide a consistent relative ordering on this dimension. An informed conversion scheme using estimates of self-affine structure obtained from PSD, DFA, and SDA analyses give similar results. Some exceptions were predicted, but ARFIMA modeling could not be included in the approach due to inconsistent analysis results. A mono-fractal perspective was explored here, but there is no reason to assume it cannot be extended to the multi-fractal framework as well.

Exact numerical similarity of estimates is sacrificed for the convergence of estimates to a similar relative ordering. This sacrifice is acceptable given that in principle, even the best estimates of dimension and self-affinity leave us blind to the physical processes that generated the waveform. I suggest that claims about the physics of the system need to be evaluated by comparing the empirical accuracy of theoretical predictions in a program of strong inference, not by comparing fit indices.

REFERENCES

Correll, J. (2011). Order from chaos? 1/f Noise predicts performance on reaction time measures. *J. Exp. Soc. Psychol.* 47, 1–6.

Diniz, A., Wijnants, M. L., Torre, K., Barreiros, J., Crato, N., Bosman, A. M. T., et al. (2011). Contemporary theories of 1/f noise in motor control. *Hum. Mov. Sci.* 30, 889–905.

Einstein, A. (1916). Die Grundlage der allgemeinen Relativitätstheorie. *Annalen der Physik.* 354, 769–822.

Fiedler, K., Kutzner, F., and Krueger, J. I. (2012). The long way from α-error control to validity proper: problems with a short-sighted false-positive debate. *Perspect. Psychol. Sci.* 7, 661–669.

Gilden, D. L., and Hancock, H. (2007). Response variability in attention-deficit disorders. *Psychol. Sci.* 18, 796–802.

Goldberger, A. L., Amaral, L. A. N., Hausdorff, J. M., Ivanov, P. C., Peng, C.-K., and Stanley, H. E. (2002). Fractal dynamics in physiology: alterations with disease and aging. *Proc. Natl. Acad. Sci. U.S.A.* 99(Suppl. 1), 2466–2472.

Hausdorff, F. (1919). Dimension and äusseres Mass. *Math. Ann.* 79, 157–179.

Heisenberg, W. (1963). *Oral History Interview of Werner Heisenberg by Thomas Kuhn. Archive for the History of Quantum Physics*. Cambridge, MA: Harvard University. [deposit at Harvard University, Cambridge, MA].

Higuchi, T. (1988). Approach to an irregular time series on the basis of the fractal theory. *Physica D* 31, 277–283.

Holden, J. G., Choi, I., Amazeen, P. G., and Van Orden, G. (2011). Fractal 1/*f* dynamics suggest entanglement of measurement and human performance. *J. Exp. Psychol. Hum. Percept. Perform.* 37, 935–948.

Kantz, H., and Schreiber, T. (2003). *Nonlinear Time Series Analysis, 2nd Edn.* Cambridge, UK: Cambridge University Press.

Katz, M. J. (1988). Fractals and the analysis of waveforms. *Comput. Biol. Med.* 18, 145–156.

Kello, C. T., Beltz, B. C., Holden, J. G., and Van Orden, G. C. (2007). The emergent coordination of cognitive function. *J. Exp. Psychol. Gen.* 136, 551–568.

Kello, C. T., Brown, G. D. A., Ferrer-i-Cancho, R., Holden, J. G., Linkenkaer-Hansen, K., Rhodes, T., et al. (2010). Scaling laws in cognitive sciences. *Trends Cogn. Sci.* 14, 223–232.

Kuznetsov, N. A., Wallot, S., Alexander, E., and Ihlen, F. (2011). Effects of accuracy feedback on fractal characteristics of time estimation. *Front. Integr. Neurosci.* 5:62. doi: 10.3389/fnint.2011.00062

Mandelbrot, B. B. (2001). Scaling in financial prices: III. Cartoon Brownian motions in multifractal time. *Quant. Finance* 1, 427–440.

Mandelbrot, B. B., and Van Ness, J. (1968). Fractional brownian motions, fractional noises and applications. *SIAM Rev.* 10, 422–437.

Morrison, F. (2008). *The Art of Modeling Dynamic Systems: Forecasting for Chaos, Randomness and Determinism.* Mineola, NY: Dover Publications, Inc.

Platt, J. (1964). Strong inference. *Science* 146, 347–353.

Poincaré, H. (1905). *Science and Hypothesis (Trans. p. Science and Hypothesis)*. New York, NY: The Walter Scott Publishing Co., Ltd.

Raghavendra, B. S., and Dutt, D. N. (2010). Computing fractal dimension of signals using multiresolution box-counting method. *Int. J. Inf. Math. Sci.* 6, 50–65.

Reisen, V. A., and Lopes, S. (1999). Some simulations and applications of forecasting long-memory time-series models. *J. Stat. Plan. Inference* 80, 269–287.

Roberts, S., and Pashler, H. (2000). How persuasive is a good fit? A comment on theory testing. *Psychol. Rev.* 107, 358–367.

Roberts, S., and Pashler, H. (2002). Reply to Roders and Rowe (2002). *Psychol. Rev.* 109, 605–605.

Sevcik, C. (1998). A procedure to estimate the fractal dimension of waveforms. *Complexity International*, 05. Available online at: http://www.complexity.org.au/ci/vol05/sevcik/sevcik.html

Sevcik, C. (2006). On fractal dimension of waveforms. *Chaos Solitons Fractals* 28, 579–580.

Silva, E. M., Franco, G. C., Reisen, V. A., and Cruz, F. R. B. (2006). Local bootstrap approaches for fractional differential parameter estimation in ARFIMA models. *Comput. Stat. Data Anal.* 51, 1002–1011.

Stadnitski, T. (2012). Measuring fractality. *Front. Physiol.* 3:127. doi: 10.3389/fphys.2012.00127

Stephen, D. G., Anastas, J. R., and Dixon, J. A. (2012). Scaling in cognitive performance reflects multiplicative multifractal cascade dynamics. *Front. Physiol.* 3:102. doi: 10.3389/fphys.2012.00102

Theiler, J. (1990). Estimating fractal dimension. *J. Opt. Soc. Am. A* 7, 1055.

Thornton, T. L., and Gilden, D. L. (2005). Provenance of correlations in psychological data. *Psychon. Bull. Rev.* 12, 409–441.

Toomer, G. J. (1984). *Ptolemy's Almagest*. New York, NY: Springer-Verlag.

Torre, K., and Wagenmakers, E.-J. (2009). Theories and models for 1/f(beta) noise in human movement science. *Hum. Mov. Sci.* 28, 297–318.

Turvey, M. T. (2007). Action and perception at the level of synergies. *Hum. Mov. Sci.* 26, 657–697.

Van Orden, G. C., Kello, C. T., and Holden, J. G. (2010). Situated behavior and the place of measurement in psychological theory. *Ecol. Psychol.* 22, 24–43.

Van Orden, G. C., Kloos, H., and Wallot, S. (2009). "Living in the pink: intentionality, wellbeing, and complexity," in *Handbook of the Philosophy of Science,* ed C. Hooker (Amsterdam: Elsevier), 639–682.

Vicsek, T. (2001). *Fluctuations and Scaling in Biology*. Oxford: Oxford University Press.

Wagenmakers, E.-J., Farrell, S., and Ratcliff, R. (2005). Human cognition and a pile of sand: a discussion on serial correlations and self-organized criticality. *J. Exp. Psychol. Gen.* 134, 108–116.

West, B. J. (2010). Homeostasis and Gauss statistics: barriers to understanding natural variability. *J. Eval. Clin. Pract.* 16, 403–408.

Wijnants, M. L., Bosman, A. M. T., Hasselman, F., Cox, R. F. A., and Van Orden, G. C. (2009). 1/f scaling in movement time changes with practice in precision aiming. *Nonlin. Dyn. Psychol. Life Sci.* 13, 79–98.

Wijnants, M. L., Hasselman, F., Cox, R. F. A., Bosman, A. M. T., and Van Orden, G. (2012a). An interaction-dominant perspective on reading fluency and dyslexia. *Ann. Dyslexia* 62, 100–119.

Wijnants, M. L., Cox, R. F. A., Hasselman, F., Bosman, A. M. T., and Van Orden, G. (2012b). A trade-off study revealing nested timescales of constraint. *Front. physiol.* 3:116. doi: 10.3389/fphys.2012.00116

Will, C. (2005). "Special relativity: a centenary perspective," in *Einstein, 1905–2005: Poincaré Seminar 2005,* Vol. 47, eds T. Damour, O. Darrigol, B. Duplantier, and V. Rivasseau (Basel-Boston-Berlin: Birkhäuser Verlag), 33–58.

Xiao, Y. (2008). Packing dimension, Hausdorff dimension and Cartesian product sets. *Math. Proc. Camb. Philos. Soc.* 120, 535.

Received: 18 January 2013; accepted: 21 March 2013; published online: 08 April 2013.

Citation: Hasselman F (2013) When the blind curve is finite: dimension estimation and model inference based on empirical waveforms. Front. Physiol. ***4****:75. doi: 10.3389/fphys.2013.00075*

This article was submitted to Frontiers in Fractal Physiology, a specialty of Frontiers in Physiology.

frontiers in
PHYSIOLOGY

METHODS ARTICLE
published: 15 November 2012
doi: 10.3389/fphys.2012.00417

Pitfalls in fractal time series analysis: fMRI BOLD as an exemplary case

***Andras Eke*[1,2]*, *Peter Herman*[2], *Basavaraju G. Sanganahalli*[2], *Fahmeed Hyder*[2,3], *Peter Mukli*[1] and *Zoltan Nagy*[1]**

[1] *Institute of Human Physiology and Clinical Experimental Research, Semmelweis University, Budapest, Hungary*
[2] *Diagnostic Radiology, Yale University, New Haven, CT, USA*
[3] *Biomedical Engineering, Yale University, New Haven, CT, USA*

Edited by:
John G. Holden, University of Cincinnati, USA

Reviewed by:
Jianbo Gao, Wright State University, USA
Maarten Wijnants, Radboud University Nijmegen, Belgium

***Correspondence:**
Andras Eke, Institute of Human Physiology and Clinical Experimental Research, Faculty of Medicine, Semmelweis University, Tűzoltó Street 37-47, Budapest 1094, Hungary.
e-mail: eke.andras@med.semmelweis-univ.hu

This article will be positioned on our previous work demonstrating the importance of adhering to a carefully selected set of criteria when choosing the suitable method from those available ensuring its adequate performance when applied to real temporal signals, such as fMRI BOLD, to evaluate one important facet of their behavior, fractality. Earlier, we have reviewed on a range of monofractal tools and evaluated their performance. Given the advance in the fractal field, in this article we will discuss the most widely used implementations of multifractal analyses, too. Our recommended flowchart for the fractal characterization of spontaneous, low frequency fluctuations in fMRI BOLD will be used as the framework for this article to make certain that it will provide a hands-on experience for the reader in handling the perplexed issues of fractal analysis. The reason why this particular signal modality and its fractal analysis has been chosen was due to its high impact on today's neuroscience given it had powerfully emerged as a new way of interpreting the complex functioning of the brain (see "intrinsic activity"). The reader will first be presented with the basic concepts of mono and multifractal time series analyses, followed by some of the most relevant implementations, characterization by numerical approaches. The notion of the dichotomy of fractional Gaussian noise and fractional Brownian motion signal classes and their impact on fractal time series analyses will be thoroughly discussed as the central theme of our application strategy. Sources of pitfalls and way how to avoid them will be identified followed by a demonstration on fractal studies of fMRI BOLD taken from the literature and that of our own in an attempt to consolidate the best practice in fractal analysis of empirical fMRI BOLD signals mapped throughout the brain as an exemplary case of potentially wide interest.

Keywords: fractals, monofractals, multifractals, time series analysis, numerical testing, fMRI BOLD, brain

INTRODUCTION

Fractality (Mandelbrot, 1967, 1980, 1985; Bassingthwaighte et al., 1994; Gouyet, 1996; Eke et al., 2002), – in addition to deterministic chaos, modularity, self-organized criticality, "small word" network-connectivity – by now has established itself as one of the fundaments of complexity science (Phelan, 2001) impacting many areas including the analysis of brain imaging data such as fMRI BOLD (Zarahn et al., 1997; Thurner et al., 2003; Maxim et al., 2005; Raichle and Mintun, 2006; Fox et al., 2007; Razavi et al., 2008; Wink et al., 2008; Bullmore et al., 2009; Herman et al., 2009, 2011; Ciuciu et al., 2012).

The interest in fractal analysis accelerated the development of the new paradigm beyond a rate when the new – essentially mathematical or physical (i.e., statistical mechanics) – knowledge could be consolidated, their tools thoroughly evaluated and tested before being put to wide-spread use in various fields of science; typically beyond the frontiers of mathematics. The lack of an in-depth understanding of the implications of the methods when applied to empirical data, often generated conflicting results, but also prompted efforts at making up for this deficiency. Early, with the migration of the fractal concept from mathematics to various fields of science like physiology, the groups of Bassingthwaighte (Bassingthwaighte, 1988; Bassingthwaighte et al., 1994) and Eke et al. (1997) realized the need to adopt a systematic approach in developing needed analytical and testing frameworks to characterize and evaluate various monofractal time series methods (Bassingthwaighte and Raymond, 1994, 1995; Caccia et al., 1997; Eke et al., 2000, 2002). Eke and coworkers demonstrated that conscious and precise monofractal time series analysis could only be done when one has an *a priori* concept of the nature of the observed signals. They introduced the dichotomous fractional Gaussian noise (fGn)/fractional Brownian motion (fBm) model of Mandelbrot and Ness (1968) as the basis of monofractal time series analysis (Eke et al., 2000, 2002) and offered a strategy for choosing tools according to a proven selection criteria (Eke et al., 2000). Given the continuing advance in the fractal field and in sync with the increasing awareness to avoid potential pitfalls and misinterpretation of results in various forms of fractal analyses (Delignieres et al., 2005; Gao et al., 2007; Delignieres and Torre, 2009; Marmelat and Delignieres, 2011; Ciuciu et al., 2012), in this article we apply our evaluation strategy to multifractal tools, and characterize their most widely used implementations. Our motivation in doing so stems from the potentials of fMRI BOLD multifractal analysis in revealing the physiological underpinnings of activation-related change in scaling properties in the brain (Shimizu et al., 2004).

fMRI BOLD (Ogawa et al., 1990, 1993b; Kwong et al., 1992; Bandettini, 1993) has been selected as an exemplary empirical signal in our demonstrations, because its impact on contemporary neuroscience (Fox and Raichle, 2007). The human brain represents the most complex form of the matter (Cramer, 1993) whose inner workings can only be revealed if signals reflecting on neuronal activities are recorded at high spatio-temporal resolution. One of the most powerful methods, which can record spatially registered temporal signals from the brain, is magnetic resonance imaging (MRI; Lauterbur, 1973). The MRI scanner can non-invasively record a paramagnetic signal (referred to as blood oxygen level dependent, BOLD; Ogawa et al., 1990, 1993a) that can be interpreted as the signature of the functioning brain via its metabolic activity continuously modulating the blood content, blood flow, and oxygen level of the blood within the scanned tissue elements (voxels). Recently, a rapidly increasing volume of experimental data has demonstrated that BOLD is a complex signal, whose fractality – if properly evaluated – can reveal fundamental properties of the brain among them the so called "intrinsic or default mode" of operation that appears complementing the stimulus-response paradigm in the understanding the brain in a powerful way (Raichle et al., 2001). We hope, our paper could contribute to this major effort from the angle of consolidating some relevant issues concerning fractal analysis of fMRI BOLD.

CONCEPT OF FRACTAL TIME SERIES ANALYSES

MONOFRACTALS

All fractals are self-similar structures (mathematical fractals in an exact, natural fractals in a statistical sense), with their fractal dimension falling between the Euclidian and topologic dimensions (Mandelbrot, 1983; Eke et al., 2002). When self-similarity is anisotropic, the structure is referred to as self-affine; a feature, which applies to fractal time series (Mandelbrot, 1985; Barabási and Vicsek, 1991; Eke et al., 2002), too. Statistical fractals cannot be described comprehensively by descriptive statistical measures, as mean and variance, because these do depend on the scale of observation in a power law fashion:

$$\frac{\mu_2}{\mu_1} = \left(\frac{s_2}{s_1}\right)^{\varepsilon}, \tag{1}$$

where μ_1, μ_2 are descriptive statistical measures, and s_1, s_2 are scales within the scaling range where self-affinity is present, and ε is the power law scaling exponent. From this definition a universal scale-free measure of fractals can be derived:

$$D = -\lim_{s\to 0}\left(\inf \frac{\log\left(N\left(s\right)\right)}{\log\left(s\right)}\right). \tag{2}$$

D is called capacity dimension (Barnsley, 1988; Liebovitch and Tóth, 1989; Bassingthwaighte et al., 1994), which is related but not identical to the Hausdorff dimension (Hausdorff, 1918; Mandelbrot, 1967), s is scale and $N(s)$ is the minimum number of circles with size s needed to cover the fractal object to quantify its capacity on the embedding dimensional space (it corresponds to μ in Eq. 1). For fractal time series, the power law scaling exponent ε is typically calculated in the time domain as the Hurst exponent (H), or in the frequency domain as the spectral index (β). H and D relate (Bassingthwaighte et al., 1994) as:

$$H = 2 - D. \tag{3}$$

Further, β can also be obtained from H as $(H-1)/2$ for fGn and $(H+1)/2$ for fBm processes (Eke et al., 2000).

MULTIFRACTALS

While D does not vary along a monofractal time series, it is heterogeneously distributed along the length of a multifractal signal.

This phenomenon gave rise to the term "singular behavior," as self-affinity can be expressed by differing power law scaling along a multifractal time series, X_i as:

$$X_{i+\Delta i} - X_i \propto |\Delta i|^{h(i)}, \tag{4}$$

where h is the Hölder exponent defining the degree of singularity at time point, i. Calculating the fractal dimension for each subsets of X_i of the same h, one obtains the singularity spectrum, $D(h)$ (Mandelbrot spectrum), which describes the distribution of singularities (Frisch and Parisi, 1985; Falconer, 1990; Turiel et al., 2006).

$$D(h) = \frac{\log(\rho(h)/\rho(h_{\max}))}{\log s_{\min}}, \tag{5}$$

where $h_{\max}$ is the Hölder exponent corresponding to maximal fractal dimension, $s_{\min}$ is the finest scale corresponding to Hölder trajectory, and $\rho(h)$ is the distribution of singularities.

The singular behavior of a multifractal is a local property. Separation of the singularities can be difficult, given the finite sampling frequency of the signal of interest (Mallat, 1999). Thus, in contrast with monofractality, a direct evaluation of multifractality is a demanding task in terms of the amount of data and the computational efforts needed, which can still not guarantee precise results under all circumstance.

With the aid of different moments of appropriate measure, μ, a set of equations can be established to obtain the singularity spectrum, which is a common framework exploited by multifractal analysis methods referred to as *multifractal formalism* (Frisch and Parisi, 1985; Mandelbrot, 1986; Barabási and Vicsek, 1991; Muzy et al., 1993). Using a set of different moment orders, one can determine the scaling behavior of μ^q, yielding the generalized Hurst exponent, $H(q)$ (Barunik and Kristoufek, 2010; See **Figure 1**):

$$\left\langle \mu^q(s)\right\rangle \propto s^{q\cdot H(q)}. \tag{6}$$

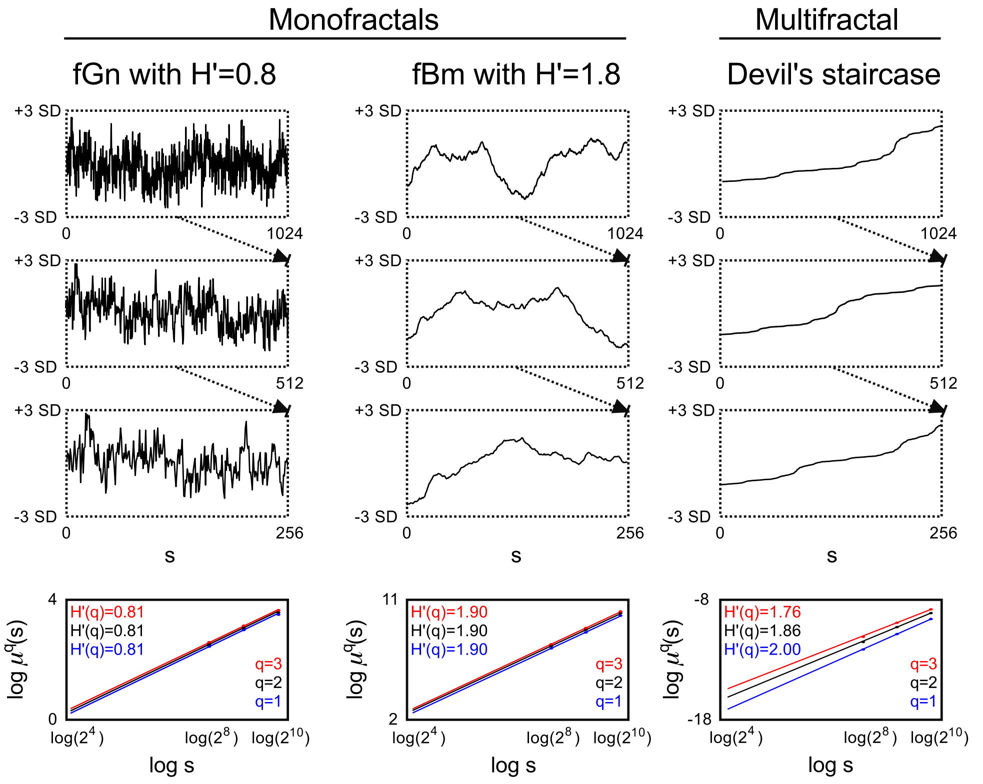

FIGURE 1 | Monofractal and multifractal temporal scaling. Three kinds of fractals are shown to demonstrate scale-free property of these structures: a stationary monofractal (fractional Gaussian noise), a non-stationary monofractal (fractional Brownian motion), and a multifractal (Devil's staircase with weight factors $p_1 = p_3 = 0.2$, $p_2 = 0.6$). Every fractal is self-similar: fGn and fBm in a statistical sense (as in empirical structures and processes where fractality is manifested in equal distributions, only) and Devil's staircase in an exact manner (as self-similar structuring in mathematical, i.e., ideal fractals is exact). For fractals, descriptive statistical measures [for example mean, variance, fluctuation (F_q) etc.] depend on the corresponding scale in a power law fashion. Thus as a scale-free descriptor, the extended Hurst exponent (*H'*) is calculated as a slope of regression line between the logarithms of the scale (*s*) and F_q (For an explanation of *H'*, see main text). The obtained slopes for different magnifications of the time series [here with the order of $q = (1, 2, 3)$, which is the order of moment of the used measure] are the same for monofractals and different for multifractals, demonstrating that power law scaling behavior is a global property of monofractals, while it is a local property of multifractals. Accordingly, note that slopes in the bottom left and middle panel are the same, while in the right panel they indeed differ. For further details, see main text.

On the right side of Eq. 4 Δi corresponds to scale, *s*, on the right side of Eq. 6. Using the partition function – introduced in context of Wavelet Transform Modulus Maxima (WTMM) method – singularities are analyzed globally for estimating the (multi)scaling exponent (Mallat, 1999):

$$Z(s, q) = \sum_{k=1}^{N(s)} \mu_i^q(s) \tag{7}$$

$$\tau(q) = \lim_{s \to 0} \inf \frac{\log Z(s, q)}{\log s}, \tag{8}$$

where $\tau(q)$ can be also expressed from $H(q)$ (Kantelhardt et al., 2002) as:

$$\tau(q) = q \cdot H(q) - D_T, \tag{9}$$

where D_T is the topological dimension, which equals 1 for time series.

The generalized fractal dimension can also describe the scale-free features of a multifractal time series:

$$D(q) = \frac{\tau(q)}{q-1} = \frac{q \cdot h(q) - 1}{q-1}. \tag{10}$$

The singularity spectrum, $D(h)$, can be derived from $\tau(q)$ with Legendre transform (**Figure 2**), via taking

$$h = \tau'(q), \tag{11}$$

the slope of the tangent line taken at q for $\tau(q)$, and yielding

$$D(h) = \inf_q (qh - \tau(q)), \tag{12}$$

that when evaluated gives the negative of the intercept at $q = 0$ for the tangent line (See **Figure 2**).

Natural signals have a singularity spectrum over a bounded set of Hölder exponents, whose width is defined by $[h_{-\infty}, h_{+\infty}]$ (**Figure 3**).

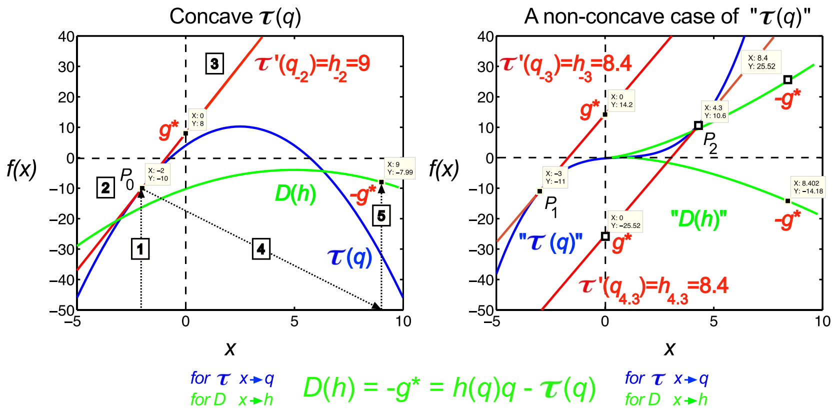

FIGURE 2 | Legendre transform. It is known that singularity spectrum, $D(h)$, has a concave shape, and provided that $\tau(q)$ is also a concave function, they can be explicitly transformed into each other via the Legendre transform (Bacry et al., 1993). Legendre transform takes a function, in our case $\tau(q)$ and produces a function of a different variable, $D(h)$. The Legendre transform is its own inverse and uses minimization as the basis of the transformation process according to Eq. 12. If minimization cannot be achieved, the transformation would fail. On the left a real (concave), on the right a non-concave case for $\tau(q)$ is shown. A simple concave function, $f(x) = -x^2 + 5x + 4$ (shown in blue) is used for modeling $\tau(q)$. If $f(x)$ is differentiable, hence a tangent line (shown in red) can be taken at point of P_0 (q_0, τ_0) with a slope $\tau'(q)$, then $g^*(q_0)$ is the y-intercept, $(0, g^*)$, and $-g^*$ is the value of the Legendre transform (See Eq. 11). Maximization at (q_0, τ_0) is valid since for any other point on the blue curve, a line drawn through that point with the same slope as the red line will yield a τ_0-intercept below the point $(0, g^*)$, showing that g^* is indeed obtained as a boundary value (maximum), thus the transformation for $D(h)$ would also yield a single boundary value (minimum) on the green curve as $D(h) = -g^* = \tau'(q)q - \tau(q)$. Steps of the transformation process are shown (1) select q, (2) read $\tau(q)$, (3) take a tangent line at (q, τ) and determine its slope, $h = \tau'(q)$, (4) select h, (5) determine $D(h)$ using the above equation; repeat for the set. On the right side, a non-concave function is shown (blue) for demonstrating a case, when due to the non-concave shape of $\tau(q)$ the shape of the transformed function, $D(h)$, does not yield a realistic singularity spectrum given that in this case the transform by failing on minimization is poorly behaved yielding ambiguous values.

A combination parameter, P_c, can be calculated (definitions on **Figure 3**) to facilitate the separation of time series characteristics (Shimizu et al., 2004), which can aid the exploration of the physiological underpinnings, too.

$$P_c = \frac{h_{\max}}{D_{\max}} \cdot FWHM. \tag{13}$$

A similar parameter is W (Wink et al., 2008) calculated as

$$W = \frac{W+}{W-}. \tag{14}$$

IMPLEMENTATION OF FRACTAL TIME SERIES ANALYSES

Implementation of concepts in reliable algorithms is a critical task, as stationary and non-stationary signals require different methods when analyzed for their fractality. For a stationary signal the probability distribution of signal segments is independent of the (temporal) position of the segment and segment length, which translates into constant descriptive statistical measures such as mean, variance, correlation structure etc. over time (Eke et al., 2000, 2002).

Accordingly, signals can be seen as realizations of one of two temporal processes: fBm, and fGn (Eke et al., 2000). The fBm signal is non-stationary with stationary increments. An fBm signal, X_i, is self-similar in that its sampled segment $X_{i,n}$ of length n is equal in distribution with a longer segment $X_{i,sn}$ of length sn when the latter is rescaled (multiplied) by s^{-H}. This means that every statistical measure, m_n, of an fBm time series of length n is proportional to n^H

$$X_{i,n} \propto s^{-H} X_{i,sn}, \tag{15}$$

$$m_n \propto pn^H, \text{ which yields } \log\ m_n \propto \log p + H \log n, \tag{16}$$

where H is the Hurst exponent. H ranges between 0 and 1. Increments $Y_i = X_i - X_{i-1}$ of a non-stationary fBm signal yield a stationary fGn signal and vice versa, cumulative summation of an fGn signal results in an fBm signal. Note that most methods listed below that have been developed to analyze statistical fractal processes share the philosophy of Eq. 15 in that in their own ways all attempt to capture the power law scaling in the various statistical measures of the evaluated time series (Eke et al., 2002).

MONOFRACTAL METHODS

Here we focus on widely used monofractal methods selected from those in the literature.

Time domain methods

Detrended fluctuation analysis. The method of Peng et al. (1994) begins with the signal summed and the mean subtracted

$$Y_j = \sum_{i=1}^{j} X_i - \langle X \rangle . \tag{17}$$

Then the local trend $Y_{j,n}$ is estimated in non-overlapping windows of equal length n, using least-square fit on the data. For a

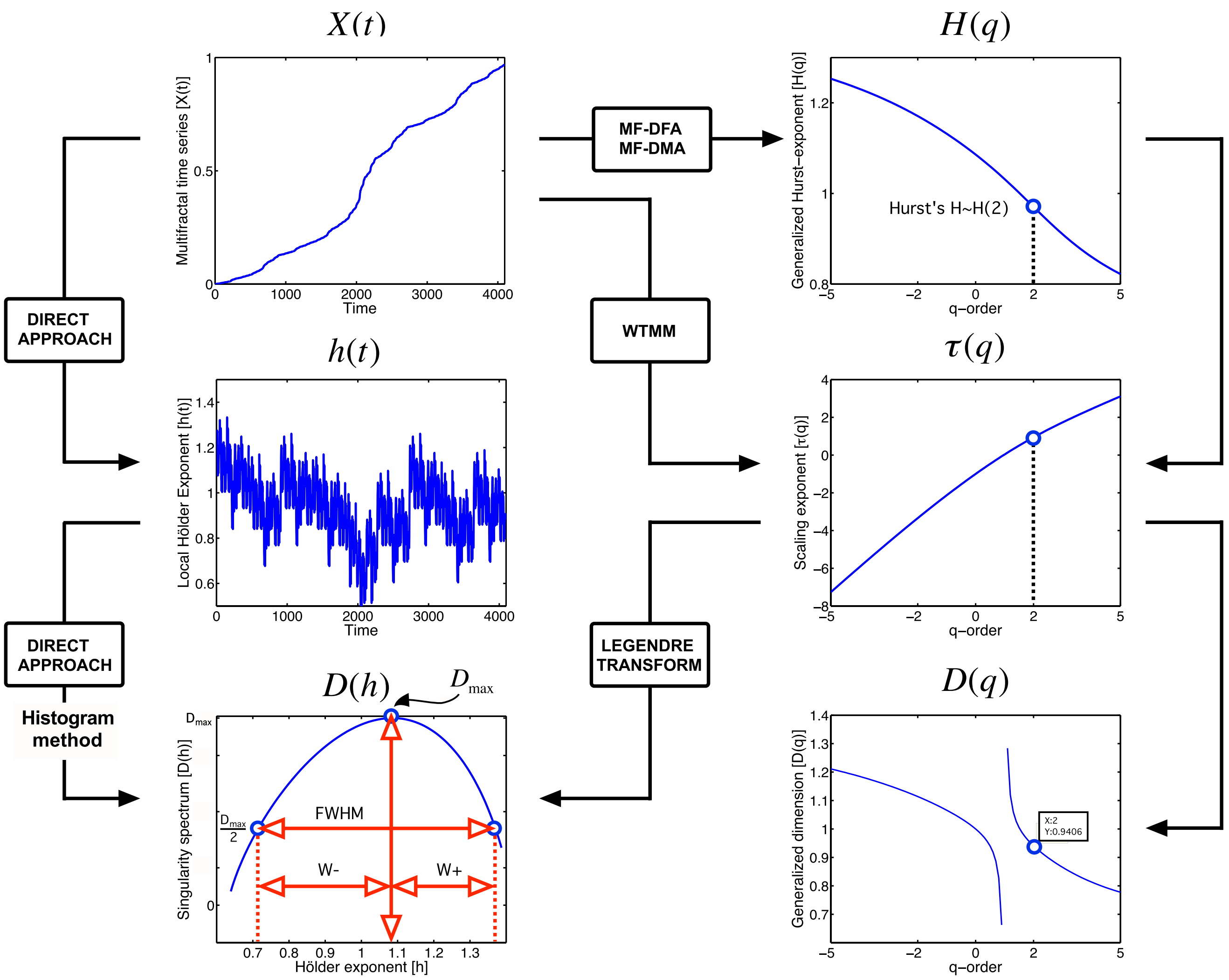

FIGURE 3 | Approaches to multifractal analyses. Direct approach of multifractal analysis means exploiting the local power law scaling behavior to obtain local Hölder exponents (Eq. 4), from which the Mandelbrot spectrum is calculated with histogram method (Falconer, 1990; Eq. 5). Indirect approaches shown here (MF-DFA, multifractal detrended fluctuation analysis; MF-DMA, multifractal detrended moving average; WTMM, Wavelet Transform Modulus Maxima) estimates the scaling exponent, τ as a function of *q*. It is worth to note, that this is carried out differently for MF-DFA, MF-DMA (Eq. 9), and for WTMM (Eq. 8). From τ(*q*), the Mandelbrot spectrum can be obtained with the application of the Legendre transform, while its relation to generalized fractal dimension *D*(*q*) is given by Eq. 10. Singularity spectrum, *D*(*h*), is an important endpoint of the analysis. The spectrum is concave and has a nearly parabolic shape with a maximum identified by the capacity dimension at $q = 0$ (Mallat, 1999; Shimizu et al., 2004; Ihlen, 2012). Please note that some of its measures (*FWHM*, D_{max}, *W*+, *W*–) can be used to calculate meaningful combined parameters (such as *Pc*, and *W* in Eqs 13 and 14, respectively) with potential in correlating with key features of fMRI BOLD time series.

given window size n the fluctuation is determined as the variance upon the local trend:

$$F_n = \sqrt{\frac{1}{N}\sum_{j=1}^{N}(Y_j - Y_{j,n})^2}, \tag{18}$$

For fBm processes of length N with non-overlapping windows of size n the fluctuation depends on the window size n in a power law fashion:

$$F_n \propto pn^{\alpha}, \text{ and} \tag{19}$$

$$\alpha = \lim_{n \to 0} \frac{\log F_n}{\log n}. \tag{20}$$

If X_i is an fGn signal then Y_j will be an fBm signal. F_n then is equivalent to m_n of Eq. 16 yielding $F_n \propto pn^H$ therefore in this case $\alpha = H$. If X_i is an fBm signal then Y_j will be a summed fBm signal. Then $F_n \propto pn^{H+1}$, where $\alpha = H + 1$ (Peng et al., 1994).

Signal summation conversion method. This method was first introduced by Eke et al. (2000) for enhancing signal classification as a variant of the scaled windowed variance (SWV) analysis of Mandelbrot (1985) as further developed by Peng et al. (1994).

Fluctuations of a parameter over time can be characterized by calculating the standard deviation

$$SD_n = \sqrt{\frac{1}{N-1}\sum_{i=1}^{N}(X_i - \langle X \rangle)^2}. \tag{21}$$

For fBm processes of length N when divided into non-overlapping windows of size n as Eq. 21 predicts the standard deviation within the window, s_n, depends on the window size n in a power law fashion:

$$SD_n \propto pn^H, \tag{22}$$

and

$$H = \lim_{n \to 0} \frac{\log SD_n}{\log n}. \tag{23}$$

In practice SD$_n$'s calculated for each segment of length n of the time series are averaged for the signal at each window size. The standard method applies no trend correction. Trend in the signal seen within a given window can be corrected either by subtracting a linearly estimated trend (line detrended version) or the values of a line bridging the first and last values of the signal (bridge detrended version; Cannon et al., 1997). This method can only be applied to fBm signals or cumulatively summed fGn signals.

The signal summation conversion (SSC) method was first used for enhanced signal classification according to the dichotomous fGn/fBm model (Eke et al., 2000). There are two steps: (1) calculate from X_i its cumulative sum (this converts an fGn to an fBm or converts an fBm to its cumulant), and (2) use the bdSWV method to calculate from the cumulant series $\hat{H}'$. The interpretation of $\hat{H}'$ is that when $0 < \hat{H}' \leq 1$, then X_i is an fGn with $\hat{H}'$. Alternatively, when $\hat{H}' > 1$, then the cumulant series is identified as an fBm signal of $\hat{H} = \hat{H}' - 1$. As seen, in order to keep $\hat{H}'$ scaled within the [0,1] range, in the original version of the method in the fBm case 1 was subtracted from the estimate of H. Given that the SSC method handles fGn and fBm signals alike, we eliminate this step and report values as $0 < \hat{H}' < 1$ for fGn and $1 < \hat{H}' < 2$ for fBm signals referring $\hat{H}'$ as the "extended" Hurst exponent. This way, the mere value of the Hurst exponent would reflect on signal class, the focus of fractal time series analysis strategy. Also the use of $\hat{H}'$ would greatly facilitate reviewing the results of numerical performance analyses.

Real-time implementations of SSC and Detrended Fluctuation Analysis (DFA) methods have been recently reported (Hartmann et al., 2012).

Frequency domain method

Fractal analysis can also be done in the frequency domain using methods such as the power spectral density (PSD) analysis (Fougere, 1985; Weitkunat, 1991; Eke et al., 2000).

Power spectral density analysis (${}^{low}PSD_{w,e}$). A time series can be represented as a sum of cosine wave components of different frequencies:

$$X_i = \sum_{n=0}^{N/2} A_n \cos\left[\omega_n t_i + \varphi_n\right] = \sum_{n=0}^{N/2} A_n \cos\left[\frac{2\pi n}{N} i + \varphi_n\right], \tag{24}$$

where A_n is the amplitude and ϕ_n is the phase of the cosine-component with ω_n angular frequency. The commonly used sample frequency is $f_n = \omega_n/2\pi$. The $A_n(f_n)$, $\phi_n(f_n)$, and $A_n^2(f_n)$ functions are termed amplitude, phase, and power spectrum of the signal, respectively. These spectra can be determined by an effective computational technique, the fast Fourier transform (FFT). The power spectrum (periodogram, PSD) of a fractal process is a power law relationship

$$A_n^2 \propto p\omega_n^{-\beta},\ \text{or} \left|A(f)\right|^2 \propto 1/f^{\beta} \text{ which yields } \beta = \lim_{n \to 0} \frac{\log A_n^2}{\log f_n}, \tag{25}$$

where β is termed spectral index. The power law relationship expresses the idea that as one doubles the frequency the power changes by the same fraction ($2^{-\beta}$) regardless of the chosen frequency, i.e., the ratio is independent of where one is on the frequency scale.

The signal has to be preprocessed before applying the FFT (subtraction of mean, windowing, and endmatching, i.e., bridge detrending). Discarding the high power frequency estimates improves the precision of the estimates of β (Fougere, 1985; Eke et al., 2000). Eke et al. (2000) introduced this version denoted as ${}^{low}\text{PSD}_{w,e}$ as a fractal analytical tool.

Time-frequency domain method

Fractal wavelet analysis uses a waveform of limited duration with an average value of zero for variable-sized windowing allowing an equally precise characterization of low and high frequency dynamics in the signal. The wavelet analysis breaks up a signal into shifted and stretched versions of the original wavelet. In other words, instead of a time-frequency domain it rather uses a time-scale domain, which is extremely useful not only in monofractal but multifractal analysis, too. One such way to estimate H is by the averaged wavelet coefficient (AWC) method (Simonsen and Hansen, 1998). The most commonly used analyzing wavelet is the second derivative of a standard normalized Gaussian function, which is:

$$\psi(t) = \frac{d^2}{dt^2} e^{-\frac{t^2}{2}}. \tag{26}$$

The scaled and translated version of the analyzing wavelet is given by

$$\psi_{a;b}(t) = \psi\left(\frac{t-b}{a}\right), \tag{27}$$

where the scale parameter is a, and the translation parameter b.

The wavelet transformation is essentially a convolution operation in the time domain:

$$W_{\psi}[X](a,b) = \frac{1}{a}\int_{-\infty}^{+\infty} X(t)\cdot\psi_{a;b}dt. \tag{28}$$

From Eq. 16, one can easily derive how the self-affinity of an fBm signal $X(t)$ determines its continuous wavelet transform (CWT) coefficients:

$$W[X](sa,sb) =_{d} s^{\frac{1}{2}+H}\, W[X](a,b). \tag{29}$$

The AWC method is based on Eq. 29 (Simonsen and Hansen, 1998) and can be applied to fBm signals or to cumulatively summed fGn signals.

MULTIFRACTAL METHODS

Three analysis methods are described here; all use different statistical moments (termed q-th order) of the selected measure to evaluate the signal's multifractality. Despite of certain inherent drawbacks, these methods are widely used in the literature, and can obtain reliable results if their use is proper with limitations considered.

Time domain methods

Below, the Multifractal DFA (MF-DFA; Kantelhardt et al., 2002) and the recently published Multifractal Detrended Moving Average (MF-DMA; Gu and Zhou, 2010) will be reviewed. We will focus on MF-DMA, but since it is similar to MF-DFA, their differences will be pointed out, too. They rely on a measure of fluctuation, F, as in their monofractal variant (Peng et al., 1994), and differ in calculating the q-th order moments of the fluctuation function.

Step 1 – calculating signal profile, Y_j, by cumulative summation. It is essentially the same as in Eq. 17, however note that in DFA methods, the mean of the whole signal is subtracted before summation, while in DMA methods this is carried out locally in step 3.

Step 2 – calculating the moving average function, $\tilde{Y}_j$.

$$\tilde{Y}_j = \frac{1}{n}\cdot\sum_{k=-[(n-1)\theta]}^{[(n-1)(1-\theta)]} y_{t-k} \tag{30}$$

For further details, see **Figure 4**.

Step 3 – detrending by moving average: By subtracting $\tilde{Y}_t$ a residual signal, ε_t, is obtained:

$$\varepsilon_t = Y_t - \tilde{Y}_t, \tag{31}$$

where $n-[(n-1)\cdot\theta] \leq t \leq N-[(n-1)\cdot\theta]$.

This fundamental step of the DMA methods is essentially different from the detrending step of DFA methods (See **Figure 4**).

Step 4 – calculation of fluctuation measure. The signal is split into $N_n = [N/n - 1]$ number of windows (See **Figure 4**), $\varepsilon(\nu)$, where ν refers to the index of a given window. The fluctuating process is characterized by $F_\nu(n)$, which is given as a function of window size, n:

$$F_{\nu}^{2}(n) = \frac{1}{n}\cdot\sum_{t=1}^{n}\varepsilon_{t}^{2}(\nu). \tag{32}$$

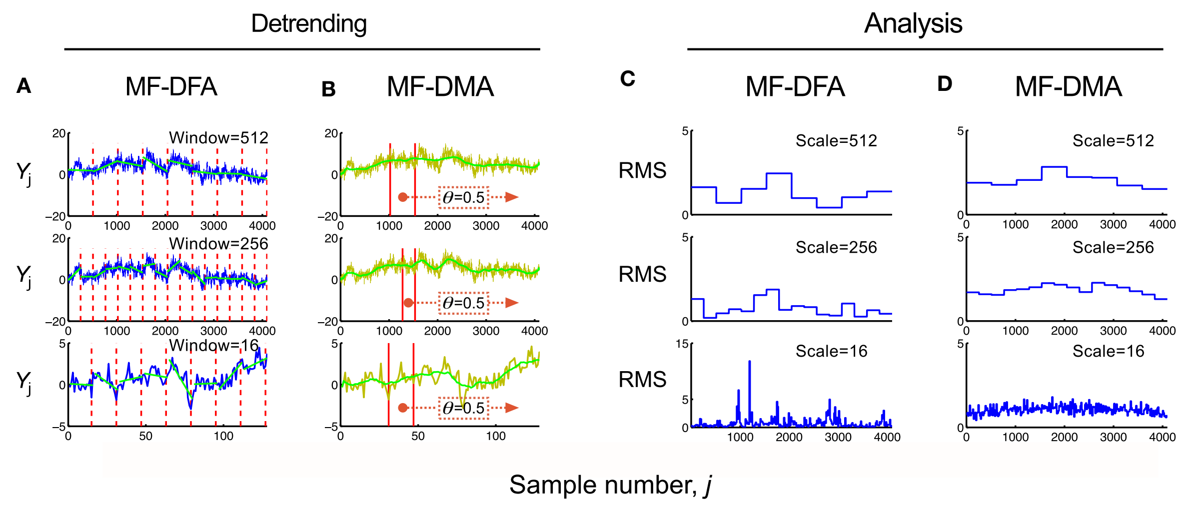

FIGURE 4 | Detrending scheme and fluctuation analysis for MF-DFA and MF-DMA methods. The detrending strategy for MF-DFA **(A)** is that the signal is divided into a set of non-overlapping windows of different sizes, and a local low-order polynomial (typically linear) fit (shown in green) is removed from each window's data. In contrast, MF-DMA **(B)** removes the moving average point-by-point calculated in different window sizes around the processed point with a position given by θ. This parameter describes the delay between the moving average function and the original signal. Its value is taken from [0, 1] interval, 0 meaning only from signal values on the left ("*backward*," past), in contrast with 1 meaning that only signal values to the right ("*forward*," future) are used for calculating $\tilde{Y}_j$. The centrally positioned sliding window corresponds to the case of $\theta = 0.5$ balancing contributions from the past and the future to the reference point. The approaches of MF-DFA and MF-DMA thus ought to yield different detrended signals, whose calculated moments **(C,D)** and Eqs 33 and 34 obtained by the analysis should also be somewhat different.

Step 5 – calculation of q-th order moments of the fluctuation function.

$$F_q(n) = \left(\frac{1}{N_n} \cdot \sum_{\nu=1}^{N_n} F_\nu^q(n) \right)^{1/q}. \tag{33}$$

For $q = 2$, the algorithm reduces to the monofractal DMA method. For the special case $q = 0$, $F_q(n)$ can be obtained as a limit value that can be expressed in a closed form:

$$\log[F_0(n)] = \frac{1}{N_n} \cdot \sum_{\nu=1}^{N_n} \log[F_\nu(n)]. \tag{34}$$

Relation of the q-th order moment of the fluctuation measure and $H(q)$ follows a power law:

$$F_q(n) \propto n^{H(q)}. \tag{35}$$

Thus $H(q)$ can be estimated as the slope of the least-square fitted regression line between log n and log $[F_q(n)]$. Finally, Mandelbrot spectrum is obtained with subsequent application of multifractal formalism equations (Eqs 9–12) yielding multifractal features $\tau(q)$, $D(h)$.

Time-frequency domain methods

Wavelet analysis methods can be used to estimate the singularity spectrum of a multifractal signal by exploiting the multifractal formalism (Muzy et al., 1991, 1993, 1994; Mallat and Hwang, 1992; Bacry et al., 1993; Arneodo et al., 1995, 1998; Mallat, 1999; **Figure 5**). Wavelet transform modulus maxima (WTMM) has strong theoretical basis and has been widely used in natural sciences to assess multifractality.

Step 1 – continuous wavelet transformation: This step is essentially the same as described previously in Eqs 26–28 yielding a matrix of wavelet coefficients (**Figure 5B**):

$$W \equiv [w(i_t, i_s)], \tag{36}$$

where $w(i_t, i_s) = |W_\psi[X](t, s)|$, i_s is the scaling index, where $s = s_{\min}, \ldots, s_{\max}$ and $i_t = 1, 2, \ldots, N$, where t is the sampling time of each successive data point.
Step 2 – chaining local maxima: The term modulus maxima describes any point (t_0, s_0) where $|W_\psi = [X](t, s)|$ is a local maximum at $t = t_0$:

$$\frac{\partial W_\psi\, [X]\, (t_0, s_0)}{\partial t} = 0. \tag{37}$$

This local maximum is strict in terms of its relation to t_0 in its immediate vicinity. These local maxima are to be chained by interconnection to form a local maxima line in the space-scale plane (t, s) (See **Figure 5C**).
Step 3 – calculating partition function. With the aid of partition function (Eq. 7, **Figure 5D**), singular behavior of the multifractal time series can be isolated. Wavelet coefficients along maxima chains are considered as μ measures.

$$Z(s, q) = \sum_{\ell \in L(s)} |w(i_s, i_t)|^q. \tag{38}$$

Summation is executed along maxima chains (ℓ), the set of all maxima lines is marked by $L(s)$.
Step 4 – calculating singularity spectra and parameters of multifractality. The following step is to determine the multiscaling exponent, $\tau(q)$ by $H(q)$, and then using Eqs 10–12 to give full quantification of the multifractal nature.

CHARACTERIZATION OF METHODS

Before the application of fractal analysis methods, their behavior should be thoroughly evaluated on a large set of signals with known scale-free structure and broad representation (Bassingthwaighte and Raymond, 1994, 1995; Caccia et al., 1997; Cannon et al., 1997; Eke et al., 2000, 2002; Turiel et al., 2006). Signal classification, estimating performance in terms of precision and limitations of the methods should be clarified during characterization. The capability of multifractal analysis to distinguish between mono- and multifractal processes should also be evaluated.

Stationarity of a signal is an important property for pairing with a compatible fractal analysis tool (see Table 2 in Eke et al., 2002). In addition, all methods have some degree of inherent bias and variance in their estimates of the scaling exponent bearing great importance due to their influence on the results, which can be misinterpreted as a consequence of this effect. The goal of performance analysis is therefore to characterize the reliability of selected fractal tools in estimating fractal parameters on synthesized time series. This should be carried out at least for a range of signal sizes and structures similar to the empirical dataset, so that the reliability of fractal estimates could be accurately determined.

Extensive results obtained with our monofractal framework have been reported elsewhere (Eke et al., 2000, 2002), but for the sake of comparison it will be briefly described. Our multifractal testing framework is aimed to demonstrate relevant features of MF-DFA and MF-DMA method, utilizing the equations described in Section "Implementation of Fractal Time Series Analyses."

TESTING FRAMEWORK FOR MULTIFRACTAL TOOLS ON MONOFRACTALS

Monofractal signals of known autocorrelation (AC) structure can be synthesized based on their power law scaling. The method of Davies and Harte (1987) (DHM for short) produces an exact fGn signal using its special correlation structure, which is a consequence of the power law scaling of the related fBm signal in the *time domain* (Eq. 19). It is important, that different realizations can be generated with DHM at a given signal length and Hurst exponent, which consists of a statistical distribution of similarly structured and sized monofractals.

The next question is how to define meaningful end-points for the tests? For ideal monofractals with a given length and true H, Mean Square Error (MSE) is a good descriptor: it can be calculated for each set of series of known H and particular signal length, N (Eke et al., 2002). It carries a combined information about bias and variance, as MSE = bias^2 + variance.

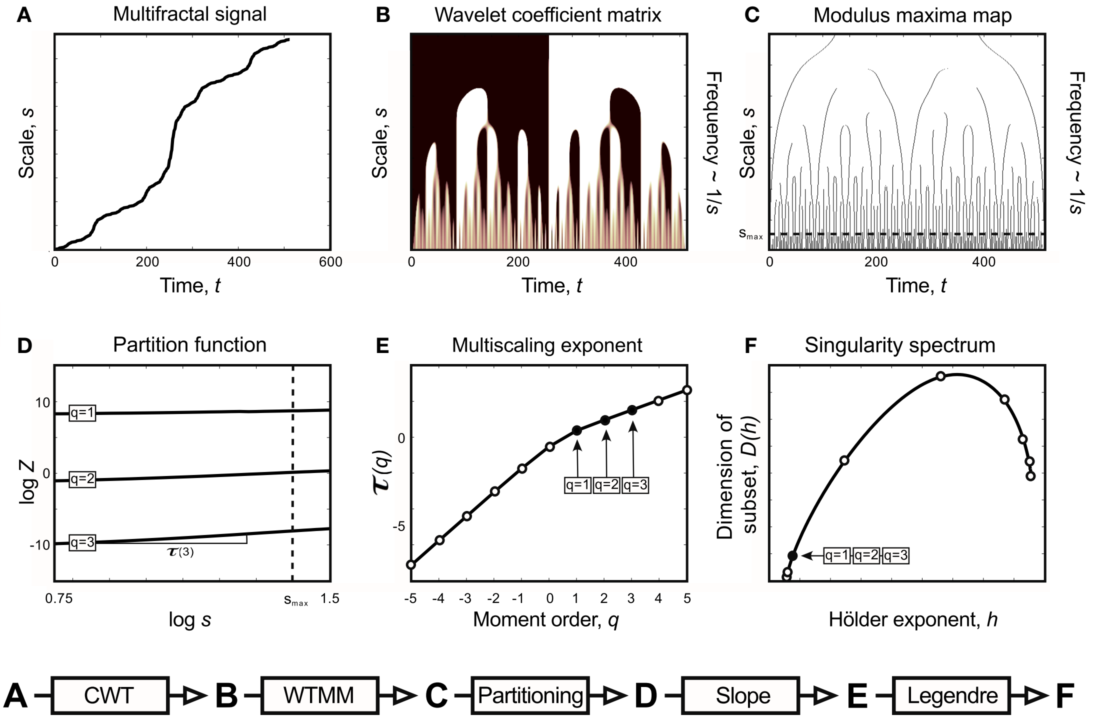

FIGURE 5 | Relations of Continuous Wavelet Transform operation, Wavelet Transform Modulus Maxima method, and multifractal formalism to obtain singularity spectrum of an ideal multifractal. Devil's staircase with weight factors $p_1 = p_3 = 0.2$, $p_2 = 0.6$ was used to model an ideal multifractal time series **(A)**. The wavelet coefficient matrix **(B)** is obtained by continuous wavelet transform in the time-scale space. Modulus maxima map **(C)** containing the maxima lines across the scales defined by CWT. We call modulus maximum of the wavelet transform $|W_\psi[X](t, s_0)|$; any point (t_0, s_0), which corresponds to a local maximum of the modulus of $|W_\psi[X](t, s_0)|$ is considered as a function of t. For a given scale, it means that $|W_\psi[X](t_0, s_0)| > |W_\psi[X](t, s_0)|$ for all t in the neighborhood right of t_0, and $|W_\psi[X](t_0, s_0)| \geq |W_\psi[X](t, s_0)|$ for all t in the neighborhood left of t_0. Local maxima are chained, and in the subsequent calculations only maxima chains propagating to the finest scales are used (Mallat, 1999). Chaining local maxima is important, because it is proven that their distribution along multiple scales identifies and measures local singularities, which is tightly linked to the singularity spectrum. The moment-based partition function **(D)** separates singularities of various strength as coded in **(B,C)** as follows. Z is obtained for the range $[s_{min}, s]$ as the sum of moments of the wavelet coefficients belonging to those along a set of maxima lines at s [shown as circles in **(C)**]. This definition corresponds to a "scale-adapted" partition with wavelets at different sizes. A moment-based set of Z are plotted in a log-log representation as shown in **(D)**. Notice that these log Z(log s) functions are lines representing the power law behavior of the multifractal signal within the scaling range shown. Therefore when the slope of each and every log Z(log s) lines are plotted as a function of moment order, q, it yields $\tau(q)$ **(E)**. From $\tau(q)$ via Legendre transform the singularity spectrum, $D(h)$ **(F)**, is obtained (See Chapter 2, Figure 3).

Interpreting the multifaceted results of numerical experiments is a complex task. It can be facilitated if they are plotted in a properly selected set of independent variable with impact shown in intensity-coded representations (**Figure 6**; Eke et al., 2002). Precision index is determined as the ratio of results falling in the interval of $[H_{\text{true}} - H_{\text{dev}}, H_{\text{true}} + H_{\text{dev}}]$, where H_{dev} is an arbitrarily chosen value referring to the tolerable degree of deviation.

In the monofractal testing framework, we used DHM-signals to evaluate the performance of MF-DMA (Gu and Zhou, 2010) and MF-DFA (Gu and Zhou, 2006), by the code obtained from http://rce.ecust.edu.cn/index.php/en/research/129-multifractalanalysis. It was implemented in Matlab, in accordance with Eqs 17 and 30–35. As seen in **Figure 6**, precision of MF-DFA and MF-DMA depends on N, H, and the order of moment.

In order to compare the methods in distinguishing multifractality, end-points should be defined reflecting the narrow or wide distribution of Hölder exponents. We select a valid endpoint Δh proposed by Grech and Pamula (2012), which is the difference of Hölder exponents corresponding to $q = -15$ and $q = +15$ (**Figure 7**).

TESTING APPROACHES FOR MULTIFRACTAL TOOLS ON MULTIFRACTALS

Extending the dichotomous model of fGn/fBm signals (introduced in context of monofractals; Mandelbrot and Ness, 1968; Eke et al., 2000) toward multifractal time series is reasonable as it can account for essential features of natural processes exhibiting local power law scaling. Description of an algorithm creating multifractional Brownian motion (mBm) and multifractional Gaussian noise (mGn) can be found here (Hosking, 1984), while implementation of such code can be found on the net (URL1: http://fraclab.saclay.inria.fr/, URL2: www.ntnu.edu/inm/geri/software). Given that these algorithms require Hölder trajectories as inputs, multifractality cannot be defined exactly on a finite set, which is a common problem of such

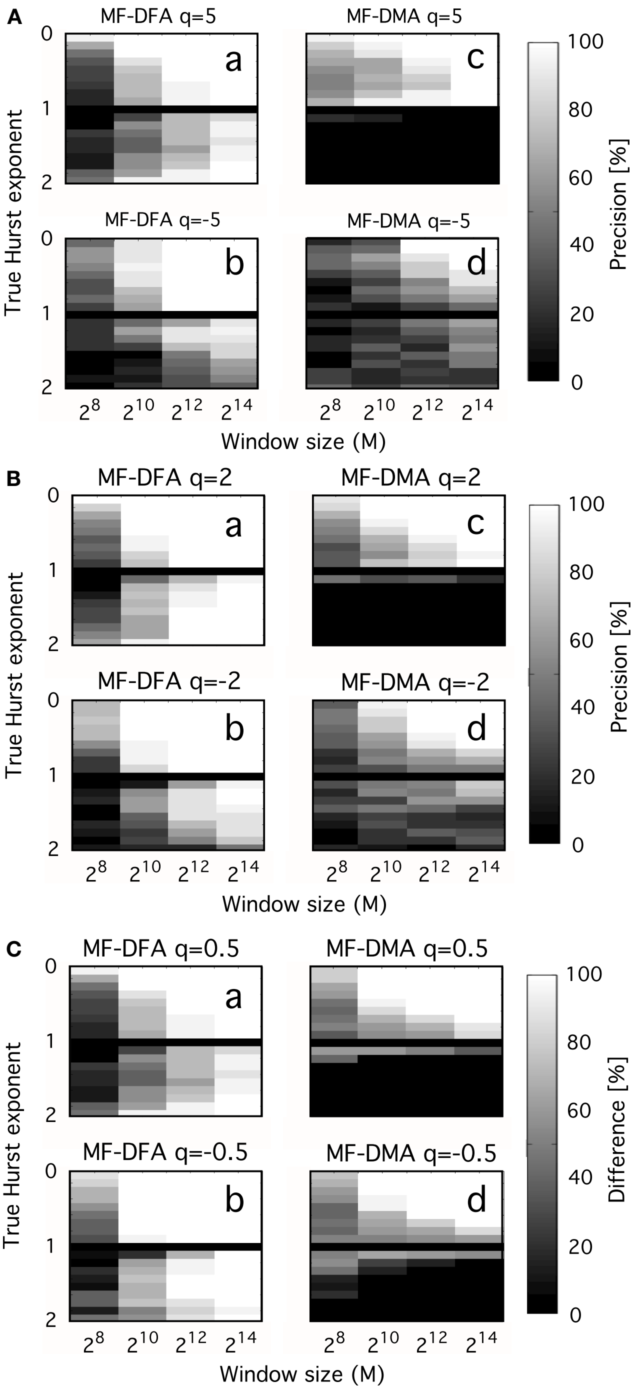

FIGURE 6 | Precision as a function of moment order, signal length, and Hurst exponent. Precision of MF-DFA [left side of **(A–C)**] and MF-DMA [right side of **(A–C)**] as a function of q, H_{true}, N. fGn and fBm signals were generated by DHM with length of 2^8, 2^{10}, 2^{12}, 2^{14}, and H_{true} increased from 0.1 to 1.9 in steps of 0.1, skipping $H_{\text{true}} = 1$ (corresponding to 1/*f* boundary seen as the black horizontal line in the middle). Estimation of the generalized Hurst exponent should not depend on q, as monofractal's $H(q)$ is a theoretically constant function scattering around H_{true} across different order of moments. The intensity-coded precision index is proportional to the number of estimates of H falling into the range of $H_{\text{true}} \pm 0.1$, with lighter

(*Continued*)

FIGURE 6 | Continued

areas indicating more precise estimation. Calculation of this measure is based on 20 realizations for each q, H_{true}, N. **(A)** Performance of methods for $q = \pm 5$. **(B)** Performance of methods for $q = \pm 2$. **(C)** Performance of methods for $q = \pm 0.5$. Besides the clear dependence of precision on H_{true} and N, influence of moment order is also evident, given that the lightest areas corresponding to the most reliable estimates tend to increase in parallel with moment order approaching 0 [Note the trend from **(A–C)**]. The lower half of the plots indicates that MF-DFA is applicable for signals of both types, while MF-DMA is reliable only on fGn signals. This result is further supported by the paper of Gao et al. (2006), who demonstrated a saturation of DMA at 1 for H when the true extended Hurst exponent exceeds 1 (thus it is non-stationary).

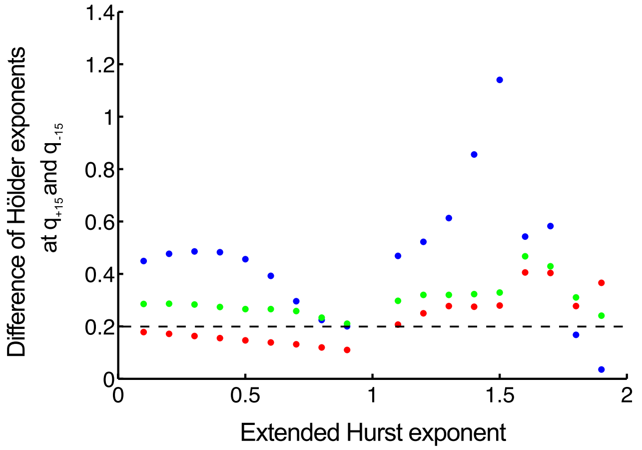

FIGURE 7 | Separating monofractals from multifractals. Δh values obtained by MF-DFA (as difference of Hölder exponents at $q = +15$ and $q = -15$) are shown for monofractals with length of 2^{10} (blue), 2^{12} (green), 2^{14} (red). It is clearly shown that longer signals are characterized by lower Δh, and its value below 0.2 means that true multifractality is unlikely present (Grech and Pamula, 2012). Signals were created by DHM at extended Hurst exponents of 0–1.9 with a step of 0.1.

synthesis methods. Selecting a set of meaningful trajectories is a challenging task: it should resemble those of empirical processes and meet the analytical criteria of the selected algorithms (such criteria are mentioned in Concept of Fractal Time Series Analyses).

On the contrary, iterative cascades defined with analytic functions are not influenced by the perplexity of definitions associated with multifractality outlined in the previous paragraph, given that their value at every real point of the theoretical singularity spectrum is known. Due to their simplicity, binomial cascades (Kantelhardt et al., 2002; Makowiec et al., 2012) and Devil's staircases (Mandelbrot, 1983; Faghfouri and Kinsner, 2005) are common examples of theoretical multifractals used for testing purposes. A major drawback of this approach is that these mathematical objects do not account for features in empirical datasets, but can still be useful in comparing reported results.

The most extensive test of multifractal algorithms which used a testing framework of signals synthesized according to the model introduced by Benzi et al. (1993) was reported by Turiel et al. (2006). Briefly, it is a wavelet-based method for constructing a signal with predefined properties of multifractal structuring with explicit relation to its singularity spectrum. Since the latter can be manipulated, the features of the resulting multifractal signal could be better controlled. The philosophy of this approach is very similar to that of Davies and Harte (1987) in that a family of multifractal signals of identical singularity spectra can be generated by incorporating predefined distributions (log-Poisson or log-Normal) giving rise to controlled variability of realizations. Additionally, using log-Poisson distribution would yield multifractals with a bounded set of Hölder exponents in that being similar to those of empirical multifractals. To conclude, this testing framework should merit further investigation.

ANALYTICAL STRATEGY

In this article we expand our previously published monofractal analytical strategy to incorporate some fundamental issues associated with multifractal analyses keeping how these can be applied to BOLD time series in focus. Progress along the steps of the perplexed fractal analysis should be guided by a consolidated – preferably model-based– view on the issues involved (See **Figure 8**).

A fundamental question should be answered whether it is worthy at all to take on the demanding task of fractal analysis? This can only be answered if one characterizes the signal in details according to the guideline shown in **Figure 8** using tools of descriptive statistics and careful testing; first for the presence of monofractal and later that of multifractal scale-free features. At this end, we present here a new tool for an instantaneous and easy-to-do performance analysis (called "performance vignette"), which can facilitate this process and does not require special knowledge needed to carry out detailed numerical experiments on synthesized signals (**Figure 9**). The latter, however, cannot be omitted when full documentation of any particular fractal tool's performance is needed. In that the vignette has been designed for prompt selection, overview, and comparison of various methods; not for their detailed analysis.

We sustain our recommendation that proper class-dependent or class-independent methods should be chosen.

We feel, that calculating global measures of multifractal scaling, such as P_c (Shimizu et al., 2004) or W (Wink et al., 2008), can help consolidating experimental findings in large fMRI BOLD volumes across many subjects and experimental paradigms. Based on our tests, we conclude that straightforward recommendations for multifractal analysis for the purpose of fMRI BOLD time series analysis needs further investigations.

PITFALLS

SOURCES OF ERROR

Problems emerging from inadequate signal definition (measurement sensitivity, length, sampling frequency)

Measurement sensitivity. The precondition of a reliable fMRI time series analysis is that the BOLD signal has adequate definition in terms of being a true-to-life representation of the underlying biology it samples. In particular, the fMRI BOLD measurement is aimed at detecting the contrast around blood filled compartments in magnetic susceptibility of blood and the surrounding medium in a uniform high field (Ogawa and Lee, 1990). A contrast develops from tissue water relaxation rate being affected by the paramagnetic vs. diamagnetic state of hemoglobin. The contrast increases with decreasing oxygenation of blood, a feature that renders the technique capable of detecting the combined effect of neuronal metabolism coupled via hemodynamics throughout the brain (Smith et al., 2002). As Ogawa and Lee (1990) demonstrated, the BOLD contrast increases with the strength of the main magnetic field, B_0 (i.e., due to the sensitivity of the relaxation rate).

In his early paper (Lauterbur, 1973), Lauterbur gave clear evidence of the fact that resolution of magnetic resonance signals will strongly depend on B_0. Newer generations of scanners with continuously improved performance were constructed utilizing this relation by incorporating magnets of increased strength (in case of human scanners from, i.e., 1.5–7T, in small animal scanners due to the smaller brain size with strength in the 4–17.2T range). Bullmore et al. (2001) showed indeed, that the performance of some statistical method and their results depended on the magnetic field used (1.5 vs. 3T); calling for caution and continuous reevaluation the methods in the given MRI settings.

In order to confirm the impact of B_0 on the sensitivity on the definition of the BOLD signal fluctuations, we have compared the spectral index (ß) of resting-state BOLD fluctuations *in vivo* to those *post mortem* and in a phantom in 4, 9.4, and 11.7T in anesthetized rats (**Figure 10**). What we have learned from this study was that in contrast with amplitude-wise optical measurements of cerebral oxygenation and hemodynamics such as near infrared spectroscopy (Eke et al., 2006), due to the contrast-detecting foundations of fMRI, signal definition cannot be characterized by comparing fluctuation ranges *in vivo* vs. *post mortem*. After death deoxyhemoglobin molecules are still present in the MRI voxels post-sacrifice and thus generate susceptibility-induced magnetic field gradients that would impact diffusion of tissue water molecules (Herman et al., 2011), a process that can generate fluctuating BOLD contrast without ongoing physiology. What matters is that *in vivo* the blood gets oxygenated and via the combined impact of neuronal metabolism, blood flow, and blood volume, the internal structuring of the BOLD contrast signal will change from close to random to a more correlated level as indicated by β, which is *in vivo* significantly higher than *post mortem*. Increasing field strength enhances this effect and yields a more articulated topology of β throughout the brain. Conversely, low field measurements favor the dominance of instrument noise in addition to being less sensitive in detecting the BOLD contrast. The inference of these preliminary data is that, given the BOLD contrast (and presumably even the spatial resolution) of our animal imaging, a 1.5T human scanner may not be of sufficient sensitivity to detect BOLD fluctuations at adequate definition for a reliable monofractal analysis, not to mention multifractal analysis known to require a much higher signal definition for an optimal performance that can be achieved in higher field scanners (Ciuciu et al., 2012).

While the use of fMRI is typically qualitative where the baseline is conveniently differenced away to reveal focal area(s) of interest (Shulman et al., 2007), this practice would not interfere with fractal time series analysis, given that scaling exponent is invariant to mean subtraction.

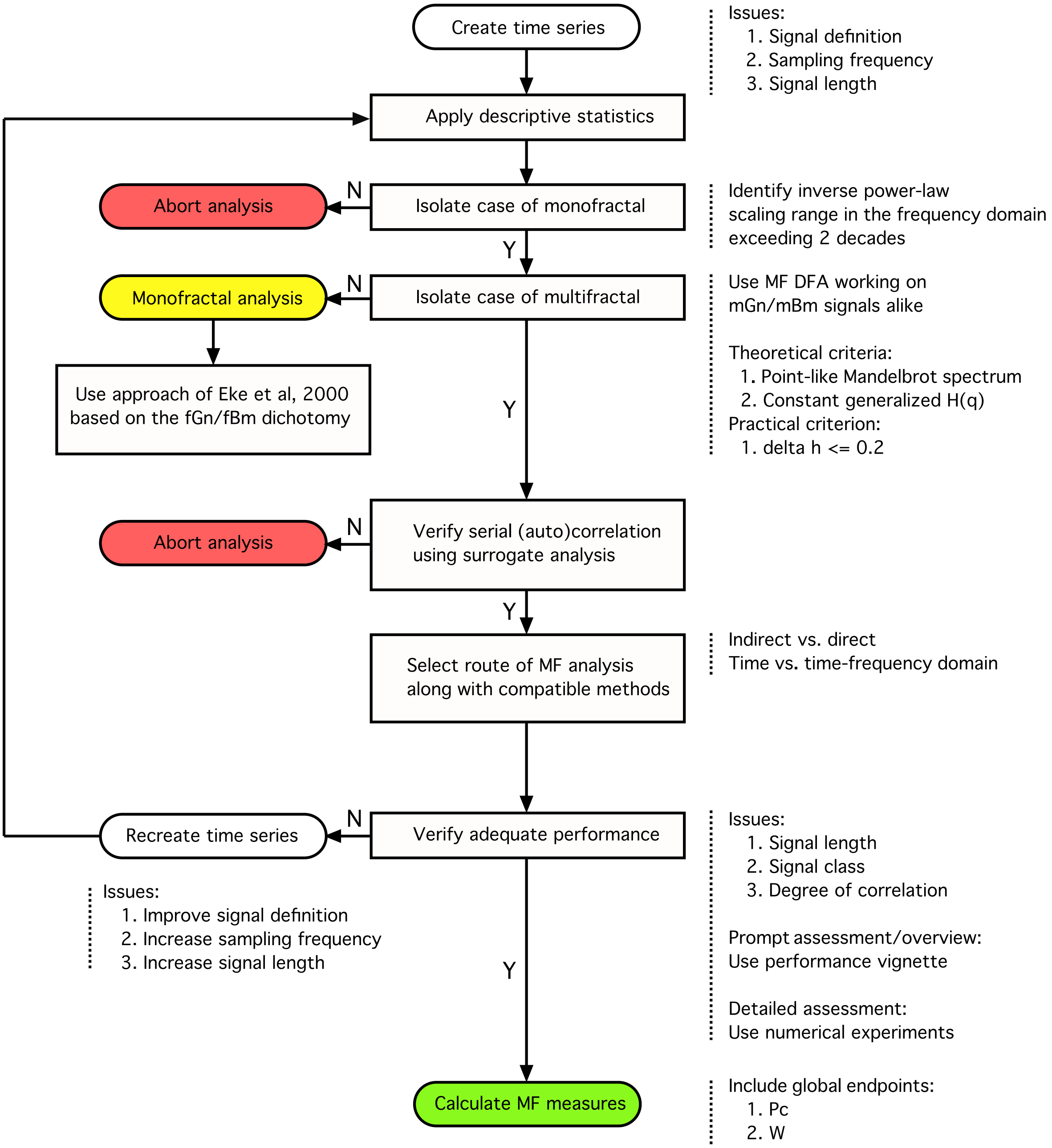

FIGURE 8 | Analytical strategy for fractal time series analysis. Toward obtaining a reliable (multi)fractal parameter, which is the purpose of the analysis, the first step to take is to collect a high definition dataset representing the temporal signal, $X(t)$, ensuring adequate definition. Provided that quality-controlled, adequate length of signal, X_i, was acquired at a sufficient frequency sampling $X(t)$ (Eke et al., 2002), scale-free processes can be characterized in terms of either a single global or a distribution of many local scaling exponents, the former pertinent to a monofractal, the latter to a multifractal signal, respectively (**Figure 1**). A detailed flowchart of our monofractal analytical strategy has been reported earlier (Eke et al., 2000, 2002), hence only some of its introductory elements are incorporated here. The signal-to-noise ratio – as part of signal definition – is a source of concern in preprocessing the signal. Ensuring the domination of the underlying physiological processes over inherent noise is a critical issue, which – if not dealt with properly – will have a detrimental effect on the correlation structure of the signal. Endogenous filtering algorithms of the manufacturers of MRI scanners could be operating in potentially relevant frequency ranges of fractal analysis aimed at trend or noise removal (Jezzard and Song, 1996). In case of BOLD signals, this problem may prove hard to track as the system noise may cause a temporally (i.e., serially) correlated error in the measurement (Zarahn et al., 1997). This may alter the autocorrelation structure of the signal with embedded physiological content (Herman et al., 2011). Various aspects of temporal smoothing have been discussed in Friston et al. (2000). To conclude, scale-free properties of the signal must be preserved during steps carried out before fractal analysis, otherwise the physiologically relevant internal structuring of the BOLD signal cannot possibly be revealed (Herman et al., 2011). Once a multifractal has been isolated by a class-independent method, such as MF-DFA, we can only assume that the multifractal structuring of the signal is due to serial correlation.

(*Continued*)

FIGURE 8 | Continued
As autocorrelation structure of the signal can reflect a broad probability distribution, surrogate analysis is needed on a shuffled signal – which destroys this correlation – to ensure that the origin of the scale-invariance is due to genuine autocorrelation in the signal (Kantelhardt et al., 2002). The null-hypothesis (the signal is not multifractal) is rejected if multifractal measures determined for the raw and surrogate sets are different. This procedure is similar to verifying the presence of deterministic chaos (Herman and Eke, 2006). Attention should be given to select the scaling range properly: involving the finest and coarsest scales in calculating $H(q)$ would greatly impair its estimate. The range of moments should be selected such that sufficient range of singularity spectrum is revealed, allowing for the calculation of scalar multifractal descriptors such as P_c. Next, one has to decide as to which path of the detailed multifractal analysis to choose (indirect vs. direct or time vs. time-frequency domain)? Each of these paths would have advantageous and disadvantageous contributions to the final results to consider. The methods of analysis must be selected compatible to the path taken. Once methods have been chosen, their performance (precision) ought to be evaluated. With adequate performance verified, the multifractal analyses can then be followed by attempts to find physiological correlates for the estimates of (multi)fractal parameters.

Length and sampling frequency. A signal is a sampled presentation of the underlying process, which generates it. Hence the sampling frequency must influence the extent the signal captures the true dynamics of the process, which is in the focus of fractal analysis irrespective if its analyzed in the time (in form of fluctuations) or in the frequency domain (in form of power distribution across the frequency scale). The sampling frequency should preferably be selected at least a magnitude higher than the highest frequency of the observed dynamics we would aim to capture.

The relationship between length and frequency can best be overviewed in the frequency domain along with the frequency components and aliasing artifact of the spectrum as seen in Figure 12 of Eke et al. (2002). Note, that the dynamics of interest can be best captured hence analyzed if the signal length is long; the sampling frequency is high, because it will provide a spectrum of many components with a weak artifactual impact of aliasing. Herman et al. (2011) have recently demonstrated this relationship on resting-state BOLD time series and concluded that lower frequency dynamics are better sampled by longer BOLD signals, whereas a high sampling rate is needed to capture dynamics in a wide bandwidth signal (See Figure 3 in Herman et al., 2011). In other words, inadequately low frequency is more detrimental to the result of fractal analysis than somewhat truncated signal.

Due to the discrete representation within the bounded temporal resolution of the signal, the precision of its fractal analysis increases with its length as demonstrated on simulated signals of known (true) fractal measures by the bias and variance of its estimates. The minimum length at which reasonable results can be expected depends not only on signal length but on the method of analysis and the degree of long-range correlation in the signal (as characterized by its H); an issue that has been explored in details for monofractal time series by the groups of Bassingthwaighte and Raymond (1994, 1995); Eke et al. (2000, 2002); Delignieres et al. (2006), and for multifractal methods by Turiel et al. (2006).

Multifractal analysis can be considered as an extension of monofractal analysis, which is explicitly true for moment-based methods: while in case of monofractals a scale-free measure is obtained at $q = 2$, the procedure for multifractals uses a set of different q-order moments. Think of q as a magnifier glass: different details of the investigated scale-free structure can be revealed at different magnification. However, if signal definition is poor due to short length or small sampling frequency, estimates of $D(h)$ will become imprecise at large $\pm q$ (**Figure 6**). Since the order of q needed to obtain characteristic points of the singularity spectrum usually falls beyond $q = \pm 2$, a longer time series is required to guarantee the needed resolution in this range. Hence, dependence of precision on signal length in case of multifractals is a more complicated issue, where the effect of spectral characteristics interacts with that of signal length (Turiel et al., 2006).

A reasonable conclusion is that the recommended minimum length for a reliable multifractal analysis ought to be longer than that found earlier for monofractal series (Eke et al., 2002; Delignieres et al., 2006).

Problem of signal class (fGn vs. fBm)

In fractal analysis, signal classification is a central issue (Eke et al., 2000) and should be regarded as a mandatory step when a tool is to be chosen from the class-dependent group. Living with the relative convenience of using a class-independent method does not render signal classification unnecessary given the great importance of proper interpretation of the findings that can be enhanced by knowing signal class.

Recently, Herman et al. (2011) found in the rat brain using monofractal analysis (PSD) that a significant population of fMRI BOLD signal fell into the non-stationary range of β. These non-stationary signals potentially interfere with resting-state connectivity studies using spatio-temporal volumes of fMRI BOLD. It is even more so, if SSC is used for signal classification (**Figure 11**) and analysis (**Figure 12**) shifting the histogram of H' to the right.

For multifractals the problem and proposed solution is generally the same, but the impact of the fGn/fBm dichotomy on the multifractal measures is not a trivial issue. Our preliminary results reported here (**Figure 12**) are steps in this direction, but this issue calls for continuing efforts in the future. It seems that at least stationarity vs. non-stationarity is a valuable piece of information for selecting a concise model of multifractals.

Distinguishing monofractals from multifractals

Multifractal analysis of an exact monofractal rendered at ideal resolution (in infinite length, sampled at infinite frequency, at infinite sensitivity of detection) would yield a constant $H(q)$, a linear dependence of τ on q and a point-like Mandelbrot spectrum with its Hölder exponent ($h_{\max}$) equal with its Hurst exponent.

Due to the finite and discrete nature of the signal, the singular behavior of a suspected scale-free process cannot be quantified perfectly. As a consequence, the homogeneity of a monofractal's

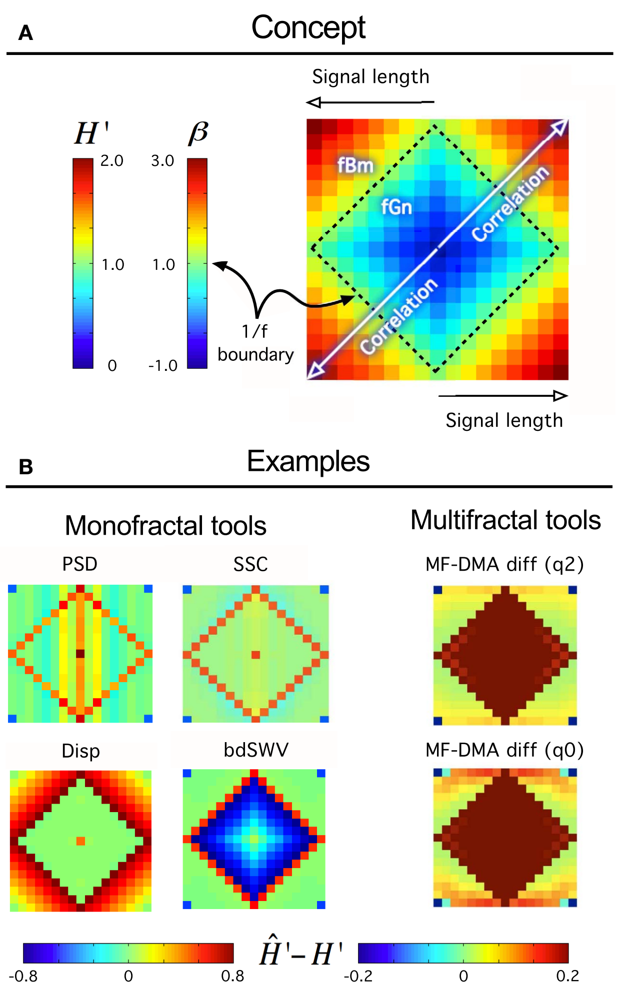

FIGURE 9 | Fractal tool performance vignette. It provides a quick assessment of any fractal time series tool's performance. As such can be useful as a method of standardization and/or comparison of various algorithms. Technically, a vignette is created as any given fractal time series method evaluates a volume of synthesized time series for a particular fractal parameter. The results are converted to extended H' as $H' = H_{\text{fGn}}$, $H' = H_{\text{fBm}} + 1$ using a conversion table between H and other fractal parameters (Eke et al., 2002). The signals are generated for a range of length, L [$L_{\min}$, $L_{\max}$] in increments of ΔL, and for the full range of the fGn/fBm dichotomy at β or H' at given increments of the exponent, $\Delta H'$ by the DHM method (Davies and Harte, 1987; Eke et al., 2000). The volume is created from these signals arranged in a square raster, which will correspond to one of four identical quadrants of the vignette. Once the analysis by a fractal tool has been carried out the results are plotted in a square array as shown in **(A)** such a way that fGn signals occupy a square created by the four identical quadrants. The 1/*f* boundary separating the fGn from the fBm range can be easily identified as plotted with a midscale color. Warmer colors indicate over-, cooler colors underestimation of the scaling exponent at the particular signal length or degree of correlation. When applied to class-independent or dependent methods **(B)**, like PSD, SSC (**B**, upper half) or Disp (dispersional analysis) and bdSWV (bridge detrended Scaled Window Variance) (**B**, lower half), respectively, an immediate conclusion on signal performance can be drawn: PSD and SSC can be used for fGn and fBm signals alike (except in the vicinity of the 1/*f* boundary) and SSC is more precise. Disp (Bassingthwaighte and Raymond, 1995; Eke et al., 2000, 2002) and bdSWV (Eke et al., 2000, 2002), two class-dependent methods of excellent performance (note the

(*Continued*)

FIGURE 9 | Continued
midscale colored area in the fGn and fBm domains, respectively) do show up accordingly. The vignette is applicable to indicate the performance of multifractal methods, too. The monofractal H can be determined in two ways: in case of $q = 2$ from $\tau(q)$, and in case of $q = 0$ from $h_{\max}$ in the singularity spectrum.

singularities cannot be captured by a multifractal analysis. The reason being is that due to numerical background noise (Grech and Pamula, 2012) – resulting from factors mentioned above – it would always smear the point-like singularity spectrum into one mimicking that of a multifractal. This is confirmed by the apparent uncertainties associated with the estimates of $H(q)$ obtained at various moments in our simulations. All in all, multifractal analyses have been conceived in a manner that tends to view a monofractal as a multifractal.

In order to avoid false interpretation of the data, time series should be produced at the highest possible definition to ameliorate this effect and criteria should also be set up to distinguish the two entities in the signal to be analyzed. Numerical simulation has been demonstrated as a useful tool to work out a parameter that can be used to substantiate a monofractal/multifractal classification (Grech and Pamula, 2012; **Figure 6**).

Trends and noises

Empirical time series are typically non-linear, non-stationary and can be contaminated by noise and other signal components foreign to the fractal analysis of the system under observation. Trend is deterministic in its character and of typically low frequency in contrast with noise, which has a completely random structuring in a higher frequency range. Monofractal analysis methods are quite robust with respect of noise, thus in case of monofractals do not require preprocessing (Bassingthwaighte and Raymond, 1995). When uncorrelated noise is added to a multifractal process, the shape of its singularity spectrum will also be preserved (Figliola et al., 2010). However with correlated noise present, – known to impact fMRI BOLD time series – preprocessing should be considered (Friston et al., 2000), and if carried out, it should be done with an appropriate adaptive filter (Gao et al., 2010, 2011; Tung et al., 2011).

In case of wavelet-based methods, a polynomial trend can be removed based on the analyzing wavelet's properties. However, if the trend has a different character (i.e., trigonometric or exponential), or it has more vanishing moments than that of the analyzing wavelet, the estimation of singularity spectrum will be impaired (See theorem 6.10 in Mallat's book; Mallat, 1999).

Various detrending schemes have been developed to enhance performance of fluctuation analysis (FA) on detrended signals, which has been compared (Bashan et al., 2008). The most common trend removal is based on fitting a low-degree polynomial to local segments of the signal such as employed in DFA (**Figure 4**). In particular, DFA's trend removal is credited for being very effective, however – as recently reported (Bryce and Sprague, 2012) – it can become inadequate if the trend ends up having a character different from the coded algorithm, which scenario cannot at all be excluded. A further problem is that the signal arbitrarily divided

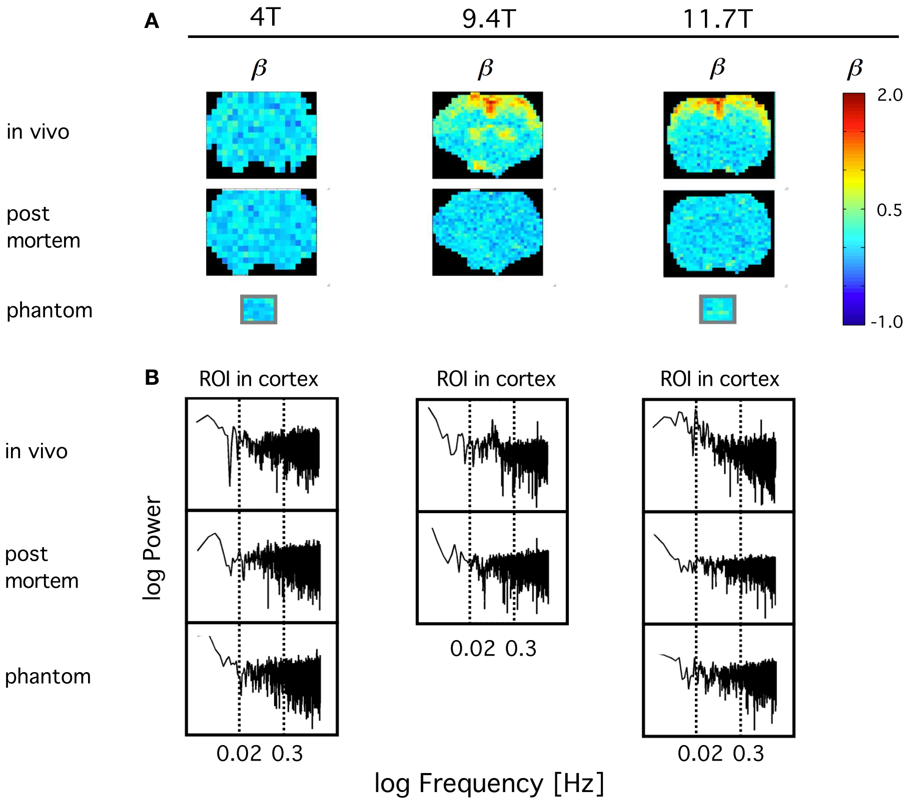

FIGURE 10 | Definition of spontaneous BOLD fluctuations critically depends on main field strength. Exemplary coronal scans are shown obtained in anesthetized rat in MR scanner applying 4, 9.4, and 11.7T main external field. All fMRI data were collected at 5 Hz in length of 4096 (2^{12}) images with gradient echo planar imaging (EPI) sequence using ^{1}H surface coils (Hyder et al., 1995). **(A)** shows *in vivo* and *post mortem* maps of spectral index, β. β was calculated from the spectra of the voxel-wise BOLD time series by the PSD method for a restricted range of fluctuation frequency (0.02–0.3 Hz) found to exhibit inverse power law relationship [fractality; indicated by vertical dashed lines on the PSD plots in **(B)**]. In order to achieve a suitable contrast for the topology, β are color coded within the fGn range (from 0 to 1). Hence voxel data with $\beta > 1$ indicating the presence of fBm type fluctuations are displayed saturated (in red). β maps for water phantoms placed in the isocenter are also shown for comparison. Note, that the fractal pattern of internal structuring of the spontaneous BOLD signal cannot be captured at adequate definition at 4T as opposed to 11.7T, where the rate of scale-free rise of power toward low frequencies are thus the highest at about the same region of interest (ROI) located in the brain cortex. This dependence translates into an articulate *in vivo* topology with increasing B_0. Also note that *in vivo* 4T cannot yield a clear topology of β when compared to *post mortem*, and that the well defined topology achieved at higher fields vanished *post mortem* indicating the link between β and the underlying physiology.

into analyzing window of different sizes in which trend removal is carried out based on *a priori* assumption (e.g., polynomial). This problem is exaggerated as by using partitioning of the signal into a set of non-overlapping windows and performing detrending in a window-based manner would not guarantee that the trend in each and every window would be identical with the assumed one. This is especially true for small windows, where trend tends to deviate from that in larger windows. Contrary to expectations, this critical finite size effect is always present, thus this pitfall can only be avoided if explicit detrending is applied by using adaptive methods (Gao et al., 2011).

To conclude, the recently reported uncontrollable bias to the results of DFA (Bryce and Sprague, 2012) raised major concern as to the reliability of FA with this detrending scheme. Thus if DFA is to be used, it should be done with special care taken in the application of more adaptive detrending analyses.

Finally, empirical mode decomposition (EMD) is a promising adaptive approach, one of whose feature is the ability to estimate trend explicitly. It also creates an opportunity to combine EMD with other fractal analysis methods like those based on FA to achieve a more reliable scale-free method (Qian et al., 2011).

Problems of moment-based methods

Using moment-based methods to estimate the Mandelbrot spectrum is a common approach with some drawbacks. Due to the discretized nature of the signal under analysis, small fluctuations cannot be resolved perfectly and therefore the Hölder exponents become biased in the range of their large negative moments (corresponding to the right tail of the singularity spectrum; Turiel et al., 2006). All moment-based methods are influenced by the linearization of the right tail thus yielding biased estimates of the negative statistical moments of the measure, μ (Turiel et al., 2006).

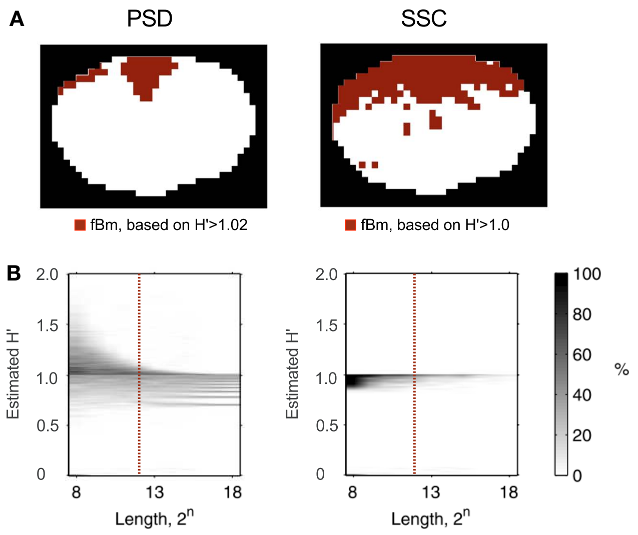

FIGURE 11 | Classifying rat fMRI BOLD data. Signal classification was performed on the 11.7T BOLD dataset shown in **Figure 10** by the PSD and SSC methods **(A)** previous tested in this capacity by Eke et al. (2002); misclassification rates for PSD and SSC are shown in the plots of **(B)** the lower panel. Because SSC is a much better classification tool, than PSD is, the classification topology will be drastically different for these two methods. The ROI's corresponding to voxel-wise signals identified by SSC as non-stationary indeed do clearly delineate the anatomical boundaries of the brain cortex, while those by the PSD only the spots of highest β.

This type of error cannot be eliminated with increasing the signal's length (Turiel et al., 2006). In case of large fluctuations in the signal, numerical limitations become problematic when calculating large positive moments.

Problems associated with moment-based methods can be summarized as follows. Firstly, a carefully selected set of different order (q) statistical moments of μ should be calculated. Selecting too large negative and positive moments would lead to imprecise generalized Hurst exponent [$H(q)$] or multiscaling exponent (**Figure 6**; Ihlen, 2012). A sufficient range of q is needed, however, in order to characterize the global singular behavior of the studied time series. This is especially important in the evaluation of the spectrum, but from a practical point of view, the spectrum width at half maximum is sufficient to obtain P_c, or $W+/W-$, that are frequently used lumped parameters in describing multifractal fMRI BOLD signals, too (Shimizu et al., 2004; Wink et al., 2008). In summary, precise estimation of singularity strength is needed at characteristic points of the spectrum: around its maximum (i.e., at $q \approx 0$) and at its half maximum a dense definition is recommended. Thus, the optimal selection depends on the signal character and needs to be analyzed with several sets of q. In general, estimating spectrum between $q = -5$ and $q = 5$ is sufficient in biomedical applications, as proposed by Lashermes and Abry (2004). Secondly, methods implementing direct estimation of singularity spectra can be applied (**Figure 3**). One typical example is the gradient modulus wavelet projection (GMWP) method, which turned out to be superior to all other tested methods (WTMM, too) in terms of precision as reported by Turiel et al. (2006). It was shown that direct approaches can give quite good results in spite of the numerical challenges imposed by calculating the Hölder exponents (h) locally and without the need of using statistical moments and Legendre transform (Turiel et al., 2006). Strategies including the latter two approaches are widely used and can be considered reasonably, but not exclusively reliable in terms of their handling the numerical difficulties associated with multifractal analysis.

Problems of wavelet transform modulus maxima methods

In case of monofractals, the average wavelet coefficient method is the most effective and the easiest to implement (Simonsen and Hansen, 1998; Eke et al., 2002). It can be used for fBm and cumulatively summed fGn signals.

There are other issues related to this method, whose nature can be numerical on the one hand and theoretical on the other. For example, the first and last points of the signal exhibits artifactual scaling, improperly selected scales would impair the results considerably, etc. A well-selected analyzing wavelet also ensures reliable results, which is also proven for certain indirectly calculated partition functions (via Boltzmann weights; Kestener and Arneodo, 2003). The effect of the modifications addressing these issues is discussed in Faghfouri and Kinsner (2005) and a detailed test of WTMM is reported by Turiel et al. (2006).

Due to the difficulties in the reliable application of WTMM, other methods were developed in the field, the most promising one being the Wavelet Leader method (Lashermes et al., 2005; Serrano and Figliola, 2009), which has recently been applied to human fMRI BOLD signals (Ciuciu et al., 2012). As refinements of WTMM, the wavelet leader is beyond the scope of this review, the reader is referred to the cited references.

Identifying the spectral extent of monofractality within a signal

Verifying the presence of self-similarity, as one of the fundamental properties of monofractals is a key element of the analytical strategy of fractal time series analysis (Eke et al., 2000; **Figure 8**). It should be present within a sufficiently wide scaling range. In case of exact (mathematical) fractals the scaling range is unbounded. In natural fractal time series however it is typically restricted to a set of continuous temporal scales as demonstrated by Eke et al. (2006) for fluctuating cerebral blood volume in humans and Herman et al. (2011) for resting-state fMRI BOLD signals in rat. As shown in the frequency domain by spectral analysis, in both species, scale-free structuring of the signal was present across a range of frequencies well below the Nyquist frequency (half of the sampling frequency). It was characterized by a systematically and self-similarly increasing power toward lower frequencies that could be modeled by Eq. 25 yielding a spectral index of $\beta > 0$, which is an indication of serial correlation between the temporal events (long-term memory). Above this range, the fluctuations were found random with $\beta \approx 0$ meaning that subsequent temporal events were not correlated. The separation of these ranges therefore is crucial because failing to do so would cause a bias in the estimate of β.

For fractal time series analysis a proper scaling range should be selected where fluctuations are scale-invariant. Optimization of the sampling process, as well as the regression analysis on log-log representations of measures vs. scales yielding the scaling exponent

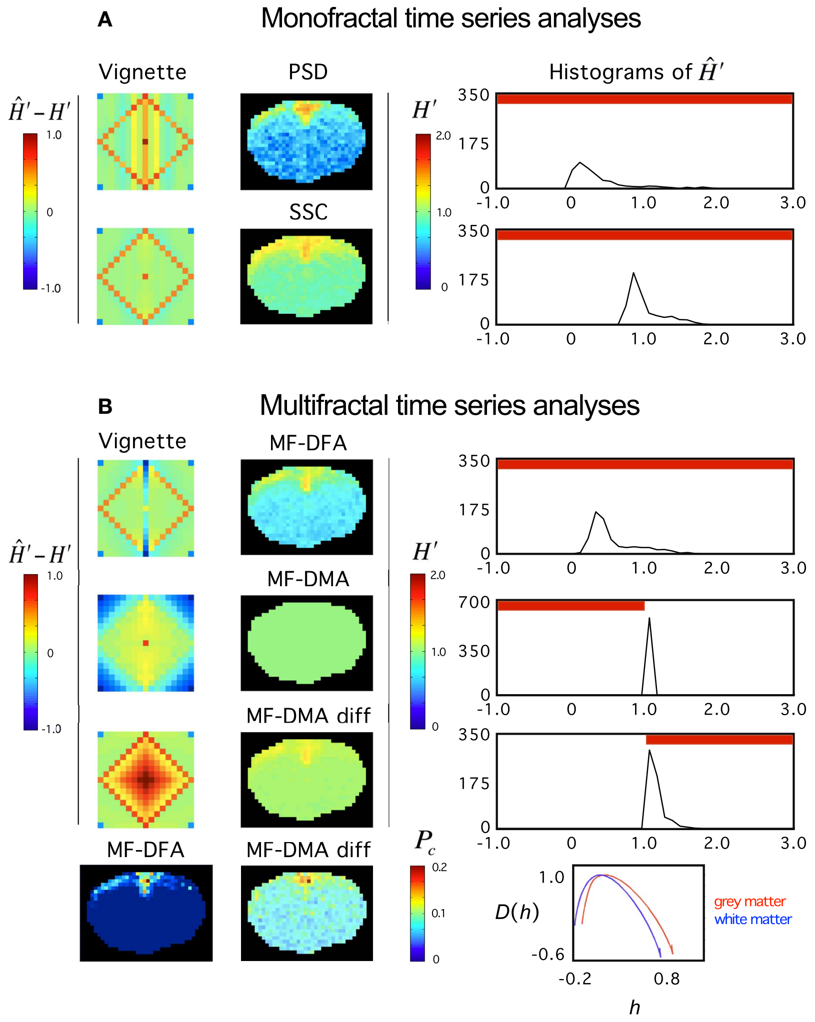

FIGURE 12 | Fractal analyses of rat fMRI BOLD data. The 11.7T BOLD dataset shown in **Figure 10** was analyzed monofractally **(A)** in the frequency domain by PSD, in the time domain by SSC, and multifractally **(B)** in the time domain by MF-DFA and MF-DMA methods. Estimates of spectral index were converted to extended Hurst exponent, H'. Our tool performance vignette is displayed next to the methods. Histograms of H' computed from the fractal image data by SSC are shown. The vignette data reconfirms that SSC is superior over PSD as a monofractal tool. Due to the downward bias of PSD in the anticorrelated fGn range, H' are significantly underestimated. Because SSC's estimates are unbiased, the SSC topology should be considered realistic, which translates into a right shift of the SSC H' histogram relative to that of PSD's. Based on the vignette pattern, among the multifractal tools, MF-DFA works quite well on fGn and fBm signals, alike, while MF-DMA with fair performance in the fGn range but closer to the $1/f$ boundary, and fails on fBm signals of the set. For reasons mentioned above, the estimates of SSC should be taken as precise. Given that most values in the fGn range fall into the range of complete uncertainty of the MF-DMA (See **Figure 6** at $q = 2$) and that MF-DMA cannot handle fBm signals, all estimates ends up being 1.0. Differencing the signals (including those of the vignette) changed the situation dramatically. As seen on the vignette, the originally fBm signals would be mapped into the fGn range that can be handled by MF-DMA very well. Actually better than the original fGn signals where slight overestimation is seen. This kind of behavior of MF-DMA may have inference with the findings of Gao et al. (2006). Also note, that the double differenced fGn signals end up being overestimated. These effects are worth to investigate in order to characterize the impact of the fGn/fBm dichotomy on the performance of these time domain multifractal tools when signals are being converted between the two classes. P_c – as a global multifractal measure – captures a topology similarly to the monofractal estimates. The corresponding singularity spectra do separate with the likelihood that the underlying multifractalities indeed differ.

is essential (Eke et al., 2002). In case of time domain methods such as DFA, DMA, and AFA as well introduced by Gao et al. (2011), optimizing the goodness-of-fit of the regression analysis is an example. Detailed recommendations as to how to deal with this problem can be found elsewhere (Peng et al., 1994; Cannon et al., 1997; Eke et al., 2002; Gao et al., 2006). When a signal's spectrum contains other than monofractal components, it may prove difficult to select a monofractal scaling range even by isolating local scaling ranges and fitting local slopes for the spectral index. This procedure should be carefully carried out given that local ranges may end up containing inadequately few spectral estimates for a reliable fitting of the trendline. When the aim is to assess the topology of the measure, this criterion can be relaxed (Herman et al., 2011).

Faghfouri and Kinsner (2005) reported that improper selection of scaling range has a detrimental effect on the results of WTMM. Different scales correspond to different window sizes in MF-DFA and MF-DMA method, and discarding the smallest and largest window sizes was even suggested by Peng et al. (1994) for the original DFA. Cannon et al. (1997) and Gao et al. (2006) suggested an optimization for the appropriate range of analyzing window sizes (i.e., scales). While this can be regarded as best practice in carrying out MF-DFA, some degree of bias is still introduced to the results arising mainly from the smallest window sizes (Bryce and Sprague, 2012).

Dualism in multifractal formalism

Amongst the indirect, moment-based methods, WTMM uses a different approach to obtain the singularity spectrum than MF-DFA and MF-DMA. Convergence of this dualism is very unlikely, as the relationship of exponents in MF-DFA to the multifractal formalism is reported to be valid only in special cases (Yu and Qi, 2011). The seminal paper of MF-DFA Kantelhardt et al. (2002) established a relationship between the generalized Hurst exponent and multiscaling exponent. The validity of this equation was reported to be valid only if $H = 1$ (Yu and Qi, 2011), and thus another derivation for $\tau(q)$ was proposed. In addition, singularity spectra reported with MF-DFA – as it follows from the Legendre transform of $\tau(q)$ (Eq. 9) – always reaches their maxima at 1, while this does not hold for wavelet methods. In our opinion, revision of results obtained with MF-DFA may be necessary along with consolidating the multifractal formalism published in the field, using the original papers as a starting point of reinvestigation (Frisch and Parisi, 1985; Mandelbrot, 1986; Barabási and Vicsek, 1991; Muzy et al., 1993; Arneodo et al., 1998).

DEMONSTRATION

Scrutinizing relevant data in selected previous works recognized as having proven or potential impact on the development of the field will likely demonstrate some typical pitfalls.

SIGNIFICANCE OF SYSTEM NOISE IN THE INTERPRETATION OF fMRI BOLD FLUCTUATIONS

Zarahn et al. (1997) demonstrated early in a careful analysis on spatially unsmoothed empirical human fMRI BOLD data (collected under null-hypothesis conditions) that the examined datasets showed a disproportionate power at lower frequencies resembling of $1/f$ type noise. In spite of the very detailed analysis, these authors treated the $1/f$ character as a semi-quantitative feature of fMRI noise and accepted its validity over a decaying exponential model as the form of the frequency domain description of the observed intrinsic serial, or autocorrelation. The spectral index, β, however was not reported but can be reconstructed from the power slope by converting the semilog plot of power vs. frequency in their Figure 3D panel to a log-log plot compatible to $|A(f)|^2 \propto 1/f^\beta$ model. A β value of ~3.3 is yielded, which is exceedingly higher than the values of $0.6 < \beta < 1.2$ reported recently for an extensive 3T dataset by He (2011). This precludes the possibility that the collected resting-state 1.5T BOLD dataset would have been of physiological origin. Our recently reported results for the rat brain with $-0.5 < \beta < 1.5$ reconfirms this assertion (Herman et al., 2011). In fact, Zarahn et al. (1997) wished to determine if the $1/f$ component of the noise observed in human subjects was necessarily due to physiological cause, but had to reject this hypothesis because they found no evidencing data to support this hypothesis. Zarahn et al. (1997) felt the AC structure (in the time domain, which is equivalent to the inverse power law relationship in the frequency domain) may not be the same for datasets acquired in different magnets, not to mention the impact of using various fMRI scanning schemes (Zarahn et al., 1997). Accordingly, and in light of our rat data for magnets 4, 9.4, and 11.7T, a less than optimal field strength could have led to a signal definition inadequate to capture the $1/f^\beta$ type structuring of the BOLD signal of biological origin that must have been embedded in the human datasets Zarahn et al. (1997) but got overridden by system noise. Most recently, Herman et al. (2011) and He (2011) referred to the early study of Zarahn et al. (1997) as one demonstrating the impact of system noise on fMRI data, while Fox et al. (2007) and Fox and Raichle (2007) as the first demonstration of $1/f$ type BOLD noise with the implication that the $1/f$ pattern implied fluctuations of biological origin.

SIGNIFICANCE OF THE GENERAL $1/f^\beta$ VS. THE STRICT 1/f MODEL IN THE INTERPRETATION OF fMRI BOLD NOISE DATA

Fox et al. (2007) reported on the impact of intrinsic BOLD fluctuations within cortical systems on inter-trial variability in human behavior (response time). In conjecture of the notion that the variability of human behavior often displays a specific $1/f$ frequency distribution with greater power at lower frequencies, they remark "This observation is interesting given that spontaneous BOLD fluctuations also show $1/f$ power spectrum (Figure S4). While the $1/f$ nature of BOLD fluctuations has been noted previously (Zarahn et al., 1997), we show that the slope is significantly between −0.5 and −1.5 (i.e., $1/f$) and that this is significantly different from the frequency distribution of BOLD fluctuations observed in a water phantom," and in their Figure S4 conclude that "the slope of the best fit regression line (red) is −0.74, close to the −1 slope characteristic of 1/f signals." This interpretation of the findings implies that the spontaneous BOLD fluctuations can be adequately described by the "strict" $1/f$ model, where the spectral index, β, in $1/f^\beta$ – known as the "general" inverse power law model – is treated as a constant of 1, not a variable carrying information on the underlying physiology. Incidentally, studies of Gilden and coworkers (using a non-fMRI approach) have indeed demonstrated (Gilden et al., 1995; Gilden, 2001; Gilden and Hancock, 2007) that response time exhibits variations that could not be modeled by a strict $1/f$ spectrum but by one incorporating a varying scaling exponent (Gilden, 2009).

Scrutinizing the data of Figure S4 can offer an alternative interpretation as follows. In terms of the hardware, the use of 3T magnet must have ensured adequate signal definition for the study. In their Figure S4, spectral slopes were reported in a lumped manner, in that power at each and every frequency were averaged for the 17 human subjects first (thus creating frequency groups), and then mean slopes along with their statistical variation were plotted for the frequency groups. The mean slope of

−0.74 (of thee lumped spectrum) was obtained by regression analysis. This treatment of the data implies that the $|A(f)|^2 \propto 1/f^\beta$ model (Mandelbrot and Ness, 1968; Eke et al., 2000, 2002) was *a priori* rejected otherwise the slope should have been determined for each and every subject in the group across the range of observed frequencies and their associated power estimates (of the true spectrum) first, followed by the statistical analysis for the mean and variance within the group of 17 subjects, for the following reasons. The spectral index is found by fitting a linear model of $|A(f)|^2 \propto 1/f^\beta$ across spectral estimates for a range of frequencies. In our opinion when it comes to provide the mean spectral index, it is indeed reasonable (Gilden and Hancock, 2007; Gilden, 2009) to come up with statistics on the fractal estimates for a group of time series data first by obtaining the estimates, proper. Averaging spectral estimates at any particular frequencies and assembling an average spectrum from them tend to abolish the fractal correlation structure for any particular time series and develop one for which the underlying time series is indeed missing. Because the transformation between the two treatments is not linear, the true mean slope of the scale-free analysis cannot be readily reconstructed from the reported slope of the means. Nevertheless, if we regard its value as an approximation and convert it to β, which being less than 1 warrants the use of $H' = (\beta_{\mathrm{fGn}} + 1)/2$, one would yield a value of $\beta = 0.77$ and $H' = 0.87$, respectively.

A recent review by Fox and Raichle (2007) offers an impressive overview and insight of how to delineate cooperative areas (or systems) in the brain based on functional connectivity that emerges from spatial cross-correlation maps of regional fluctuating BOLD signals in the resting brain (Biswal et al., 1995). These authors place the spontaneous activity of the brain as captured in BOLD fluctuations in spatio-temporal domains of fMRI data in the focus of the review emphasizing that itis a fingerprint of a newly recognized mode of functional operation of the brain referred to as default or intrinsic mode (Fox and Raichle, 2007). They argue that the ongoing investigation of this novel aspect of the mode of brain's operation using fractal analysis of resting-state fMRI BOLD may lead to a deeper and better understanding of the way the brain – on the expense of very high baseline energy production and consumption by glucose and oxidative metabolism – maintains a mode capable of selecting and mobilizing these systems in order to respond to a task adequately (Hyder et al., 2006). One has to add that the default or intrinsic mode of operation has been demonstrated and investigated in overwhelming proportions by connectivity analyses based on cross-correlating BOLD voxel-wise signals as opposed on AC of single voxel-wise BOLD time series.

Fox and Raichle (2007) emphasize "spontaneous BOLD follows a *1/f distribution*, meaning that there is an increasing power in the low frequencies." In their furthering on the nature of this $1/f$ type distribution they refer to the studies of Zarahn et al. (1997) and Fox et al. (2007) in the context it was described above (Fox et al., 2007) reaching the same conclusion, in that the characteristic model of human spontaneous BOLD is the $1/f$ (meaning the "strict") model. We would like to suggest that the notion of *1/f distribution* having a regression slope of close to −1 on the log-log PSD plot is somewhat misleading.

In an attempt to consolidate this issue, we suggest that the data be fitted to a model in the form of $1/f^\beta$, where β is a variable (Eke et al., 2000, 2002) responding to states of physiology (Thurner et al., 2003; He, 2011) of characteristic topology (Thurner et al., 2003; Herman et al., 2011) in the brain, not a constant of 1. A potential advantage of this model is that by regarding β as a scaling exponent the distribution can then be described to be scale-free (or fractal).

SIGNIFICANCE OF THE $1/f^\beta$ MODEL AND THE DICHOTOMOUS fGn/fBm ANALYTICAL STRATEGY IN ANALYZING SCALING LAWS AND PERSISTENCE IN HUMAN BRAIN ACTIVITY

As seen above, from the modeling point of view the issue of a reliable description of the autoregressive signal structuring of spontaneous BOLD, is fundamental and critical in resting-state. If it is done properly, it can lend a solid basis for assessing changes in the scaling properties in response to changing activity of the brain. The study of Thurner et al. (2003) was probably the first to demonstrate that spontaneous BOLD in the brain was scale-free and that the scaling exponent of inactive and active voxels during sensory stimulation differed. At the time of the publication of their study, the monofractal analytical strategy of Eke et al. (2000, 2002) based on the dichotomous fGn/fBm model of Mandelbrot and Ness (1968) did not yet reached the fMRI BOLD community, hence Thurner et al. (2003) did not rely on it, either. In this section we will demonstrate the implications of this circumstance in terms of the validity and conclusions of their study. We will do it in a detailed, didactical manner so that our reader should gain a hands-on experience with the perplexed nature of the issue.

Subtracting the mean from the raw fMRI signal precedes the analysis proper, $\bar{I}^{\vec{x}}(t)$, yielding $I^{\vec{x}}(t)$ in Eq. 39,

$$I^{\vec{x}}(t) = \bar{I}^{\vec{x}}(t) - \left\langle \bar{I}^{\vec{x}}(t) \right\rangle_t, \tag{39}$$

which step is compatible with (D)FA (Eke et al., 2000).

Subsequently, in Eq. 40, the temporal correlation function, $C^{\vec{x}}(\tau)$, is calculated

$$C^{\vec{x}}(\tau) = \left\langle I^{\vec{x}}(t) I^{\vec{x}}(t+\tau) \right\rangle = \frac{1}{N-\tau} \sum_{t=1}^{N-\tau} I^{\vec{x}}(t) I^{\vec{x}}(t+\tau). \tag{40}$$

In fact in this step of the analysis the covariance was calculated given that a division by variance was missing. Hence, it is slightly misleading to regard Eq. 40 as the temporal (or auto) correlation (see Eke et al., 2000, Eq. 2). Only, if assumed that the signal is fGn, whose variance is known to be constant over time, the covariance function can be taken as equivalent to the AC function. Because the authors have not tested and proven the signal's class was indeed fGn (Eke et al., 2000), there is no basis for the validity of this assertion.

In Eq. 41, the signal is summed yielding $X_n^{\vec{x}}(\tau)$, in order to eliminate problems in calculating the AC function due to noise, non-stationarity trends, etc.

$$X_n{}^{\vec{x}}(\tau) = \sum_{t=1}^{n} I^{\vec{x}}(t) \tag{41}$$

This form of the signal is further referred to as "voxel-profile."

Note, that the signal remains in this *summed* form for the rest of the analysis (i.e., analyzed as fBm). As a consequence, spectral analysis later in the study was applied to a summed – hence *processed* – signal and the results were thus reported for this and not the raw fMRI signal, which circumstance prevented reaching a clear conclusion.

Furthermore, the authors indicated that the temporal correlation function would characterize persistence. It seems the two terms (correlation vs. persistence) are used as synonyms of one another whereas they are not interchangeable terms: persistence is a property of fBm, while correlation is that of an fGn signal (Eke et al., 2000). Please note, as the raw signal has been summed, the covariance here characterized persistence that was not present in the raw fMRI signal.

In the next step (Eq. 42), the AC function is approximated by a power law function with γ as its exponent

$$C^{\vec{x}}(\tau) \sim \tau^{-\gamma}, \cdots 0 < \gamma < 1. \tag{42}$$

Based on the equation of the AC function using the Hurst exponent, H, γ must be proportional to $2H$ (Eke et al., 2000, Eq. 15).

Subsequently, as a part of a FA of the authors (cited in their Reference 19 as unpublished results of their own), the statistics ($F^{\vec{x}}(\tau)$, standard deviation) was calculated for the AC function in Eq. 43

$$F^{\vec{x}}(\tau) = \left\langle \left(X^{\vec{x}}_{n+\tau} - X^{\vec{x}}_{n} \right)^2 \right\rangle_n^{1/2}. \tag{43}$$

In the left side of Eq. 44, a general power law was applied to the fluctuation from Eq. 43 as $F^{\vec{x}}(\tau) \sim \tau^{\alpha}$

$$F^{\vec{x}}(\tau) \sim \tau^{\alpha},\ \alpha = 1 - \gamma/2. \tag{44}$$

(Note, as the fluctuations have not been detrended, this method is not the DFA of Peng et al., 1994 but strongly related to it).

Consider the scaling exponent, α, on the left side of Eq. 44. According to Peng et al. (1994) and Eke et al. (2002) $\alpha = H$ only if the raw signa l,$I^{\vec{x}}(t)$, is an fGn. However, because at this point the summed raw signal, $X^{\vec{x}}_n(\tau)$, is the object of the analysis, α and H should relate to each other as $\alpha = H + 1$. Given that the signal was summed in Eq. 41 leading up to Eq. 43, and the values for "outside the brain" were reported as $\alpha \approx 0.5$, and for "inside the brain" as $0.5 < \alpha < 1$, α must have been improperly calculated because α cannot possibly yield a value of 0.5 for a summed signal given that H scales between 0 and 1 and for an fBm series $\alpha = H + 1$ holds. The reported value of $0.5 < \alpha < 1$ can be regarded correct only for$I^{\vec{x}}(t)$, the raw fMRI signal, which therefore had to be an fGn process. On the other hand, the reported values $2 < \beta < 3$ are correct for the $X^{\vec{x}}_n$ signal, only (for reasons given later). Hence the reported α and β values lacking an indication of their respective signal class ended up being ambiguous.

Next, consider the right side of Eq. 44, which expresses α by using γ introduced earlier. We just pointed out that the raw fMRI signal must have been an fGn with $\alpha \equiv H$. Consequently, α can be substituted for H in Eq. 44 as $H = 1 - \gamma/2$ and γ expressed as

$$\gamma = 2 - 2H. \tag{45}$$

The authors referring to power law decays in the correlations relate the spectral index, β, to γ as

$$\beta = 3 - \gamma, \tag{46}$$

and further to α as

$$\beta = 2\alpha + 1.$$

Note, that these relations between β, γ, and α in principle do depend on signal class that was not reported.

Now, let us substitute γ as expressed in Eq. 45 into Eq. 46

$$\beta = 3 - 2 + 2\mathrm{H} = 1 + 2\mathrm{H},$$

then express H

$$H = \frac{\beta - 1}{2}. \tag{47}$$

As shown by Eke et al. (2000), Figure 2; in Eke et al. (2002), Table 1, based on the dichotomous fGn/fBm model, Eq. 47 would have equivocally identified the case of an fBm signal. As pointed out earlier, the raw fMRI signal was summed before the actual fractal analysis. Consequently, the relationship $\beta = 3 - \gamma$ ends up holding only if the raw fMRI signal was an fGn process. This is therefore the second piece of evidence suggesting that the class of the raw fMRI signal must have been fGn. Nevertheless, the relationship $\beta = 2\alpha + 1$ could not hold concomitantly for reasons that follow. In an earlier paper of the group (Thurner et al., 2003), the authors stated "The relationship is ambiguous, however, since some authors use the formula $\alpha = 2H + 1$ for all values of α, while others use $\alpha = 2H - 1$ for $\alpha < 1$ to restrict H to range (0,1). In this paper, we avoid this confusion by considering α directly instead of H." The fGn/fBm model (Eke et al., 2002) helps resolving this issue as neither of these relationships between α and H holds because if α is calculated with the signal class recognized and determined, the relationship between α and H is equivocally $\alpha = H_{\mathrm{fGn}}$ and $\alpha = H_{\mathrm{fBm}} + 1$. Based on the fGn/fBm model, the relationship between β and α given in Eq. 46 as $\beta = 2\alpha + 1$ needs to be revised, too, to is correct form of $\beta = 2\alpha - 1$ (See Table 1 in Eke et al., 2002).

Thurner et al. (2003) concluded: "Outside the brain and in non-active brain regions voxel-profile activity is well described by classical Brownian motion (random walk model, $\alpha \sim 0.5$ and $\beta \sim 2$)." Recall, the "voxel-profile" is not the raw fMRI signal (intensity signal, $I^{\vec{x}}(t)$, most probably an fGn), but its summed form, $X^{\vec{x}}_n(\tau)$, an fBm.

Our conclusion on the above analysis by Thurner et al. (2003) is as follows: (i) α was improperly calculated by the authors' FA method because $\alpha \sim 0.5$ cannot possibly be valid for an fBm signal given that $\alpha_{\mathrm{fBm}} > 1$ (Peng et al., 1994), (ii) $\beta \sim 2$ is only formally valid given that it was calculated based on Eq. 46 from an improperly calculated α and by using an arbitrary relationship between α and β. The subsequent and opposite effects of these rendered the value of β to $\beta \sim 2$.

When the results of Thurner et al. (2003) are interpreted according to the analytical strategy of Eke et al. (2000) based on the dichotomous fGn/fBm model of Mandelbrot and Ness (1968), the reported values of Thurner et al. can be converted for their fMRI "voxel-profile" data $X_n^{\vec{x}}$ to $\alpha_{\mathrm{fBm}} \sim 1.5$, $\beta_{\mathrm{fBm}} \sim 2$, $H_{\mathrm{fBm}} \sim 0.5$ or for the raw fMRI intensity signal $I^{\vec{x}}(t)$ to $\alpha_{\mathrm{fGn}} \sim 0.5$, $\beta_{\mathrm{fGn}} \sim 0$, $H_{\mathrm{fGn}} \sim 0.5$. This interpretation of the data reported for humans by Thurner et al. (2003) is fully compatible with the current findings by He (2011) on the human and by Herman et al. (2009, 2011) on the rat brain.

MULTIFRACTAL ANALYSES ON RAT fMRI BOLD DATA

Exemplary analysis on empirical BOLD data is presented on the 11.7T coronal scan shown in **Figure 10** to demonstrate the inner workings of these methods when applied to empirical data, and point to potential artifacts, too (See **Figure 12**). For monofractal analysis, we recommend using monofractal SSC for it gives unbiased estimates across the full range of the fGn/fBm dichotomy. For this reason, the topology is well defined and not as noisy as on the PSD maps. MF-DFA, due to its inferior performance in the strongly correlated fGn range (See **Figure 6** at $q = 2$), failed with this particular BOLD dataset. Also note, that the histograms obtained for the same datasets evaluated by these different methods do differ indicating that method's performance were different. Proper interpretation of the data therefore assumes an in-depth understanding of the implication of method's performance on the analysis. P_{c} and most certainly W seems a promising parameter to map from the BOLD temporal datasets. Their proper statistical analyses along with those of singularity spectra for different anatomical locations in the brain should be a direction of future research.

PHYSIOLOGICAL CORRELATES OF FRACTAL MEASURES OF fMRI BOLD TIME SERIES

Eke and colleagues suggested and demonstrated that β should be regarded as a variable responding to physiology (Eke et al., 1997, 2000, 2002, 2006; Eke and Herman, 1999; Herman and Eke, 2006; Herman et al., 2009, 2011).

Soon, Bullmore et al. (2001) suggested treating $1/f$ type fMRI BOLD time series as realizations of fBm processes for the purpose of facilitating their statistical analysis using pre-whitening strategies. For this reason, signal classification did not emerge as an issue to address. Then Thurner et al. (2003) demonstrated that human resting-state fMRI BOLD is not only a scale-free signal, but do respond to stimulation of the brain. Their analysis yielded this conclusion in a somewhat arbitrary manner in that the importance of the fGn/fBm dichotomy was not recognized at the time that led to flaws in the calculation of the scaling exponent as demonstrated above. Hu et al. (2008) and Lee et al. (2008) also reported that H obtained by DFA can discriminate activation from noise in fMRI BOLD signal.

In later studies dealing with the complexity of resting-state and task-related fluctuations of fMRI BOLD, the issue of signal class has gradually shifted into the focus (Maxim et al., 2005; Wink et al., 2008; Bullmore et al., 2009; He, 2011; Ciuciu et al., 2012).

Recently Herman et al. (2011) found in the rat brain using PSD that a significant population of fMRI BOLD signal fell into the non-stationary range of β. The inference of this finding is the potential interference of non-stationary signals with resting-state connectivity studies using spatio-temporal volumes of fMRI BOLD. It is even more so, if SSC is used for signal classification (**Figure 11**) and analysis (**Figure 12**) shifting the population histogram of H' to the right.

The β value converted from the reported human spectral slopes by Fox et al. (2007) (see above) fits very well within the range of human data reported most recently by He (2011) for the same instrument (3T Siemens Allegra MR scanner). He (2011) adopting the dichotomous monofractal analytical strategy of Eke et al. (2002) demonstrated that β of spontaneous BOLD obtained for multiple regions of the human brain correlates with brain glucose metabolism, a fundamental functional parameter offering grounds for the assertion that that β itself is a functional parameter. Herman et al. (2011) using the same analytical strategy (Eke et al., 2000, 2002) on resting-state rat BOLD datasets showed that β maps capture a gray vs. white matter topology speaking for the correlation of β and functional activity of the brain regions being higher in the gray than in the white matter.

With near infrared spectroscopy, – recommended by Fox and Raichle (2007) as a cost-effective, mobile measurement alternative of fMRI to capture resting-state hemodynamic fluctuations in the brain – a $1/f^{\beta}$ temporal distribution of cerebral blood volume (one of the determinant of BOLD) was found in humans, with an age and gender dependence on β (Eke et al., 2006). Furthermore, β determined from heart rate variability time series was found to differ between healthy and unhealthy individuals (Makikallio et al., 2001).

The above physiological correlates seem to have opened a new perspective in basic and clinical neurosciences (Hausdorff et al., 1997) by recognizing β as an experimental variable and applying adequate tools for its reliable assessment (Pilgram and Kaplan, 1998; Eke et al., 2000, 2002; Bullmore et al., 2009; He, 2011) with multifractal analyses as a dynamically expanding perspective (Ciuciu et al., 2012; Ihlen, 2012), too.

We propose that the inter-regional spatial cross-correlation (connectivity) as a means of revealing *spatial organization* in the brain be supplemented by a temporal AC analysis of extended BOLD signal time series by mapping β as an index of *temporal organization* of the brain's spontaneous activity.

ACKNOWLEDGMENTS

The authors thank the technicians, scientists, and engineers at MRRC (mrrc.yale.edu), and QNMR (qnmr.yale.edu). This work was supported by grants from the National Institutes of Health (R01 MH-067528 and P30 NS-52519 to Fahmeed Hyder) and from the Hungarian Scientific Research Found (OTKA grants I/3 2040, T 016953, T 034122, NIH Grants TW00442, and RR1243 to Andras Eke). Dr. Peter Mukli has been supported by the Semmelweis University Magister Project (TÁMOP-4.2.2/B-10/1-2010–0013).

REFERENCES

Arneodo, A., Audit, B., Bacry, E., Manneville, S., Muzy, J. F., and Roux, S. G. (1998). Thermodynamics of fractal signals based on wavelet analysis: application to fully developed turbulence data and DNA sequences. *Physica A* 254, 24–45.

Arneodo, A., Bacry, E., and Muzy, J. F. (1995). The thermodynamics of fractals revisited with wavelets. *Physica A* 213, 232–275.

Bacry, E., Muzy, J. F., and Arneodo, A. (1993). Singularity spectrum of fractal signals from wavelet analysis – exact results. *J. Stat. Phys.* 70, 635–674.

Bandettini, P. A. (1993). "MRI studies of brain activation: temporal characteristic," in *Proceedings of the First Annual Meeting of the International Society of Magnetic Resonance in Medicine* (Dallas: Society of Magnetic Resonance in Medicine), 143–151.

Barabási, A. L., and Vicsek, T. (1991). Multifractality of self-affine fractals. *Phys. Rev. A* 44, 2730–2733.

Barnsley, M. F. (1988). *Fractals Everywhere*. Boston: Academic Press.

Barunik, J., and Kristoufek, L. (2010). On Hurst exponent estimation under heavy-tailed distributions. *Physica A* 389, 3844–3855.

Bashan, A., Bartsch, R., Kantelhardt, J. W., and Havlin, S. (2008). Comparison of detrending methods for fluctuation analysis. *Physica A* 387, 5080–5090.

Bassingthwaighte, J. B. (1988). Physiological heterogeneity: fractals link determinism and randomness in structures and functions. *News Physiol. Sci.* 3, 5–10.

Bassingthwaighte, J. B., Liebovitch, L. S., and West, B. J. (1994). *Fractal Physiology*. New York: Published for the American Physiological Society by Oxford University Press.

Bassingthwaighte, J. B., and Raymond, G. M. (1994). Evaluating rescaled range analysis for time series. *Ann. Biomed. Eng.* 22, 432–444.

Bassingthwaighte, J. B., and Raymond, G. M. (1995). Evaluation of the dispersional analysis method for fractal time series. *Ann. Biomed. Eng.* 23, 491–505.

Benzi, R., Biferale, L., Crisanti, A., Paladin, G., Vergassola, M., and Vulpiani, A. (1993). A random process for the construction of multiaffine fields. *Physica D* 65, 352–358.

Biswal, B., Yetkin, F. Z., Haughton, V. M., and Hyde, J. S. (1995). Functional connectivity in the motor cortex of resting human brain using echo-planar MRI. *Magn. Reson. Med.* 34, 537–541.

Bryce, R. M., and Sprague, K. B. (2012). Revisiting detrended fluctuation analysis. *Sci. Rep.* 2, 1–6.

Bullmore, E., Barnes, A., Bassett, D. S., Fornito, A., Kitzbichler, M., Meunier, D., et al. (2009). Generic aspects of complexity in brain imaging data and other biological systems. *Neuroimage* 47, 1125–1134.

Bullmore, E., Long, C., Suckling, J., Fadili, J., Calvert, G., Zelaya, F., et al. (2001). Colored noise and computational inference in neurophysiological (fMRI) time series analysis: resampling methods in time and wavelet domains. *Hum. Brain Mapp.* 12, 61–78.

Caccia, D. C., Percival, D., Cannon, M. J., Raymond, G., and Bassingthwaighte, J. B. (1997). Analyzing exact fractal time series: evaluating dispersional analysis and rescaled range methods. *Physica A* 246, 609–632.

Cannon, M. J., Percival, D. B., Caccia, D. C., Raymond, G. M., and Bassingthwaighte, J. B. (1997). Evaluating scaled windowed variance methods for estimating the Hurst coefficient of time series. *Physica A* 241, 606–626.

Ciuciu, P., Varoquaux, G., Abry, P., Sadaghiani, S., and Kleinschmidt, A. (2012). Scale-free and multifractal time dynamics of fMRI signals during rest and task. *Front. Physiol.* 3:186. doi:10.3389/fphys.2012.00186

Cramer, F. (1993). *Chaos and Order*. New York: VCH Verlagsgesellschaft.

Davies, R. B., and Harte, D. S. (1987). Test for Hurst effect. *Biometrika* 74, 95–101.

Delignieres, D., Ramdani, S., Lemoine, L., Torre, K., Fortes, M., and Ninot, G. (2006). Fractal analyses for 'short' time series: a re-assessment of classical methods. *J. Math. Psychol.* 50, 525–544.

Delignieres, D., and Torre, K. (2009). Fractal dynamics of human gait: a reassessment of the 1996 data of Hausdorff et al. *J. Appl. Physiol.* 106, 1272–1279.

Delignieres, D., Torre, K., and Lemoine, L. (2005). Methodological issues in the application of monofractal analyses in psychological and behavioral research. *Nonlinear Dynamics Psychol. Life Sci.* 9, 435–461.

Eke, A., and Herman, P. (1999). Fractal analysis of spontaneous fluctuations in human cerebral hemoglobin content and its oxygenation level recorded by NIRS. *Adv. Exp. Med. Biol.* 471, 49–55.

Eke, A., Herman, P., Bassingthwaighte, J. B., Raymond, G. M., Balla, I., and Ikrenyi, C. (1997). Temporal fluctuations in regional red blood cell flux in the rat brain cortex is a fractal process. *Adv. Exp. Med. Biol.* 428, 703–709.

Eke, A., Herman, P., Bassingthwaighte, J. B., Raymond, G. M., Percival, D. B., Cannon, M., et al. (2000). Physiological time series: distinguishing fractal noises from motions. *Pflugers Arch.* 439, 403–415.

Eke, A., Herman, P., and Hajnal, M. (2006). Fractal and noisy CBV dynamics in humans: influence of age and gender. *J. Cereb. Blood Flow Metab.* 26, 891–898.

Eke, A., Herman, P., Kocsis, L., and Kozak, L. R. (2002). Fractal characterization of complexity in temporal physiological signals. *Physiol. Meas.* 23, R1–R38.

Faghfouri, A., and Kinsner, W. (2005). "Local and global analysis of multifractal singularity spectrum through wavelets," in *Canadian Conference on Electrical and Computer Engineering 2005*, Saskatoon, 2163–2169.

Falconer, K. J. (1990). *Fractal Geometry: Mathematical Foundations and Applications*. Chichester: Wiley.

Figliola, A., Serrano, E., Paccosi, G., and Rosenblatt, M. (2010). About the effectiveness of different methods for the estimation of the multifractal spectrum of natural series. *Int. J. Bifurcat. Chaos* 20, 331–339.

Fougere, P. F. (1985). On the accuracy of spectrum analysis of red noise processes using maximum entropy and periodogram methods: simulation studies and application to geographical data. *J. Geogr. Res.* 90, 4355–4366.

Fox, M. D., and Raichle, M. E. (2007). Spontaneous fluctuations in brain activity observed with functional magnetic resonance imaging. *Nat. Rev. Neurosci.* 8, 700–711.

Fox, M. D., Snyder, A. Z., Vincent, J. L., and Raichle, M. E. (2007). Intrinsic fluctuations within cortical systems account for inter-trial variability in human behavior. *Neuron* 56, 171–184.

Frisch, U., and Parisi, G. (1985). "Turbulence and predictability in geophysical fluid dynamics and climate dynamics," in *Fully Developed Turbulence and Intermittency Appendix: On the Singularity Structure of Fully Developed Structure*, eds M. Ghil, R. Benzi, and G. Parisi (Amsterdam: North-Holland), 823.

Friston, K. J., Josephs, O., Zarahn, E., Holmes, A. P., Rouquette, S., and Poline, J. B. (2000). To smooth or not to smooth? Bias and efficiency in fMRI time-series analysis. *Neuroimage* 12, 196–208.

Gao, J., Hu, J., and Tung, W.-W. (2011). Facilitating joint chaos and fractal analysis of biosignals through nonlinear adaptive filtering. *PLoS ONE* 6, e24331. doi:10.1371/journal.pone.0024331

Gao, J., Hu, J., Tung, W. W., Cao, Y., Sarshar, N., and Roychowdhury, V. P. (2006). Assessment of long-range correlation in time series: how to avoid pitfalls. *Phys. Rev. E Stat. Nonlin. Soft Matter Phys.* 73, 016117.

Gao, J., Sultan, H., Hu, J., and Tung, W. W. (2010). Denoising nonlinear time series by adaptive filtering and wavelet shrinkage: a comparison. *IEEE Signal Process. Lett.* 17, 3.

Gao, J. B., Cao, Y. Tung, W.-W., and Hu, J. (2007). *Multiscale Analysis of Complex Time Series – Integration of Chaos and Random Fractal Theory, and Beyond*. Hoboken, NJ: Wiley Interscience.

Gilden, D. L. (2001). Cognitive emissions of 1/f noise. *Psychol. Rev.* 108, 33–56.

Gilden, D. L. (2009). Global model analysis of cognitive variability. *Cogn. Sci.* 33, 1441–1467.

Gilden, D. L., and Hancock, H. (2007). Response variability in attention-deficit disorders. *Psychol. Sci.* 18, 796–802.

Gilden, D. L., Thornton, T., and Mallon, M. W. (1995). 1/f Noise in human cognition. *Science* 267, 1837–1839.

Gouyet, J. F. (1996). *Physics and Fractal Structure*. Paris: Masson.

Grech, D., and Pamula, G. (2012). Multifractal background noise of monofractal signals. *Acta Phys. Pol. A* 121, B34–B39.

Gu, G. F., and Zhou, W. X. (2006). Detrended fluctuation analysis for fractals and multifractals in higher dimensions. *Phys. Rev. E Stat. Nonlin. Soft Matter Phys.* 74, 1–7.

Gu, G.-F., and Zhou, W.-X. (2010). Detrending moving average algorithm for multifractals. *Phys. Rev. E Stat. Nonlin. Soft Matter Phys.* 82, 1–12.

Hartmann, A., Mukli, P., Nagy, Z., Kocsis, L., Herman, P., and Eke, A. (2012). Real-time fractal signal processing in the time domain. *Physica A* 392, 89–102.

Hausdorff, F. (1918). Dimension und äuß eres Maß. *Math. Ann.* 79, 157–179.

Hausdorff, J. M., Mitchell, S. L., Firtion, R. E., Peng, C. K., Cudkowicz, M. E., Wei, J. Y., et al. (1997). Altered fractal dynamics of gait: reduced stride-interval correlations with aging and Huntington's disease. *J. Appl. Physiol.* 82, 262–269.

He, B. J. (2011). Scale-free properties of the functional magnetic resonance imaging signal during rest and task. *J. Neurosci.* 31, 13786–13795.

Herman, P., and Eke, A. (2006). Nonlinear analysis of blood cell flux fluctuations in the rat brain cortex during stepwise hypotension challenge. *J. Cereb. Blood Flow Metab.* 26, 1189–1197.

Herman, P., Kocsis, L., and Eke, A. (2009). Fractal characterization of complexity in dynamic signals: application to cerebral hemodynamics. *Methods Mol. Biol.* 489, 23–40.

Herman, P., Sanganahalli, B. G., Hyder, F., and Eke, A. (2011). Fractal analysis of spontaneous fluctuations of the BOLD signal in rat brain. *Neuroimage* 58, 1060–1069.

Hosking, J. R. M. (1984). Modeling persistence in hydrological time series using fractional differencing. *Water Resour. Res.* 20, 1898–1908.

Hu, J., Lee, J. M., Gao, J., White, K. D., and Crosson, B. (2008). Assessing a signal model and identifying brain activity from fMRI data by a detrending-based fractal analysis. *Brain Struct. Funct.* 212, 417–426.

Hyder, F., Patel, A. B., Gjedde, A., Rothman, D. L., Behar, K. L., and Shulman, R. G. (2006). Neuronal-glial glucose oxidation and glutamatergic-GABAergic function. *J. Cereb. Blood Flow Metab.* 26, 865–877.

Hyder, F., Rothman, D. L., and Blamire, A. M. (1995). Image reconstruction of sequentially sampled echoplanar data. *Magn. Reson. Imaging* 13, 97–103.

Ihlen, E. A. F. (2012). Introduction to multifractal detrended fluctuation analysis in matlab. *Front. Physiol.* 3:141. doi:10.3389/fphys.2012.00141

Jezzard, P., and Song, A. W. (1996). Technical foundations and pitfalls of clinical fMRI. *Neuroimage* 4, S63–S75.

Kantelhardt, J. W., Zschiegner, S. A., Koscielny-Bunde, E., Havlin, S., Bunde, A., and Stanley, H. E. (2002). Multifractal detrended fluctuation analysis of nonstationary time series. *Physica A* 316, 87–114.

Kestener, P., and Arneodo, A. (2003). Three-dimensional wavelet-based multifractal method: the need for revisiting the multifractal description of turbulence dissipation data. *Phys. Rev. Lett.* 91, 194501.

Kwong, K. K., Belliveau, J. W., Chesler, D. A., Goldberg, I. E., Weisskoff, R. M., Poncelet, B. P., et al. (1992). Dynamic magnetic resonance imaging of human brain activity during primary sensory stimulation. *Proc. Natl. Acad. Sci. U.S.A.* 89, 5675–5679.

Lashermes, B., and Abry, P. (2004). New insight in the estimation of scaling exponents. *Int. J. Wavelets Multi.* 2, 497–523.

Lashermes, B., Jaffard, S., and Abry, P. (2005). "Wavelet leader based multifractal analysis," in *IEEE International Conference on Acoustics, Speech, and Signal Processing, ICASSP ’05. IV* (Philadelphia: Institute of Electrical and Electronics Engineers, IEEE), 161–164.

Lauterbur, P. C. (1973). Image formation by induced local interactions: examples employing nuclear magnetic resonance. *Nature* 242, 190–191.

Lee, J. M., Hu, J., Gao, J., Crosson, B., Peck, K. K., Wierenga, C. E., et al. (2008). Discriminating brain activity from task-related artifacts in functional MRI: fractal scaling analysis simulation and application. *Neuroimage* 40, 197–212.

Liebovitch, L. S., and Tóth, T. (1989). A fast algorithm to determine fractal dimensions by box counting. *Phys. Lett. A* 141, 386–390.

Makikallio, T. H., Huikuri, H. V., Hintze, U., Videbaek, J., Mitrani, R. D., Castellanos, A., et al. (2001). Fractal analysis and time- and frequency-domain measures of heart rate variability as predictors of mortality in patients with heart failure. *Am. J. Cardiol.* 87, 178–182.

Makowiec, D., Rynkiewicz, A., Wdowczyk-Szulc, J., and Zarczynska-Buchowiecka, M. (2012). On reading multifractal spectra. Multifractal age for healthy aging humans by analysis of cardiac interbeat time intervals. *Acta Phys. Pol B* 5, 159–170.

Mallat, S. (1999). *A Wavelet Tour in Signal Processing.* San Diego: Academic Press.

Mallat, S., and Hwang, W. L. (1992). Singularity detection and processing with wavelets. *IEEE Trans. Inf. Theory* 38, 617–643.

Mandelbrot, B. B. (1967). How long is the coast of Britain? Statistical self-similarity and fractional dimension. *Science* 155, 636–638.

Mandelbrot, B. B. (1980). Fractal aspects of the iteration of z → Λ (1- z) for complex l and z. *Ann. N. Y. Acad. Sci.* 357, 249–259.

Mandelbrot, B. B. (1983). *The Fractal Geometry of Nature.* New York: W. H. Freeman and Co.

Mandelbrot, B. B. (1985). Self-affine fractals and fractal dimension. *Phys. Scripta* 32, 257–260.

Mandelbrot, B. B. (1986). "Fractals and multifractals: noise, turbulence and non-fractal patterns in Physics," in *On Growth and Form: Fractal and Non-Fractal Pattern in Physics*, eds H. E. Stanley, and N. Ostrowski (Dordrecht: Nijhof), 279.

Mandelbrot, B. B., and Ness, J. W. V. (1968). Fractional Brownian motion, fractional noises and applications. *SIAM Rev. Soc. Ind. Appl. Math.* 10, 422–437.

Marmelat, V., and Delignieres, D. (2011). Complexity, coordination, and health: avoiding pitfalls and erroneous interpretations in fractal analyses. *Medicina (Kaunas)* 47, 393–398.

Maxim, V., Sendur, L., Fadili, J., Suckling, J., Gould, R., Howard, R., et al. (2005). Fractional Gaussian noise, functional MRI and Alzheimer's disease. *Neuroimage* 25, 141–158.

Muzy, J. F., Bacry, E., and Arneodo, A. (1991). Wavelets and multifractal formalism for singular signals: application to turbulence data. *Phys. Rev. Lett.* 67, 3515–3518.

Muzy, J. F., Bacry, E., and Arneodo, A. (1993). Multifractal formalism for fractal signals – the structure-function approach versus the wavelet-transform modulus-maxima method. *Phys. Rev. E Stat. Phys. Plasmas Fluids Relat. Interdiscip. Topics* 47, 875–884.

Muzy, J. F., Bacry, E., and Arneodo, A. (1994). The multifractal formalism revisited with wavelets. *Int. J. Bifurcat. Chaos* 4, 245–302.

Ogawa, S., and Lee, T. M. (1990). Magnetic resonance imaging of blood vessels at high fields. *Magn. Reson. Med.* 16, 9–18.

Ogawa, S., Lee, T. M., Kay, A. R., and Tank, D. W. (1990). Brain magnetic resonance imaging with contrast dependent on blood oxygenation. *Proc. Natl. Acad. Sci. U.S.A.* 87, 9868–9872.

Ogawa, S., Menon, R. S., Tank, D. W., Kim, S., Merkle, H., Ellermann, J. M., et al. (1993a). Functional brain mapping by blood oxygenation level-dependent contrast magnetic resonance imaging – a comparison of signal characteristics with a biophysical model. *Biophys. J.* 64, 803–812.

Ogawa, S., Lee, T. M., and Barrere, B. (1993b). The sensitivity of magnetic resonance image signals of a rat brain to changes in the cerebral venous blood oxygenation. *Magn. Reson. Med.* 29, 205–210.

Peng, C.-K., Buldyrev, S. V., Havlin, S., Simons, M., Stanley, H. E., and Goldberger, A. L. (1994). Mosaic organization of DNA nucleotides. *Phys. Rev. E Stat. Phys. Plasmas Fluids Relat. Interdiscip. Topics* 49, 1685–1689.

Phelan, S. E. (2001). What is complexity science, really? *Emergence* 3, 120–136.

Pilgram, B., and Kaplan, D. T. (1998). A comparison of estimators for 1/f noise. *Physica D* 114, 108–122.

Qian, X. Y., Gu, G. F., and Zhou, W. X. (2011). Modified detrended fluctuation analysis based on empirical mode decomposition for the characterization of anti-persistent processes. *Physica A* 390, 4388–4395.

Raichle, M. E., MacLeod, A. M., Snyder, A. Z., Powers, W. J., Gusnard, D. A., and Shulman, G. L. (2001). A default mode of brain function. *Proc. Natl. Acad. Sci. U.S.A.* 98, 676–682.

Raichle, M. E., and Mintun, M. A. (2006). Brain work and brain imaging. *Annu. Rev. Neurosci.* 29, 449–476.

Razavi, M., Eaton, B., Paradiso, S., Mina, M., Hudetz, A. G., and Bolinger, L. (2008). Source of low-frequency fluctuations in functional MRI signal. *J. Magn. Reson. Imaging* 27, 891–897.

Serrano, E., and Figliola, A. (2009). Wavelet leaders: a new method to estimate the multifractal singularity spectra. *Physica A* 388, 2793–2805.

Shimizu, Y., Barth, M., Windischberger, C., Moser, E., and Thurner, S. (2004). Wavelet-based multifractal analysis of fMRI time series. *Neuroimage* 22, 1195–1202.

Shulman, R. G., Rothman, D. L., and Hyder, F. (2007). A BOLD search for baseline. *Neuroimage* 36, 277–281.

Simonsen, I., and Hansen, A. (1998). Determination of the Hurst Exponent by use of wavelet transforms. *Phys. Rev. E Stat. Nonlin. Soft Matter Phys.* 58, 79–87.

Smith, A. J., Blumenfeld, H., Behar, K. L., Rothman, D. L., Shulman, R. G., and Hyder, F. (2002). Cerebral energetics and spiking frequency: the neurophysiological basis of fMRI. *Proc. Natl. Acad. Sci. U.S.A.* 99, 10765–10770.

Thurner, S., Windischberger, C., Moser, E., Walla, P., and Barth, M. (2003). Scaling laws and persistence in human brain activity. *Physica A* 326, 511–521.

Tung, W., Gao, J., Hu, J., and Yang, L. (2011). Detecting chaos in heavy-noise environments. *Phys. Rev. E Stat. Nonlin. Soft Matter Phys.* 83, 046210.

Turiel, A., Pérez-Vicente, C. J., and Grazzini, J. (2006). Numerical methods for the estimation of multifractal singularity spectra on sampled data: a comparative study. *J. Comput. Phys.* 216, 362–390.

Weitkunat, R. (1991). *Digital Biosignal Processing*. New York: Elsevier Science Inc.

Wink, A., Bullmore, E., Barnes, A., Bernard, F., and Suckling, J. (2008). Monofractal and multifractal dynamics of low frequency endogenous brain oscillations in functional MRI. *Hum. Brain Mapp.* 29, 791–801.

Yu, L., and Qi, D. W. (2011). Applying multifractal spectrum combined with fractal discrete Brownian motion model to wood defects recognition. *Wood Sci. Technol.* 45, 511–519.

Zarahn, E., Aguirre, G. K., and D'Esposito, M. (1997). Empirical analyses of BOLD fMRI statistics. I. Spatially unsmoothed data collected under null-hypothesis conditions. *Neuroimage* 5, 179–197.

Conflict of Interest Statement: The authors declare that the research was conducted in the absence of any commercial or financial relationships that could be construed as a potential conflict of interest.

Received: 15 July 2012; paper pending published: 07 August 2012; accepted: 12 October 2012; published online: 15 November 2012.

Citation: Eke A, Herman P, Sanganahalli BG, Hyder F, Mukli P and Nagy Z (2012) Pitfalls in fractal time series analysis: fMRI BOLD as an exemplary case. Front. Physio. ***3****:417. doi: 10.3389/fphys.2012.00417*

This article was submitted to Frontiers in Fractal Physiology, a specialty of Frontiers in Physiology.

frontiers in
PHYSIOLOGY

METHODS ARTICLE
published: 04 June 2012
doi: 10.3389/fphys.2012.00141

Introduction to multifractal detrended fluctuation analysis in Matlab

Espen A. F. Ihlen*

Department of Neuroscience, Norwegian University of Science and Technology, Trondheim, Norway

Edited by:
John G. Holden, University of Cincinnati, USA

Reviewed by:
Christopher Kello, University of California, USA
Jianbo Gao, Wright State University, USA
Sebastian Wallot, Aarhus University, Denmark

***Correspondence:**
Espen A. F. Ihlen, Department of Neuroscience, Norwegian University of Science and Technology, N-7489 Trondheim, Norway.
e-mail: espen.ihlen@ntnu.no

Fractal structures are found in biomedical time series from a wide range of physiological phenomena. The multifractal spectrum identifies the deviations in fractal structure within time periods with large and small fluctuations. The present tutorial is an introduction to *multifractal detrended fluctuation analysis* (MFDFA) that estimates the multifractal spectrum of biomedical time series. The tutorial presents MFDFA step-by-step in an interactive Matlab session. All Matlab tools needed are available in *Introduction to MFDFA* folder at the website www.ntnu.edu/inm/geri/software. MFDFA are introduced in Matlab code boxes where the reader can employ pieces of, or the entire MFDFA to example time series. After introducing MFDFA, the tutorial discusses the best practice of MFDFA in biomedical signal processing. The main aim of the tutorial is to give the reader a simple self-sustained guide to the implementation of MFDFA and interpretation of the resulting multifractal spectra.

Keywords: Matlab, multifractal, heart rate, gait, posture, EEG, MR, fMRI

INTRODUCTION

The structural characteristics of biomedical signals are often visually apparent, but not captured by conventional measures like the average amplitude of the signal. Biomedical signals from a wide range of physiological phenomena posses a scale invariant structure. A biomedical signal has a scale invariant structure when the structure repeats itself on subintervals of the signal. Formally, the biomedical signal $X(t)$ are scale invariant when $X(ct) = c^H X(t)$. Fractal analyses estimates the power law exponent, H, that defines the particular kind of scale invariant structure of the biomedical signal. Fractal analyses are frequently employed in biomedical signal processing to define the scale invariant structure in ECG, EEG, MR, and X-ray pictures (cf. Lopes and Betrouni, 2009). The scale invariant structures of inter-spike-interval of neuron firing, inter-stride-interval of human walking, inter-breath-interval of human respiration, and inter-beat intervals of the human heart has differentiated between healthy and pathological conditions (e.g., Ivanov et al., 1999; Peng et al., 2002; Zheng et al., 2005; Hausdorff, 2007), and between different types of pathological conditions (e.g., Wang et al., 2007). Scale invariant structures are also found in spatial phenomena like the branching of the nervous system and lungs (e.g., Bassingthwaighte et al., 1990; Abbound et al., 1991; Weibel, 1991; Krenz et al., 1992), bone structure (Parkinson and Fazzalari, 1994), and are able to differentiate between healthy and cancer tissues (Atupelage et al., 2012). Several reports during the last decade suggest that changes in the scale invariant structure of biomedical signals reflect changes in the adaptability of physiological processes and successful treatment of pathological conditions might change fractal structure and improve health (Goldberger, 1996; Goldberger et al., 2002). Fractal analyses are therefore promising prognostic and diagnostic tools in biomedical signal processing.

Monofractal and multifractal structures of the biomedical signal are particular kind of scale invariant structures. Most commonly, the monofractal structure of biomedical signals are defined by a single power law exponent and assumes that the scale invariance is independent on time and space. However, spatial and temporal variation in scale invariant structure of the biomedical signal often appears. These spatial and temporal variations indicate a multifractal structure of the biomedical signal that is defined by a multifractal spectrum of power law exponents. As an example, age related changes in the scale invariant structure of heart rate variability are indicated by changes of the multifractal spectrum rather than a single power law exponent (e.g., Makowiec et al., 2011). The width and shape of the multifractal spectrum can also differentiate between the heart rate variability from patients with heart diseases like ventricular tachycardia, ventricular fibrillation and congestive heart failure (e.g., Ivanov et al., 1999; Wang et al., 2007). The multifractal structure of heart rate variability is therefore suggested to reflect important properties of the autonomic regulation of the heart rate (Goldberger et al., 2002). Furthermore, the multifractal spectrum of endogenous brain dynamics and response times is more sensitive to the influence of age and cognitive performance compared to a single power law exponent alone (Suckling et al., 2008; Ihlen and Vereijken, 2010). Furthermore, the multifractal structure of EEG and series of inter-spike intervals have been able to differentiate between the neural activities of brain areas (Zheng et al., 2005). Multifractal analyses might therefore be important as a computer aided tool to increase the precision of neurosurgeries. The main aim of the present tutorial is to introduce a robust analysis called the *multifractal detrended fluctuation analysis* (MFDFA) that can estimate the multifractal spectrum of power law exponents from a biomedical time series (Kantelhardt et al., 2002). Those readers not familiar with analysis of monofractal fluctuations in biomedical signals are referred to Eke et al. (2000).

The tutorial is intended to be a self-sustained guide to the implementation of MFDFA to time series and interpretation of the resulting multifractal spectra to the readers that are unfamiliar to fractal analysis. In order to be a self-sustained guide, the tutorial decomposes MFDFA into a series of simple Matlab codes that are introduced in a step-wise manner to the reader. The tutorial is meant to be interactive where the reader can employ the Matlab codes while reading the text to enhance the understanding of MFDFA. The reader is therefore advised to download the folder "*Introduction to MFDFA*" at the web site www.ntnu.edu/inm/geri/software where all Matlab codes used in the tutorial are available. The reader should set the folder as the current directory folder in Matlab before reading the following sections of the tutorial. The folder can be set as current directory folder by pasting it into the current directory window after opening Matlab. Matlab `variables`, `parameters`, and `commands` are written in the Matlab command font and a red color to separate them from the rest of the text. The reader can type the red commands in the Matlab command window wherever they appear in the text to access `variables` and `parameters` or plot them with Matlab's `plot` function. A translation of the Matlab codes of MFDFA to the mathematical notations used by Kantelhardt et al. (2002) are given for the readers interested in the mathematical details of the MFDFA. The rest of the tutorial is divided into two sections: the implementation of MFDFA in Matlab is introduced step-by-step in Section "*Multifractal Detrended Fluctuation Analysis in Matlab*" where the interpretation of the resulting multifractal spectrum is emphasized. Important issues for the best practice of MFDFA are discussed in Section "*The Best Practice of Multifractal Detrended Fluctuation Analysis.*"

MULTIFRACTAL DETRENDED FLUCTUATION ANALYSIS IN MATLAB

The construction of MFDFA is divided into eight steps: Section "*Noise and Random Walk Like Variation in a Time Series*" introduces a method to convert a noise like time series into a random walk like time series that is a preliminary step for MFDFA. Section "*Computing the Root-Mean-Square Variation of a Time Series*" introduces root-mean-square (RMS) that is the basic computation within MFDFA and a typical way to compute the average variation of biomedical time series. Section "*Local Root-Mean-Square Variation in the Time Series*" introduces the computation of local fluctuation in the time series as RMS of the time series within non-overlapping segments. In Section "*Local Detrending of the Time Series,*" the same local RMS is computed around trends that are often encountered in biomedical time series. In Section "*Monofractal Detrended Fluctuation Analysis,*" the amplitudes of the local RMS are summarized into an overall RMS. The overall RMS of the segments with small sample sizes is dominated by the fast fluctuations in the time series. In contrast, the overall RMS for segments with large sample sizes is dominated by slow fluctuations. The power law relation between the overall RMS for multiple segment sample sizes (i.e., scales) is defined by a monofractal detrended fluctuation analysis (DFA) and is called the Hurst exponent. In Section "*Multifractal Detrended Fluctuation Analysis of Time Series,*" MFDFA is obtained by the q-order extension of the overall RMS. The q-order RMS can distinguish between segments with small and large fluctuations. The power law relation between the q-order RMS is numerical identified as the q-order Hurst exponent. In Section "*The Multifractal Spectrum of Time Series,*" several multifractal spectra are computed from the q-order Hurst exponent. In Section "*A Direct Estimation of the Multifractal Spectrum,*" an alternative version of MFDFA is introduced that compute the multifractal spectrum directly from the local fluctuations without the q-order overall RMS.

Before starting the introduction of MFDFA, the reader can type `load fractaldata.mat` in the Matlab command window to access the time series, `whitenoise`, `monofractal`, and `multifractal`. These time series will be used as test series in the rest of Section "*Multifractal Detrended Fluctuation Analysis in Matlab*" while constructing MFDFA piece-by-piece. The construction of the Matlab code for MFDFA is represented as Matlab code boxes within the text. The main intention of these Matlab code boxes is that the reader should paste the Matlab code into the Matlab command window while reading the tutorial. Figures are accessed by typing the plot command at the end of the Matlab code boxes. The reader can access all Matlab code boxes by opening the m-file `Matlabcodes` contained in the "*Introduction to MFDFA*" folder.

NOISE AND RANDOM WALK LIKE VARIATION IN A TIME SERIES

The red traces in **Figure 1** show an ordinary random walk (*lower panel*), a monofractal random walk (*middle panel*) and a multifractal random walk (*upper panel*). The fractal property of these random walks is reflected by their picture-in-picture similarity as illustrated in the upper panel of **Figure 1**. Small "hills" and "valleys" with similar structure appear when you zoom on the large "hills" and "valleys" of the random walk. The DFA is employed to time series with a random walk like structure (Peng et al., 1995). However, most biomedical time series have fluctuations that are more similar to the increments of the random walks (see the blue traces in **Figure 1**). If the biomedical time series has the noise like structure of the blue traces in **Figure 1**, it should be converted to a random walk like time series before employing DFA. Noises can be converted to random walks by subtracting the mean value and integrate the time series. Time series `whitenoise`, `monofractal`, and `multifractal` are all noise like time series and are converted to random walk like time series by Matlab code 1 below:

Matlab code 1:

```
RW1=cumsum(whitenoise-mean(whitenoise));
RW2=cumsum(monofractal-mean(monofractal));
RW3=cumsum(multifractal-mean(multifractal));
```

Type `plot1` in the command window to access **Figure 1**.

COMPUTING THE ROOT-MEAN-SQUARE VARIATION OF A TIME SERIES

A conventional analysis of variation in biomedical time series is to compute the average variation as a RMS. The reader can use Matlab

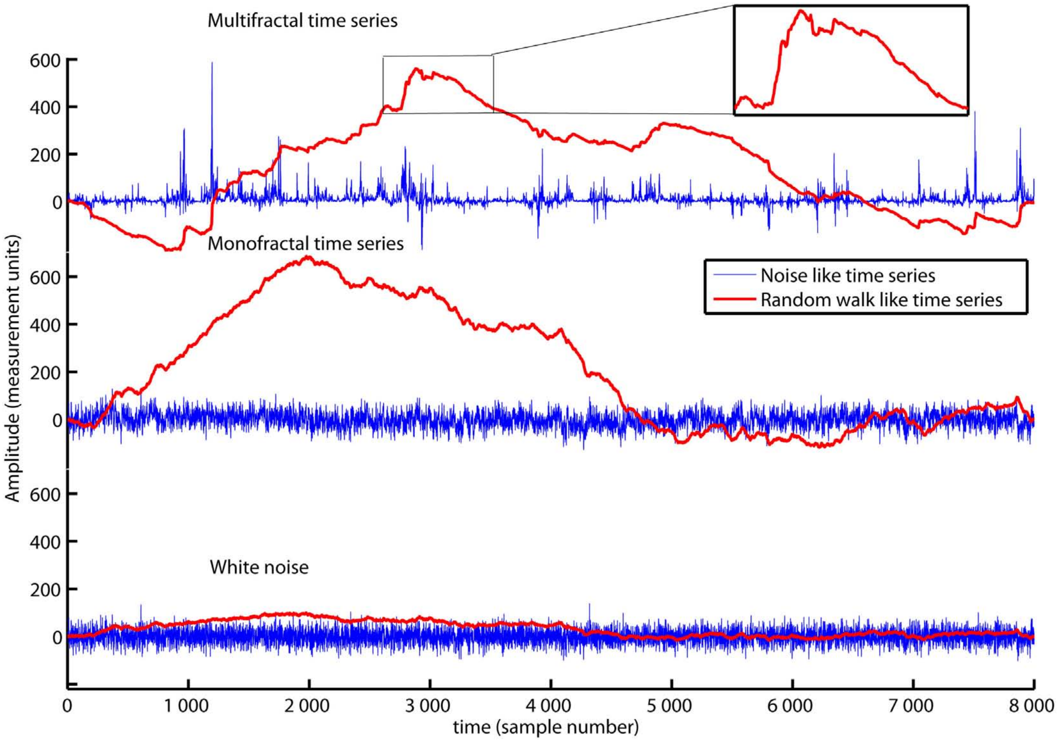

FIGURE 1 | The time series `multifractal` (upper panel), `monofractal` (middle panel), and `whitenoise` (lower panel) are shown as blue traces. They are examples of noise like time series used in the present tutorial. All time series contain 8000 data samples each where the sample numbers are indicated by the horizontal axis. Matlab code 1 converts the noises (*blue traces*) to random walks (*red traces*) that have a picture-in-picture similarity (subplot in the upper panel). Notice that the time series `multifractal` has distinct periods with small and large fluctuations in contrast to time series `monofractal` and `whitenoise`. The aim of this section is to introduce MFDFA that quantify the structure of fluctuations within the periods with small and large fluctuations.

code 2 below to compute RMS for the time series `whitenoise`, `monofractal`, and `multifractal`:

Matlab code 2:

```
RMS_ordinary=sqrt(mean(whitenoise.^2));
RMS_monofractal=sqrt(mean(monofractal.^2));
RMS_multifractal=sqrt(mean(multifractal.^2));
```

Type `plot2` in the Matlab command window to access **Figure 2**.

Figure 2 illustrates that the average amplitude of variation (i.e., RMS) is equal for all three time series, `whitenoise`, `monofractal`, and `multifractal`, even though they have quite different structures. MFDFA will be able to distinguish between these structures as we will see in the sections below.

LOCAL ROOT-MEAN-SQUARE VARIATION IN THE TIME SERIES

The multifractal time series in the upper panel have local fluctuations with both large and small magnitudes. RMS in Matlab code 2 can be computed for segments of the time series to differentiate between the magnitudes of the local fluctuations. A simple procedure is to cut the time series into equal-sized non-overlapping segments and compute a local RMS for each segment. This can be done by Matlab code 3 below and is the core procedure of MFDFA:

Matlab code 3:

```
X=cumsum(multifractal-mean(multifractal));
X=transpose(X);
scale=1000;
m=1;
segments=floor(length(X)/scale);
for v=1:segments
    Idx_start=((v-1)*scale)+1;
    Idx_stop=v*scale;
    Index{v}=Idx_start:Idx_stop;
    X_Idx=X(Index{v});
    C=polyfit(Index{v},X(Index{v}),m);
    fit{v}=polyval(C,Index{v});
    RMS{1}(v)=sqrt(mean((X_Idx-fit{v}).^2));
end
```

Type `plot3` in Matlab command window to access **Figure 3**.

The first line of Matlab code 3 converts the noise like time series, `multifractal`, to a random walk like time series `X` (i.e., Matlab code 1). The third line of Matlab code 3 set the parameter `scale` that defines the sample size of the non-overlapping segments in which the local RMS, `RMS{1}`, are computed. The fifth line is the number of `segments` that the time series `X` can be divided into where `length(X)` is the sample size of time series `X`. Thus, `segments` = 8 when `length(X)` = `8000` and `scale` = `1000`. The sixth to fourteenth line is a loop that computes the local RMS around a trend `fit{v}` for each segment by

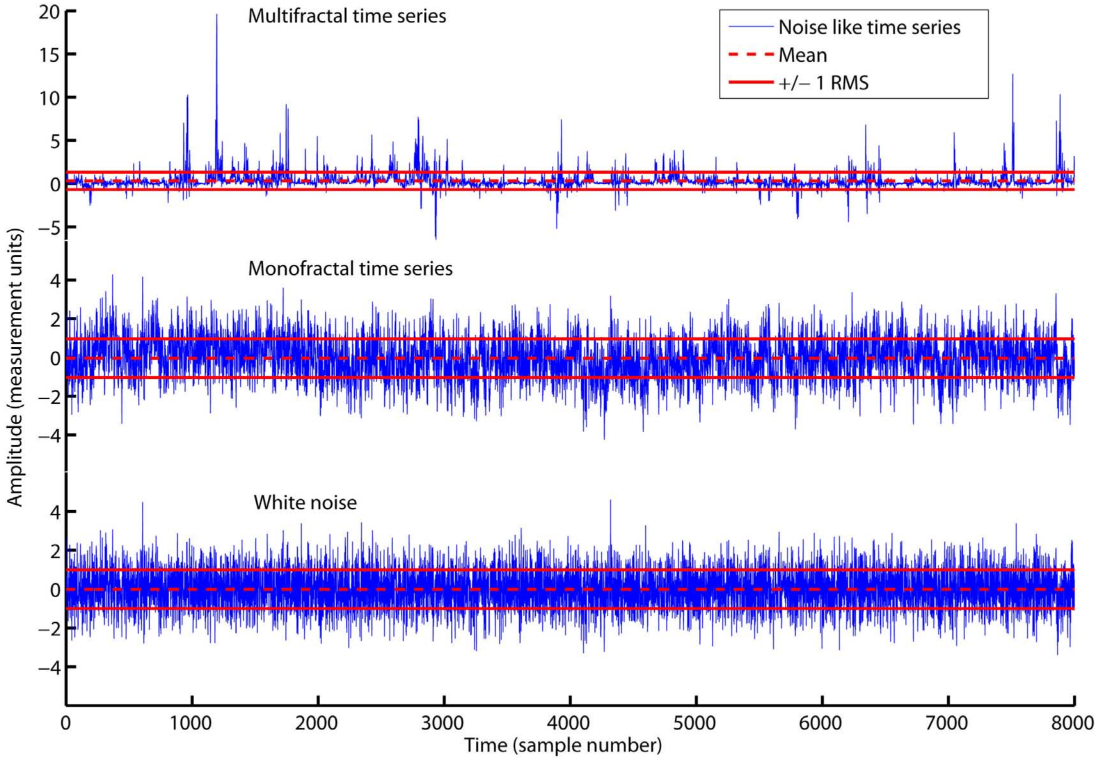

FIGURE 2 | The time series `multifractal` (*upper panel*), `monofractal` (*middle panel*), and `whitenoise` (*lower panel*) with zero average (*red dashed lines*) and ±1 RMS (*red solid lines*). All time series have equal RMS = 1, but quite different structure. RMS is only sensitive to differences in the amplitude of variation and not differences in the structure of variation. Notice the different scaling for the vertical axis of the multifractal time series.

updating the time `Index` (see red `v` arguments in Matlab code 3). In the first loop `v = 1`, the `Index{1}` goes from sample 1 to sample 1000. In the second loop `v = 2`, the `Index{2}` goes from sample 1001 to sample 2000. In the final loop `v = 8`, the `Index{8}` goes from sample 7001 to 8000.

LOCAL DETRENDING OF THE TIME SERIES

Slow varying trends are present in biomedical time series and detrending of the signal is therefore necessary to quantify the scale invariant structure of the variation around these trends. In Matlab code 3, a polynomial trend `fit{v}` is fitted to `X` within each segment `v` (see blue command lines in Matlab code 3). The first blue command line is the parameter `m` that defines the order of the polynomial. The polynomial trend are linear when `m = 1`, quadratic when `m = 2`, and cubic when `m = 3` (see **Figures 3A–C**). The first blue command line within the loop defines the polynomial coefficients `C` used to create the polynomial trend `fit{v}` of each segment (see dashed red lines in **Figure 3**). The local fluctuation, `RMS{1}(v)`, is then computed for the residual variation, `X(Index{v})-fit{v}`, within each segment `v`. The local fluctuation, `RMS{1}(v)`, is illustrated in **Figure 3** as the distance between the red dashed trends and the red solid lines.

MONOFRACTAL DETRENDED FLUCTUATION ANALYSIS

In the DFA the variation of the local `RMS{1}` are quantified by an overall RMS (`F`) in Matlab code 4 below:

Matlab code 4:

```
F=sqrt(mean(RMS{1}.^2));
```

The fast changing fluctuations in the time series `X` will influence the overall RMS, `F`, for segments with small sample sizes (i.e., small `scale`) whereas slow changing fluctuations will influence `F` for segments with large sample sizes (i.e., large `scale`). The scaling function, `F`, should therefore be computed for multiple segments sizes (i.e., multiple `scale`s) to emphasize both fast and slow evolving fluctuations that influence the structure of the time series. The scaling function, `F(ns)`, can be computed for multiple `scale`s by including Matlab code 3 and 4 within a new loop marked as red command lines and arguments `ns` below:

Matlab code 5 Part 1 of DFA

```
X=cumsum(multifractal-mean(multifractal));
X=transpose(X);
scale=[16,32,64,128,256,512,1024];
m=1;
for ns=1:length(scale),
   segments(ns)=floor(length(X)/scale(ns));
   for v=1:segments(ns),
     Idx_start=((v-1)*scale(ns))+1;
     Idx_stop=v*scale(ns);
     Index{v,ns}=Idx_start:Idx_stop;
     X_Idx=X(Index{v,ns});
     C=polyfit(Index{v,ns},X(Index{v,ns}),m);
     fit{v,ns}=polyval(C,Index{v,ns});
```

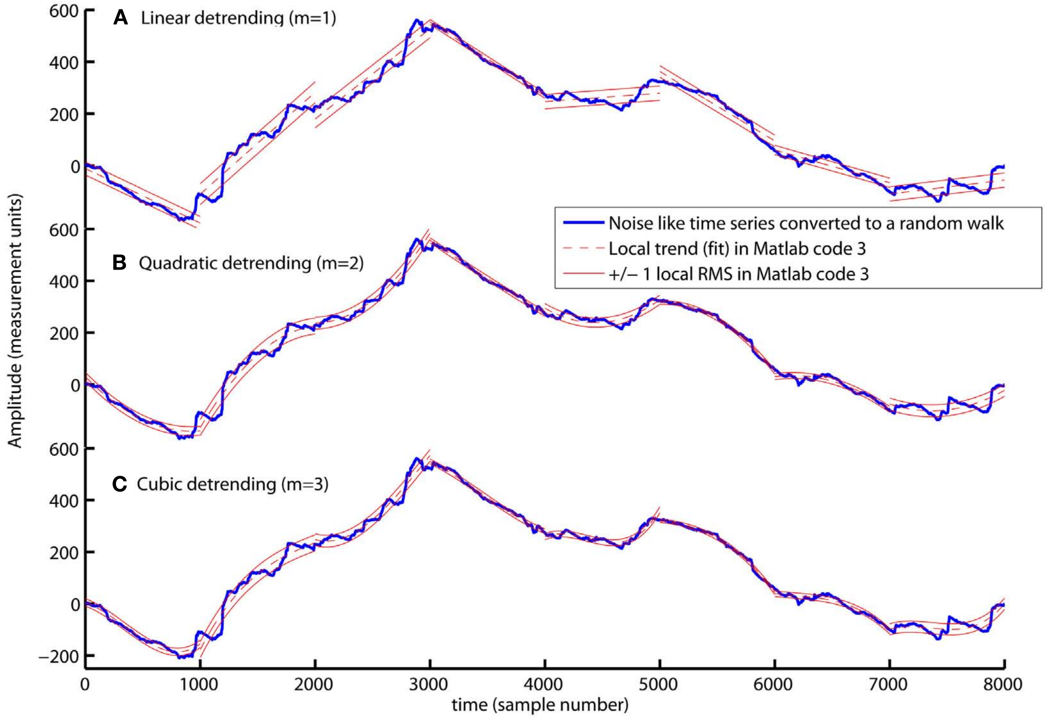

FIGURE 3 | The computation of local fluctuations, RMS{1}, around linear (A), quadratic (B), and cubic trends (C) by Matlab code 3 (m = 1, m = 2, and m = 3, respectively). The red dashed line is the fitted trend, fit{v}, within eight segments of sample size 1000. The distance between the red dashed trend and the solid red lines represents ±1 RMS{1}. The local fluctuation, RMS{1}, around trends is the basic "building block" of the *detrended fluctuation analysis*.

```
      RMS{ns}(v)=sqrt(mean((X_Idx-fit{v,ns}).^2));
    end
    F(ns)=sqrt(mean(RMS{ns}.^2));
end
```

Type `plot4` in the Matlab command window to access **Figure 4**.

In the first red command line, a vector with multiple segment sizes (i.e., scales) is set by the reader. In the second red command line, a loop is initiated where Matlab code 3 is computed from the smallest to the largest scale. The segment sample size, `scale(ns)`, are updated by the red index `ns`. The local fluctuation, `RMS{ns}`, is a set of vectors where each vector have a length equal to the number of segments [i.e., `segments(ns)`]. In the first loop for `ns = 1`, the local fluctuation `RMS{1}` is a vector of local RMS values computed for 500 segments [i.e., `segments(1)`] each containing 16 samples [i.e., `scale(1)`]. In the last loop for `ns = 7`, the local fluctuation `RMS{7}` is a vector with local RMS values computed for seven segments [i.e., `segments(7)`] each containing 1024 samples [i.e., `scale(7)`]. In the last command line, the scaling function (i.e., overall RMS), `F(ns)`, are computed for multiple scales by Matlab code 4. **Figure 4** illustrates the local fluctuations, `RMS{ns}`, and the overall RMS, `F(ns)`, for multiple scales.

DFA indentifies the monofractal structure of a time series as the power law relation between the overall RMS (i.e., `F` in Matlab code 4) computed for multiple scales (i.e., `scale` in Matlab code 5). The power law relation between the overall RMS is indicated by the slope (`H`) of the regression line (`RegLine`) computed by Matlab code 6 below:

Matlab code 6: Part 2 of DFA

```
C=polyfit(log2(scale),log2(F),1);
H=C(1);
RegLine=polyval(C,log2(scale));
```

Type `plot5` in Matlab command window to access **Figure 5**.

The slope, `H`, of the regression line, `RegLine`, is called the Hurst exponent (Hurst, 1951). The Hurst exponent defines the monofractal structure of the time series by how fast the overall RMS, `F`, of local fluctuations, `RMS`, grows with increasing segment sample size (i.e., `scale`). **Figure 5** shows that the overall RMS, `F`, of local fluctuations, `RMS`, is growing faster with the segment sample size for the `monofractal` and `multifractal` time series compared with `whitenoise` time series. The larger Hurst exponent, `H`, is visually seen as more slow evolving variations (i.e., more persistent structure) in `monfractal` and `multifractal` time series compared with `whitenoise`. **Figure 6** illustrates that the Hurst exponents defines a continuum between a noise like time series and a random walk like time series. The Hurst exponent will be in the interval between 0 and 1 for noise like time series whereas above 1 for a random walk like time series. A time series has a long-range dependent (i.e., correlated) structure when the Hurst exponent is in the interval 0.5–1 and an anti-correlated

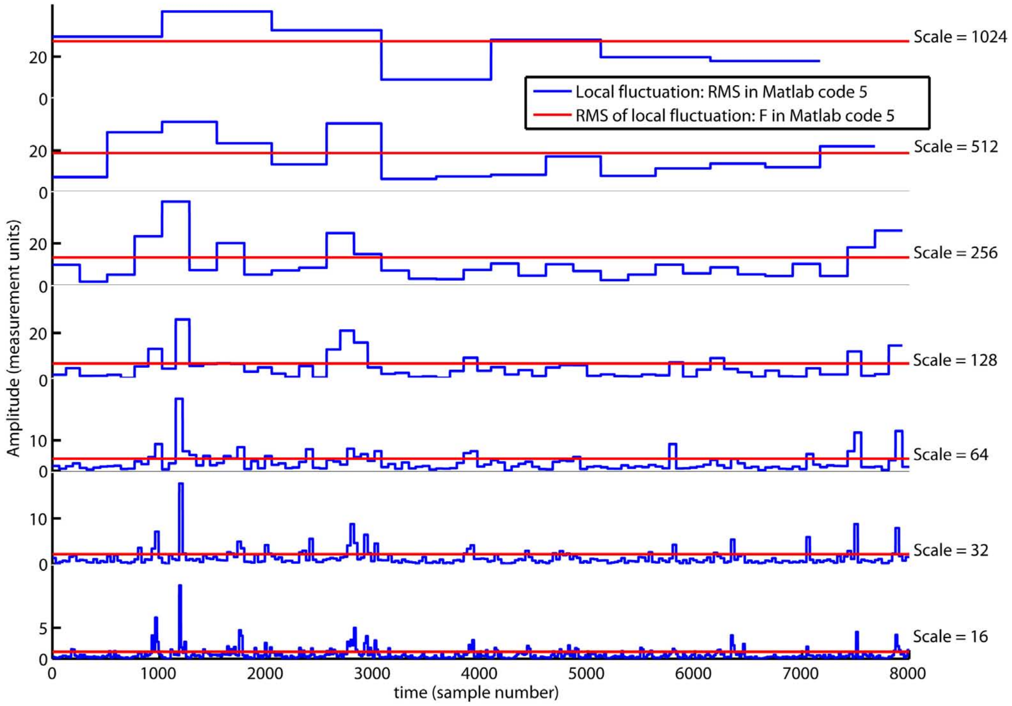

FIGURE 4 | The local fluctuations, `RMS{ns}` (*blue lines*), computed by Matlab code 5 for segments with multiple segment sizes (i.e., scale). The scaling function `F{ns}` is the overall RMS (*red line*) of the local fluctuation `RMS{ns}`. Notice that `F{ns}` decreases on smaller scales.

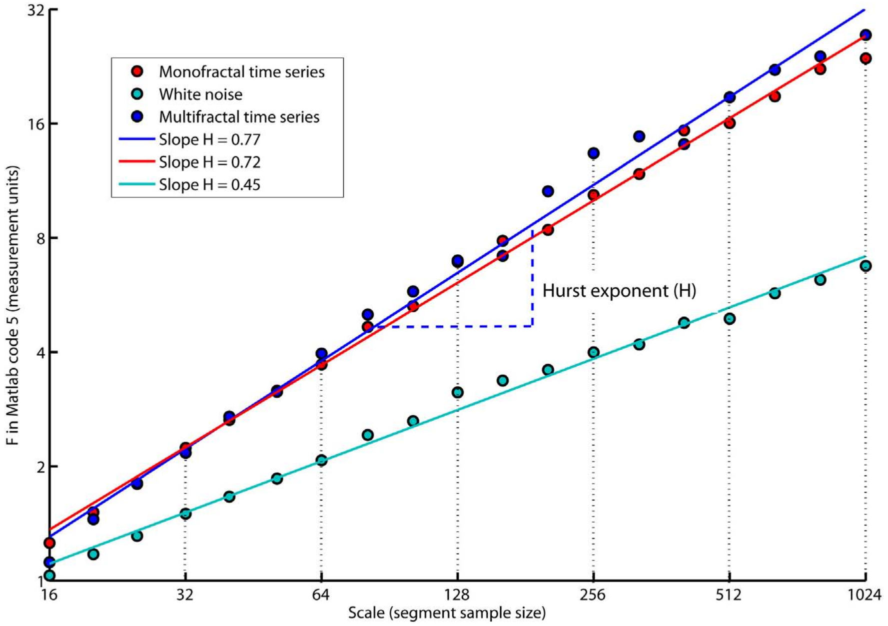

FIGURE 5 | The plot of overall RMS (i.e., `F` in Matlab code 5) versus the segment sample size (i.e., `scale` in Matlab code 5) where both `F` and `scale` are represented in log-coordinates. The scale invariant relation is indicated by the slope, `H`, of the regression lines, `RegLine`, computed by Matlab code 6. The slope, `H`, is a power law exponent called the Hurst exponent because `F` and `scale` are represented in log-coordinates. Notice that both the `monofractal` and `multifractal` time series have more apparent slow fluctuations compared to `whitenoise` indicated by larger amplitudes of the overall RMS on the larger scales.

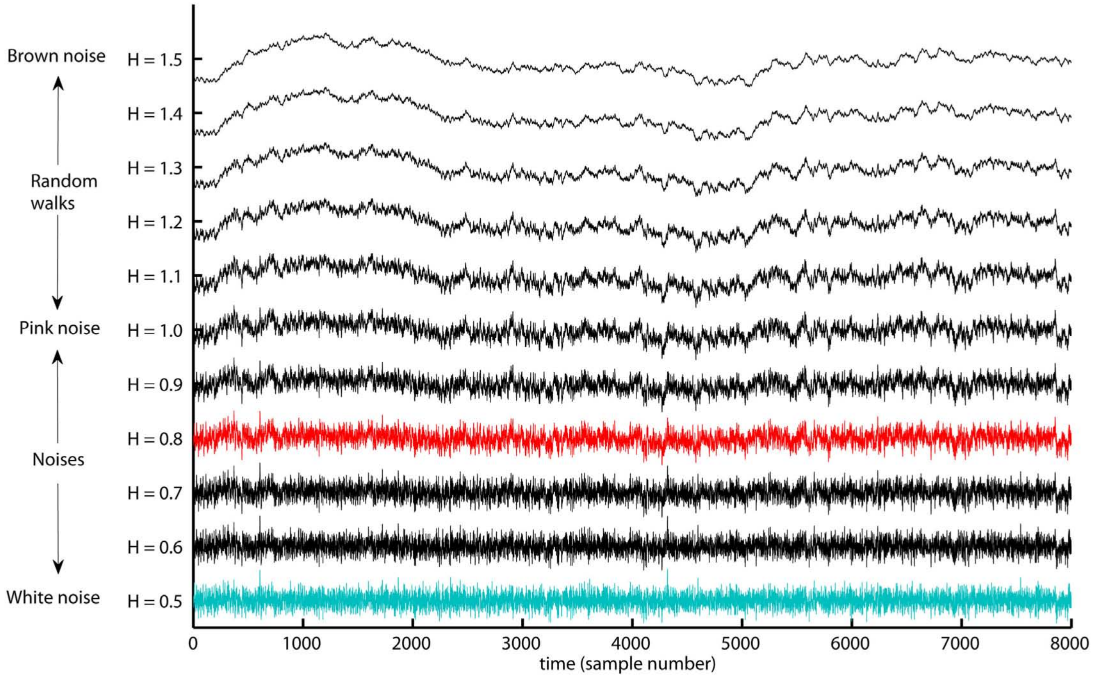

FIGURE 6 | The range of Hurst exponents defines a continuum of fractal structures between white noise (*H* = 0.5) and Brown noise (*H* = 1.5). The pink noise $H = 1$ separates between the noises $H < 1$ that have more apparent fast evolving fluctuations and random walks $H > 1$ that have more apparent slow evolving fluctuations. The examples `monofractal` (*red trace*) and `whitenoise` (*turquoise trace*) used in the present tutorial are both noise like time series. The long-range dependent structure of most biomedical signals is located within the illustrated continuum of fractal structures.

structure when the Hurst exponent is in the interval 0–0.5. The time series has an independent or short-range dependent structure in the special case when the Hurst exponent is equal to 0.5. According to **Figure 5**, time series `whitenoise` has a time independent structure with Hurst exponent close to 0.5 whereas `monofractal`, and `multifractal` has a long-range dependent structure with Hurst exponent between 0.7 and 0.8. The reader should notice that short-range dependent processes can mimic the scale invariance in **Figure 5** for certain scaling ranges (cf. Gao et al., 2006).

MULTIFRACTAL DETRENDED FLUCTUATION ANALYSIS OF TIME SERIES

The structure of the `monofractal` and `multifractal` time series are different even though they have similar overall RMS and slopes `H` in **Figure 5**. The `multifractal` time series have local fluctuations with both extreme small and large magnitudes that is absent in the `monofractal` time series. The absence of fluctuations with extreme large and small magnitudes results in a normal distribution for the monofractal time series where the variation is described by the second order statistical moment (i.e., variance) alone. The `monofractal` DFA are therefore based on the second order statistics of the overall RMS (i.e., `F` in Matlab code 4). In the `multifractal` time series, local fluctuation, `RMS{ns}(v)`, will be extreme large magnitude for segments `v` within the time periods of large fluctuations and extreme small magnitude for segments `v` within the time periods of small fluctuations. Consequently, the multifractal time series are not normal distributed and all *q*-order statistical moments should to be considered. Thus, it's necessary to extend the overall RMS in the monofractal DFA (i.e., `F` in Matlab code 4) to the following *q*-order RMS of the multifractal DFA (`Fq` in Matlab code 7 below):

Matlab code 7:

```
q=[-5,-3,-1,0,1,3,5];
for nq=1:length(q),
   qRMS{1}=RMS{1}.^q(nq);
   Fq(nq)=mean(qRMS{1}).^(1/q(nq));
end
Fq(q==0)=exp(0.5*mean(log(RMS{1}.^2)));
```

Type `plot7` in the Matlab command window to access **Figure 7**.

The first command line in Matlab code 7 defines a set of *q*-orders from −5 to 5. The second line initiates a loop that computes the overall *q*-order RMS, `Fq(nq)`, from negative to positive *q*'s (see the red arguments `nq`). The *q*-order weights the influence of segments with large and small fluctuations, `RMS{1}`, as illustrated in **Figure 7**. `Fq(nq)` for negative *q*'s (i.e., `nq` = `1`–`3`) are influenced by segments `v` with small `RMS{1}(v)`. In contrast, `Fq(nq)` for positive *q*'s (i.e., `nq` = `4`–`6`) are influenced by segments `v` with large `RMS{1}(v)`. The local fluctuations `RMS{1}` with large and small magnitudes is graded by the magnitude of the negative or positive *q*-order, respectively. `Fq` for `q` = −`3` and `3` is more influenced by the segments `v` with the smallest and largest `RMS{1}(v)`, respectively, compared to `Fq` for `q` = `-1` and `1` (see **Figure 7**). The midpoint

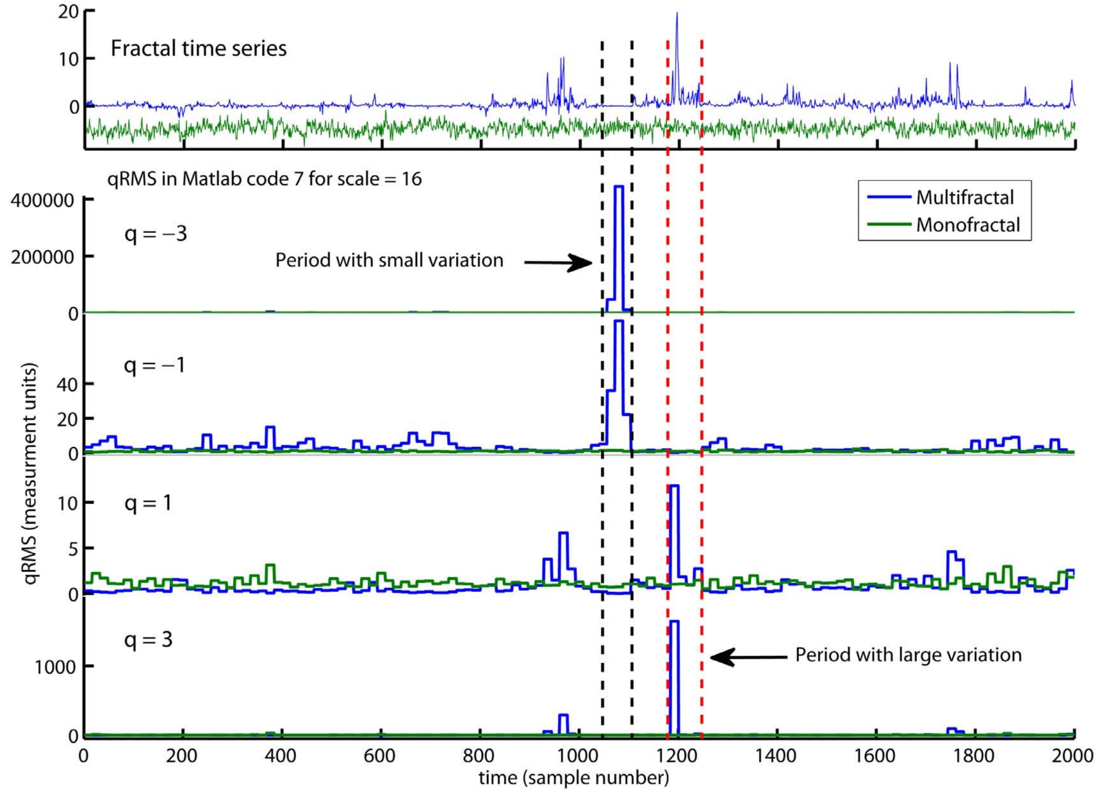

FIGURE 7 | An illustration of `qRMS{1}` computed by Matlab code 7. `qRMS{1}` is the *q*-order of the local fluctuateons (i.e., `RMS{1}`) and are the building block of the overall *q*-order RMS (i.e., `Fq` in Matlab code 7). `qRMS{1}` is represented for the `monofractal` (*green traces*) and `multifractal` (*blue traces*) time series. The negative *q*-order ($q = -3$ and -1) amplifies the segments in the `multifractal` time series with extreme small `RMS{1}` whereas positive *q*-order ($q = 3$ and 1) amplifies the segments with extreme large `RMS{1}`. Notice that $q = -3$ and $q = 3$ amplify the small and large variation, respectively, more than $q = -1$ and $q = 1$. Notice also that the `monofractal` time series has no segments with extreme large or small fluctuations and, thus, no peaks in `qRMS{1}`. The overall *q*-order RMS is able to distinguish between the structure of small and large fluctuations and, consequently, between the `monofractal` and `multifractal` time series.

`q` = `0` are neutral to influence of segments with small and large `RMS{1}`. Notice that the last line of Matlab code 7 redefines the special case `q(nq) = 0` because 1/0 goes to infinity [i.e., `1/q(q == 0) = inf` in Matlab]. The reader should also notice that `Fq(q == 2)` are equal to second order statistics `F` in Matlab code 4 because `sqrt(x) = x^(1/2)` in Matlab. The monofractal DFA in Matlab code 5 can now be extended to a MFDFA by simply changing Matlab code 4 to Matlab code 7 in the last line of Matlab code 5. This change is highlighted with red command lines in Matlab code 8 below:

Matlab code 8 Part 1 of MFDFA1

```
X=cumsum(multifractal-mean(multifractal));
X=transpose(X);
scale=[16,32,64,128,256,512,1024];
q=[-5,-3,-1,0,1,3,5];
m=1;
for ns=1:length(scale),
   segments(ns)=floor(length(X)/scale(ns));
   for v=1:segments(ns),
     Index=((((v-1)*scale(ns))+1):(v*scale(ns)));
     C=polyfit(Index,X(Index),m);
     fit=polyval(C,Index);
     RMS{ns}(v)=sqrt(mean((X(Index)-fit).^2));
   end
   for nq=1:length(q),
     qRMS{nq,ns}=RMS{ns}.^q(nq);
     Fq(nq,ns)=mean(qRMS{nq,ns}).^(1/q(nq));
   end
   Fq(q==0,ns)=exp(0.5*mean(log(RMS{ns}.^2)));
end
```

The relationship between Matlab code 8 and the mathematical equations used to introduce the MFDFA in Kantelhardt et al. (2002) are given below:

Eq. 1 in Kantelhardt et al. (2002):

`X:`	$Y(i) \equiv \sum_{k=1}^{i} [x_k - \langle x \rangle]$
`multifractal:`	x
`mean(multifractal):`	$\langle x \rangle$

The number N_s of non-overlapping segments:

`segments(ns):`	$N_s \equiv \mathrm{int}(N/s)$
`length(X):`	N
`scale(ns):`	s

Eq. 2 in Kantelhardt et al. (2002):

`RMS{ns}(v):`	$F(s,v)$
`mean((X(Index)-fit).^2):`	$\frac{1}{s}\sum_{i=1}^{s}\{Y[(v-1)s+i]-y_v(i)\}^2$
`Index:`	$(v-1)s+i \quad \text{for} \quad i=1,2,\ldots,s$
`fit:`	$y_v(i)=\sum_{k=0}^{m}C_k i^{m-k}$
`C:`	C_k

Eq. 4 in Kantelhardt et al. (2002):

`Fq(nq,ns):`	$F_q(s)\equiv\left\{\frac{1}{N_s}\sum_{v=1}^{N_s}[F^2(s,v)]^{q/2}\right\}^{1/q}$
`qRMS{nq,ns}:`	$[F^2(s,v)]^{q/2}$
`mean(qRMS{nq,ns}):`	$\frac{1}{N_s}\sum_{v=1}^{N_s}[F^2(s,v)]^{q/2}$

The q-order Hurst exponent can now be defined as the slopes (`Hq`) of regression lines (`qRegLine`) for each q-order RMS (`Fq`). Both `Hq(nq)` and `qRegLine{nq}` is computed by looping Matlab code 6 for each q-order (see red command lines and arguments `nq` in Matlab code 9 below):

Matlab code 9 Part 2 of MFDFA1

```
for nq=1:length(q),
    C=polyfit(log2(scale),log2(Fq(nq,:)),1);
    Hq(nq)=C(1);
    qRegLine{nq}=polyval(C,log2(scale));
end
```

Type `plot8` in Matlab command window to access **Figure 8**.
The relationship between Matlab code 9 are given below in the mathematical notation used in Kantelhardt et al. (2002):

`Hq(nq):`	$h(q)$
`qRegLine{nq}:`	$\log_2(F_q(s)) = h(q)\log_2(s) + C$

Figure 8 shows that the slopes `Hq` of the regression lines are q-dependent for the `multifractal` time series (see **Figure 8A**). The difference between the q-order RMS for positive and negative q's are more visual apparent at the small segment sizes compared to the large segment sizes (see **Figure 8A**). The small segments are able to distinguish between the local periods with large and small fluctuations (i.e., positive and negative q's, respectively) because the small segments are embedded within these periods. In contrast, the large segments cross several local periods with both small and large fluctuations and will therefore average out their differences in magnitude. Thus, the relationship between the q-order RMS of the `multifractal` time series becomes similar to the `monofractal` time series at the largest segment sizes (compare **Figures 8A,B**). Both the `monofractal` and `whitenoise` time series have no periods with small and large fluctuations and, consequently, the same difference between the q-order RMS irrespective of the segment sample sizes (see **Figures 8B,C**). The growing similarity between the q-order RMS of `multifractal` and `monofractal` time series with increasing segment sample size leads to a decreasing `Hq` for `multifractal` time series (see **Figure 8D**). The decreasing `Hq` indicates that the segments with small fluctuations have a random walk like structure whereas segments with large fluctuations have a noise like structure (see the continuum of Hurst exponents in **Figure 6**). The similarity between the scaling function `F` of `monofractal` and `multifractal` time series in **Figure 5** is indicated by the intercept of `Hq` around $q = 2$ (compare blue and red traces in **Figure 8D**). Thus, the monofractal DFA in Matlab code 5 and 6 will not distinguish between the structure of the `monofractal` and `multifractal` time series.

THE MULTIFRACTAL SPECTRUM OF TIME SERIES

The q-order Hurst exponent `Hq` is only one of several types of scaling exponents used to parameterize the multifractal structure of time series. The typical procedure in the literature of MFDFA is to first convert `Hq` to the q-order mass exponent (`tq`) and thereafter convert `tq` to the q-order singularity exponent (`hq`) and q-order singularity dimension (`Dq`; Kantelhardt et al., 2002). The plot of `hq` versus `Dq` is referred to as the multifractal spectrum (see **Figure 9C**). The q-order mass exponent `tq` can be computed from `Hq` by the Matlab code 10 below (see **Figure 9B**):

Matlab code 10 Part 3 of MFDFA1

```
tq=Hq.*q-1;
```

Eq. 13 in Kantelhardt et al. (2002)

The mass exponent `tq` is used to compute the q-order singularity exponent (`hq`) and the q-order singularity dimension (`Dq`) by Matlab code 11 below (see upper right **Figure 9**):

Matlab code 11 Part 4 of MFDFA1

```
hq=diff(tq)./(q(2)-q(1));
Dq=(q(1:end-1).*hq)-tq(1:end-1);
```

Equation 15 in Kantelhardt et al. (2002)
Type `plot9` in the Matlab command window to access **Figure 9**.

The `monofractal` and `whitenoise` time series has a mass exponent `tq` with a linear q-dependency. The linear q-dependency of `tq` leads to a constant `hq` of these time series because `hq` is the tangent slope of `tq` (see the first command line in Matlab code 11). The constant `hq` reduces the multifractal spectrum to a small arc for the `monofractal` and `whitenoise` time series (see **Figure 9C**). In contrast, the `multifractal` time series has mass exponents `tq` with a curved q-dependency and, consequently, a decreasing singularity exponent `hq`. The resulting multifractal spectrum is a large arc where the difference between the maximum and minimum `hq` are called the multifractal spectrum width (see arrow in **Figure 9C**).

The reader should notice that the q-order singularity exponent `hq` and corresponding dimension `Dq` computed by Matlab code 11 are referred to as α and *f*(α) in Kantelhardt et al. (2002), but as h and $D(h)$ in other literature (e.g. Ihlen and Vereijken, 2010). Furthermore, the singularity dimension can be confused with the generalized dimension and the box counting dimension that is other ways to parameterize the multifractal structure of time series (see Equation 14 in Kantelhardt et al., 2002).

The Hurst exponent defined by the monofractal DFA represents the average fractal structure of the time series as illustrated in **Figure 6** and is closely related to the central tendency of multifractal spectrum. The deviation from average fractal structure for segments with large and small fluctuations is represented by the multifractal spectrum width. Thus, each average fractal structure in the continuum of Hurst exponents (see **Figure 6**) has a new continuum of multifractal spectrum widths that represents

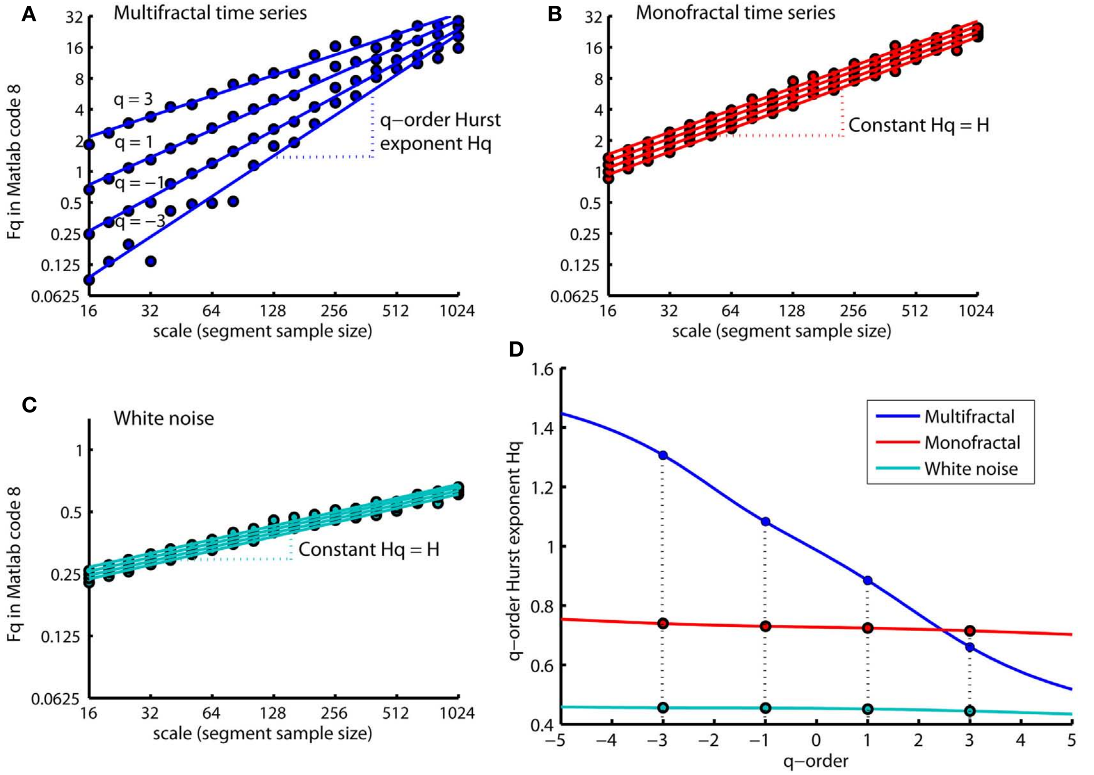

FIGURE 8 | *q*-order RMS `Fq(nq,:)` and corresponding regression line `qRegLine{nq}` computed by MFDFA (i.e., Matlab code 8 and 9) for time series `multifractal` (A), `monofractal` (B), and `whitenoise` (C). (A) The scaling functions `Fq` (*blue dots*) and corresponding regression slopes `Hq` (*blue dashed lines*) are *q*-dependent. **(B,C)** The scaling functions `Fq` (*red* and *turqouish dots*) and regression slope `Hq` (*red* and *turqouish dashed lines*) are *q*-independent. **(D)** The *q*-order Hurst exponent `Hq` for the time series `multifractal` (*blue trace*), `monofractal` (*red trace*) and `whitenoise` (*turqouish trace*) where the *colored dots* represents the slopes `Hq` for $q = -3, -1$, 1, and 3 illustrated in **(A–C)**. Notice that the intercept of `Hq` for `multifractal` and `monofractal` time series [intercept between *blue* and *red* trace in **(D)**] are close to $q = 2$. This intercept reflects the similarity between their overall RMS, `F`, in **Figure 5**.

the deviations from the average fractal structure (see **Figure 10**). Furthermore, the shape of the multifractal spectrum in **Figure 10** does not have to be symmetric. The multifractal spectrum can also have either a left or a right truncation that originate from a leveling of the *q*-order Hurst exponent for negative or positive *q*'s, respectively (see **Figure 11**). The leveling of *q*-order Hurst exponent reflects that the *q*-order RMS is insensitive to the magnitude of the local fluctuations. The multifractal spectrum will have a long left tail when the time series have a multifractal structure that is insensitive to the local fluctuations with small magnitudes (see upper **Figure 11**). In contrast, the multifractal spectrum will have a long right tail when the time series have a multifractal structure that is insensitive to the local fluctuations with large magnitudes (see lower **Figure 11**). Another continuum of right and left truncations exists for each multifractal spectrum width in the continuum illustrated in **Figure 10**. Thus, the width and shape of the multifractal spectrum is able to classify a wide range of different scale invariant structures of biomedical time series.

A DIRECT ESTIMATION OF THE MULTIFRACTAL SPECTRUM

The transformation of the *q*-order Hurst exponent `Hq` to the mass exponent `tq` and, finally, to the multifractal spectrum `Dq` and `hq` is stated as a "just-the-way-it-is" argument in the above section without mathematical details. The reader might ask at this point why one should define and interpret the multifractal spectrum `Dq` and `hq` and not only `Hq` that are directly estimated by Matlab code 8 and 9. Estimating the multifractal spectrum directly from the local fluctuation, will answer this question and give a less abstract definition of the multifractal spectrum. A local Hurst exponent can be defined directly from, `RMS{ns}(v)`, for each time instant `v`. The local Hurst exponent estimated for a `multifractal` time series will fluctuate in time in contrast to the time independent Hurst exponent estimated by the monofractal DFA (see Matlab code 5 and 6; **Figure 5**). The temporal variation of the local Hurst exponent can be summarized in a probability distribution and the multifractal spectrum is just the normalized probability distribution in log-coordinates. Thus, the width and shape of the multifractal spectrum reflect the temporal variation of the local Hurst exponent or, in other words, the temporal variation in the local scale invariant structure of the time series. In order to estimate the local Hurst exponent, the local fluctuation, `RMS{ns}(v)`, has to be defined within a translating segment centered at sample `v` instead of within non-overlapping segments. Thus, Matlab code

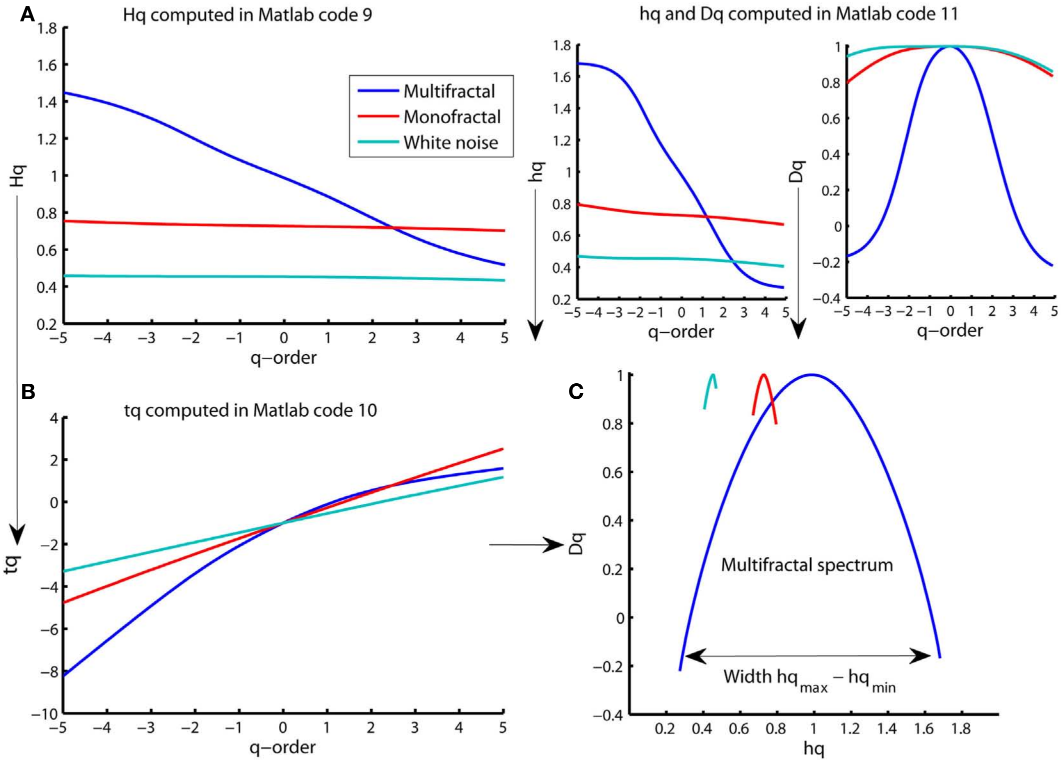

FIGURE 9 | Multiple representations of multifractal spectrum for `multifractal` (*blue traces*), `monofractal` (*red traces*), and `whitenoise` (*turquoise trace*) time series. (A) *q*-order Hurst exponent `Hq` computed in Matlab code 9. **(B)** Mass exponent `tq` computed in Matlab code 10. **(C)** Multifractal spectrum of `Dq` and `hq` (*upper right panels*) computed in Matlab code 11 and plotted against each other. The arrow indicates the difference between the maximum and minimum `hq` that are called the multifractal spectrum width. Notice that the constant `Hq` for `monofractal` and `whitenoise` times series leads to a linear `tq` that further leads to a constant `hq` and `Dq` that, finally, are joined to become only tiny arcs in **(C)**.

8 has to be modified to Matlab code 12 below (see red command lines):

Matlab code 12 Part 1 of MFDFA2

```
X=cumsum(multifractal-mean(multifractal));
X=transpose(X);
scale_small=[7,9,11,13,15,17];
halfmax=floor(max(scale_small)/2);
Time_index=halfmax+1:length(X)-halfmax;
m=1;
for ns=1:length(scale_small),
   halfseg=floor(scale_small(ns)/2);
   for v=halfmax+1:length(X)-halfmax;
      T_index=v-halfseg:v+halfseg;
      C=polyfit(T_index,X(T_index),m);
      fit=polyval(C,T_index);
      RMS{ns}(v)=sqrt(mean((X(T_index)-fit).^2));
   end
end
```

(The reader must be patient because this code might take a couple of minutes)

The first red command line defines a vector of small segment sizes (i.e., `scale_small`) where the segment sizes increases with two samples. This increase of two samples is necessary to align the center of segments according to the `Time_index`. The third red line set the `Time_index` for the local fluctuation, `RMS{ns}`, that exclude the `halfmax` number of samples at the start and the end of the time series (see second red command line). Then a loop are initiated for each segment size where the local fluctuations, `RMS{ns}(v)`, are computed for a translating segment centered at sample `v = Time_index`. The translating segment includes the local samples that are updated by `T_index` (see last red command line). The local Hurst exponent (`Ht`) can now be computed from the local fluctuation, `RMS{ns}`, by the Matlab code 13 below:

Matlab code 13 Part 2 of MFDFA2

```
C=polyfit(log2(scale),log2(Fq(q==0,:)),1);
Regfit=polyval(C,log2(scale_small));
maxL=length(X);
for ns=1:length(scale_small);
   RMSt=RMS{ns}(Time_index);
   resRMS{ns}=Regfit(ns)-log2(RMSt);
   logscale(ns)=log2(maxL)-log2(scale_small(ns));
   Ht(ns,:)=resRMS{ns}./logscale(ns)+Hq(q==0);
end
```

Type `plot12` in the Matlab command window to access **Figure 12**.

The first two command line defines the regression line `Regfit` equal to the regression line `qRegLine{q == 0}` computed by Matlab code 8. `Regfit` represents the center of the spread of local `RMS` and are the regression line of the overall *q*-order RMS, `Fq(q == 0,:)`. A loop for each scale `ns` computes

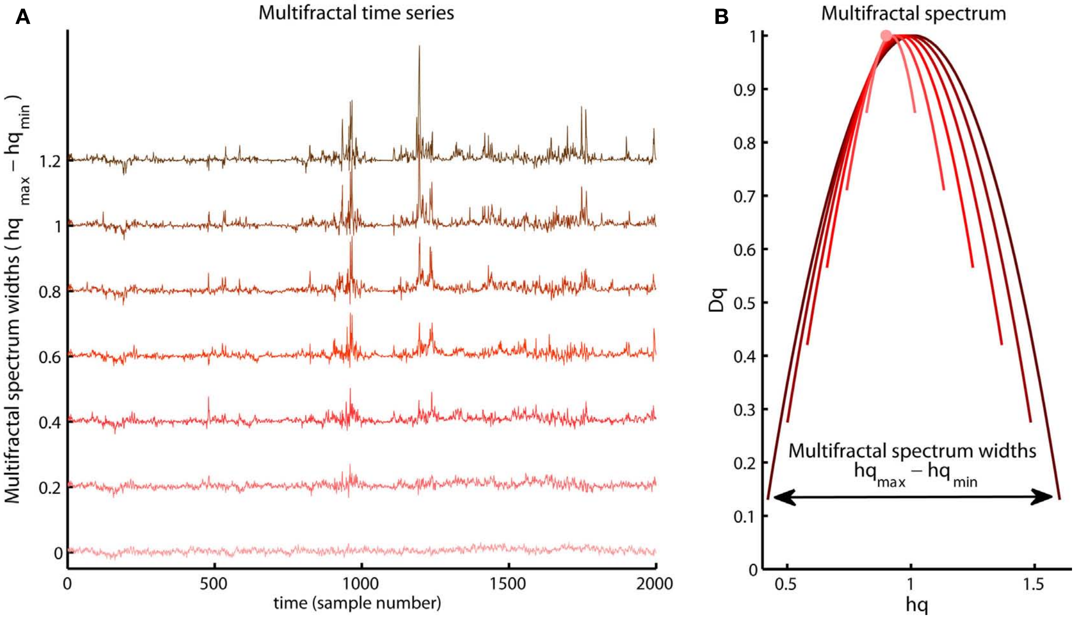

FIGURE 10 | Illustration of a continuum of multifractal time series with the same *q*-order Hurst exponent for $q = 2$ but with different multifractal spectrum width [compare *vertical axis* of the (A) and the *arrow* in the (B)]. Notice the growth of structural differences between the periods with small and large fluctuations as the multifractal spectrum width become larger.

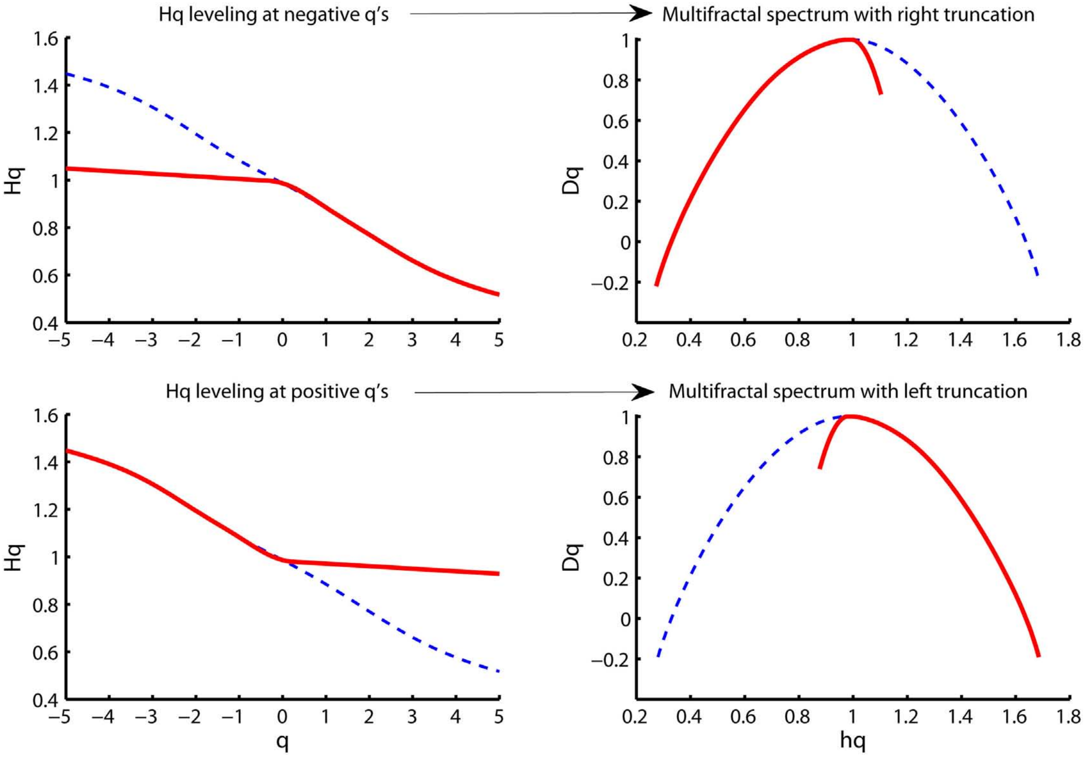

FIGURE 11 | Illustration of multifractal spectra with a right truncation (*upper right panel*) and a left truncation (*upper left panel*). These truncations originate from the leveling of the *q*-order Hurst exponents for negative *q*'s (*upper right panel*) and positive *q*'s (*upper left panel*), respectively.

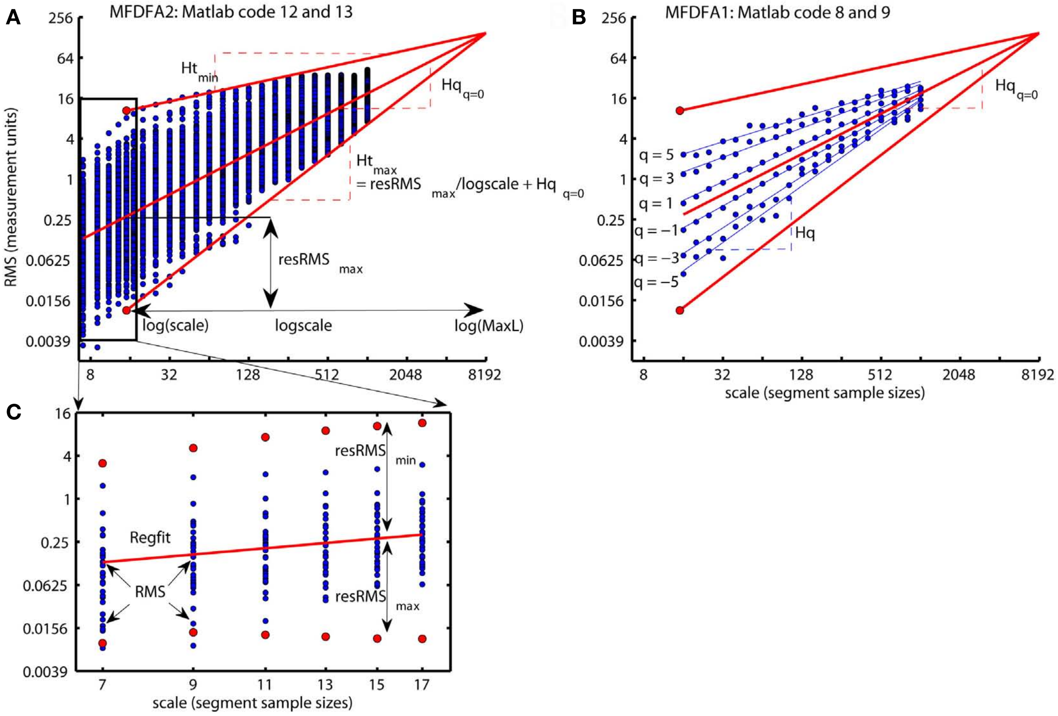

FIGURE 12 | (A) A summary of how the local Hurst exponent `Ht` is estimated in Matlab code 13. The regression line `Regfit` (red center line) is the center of the spread of local `RMS` in log-coordinates and is equal to the regression line `qRegLine{q==0}` in Matlab code 8 and 9 [see **(B)**]. The minimum and maximum local Hurst exponent `Ht(5,:)` is the slope of the upper and lower red lines, respectively, that converge from the maximum and minimum of `RMS{5}` onto the regression line `Regfit` at the maximum scale `maxL`. Consequently, the local Hurst exponent `Ht(ns,:)` estimated by dividing the residual `resRMS{ns}(v)` for each time instant `v` by `logscale(ns)` (i.e., the difference between the maximal scale `maxL` and `scale(ns)` in log-coordinates) and adding the slope $Hq_{q=0}$ of the regression line `Regfit`. **(B)** The scaling function `Fq` (blue dots) and the regression lines `qRegLine{nq}` (blue lines) computed by Matlab code 8 and 9. All `Fq` lies within the envelope between the red lines for the maximum and minimum `Ht(5,:)`, but does not cover the entire range in the same way as the local `RMS{5}` in **(A)**. **(C)** The smallest scales used to compute the local Hurst exponents and the multifractal spectrum illustrated in **Figure 13**. The red dots represent the maximum `RMS{ns}(1080)` and minimum `RMS{ns}(1199)` for multiple segment sample sizes [i.e., `scale(ns)`] at time instant `v = 1080` and `v=1199`, respectively [see **Figure 13A**] whereas blue dots represent the local fluctuations for 30 other time instants. Notice that both the horizontal and vertical axes in all panels are in log-coordinates.

the residual fluctuation `resRMS{ns}` of `log2(RMS{ns})` around the regression line `Regfit` for each sample `v` of the time series. In **Figure 12B**, the differences between the overall *q*-order RMS, `Fq`, converge toward each other with increasing scale. This convergence is inevitable for multifractal variation by the linear relationship between `Fq` for all *q*-order and the assumption of monotonical decreasing *q*-order Hurst exponent, `Hq` (see **Figure 8D**). The same convergence is seen for the local `RMS` in **Figure 12A** and is used to estimate the local Hurst exponents, `Ht(ns,:)`. `Ht(ns,:)` is estimated as the slope of the line from local `RMS` in log-coordinates to the endpoint of the regression line, `Regfit`, at the largest scale, `maxL` (see **Figure 12**). Consequently, `Ht(ns,:)` are obtained by dividing the residuals `resRMS{ns}` by `logscale` (i.e., the difference between maximal scale `maxL` and the `scale(ns)` in log-coordinates) and adding the slope `Hq(q==0)` of regression line, `Regfit` (see **Figure 12A**). **Figure 13A** illustrates the local Hurst exponent `Ht(ns,:)` for `ns = 5` (i.e., `scale(ns) = 15`) for the `multifractal`, `monofractal`, and `whitenoise` time series. The local Hurst exponent `Ht(ns,:)` has larger variation for the `multifractal` time series compared to the `monofractal` and `whitenoise` time series. The small `Ht(ns,:)` in the periods of the `multifractal` time series with local fluctuations of large magnitudes (i.e., large `RMS{ns}`) reflects the noise like structure of the local fluctuations (see red dashed lines in **Figure 13A**). In contrast, the larger `Ht(ns,:)` in the periods with local fluctuations of small magnitudes (i.e., small `RMS{ns}`) reflects the random walk like structure of the local fluctuations (see black dashed lines in **Figure 13A**). The local Hurst exponent `Ht` in periods with fluctuations of small and large magnitudes is therefore consistent with the *q*-order Hurst exponent `Hq` for negative and positive *q*'s, respectively. The advantage of local Hurst exponent `Ht` compared with *q*-order Hurst exponent `Hq` is the ability of `Ht` to identify the time instant of structural changes within the time series. In studies where the physiological phenomenon is perturbed at some time instant `v`, the local Hurst exponent `Ht(ns,v)` can identify how this perturbation affects the local scale invariant structure of the biomedical time series. The temporal variation of local Hurst exponent `Ht` can be summarized in a histogram representing the probability distribution (`Ph`) of `Ht` (see **Figure 13B**). The multifractal spectrum (`Dh`) is defined simply

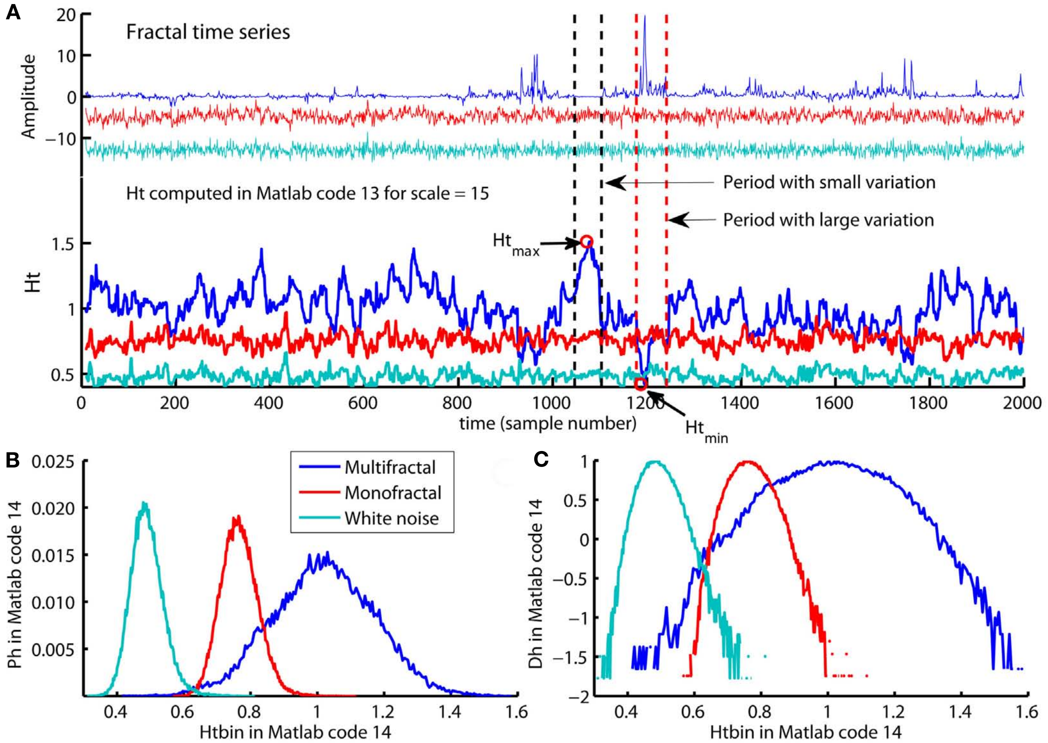

FIGURE 13 | (A) The `multifractal`, `monofractal`, and `whitenoise` time series (upper panel) and their local Hurst exponents `Ht(:,5)` computed by Matlab code 13 (lower panel). The `multifractal` time series have a larger variation in the local Hurst exponents `Ht(5,:)` compared with the `monofractal` and `whitenoise` time series. The period with the local fluctuation of the smallest magnitude in `multifractal` time series contains the maximum `Ht(5,:)` (see Ht_{max} in period between the *black dashed lines*) whereas the period with the local fluctuation of the largest magnitudes contains the smallest `Ht(5,:)` (see Ht_{min} in the period between *red dashed lines*). **(B)** The probability distribution `Ph` of the local Hurst exponents `Ht` estimated as histograms by Matlab code 14 for the `multifractal`, `monofractal`, and `whitenoise` time series. **(C)** The multifractal spectrum `Dh` estimated from distribution `Ph` by Matlab code 14 for the same time series. The distribution `Ph` and spectrum `Dh` have a larger width for the `multifractal` time series compared to the `monofractal` and `whitenoise` time series.

by the log-transformation of the normalized probability distribution (`Ph_norm`). The probability distribution (`Ph`) and multifractal spectrum (`Dh`) are computed by Matlab code 14 below:

Matlab code 14 Part 3 of MFDFA2

```
Ht_row=Ht(:);
BinNumb=round(sqrt(length(Ht_row)));
[freq,Htbin]=hist(Ht_row,BinNumb);
Ph=freq./sum(freq);
Ph_norm=Ph./max(Ph);
Dh=1-(log(Ph_norm)./-log(mean(scale)));
```

Type `plot13` in Matlab command window to access **Figure 13**.

The first line in Matlab code 14 convert the matrix `Ht` to the vector `Ht_row` that are the input argument in `hist` function used to compute the histogram for `Ht_row`. The second input argument in `hist` function are `BinNumb` that set the number of bins in the histogram. A sufficient choice for `BinNumb` is the square root of the sample size of `Ht_row` (see the second command line). The output variables of `hist` function are the center of each bin `Htbin` and the number `freq` of local Hurst exponents that fall into each bin. The probability distribution `Ph` are computed by dividing the number `freq` of local Hurst exponents in each bin by the total number of local Hurst exponents, `sum(freq)` (see **Figure 13B**). The multifractal spectrum `Dh` are computed by first define `Ph_norm` by normalizing `Ph` to the maximum probability `max(Ph)` and then divide `log(Ph_norm)` by `−log(mean(scale))` (cf. Struzik, 2000; Scafetta et al., 2003). The multifractal spectrum `Dh` are therefore directly related to the distribution `Ph` of the local fractal structure of the time series. The distribution `Ph` is the same for the local scale invariant structure of the time series as the conventional probability distribution are for the local amplitudes of the time series. The present state of the physiological system is connected to both past and future states that influence the local scale invariant structure of time series. Thus, distribution `Ph` and the multifractal spectrum `Dh` of biomedical time series might reflect important properties of the self-regulation of physiological processes.

THE BEST PRACTICE OF MULTIFRACTAL DETRENDED FLUCTUATION ANALYSIS

The MFDFA introduced piece-by-piece in Section "Multifractal Detrended Fluctuation Analysis in Matlab" can be combined into two Matlab function `MFDFA1` and `MFDFA2`, respectively:

Matlab functions for MFDFA
Matlab code 8 to 11:

```
[Hq,tq,hq,Dq,Fq]=MFDFA1(signal,scale,q,m,Fig);
```

Matlab code 12 to 14:

```
[Ht,Htbin,Ph,Dh]=MFDFA2(signal,scale,m,Fig);
```

Type `help MDFA1` or `help MFDFA2` in the Matlab command window to access the definition of the input and output variables. The help functions provide examples for the employment of `MFDFA1` and `MFDFA2` to time series.

The main aim of Section “The Best Practice of Multifractal Detrended Fluctuation Analysis” is to guide the application of `MFDFA1` and `MFDFA2` to biomedical time series. In Section “*Multifractal Detrended Fluctuation Analysis in Matlab*” the readers has gained insight into the construction of `MFDFA1` and `MFDFA2` and this insight will help them to avoid potential pitfalls in the application of `MFDFA1` and `MFDFA2`. The best practice of `MFDFA1` and `MFDFA2` has several steps. First, the structure of biomedical time series must be similar to noise before employing `MFDFA1` and `MFDFA2` (see blue traces in **Figure 1**). Section “*Random Walk or Noise Like Time Series?*” introduces conversions to make the biomedical time series similar to a noise like time series. Secondly, the local fluctuations within the biomedical time series cannot be close to zero. Section “*Local Fluctuations Close to Zero?*” discusses possible origins for local fluctuations close to zero and possible solutions to this problem. Thirdly, the biomedical time series must be scale invariant within the predefined range of scales. Section “*Is the Time Series Scale Invariant?*”3 discusses the general assumption of a scale invariant time series as input in `MFDFA1` and `MFDFA2`. Fourth, the input parameters `scale`, `q`, and `m` in `MFDFA1` and `MFDFA2` must be sufficiently defined for each biomedical time series. Section “*How to Set the Input Parameters Scale, q, and m in MFDFA1 and MFDFA2*” introduces guidelines for the optimal parameter setting. Finally, Section “*Other Multifractal Analysis*” lists other multifractal analyses where results can be compared to results from `MFDFA1` and `MFDFA2`.

RANDOM WALK OR NOISE LIKE TIME SERIES?

`MFDFA1` and `MFDFA2` have the best performance when `signal` are a noise like time series. However, it can be difficult according to **Figure 6** to visually differentiate between random walk and noise like time series. A possible solution suggested by Eke et al. (2002) is to run a monofractal DFA (i.e., Matlab code 5 and 6) before running `MFDFA1` and `MFDFA2`. The time series are noise like if Hurst exponent `H` is between 0.2 and 0.8. In this case, `MFDFA1` and `MFDFA2` can be employed directly without transformation of the time series. However, the time series are random walk like when `H` is between 1.2 and 1.8. In these cases, the time series should either be differentiated before entering the `MFDFA1` or `MFDFA2` or the conversion to random walk in the first line of Matlab code 8 and 12 should be eliminated. If the time series are random walk like + 1 should be added to the output variables `Hq`, `hq`, and `tq` from `MFDFA1` and `Ht` and `Htbin` from `MFDFA2`. **Table 1** summarize the categories of the Hurst exponent estimated by a monofractal DFA with corresponding conversion of the biomedical time series that should be performed before entering it into `MFDFA1` and `MFDFA2`.

Table 1 | Conversions of the biomedical time series `X` and adjustment of `Hq` and `Ht`.

Hurst exponent (H)	Conversion	Adjustment of `Hq` and `Ht`
<0.2	`signal=cumsum(X-mean(X))`	−1
0.2–0.8	No conversion	0
0.8–1.2	No conversion	0
1.2–1.8	`signal=diff(X)`	+1
>1.8	`signal=diff(diff(X))`	+2

LOCAL FLUCTUATIONS CLOSE TO ZERO?

The local fluctuation in the time series is defined as a local `RMS` within both `MFDFA1` and `MFDFA2`. Large error appears in the multifractal spectrum when `RMS` is close to zero because both `log2(Fq)` for negative *q*’s in Matlab code 8 and `log2(RMSt)` in Matlab code 12 becomes infinitely small (i.e., `-inf` in Matlab). Extreme large `Hq` will be present for negative *q*’s as output from `MFDFA1`. Equivalently, extreme large outliers in `Ht` will be present as output from `MFDFA2`. Consequently, local `RMS` close to zero will lead to large right tails for the multifractal spectrum. The problem of segments with `RMS` close to zero can be solved by eliminating `RMS` below a certain threshold (`eps`). The threshold `eps` can be set to the precision of the measurement device that is recording the biomedical time series. As an example, the measurement of the inter-beat intervals of the human heart is measured as the time interval between R-peaks in ECG and has a typical precision of 1 millisecond. Thus, `RMS` below 1 millisecond can be eliminated from further analysis when `MFDFA1` and `MFDFA2` are employed to series of inter-beat intervals. Elimination of local fluctuations below the measurement error is possible in `MFDFA1` by setting `eps` = 1 and `RMS{ns}(RMS < eps) = []` in Matlab code 8.

There are two main reasons why the local fluctuation `RMS` becomes zero in segments with small sample sizes. First, the polynomial trend `fit` of the time series can be overfitted in segments with small sample sizes (i.e., small scale). An overfitted trend will be similar to the time series and cause the residual fluctuations, `RMS`, to be close to zero. The sample size of the smallest segment (i.e., scale) should therefore be much larger than the polynomial order `m` to prevent an overfitted trend. Secondly, the biomedical time series might be smooth with little apparent variation and therefore similar to the polynomial trend even for low order `m`. In these cases, the value of the smallest scales should be raised and the scale invariance checked carefully (see “*Is the Time Series Scale Invariant?*” below).

IS THE TIME SERIES SCALE INVARIANT?

The application of both Matlab function `MFDFA1` and `MFDFA2` assumes that the biomedical time series are scale invariant. This means that `plot(log2(scale),log2(Fq))` yield a linear relationship between `log2(scale)` and `log2(Fq)` (see **Figure 8**)., The *q*-order Hurst exponent `Hq` should not be estimated by a linear regression if the relationship between `log2(scale)` and `log2(Fq)` is curved or S-shaped. Consequently, the first output from `MFDFA1` to be visually checked should be `plot(log2(scale),log2(Fq))`. Non-linear relation in this plot might arise from several reasons. First, an insufficient order `m` for the polynomial detrending will yield a non-linear relationship between `log2(scale)` and `log2(Fq)` for scale invariant time series with a trend. The solution is to run `MFDFA1` or `MFDFA2` multiple times with different `m` and compare their `plot(log2(scale),log2(Fq)`. Secondly, local fluctuations `RMS` close to zero for small scales would yield a non-linear dip in lower end of `plot(log2(scale),log2(Fq))`. This dip can be prevented by elimination of `RMS` below the measurement error suggested in Section "*Local Fluctuations Close to Zero?*" or by choosing a larger minimum input scale. Finally and most importantly, a non-linear relationship in `plot(log2(scale),log2(Fq))` might originate from the phenomenon recorded in the biomedical time series. As an example, respiratory frequency creates distinct oscillations in the fast fluctuations of the heart rate variability (Stein and Kleiger, 1999) and cause the scale invariance to break down at the smallest scales. Another example is postural sway in humans where the variation of the center of pressure has two distinct scaling regions thought to represent two distinct modes for human balance control (Collins and De Luca, 1993). One way to detect the sub-regions with scale invariance is to look for periods with approximately constant `log2(Fq(q==1,:)./scale)` in `plot(log2(scale),log2(Fq(q==1,:)./scale))` within the entire scaling range (cf. Gao et al., 2006). The scales where `log2(Fq(q==1,:)./scale)` are no longer constant indicates the segment sizes above and below which the local fluctuations (i.e., RMS) are no longer scale invariant. These points will in many cases have phenomenological explanations and should not be ignored.

HOW TO SET THE INPUT PARAMETERS scale, q, AND m IN MFDFA1 AND MFDFA2

The Matlab functions `MFDFA1` and `MFDFA2` have input parameters `scale`, `q` and `m`. The estimation of the multifractal spectra is dependent on these parameter settings. The rest of this section gives guidelines to the parameter settings in `MFDFA1` and `MFDFA2`:

Scale

The input parameters `scale` is the multiple segment sizes for the computation of local fluctuation `RMS` in Matlab code 8 and 12. A minimum and maximum sample size of the segments [i.e., `min(scale)` and `max(scale)` in Matlab] has to be chosen to construct the set of scales used in `MFDFA1` and `MFDFA2`. Both statistical and phenomenological arguments exist on how to choose the minimum and maximum segment size. The statistical argument is to choose minimum and maximum segment sizes that provide a numerical stable estimation of `RMS` and `Fq` in Matlab code 8 and 12. The minimum segment sample size should be large enough to prevent error in the computation of local fluctuation `RMS`. The minimum segment size larger than 10 samples is a "rule of tumb" for the computation of `RMS`. Furthermore, the minimum sample size must be considerably larger than the polynomial order `m` to prevent overfitting of polynomial trend (see "*Local Fluctuations Close to Zero?*" above). Thus, minimum segment size of 10 samples might be too small for large trend order `m` (Kantelhardt et al., 2002). In `MFDFA1`, the maximum segment size should be small enough to provide a sufficient number of segments in the computation of `Fq` in Matlab code 8. A maximum segment size below 1/10 of the sample size of the time series will provide at least 10 segments in the computation of `Fq` in Matlab code 8. Furthermore, it's favorable to have a equal spacing between scales when they are represented in `plot(log2(scale),log2(Fq))` to obtain a optimal performance of the linear regression that estimates q-order Hurst exponent `Hq`. Equal spacing between `log2(scale)` is provided by Matlab code 15 below:

Matlab code 15:

```
scmin=16;
scmax=1024;
scres=19;
exponents=linspace(log2(scmin),log2(scmax),scres);
scale=round(2.^exponents);
```

Matlab code 15 is employed before running `MFDFA1` where the minimum segment size, `scmin`, maximum segment size, `scmax`, and the total number of segment sizes, `scres`, are predefined. The segment sizes (i.e., `scale`) in `MFDFA2` should be small in order to provide a stable estimation of the probability distribution `Ph` and, consequently, the multifractal spectrum `Dh` (Scafetta et al., 2003). The local Hurst exponent `Ht` for large scale will have a smooth and slow varying dynamics that are not well described by a probability distribution `Ph`. Thus, a small scaling range like `scale= [7,9,11,13,15,17]` used in Matlab code 12 are preferable in `MFDFA2`. However, the reader should notice that the small segment sizes (i.e., `scale`) in `MFDFA2` come at the expense of a less precise estimation of the local fluctuation `RMS`. The imprecise estimation of `RMS` can be seen as measurement noise of the local Hurst exponent `Ht` present for the `monofractal` and `whitenoise` time series in **Figure 13A**. The measurement noise in `Ht` is represented as a distribution `Ph` and multifractal spectrum `Dh` for `monofractal` and `whitenoise` time series with a non-zero width (see **Figures 13B,C**).

Phenomenological argumentations are important for the choice of minimum and maximum segment sizes within the boundaries that provide numerical stable computations. For example, it is unlikely that the movement of the center of mass is faster than 10 Hz during postural sway. If ground reaction force is sampled at 200 Hz by a force plate then the minimum segment size should be larger than 200/10 Hz = 20 samples. Another example is to exclude the smallest segment sizes in heart rate variability known to be dominated by oscillations due to the respiratory frequency. Furthermore, heart rate variability operates with several ranges of scales (i.e., fluctuations with high frequency, low frequency, very low frequency, ultra low frequency) that are suggested to be influenced by different mechanisms (e.g., respiratory frequency, baroceptive responses, circadian rhythm; e.g., Stein and Kleiger, 1999). Three scale invariant sub-bands are also found in EEG signal where the Hurst exponent are able to separate between healthy subjects and epileptic subjects (Gao et al., 2011). Thus, `MFDFA1` can be employed to sub-bands of the scaling range in these phenomena (e.g., Makowiec et al., 2011).

q-order

The input parameter `q` in `MFDFA1` decides the *q*-order weighing of the local fluctuation `RMS` in Matlab code 8. The *q*-orders should consist of both positive and negative *q*'s in order to weight the periods with large and small variation in a time series. The precision of the computation of the *q*-order Hurst exponent `Hq` decreases with increasing negative and positive *q*-orders. This imprecision are explained by the result in **Figure 7**. The single segment with the smallest and largest variation `RMS` will tower up as a single skyscraper by increasing negative and positive *q*-orders, respectively, and completely dominate the scaling function `Fq` (i.e., overall *q*-order RMS in Matlab code 7). The domination of the single segments with the smallest and largest variation destabilizes `Fq` and leads to an increasing spread around the regression lines of `Fq` (see $q = 3$ and -3 in **Figure 8A**). The choice of *q*-orders should therefore avoid large negative and positive values because they inflict larger numerical errors in the tails of the multifractal spectrum. The stability of the computation of the multifractal spectrum is also dependent on the differences between the segments of largest and smallest variation. Time series that have large multifractal spectrum width will have large differences between the segments with the smallest and largest variation and, consequently, destabilize the computation of `Fq` at smaller negative and positive *q*-orders (compare multifractal scaling in **Figure 8A** with the monofractal scaling in **Figure 8B**). A sufficient choice of *q*-orders will be between – 5 and 5 for most biomedical time series (Lashermes et al., 2004). The destabilization of the `Fq` at large negative and positive *q*-orders is also dependent on the sample size of the time series. Time series with large sample size will have multiple segments with extremely large and small variation whereas time series with moderate sample size will only have a single segment. Multiple segments of large and small variation would stabilize the computation of `Fq` for large negative and positive *q*-orders. There exists no consensus for the definition of a "too small" sample sizes for multifractal analyses, but the reader should interpret the result with caution when `MFDFA1` and `MFDFA2` are employed to time series with less than 1000 samples.

Trend order m

In both `MFDFA1` and `MFDFA2`, the local fluctuation `RMS` is computed around a polynomial trend where its shape is defined by the order `m`. A higher order `m` yield a more complex shape of the trend, but might lead to overfitting for time series within small segment sizes as discussed in Section "*Local Fluctuations Close to Zero*?" above. Thus, `m` = 1–3 are probably a sufficient choice when the smallest segment sizes contains 10–20 samples. Most studies that employ DFA to biomedical time series do not report the details of the polynomial detrending. Still, the multifractal spectrum for multiple orders `m` should be compare to ensure that the multifractal spectrum are not influenced by non-stationary trends in the time series. The trends present in biomedical signals do not have to be of a polynomial shape but might have oscillatory or ramp-like shapes. Both `MFDFA1` and `MFDFA2` can be extended to include more adaptive detrending procedures like wavelet decomposition (Manimaran et al., 2009), moving average (Carbone et al., 2004), and empirical mode decomposition (Qian et al., 2009). Furthermore, an adaptive fractal analysis is shown to perform better than the DFA with polynomial detrending when employed to biomedical time series with strong trends (Gao et al., 2011). Extensions and modification of the detrending procedure in `MFDFA1` and `MFDFA2` is preferable if MFDFA are employed to biomedical time series with strong trends. Matlab functions for MFDFA with other detrending procedures are available at www.ntnu.edu/inm/geri/software.

OTHER MULTIFRACTAL ANALYSIS

The basic component of both `MFDFA1` and `MFDFA2` are the local fluctuation, `RMS`. Statistical parameters other than `RMS` can be used to define the local fluctuation in a time series. In multifractal analyses based on wavelet transformations, the local fluctuation is defined as the convolution product between the time series and a waveform fitted within local segments of the time series (cf. Daubechies, 1992; Mallat, 1999). The results from analyses called wavelet transformation modulus maxima (Muzy et al., 1991), multifractal analysis with wavelet leaders (Jaffard et al., 2006; Wendt, 2008), and gradient modulus wavelet projection (Turiel et al., 2006) can therefore be directly compared with the results from `MFDFA1` and `MFDFA2`. In an entropy-based estimation of the multifractal spectrum, the local fluctuation is defined as the sum of the time series within the local segment relative to the total sum of the entire time series (Chhabra and Jensen, 1989). This method uses a *q*-order entropy function instead of a *q*-order RMS and estimates `hq` and `Dq`, directly, as the regression slope of the q-order entropy functions. The MFDFA has been shown to perform as well as or better than these multifractal analyses (Kantelhardt et al., 2002; Oświęcimka et al., 2006; Serrano and Figliola, 2009; Huang et al., 2011). However, extensions of detrending procedure in `MFDFA1` and `MFDFA2` should be considered when the biomedical time series contains strong oscillatory or ramp-like trends (Hu et al., 2009; Huang et al., 2011).

SUMMARY

The multifractal spectrum reflects the variation in the fractal structure of the biomedical time series. The multifractal structure of the inter-beat intervals can identify pathological conditions of the human heart (e.g., Ivanov et al., 1999; Wang et al., 2007). The multifractal structure in neural activity can separate the activity of different brain areas and thereby guide more precise neurosurgery (Zheng et al., 2005). The present tutorial has introduced a multifractal time series analysis called MFDFA (Kantelhardt et al., 2002). MFDFA is simply based on the computation of local RMS for multiple segment sizes as illustrated in Section "*Multifractal Detrended Fluctuation Analysis in Matlab.*" However, special issues in Section "*The Best Practice of Multifractal Detrended Fluctuation Analysis*" for the best practice of MFDFA are of paramount importance when MFDFA are employed to biomedical time series. First, a monofractal DFA should be employed to ensure that the biomedical time series has a noise like structure. A conversion according to **Table 1** should be made if the time series has not a noise like structure. Secondly, local fluctuation close to zero should be eliminated within MFDFA. Thirdly, the presence of scale invariance should be checked by first running `MFDFA1` over a large scaling range [e.g., `scmin = 10` and `scmax = length(signal)/10` in Matlab] and then plot `log2(scale)` against `log2(Fq)`. If scale invariance is not present for the entire range, then MFDFA1 can be rerun with modified input parameter `scale` for scale invariant sub-bands within the original scaling range. `MFDFA1` should be employed with a `q`-orders between -5 and 5 and for multiple trend orders `m`. `MFDFA2` should be employed instead of `MFDFA1` when the time instant for structural change in the biomedical time series is of importance or when the biomedical time series contain less than 5000 samples.

REFERENCES

Abbound, S., Berenfeld, O., and Sadeh, D. (1991). Simulation of high-resolution QRS complex using ventricular model with a fractal conduction system. Effects of ischemia on high-requency QRS potentials. *Circ. Res.* 68, 1751–1760.

Atupelage, C., Nagahashi, H., Yamaguchi, M., Sakamoto, M., and Hashiguchi, A. (2012). Multifractal feature descriptor for histopathology. *Anal. Cell. Pathol. (Amst.)* 35, 123–126.

Bassingthwaighte, J., Van Beek, J., and King, R. (1990). Fractal branchings: the basis of myocardial flow heterogeneities? *Ann. N. Y. Acad. Sci.* 591, 392–401.

Carbone, A., Castelli, G., and Stanley, H. E. (2004). Time-dependent Hurst exponent in financial time series. *Physica A* 344, 267–271.

Chhabra, A., and Jensen, R. V. (1989). Direct determination of the $f(\alpha)$ singularity spectrum. *Phys. Rev. Lett.* 62, 1327–1330.

Collins, J. J., and De Luca, C. J. (1993). Open-loop and closed-loop control of posture: a random-walk analysis of center-of-pressure trajectories. *Exp. Brain Res.* 95, 308–318.

Daubechies, I. (1992). *Ten Lectures on Wavelets*. Philadelphia, PA: SIAM.

Eke, A., Herman, P., Bassingthwaighte, J. B., Raymond, G. M., Percival, D. B., Cannon, M., Balla, I., and Ikényi, C. (2000). Physiological time series: distinguish fractal noises from motions. *Eur. J. Physiol.* 439, 403–414.

Eke, A., Hermann, P., Kocsis, L., and Kozak, L. R. (2002). Fractal characterization of complexity in temporal physiological signals. *Physiol. Meas.* 23, R1–R38.

Gao, J. B., Hu, J., and Tung, W.-W. (2011). Facilitating joint Chaos and fractal analysis of biosignals through nonlinear adaptive filtering. *PLoS ONE* 6, e24331. doi:10.1371/journal.pone.0024331.

Gao, J. B., Hu, J., Tung, W.-W., Cao, Y. H., Sarshar, N., and Roychowdhury, V. P. (2006). Assessment of long range correlation in time series: how to avoid pitfalls. *Phys. Rev. E Stat. Nonlin. Soft Matter Phys.* 73, 016117.

Goldberger, A. L. (1996). Non-linear dynamics for clinicians: chaos theory, fractals, and complexity at the bedside. *Lancet* 347, 1312–1314.

Goldberger, A. L., Amaral, L. A., Hausdorff, J. M., Ivanov, P. C., Peng, C. K., and Stanley, H. E. (2002). Fractal dynamics in physiology: alterations with disease and aging. *Proc. Natl. Acad. Sci. U.S.A.* 99, 2466–2472.

Hausdorff, J. M. (2007). Gait dynamics, fractals and falls: finding meaning in the stride-to-stride fluctuations of human walking. *Hum. Mov. Sci.* 26, 555–589.

Hu, J., Gao, J. B., and Wang, X. S. (2009). Multifractal analysis of sunspot time series: the effects of the 11-year cycle and Fourier truncation. *J. Stat. Mech.* P02066, 1–20.

Huang, X. Y., Schmitt, F. G., Hermand, J.-P., Gagne, Y., Lu, Z. M., and Liu, Y. L. (2011). Arbitrary-order Hilbert spectral analysis for time series possessing scaling statistics: a comparison study with detrended fluctuation analysis and wavelet leaders. *Phys. Rev. E Stat. Nonlin. Soft Matter Phys.* 84, 016208.

Hurst, H. E. (1951). Long-term storage capacity of reservoirs. *T. Am. Soc. Civ. Eng.* 116, 770–808.

Ihlen, E. A. F., and Vereijken, B. (2010). Interaction dominant dynamics in human cognition: beyond $1/f^{\alpha}$ fluctuations. *J. Exp. Psychol. Gen.* 139, 436–463.

Ivanov, P. C., Amaral, L. A. N., Goldberger, A. L., Havlin, S., Rosenblum, M. G., Struzik, Z., and Stanley, H. (1999). Multifractality in human heartbeat dynamics. *Nature* 399, 461–465.

Jaffard, S., Lashermes, B., and Abry, P. (2006). "Wavelet leaders in multifractal analysis," in *Wavelet Analysis and Applications*, ed. T. Qian, M. I. Vai, and Y. Xu (Basel: Birkhäuser Verlag), 219–264.

Kantelhardt, J. W., Koscielny-Bunde, E., Rego, H. A. A., Havlin, S., and Bunde, A. (2001). Detecting long-range correlation with detrended fluctuation analysis. *Physica A* 295, 441–454.

Kantelhardt, J. W., Zschiegner, S. A., Koscielny-Bunde, E., Havlin, S., Bunde, A., and Stanley, H. E. (2002). Multifractal detrended fluctuation analysis of nonstationary time series. *Physica A* 316, 87–114.

Krenz, G., Linehan, J., and Dawson, C. (1992). A fractal continuum model of the pulmonary arterial tree. *J. Appl. Physiol.* 72 , 2225–2237.

Lashermes, B., Abry, P., and Chainais, P. (2004). New insight in the estimation of scaling exponents. *Int. J. Wavelets Multi.* 2, 497–523.

Lopes, R., and Betrouni, N. (2009). Fractal and multifractal analysis: a review. *Med. Image Anal.* 13, 634-649.

Makowiec, D., Rynkiewicz, A., Wdowczyk-Szulc, J., Zarczyńska-Buchowiecka, M., Galaska, R., and Kryszewski, S. (2011). Aging in autonomic control by multifractal studies of cardiac interbeat intervals in the VLF band. *Physiol. Meas.* 32, 1681–1699.

Mallat, S. (1999). *A Wavelet Tour in Signal Processing*, 2nd Edn. San Diego: Academic Press.

Manimaran, P., Panigrahi, P. K., and Parikh, J. C. (2009). Multiresolution analysis of fluctuations in non-stationary time series through discrete wavelets. *Physica A* 388, 2306–2314.

Muzy, J. F., Bacry, E., and Arneodo, A. (1991). Wavelets and multifractal formalism for singular signals: application to turbulence data. *Phys. Rev. Lett.* 67, 3515–3518.

Oświęcimka, P., Kwapien, J., and Drozdz, S. (2006). Wavelet versus detrended fluctuation analysis of multifractal structures. *Phys. Rev. E Stat. Nonlin. Soft Matter Phys.* 74, 016103.

Parkinson, I., and Fazzalari, N. (1994). Cancellous bone structure analysis using image analysis. *Australas. Phys. Eng. Sci. Med.* 470, 64–70.

Peng, C. K., Havelin, S., Stanley, H. E., and Goldberger, A. L. (1995). Quantification of scaling exponents and crossover phenomena in nonstationary time series. *Chaos* 5, 82–89.

Peng, C. K., Mietus, J. E., Liu, Y., Lee, C., Hausdorff, J. M., Stanley, H. E., Goldberger, A. L., and Lipsitz, L. A. (2002). Quantifying fractal dynamics of human respiration: age and gender effects. *Ann. Biomed. Eng.* 30, 683–692.

Qian, X.-Y., Zhou, W.-X., and Gu, G.-F. (2009). *Modified Detrended Fluctuation Analysis Based on Empirical Mode Decomposition*. Available at: http://arxiv.org/PS_cache/arxiv/pdf/0907/0907.3284v1.pdf

Scafetta, N., Griffin, L., and West, B. J. (2003). Hölder exponent spectra for human gait. *Physica A* 328, 561–583.

Serrano, E., and Figliola, A. (2009). Wavelet leaders: a new method to estimate the multifractal singularity spectra. *Physica A* 388, 2793–2805.

Stein, P., and Kleiger, E. (1999). Insights from the study of the heart rate variability. *Ann. Rev. Med.* 50, 249–261.

Struzik, Z. R. (2000). Determining local singularity strengths and their spectra with the wavelet transform. *Fractals* 8, 163–179.

Suckling, J., Wink, A. M., Bernard, F. A., Barnes, A., and Bullmore, E. (2008). Endogenous multifractal brain dynamics are modulated by age, cholinergic blockade and cognitive performance. *J. Neurosci. Methods* 174, 292–300.

Turiel, A., Perez-Vicente, C. J., and Grazzini, J. (2006). Numerical methods for the estimation of the estimation of the multifractal singularity spectra on sampled data: a comparative study. *J. Comp. Phys.* 216, 362–390.

Wang, G., Huang, H., Xie, H., Wang, Z., and Hu, X. (2007). Multifractal analysis of ventricular fibrillation and ventricular tachycardia. *Med. Eng. Phys.* 29, 375–379.

Weibel, E. R. (1991). Fractal geometry: a design principle for living organisms. *Am. J. Physiol.* 261, 361–369.

Wendt, H. (2008). *Contributions of Wavelet Leaders and Bootstrap to Multifractal Analysis*. Ph.D. thesis, Lyon University, Lyon.

Zheng, Y., Gao, J. B., Sanchez, J. C., Principe, J. C., and Okun, M. S. (2005). Multiplicative multifractal modeling and discrimination of human neuronal activity. *Phys. Lett. A* 344, 253–264.

Conflict of Interest Statement: The author declares that the research was conducted in the absence of any commercial or financial relationships that could be construed as a potential conflict of interest.

Received: 15 February 2012; accepted: 26 April 2012; published online: 04 June 2012.

Citation: Ihlen EAF (2012) Introduction to multifractal detrended fluctuation analysis in Matlab. Front. Physio. ***3****:141. doi: 10.3389/fphys.2012.00141*

This article was submitted to Frontiers in Fractal Physiology, a specialty of Frontiers in Physiology.

frontiers in
PHYSIOLOGY

METHODS ARTICLE
published: 01 October 2012
doi: 10.3389/fphys.2012.00382

Recurrence quantification of fractal structures

Charles L. Webber Jr.*

Department of Cell and Molecular Physiology, Stritch School of Medicine, Loyola University Chicago Health Sciences Division, Maywood, IL, USA

Edited by:
Michael A. Riley, University of Cincinnati, USA

Reviewed by:
Rick Dale, University of California Merced, USA
Adam Kiefer, Brown University, USA

***Correspondence:**
Charles L. Webber Jr., Department of Cell and Molecular Physiology, Stritch School of Medicine, Loyola University Chicago Health Sciences Division, 2160 South First Avenue, Maywood, IL 60153-3328, USA.
e-mail: cwebber@lumc.edu

By definition, fractal structures possess recurrent patterns. At different levels repeating patterns can be visualized at higher magnifications. The purpose of this chapter is three-fold. First, general characteristics of dynamical systems are addressed from a theoretical mathematical perspective. Second, qualitative and quantitative recurrence analyses are reviewed in brief, but the reader is directed to other sources for explicit details. Third, example mathematical systems that generate strange attractors are explicitly defined, giving the reader the ability to reproduce the rich dynamics of continuous chaotic flows or discrete chaotic iterations. The challenge is then posited for the reader to study for themselves the recurrent structuring of these different dynamics. With a firm appreciation of the power of recurrence analysis, the reader will be prepared to turn their sights on real-world systems (physiological, psychological, mechanical, etc.).

Keywords: dynamical systems, recurrence analysis, mathematical fractals, homeodynamics, dimensionality

DYNAMICAL SYSTEMS IN *N*-DIMENSIONAL SPACE

HOMEOSTASIS VERSUS HOMEODYNAMICS

Systems, mathematical and physical, are each framed by a set of deterministic rules defined by the interaction of multiple components (variables) as coupled by adjustable constants (parameters) and scaled by fixed constants. To the extent that such systems are time-varying, they are posited to be dynamical in nature as opposed to static. Many dynamical mathematical systems are explicit, exact, noise-free, and time-reversible. But real-world systems from physics, chemistry, and biology are at best ill-defined for they exist in noisy environments and have interactions with other neighborhood systems (changing coupling strengths). The mathematical description of real-world systems is often approximate and incomplete. The presence of noise itself has the ability to shape, even tune, dynamical systems such as in the case of stochastic resonance (Wiesenfeld and Moss, 1995).

A closed system can be conceptually portrayed as a bounded area embedded within a surrounding environment as illustrated in **Figure 1**. Although the simple systems are represented in two dimensions (flat), no dimensionality is implied or excluded. If the system is rigid the boundary is fixed and inflexible (solid line), but if the system is plastic the boundary (dashed line) can move and adapt to the surrounding environment. In this sense, experience teaches that the first system is more traditionally mathematical whereas the second system is more intrinsically biological. Flexibility and adaptability of the boundary determines system survival and success in harsh environments.

From the field of physiology came the very helpful concept of system homeostasis. The foundation of homeostasis stems back to Claude Bernard (1813–1878) and his concept of the *milieu intérieur* of the extracellular environment of multicellular living systems (Gross, 1998). However, it was Walter Cannon (1871–1945) who coined the term *homeostasis* (Cannon, 1929) which has since been elevated to the status of scientific law as it were. Principles of homeostasis assume that systems of the body are constrained within certain tight bounds whereby system variables are attracted to so-called constant or static values compatible with life. Good, if not obvious, examples include the control of arterial plasma pH at 7.40; normal body temperature near 37˚C; and mean blood pressure around 100 mm Hg to name a few.

Homeostasis implies the presence of feedback regulation of dynamical systems affected by sensors that report back to the control center of the system. A half century ago engineering sciences started impacting physiological thinking, so much so that the concept of set points was *in vogue* for living organisms. Taken to its extreme, however, homeostasis can become a straight jacket to dynamical systems. In this context, the poster child for homeostasis might be the cadaver state where all movement is disallowed! Indeed, many living physiological systems seem to be missing an error signal (Somjen, 1992), and concepts of homeostasis and Gaussian statistics may be barriers to understanding natural variability (West, 2010).

With much deeper appreciation for the rich dynamics afforded by dynamical systems, the idea of homeodynamics is much more satisfying. Homeodynamics sets trajectories free from the overbearing constraints of homeostasis (Lloyd et al., 2001). These two concepts can be simply contrasted by considering a simple physics metaphor. Think of a system represented by a marble fallen into a hole in the center of a circular plate. With tilting motion applied to the plate (noise), the marble remains locked in its fixed position, unless the disturbance becomes too great. This is rigid homeostasis where the marble is entrapped on a strong attractor. Now think of a second system also consisting of a marble on a plate, but this plate has no center hole. As the plate is tilted motion is imparted to the marble. As long as the marble remains on the plate and moves freely over its domain, the system is stable. This is homeodynamics. Only when the tilt angle becomes too steep or the marble velocity becomes too fast does the system fail.

TRANSIENTS AND NON-STATIONARITIES

For any system to be termed dynamic, it must show motions in time or contrasts in space. The state of the system can be considered

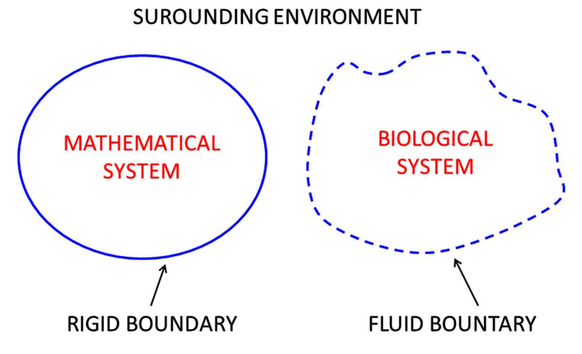

FIGURE 1 | Closed systems are distinguished from their surrounding environments by definitive boundaries, firm (left) or fuzzy (right).

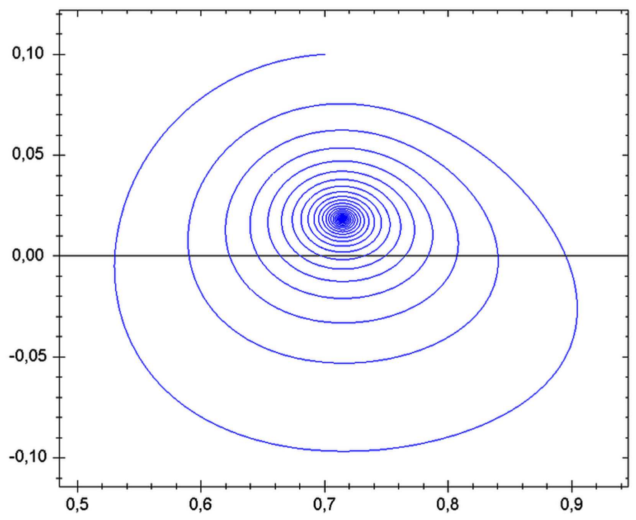

FIGURE 2 | Pathway of a transient trajectory of a dynamical system *enroute* to its stable singularity. Public source: http://en.wikipedia.org/wiki/Phase_space

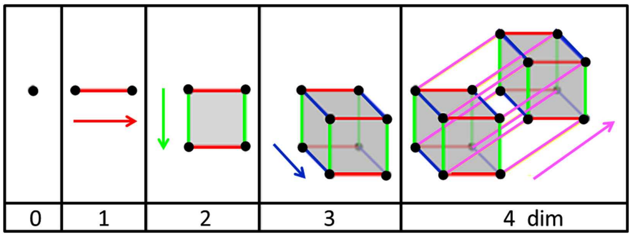

FIGURE 3 | Representation of *N* dimensions arising from points moving in orthogonal directions. Adapted from public source: http://en.wikipedia.org/wiki/Dimension

as either homeostatic or homeodynamic. Interestingly, homeostatic systems can have motions in the sense that it moves toward the well of attraction. Similar to the phase-space diagram of **Figure 2**, a marble swirling around a stationary funnel cone will soon come to rest in the smaller-diameter funnel spout where it will remain at its fixed point. The pathway traversed by the marble is called the trajectory and the destination is called the basin of attraction. Likewise, magnets will hold iron filings in complicated yet rigid patterns within multiple basins of attraction.

From the perspective of homeodynamics, however, trajectories can also be seen as non-stationarities operating over a field containing basins of attraction always changing. Living systems, especially, have weak and variable basins of attraction meaning that the dynamic is always on the move, never resting *per se*, as the wells of attraction rise and fall. This would be like the complex motions of a marble rolling over a large rubber sheet which was continually subjected to topological contour changes.

DIMENSIONALITY AND RIEMANN SPACE

Examine **Figure 3** from left to right. If one works with points (very, very small marbles), a single point is mathematically defined as occupying a dimension of zero. As soon as a second point is introduced to the system, it must be separated by a finite distance from the first point. The line connecting the two points forms a line which resides in a dimension of 1. Sliding the horizontal line vertically defines a square (or rectangle) which lives in a two-dimensional plane (flat or curved). Shifting the square forms a cube or rectangular box which exists in three-dimensional space. Movement of the cube perpendicular to the three orthogonal axes forms a hypercube or tesseract which cannot be drawn because it exits in four-dimensional space. In this type of metric space or Riemann space, the dimensions are integers with no upper limit (0, 1, 2, 3, 4, etc.). The higher the dimension the more complex is the system that can be represented. Note that a three-dimensional system moving in time (a dimension itself) requires four variables to locate the system or object.

One definition of system complexity relates to the number of interacting variables present: the more the variables, the higher the complexity. And the higher the complexity, the greater must be the dimensionality of the system. Thus systems have dimensions that can be captured by embedding methods. For example, one can compute the distance between sub-states of the system by defining the Euclidean distance between vectors of the system. The trick is to be sure that the system is being studied in the dimension in which it resides, less it be under-represented topologically as it were. To study a three-dimensional ball in two-dimensions, a plane can cut through the object and results in a circle of varying radius depending upon where the slice is made. Conversely, to study a three-dimensional ball in four-dimensions adds no new information, but is merely a waste of computational effort. System information is maximized in the dimension in which the system lives.

There are various ways to estimate the dimension of a dynamical system, but there are two cautions to remember. First, measurement of dimensionality depends upon the system being in some kind of homeostatic steady state. This is practically realized for mathematical systems, but not necessarily biological systems. Second, the algorithms employed for the estimation of dimensionality, lose their efficiency as fast as the dimension being estimated increases. This is known supposedly as "the curse of dimensionality" in which only the lower dimensions can be measured with confidence (Parker and Chua, 1989). Third, the presence of real-world noise inflates the dimension being measured. This is not a problem for mathematical systems in which there is no noise (save digital noise), but the more the noise present the greater the real dimension of the system gets inflated. The reason for this is that no dimension exists that can completely capture the full dynamic of pure stochastic noise.

With the introduction of low-dimensional chaos (Lorenz, 1963) and fractal structures (Mandelbrot, 1983) it became fashionable to hypothesize that the complexity of biological systems could be explained by few-variable systems operating in low dimensions. But since the number of quasi-steady state experimental points required to estimate the system dimension is 10^dimension, dimensions greater than six are impractical to measure and inaccurate to report. But one surprise from fractal structures was the discovery that dimensions need not be integers. Rather dimensions can be fractions (non-integers; Grassberger and Procaccia, 1983).

DIFFERENTIAL FLOWS AND DIFFERENCE MAPS

Time-varying (or space varying) systems in the real-world are smooth and continuous insofar that the distance from point to point is vanishingly small. Electrical analog systems best represent such continuous and smooth signals as measured as AC voltage waves from wall sockets (American: 110 V sinusoid at 60 Hz). But we live in an artificial digital world where reality is discretized into steps that are significantly larger than the vanishingly small limit in calculus. The higher the digitization frequency, the higher is the fidelity of reproduction. But magnification (amplification) of these signals always reveals the tell-tale steps of these artificial reproductions of reality.

These comments are made from a purist standpoint. However, it seems fair to declare a digitized system as continuous if (and only if) the signal is sampled at least 10 times faster than the fastest frequency within that signal. Here these quasi-smooth signals are considered to be flows, dynamical flows of the combined system variables interacting. For example, as a fly navigates a room (true continuous flow), high-frequency stroboscopic "stopping" of the motion faithfully captures the trajectory (fictive continuous flow). There is a caution here. The fair assumption above is disrupted when surprise events occur within the dynamic. No theory of maximal digitization frequency will suffice and the sampling theorem of Henry Nyquist (1889–1976) is violated (Nyquist, 1924).

Another way of describing a system is to divide the continuous flow into intervals. This is particularly easy if the signal possess a stereotypic marker which can serve as triggers to end one interval and start another. Thus, interspike intervals (ISIs) are easily computed from neuronal spike trains. Likewise, R-wave to R-wave intervals (RRIs) are easily computed from the PQRST flows of the English electrocardiogram (ECG) or German *elektrokardiogramm* (EKG). In general, whether or not there are distinctive features in the time series, difference maps can still be generated by defining a barrier that is one dimension below that of the system. Mathematically these difference maps are called Poincaré sections (Rasband, 1990) named after the French mathematician Henri Poincaré (1854–1912) who contributed so much to non-linear dynamics (before the invention of the computer). **Figure 4** illustrates the formation a two-dimensional Poincaré section from a smooth and continuous three-dimensional flow. Every time the dynamical flow crosses the two-dimensional surface (S), difference points are plotted on the surface. If the points in the Poincaré section form patterns, there are deterministic rules in place governing (steering) the dynamic. In this case, the next point $P(i+1)$ becomes a function of the previous point $P(i)$. Such maps can diagnose simple periodicities (single point), multi-stable systems (multiple points), and chaotic trajectories (fractal points). However, if the flow is stochastic (white noise) the Poincaré section will display points in random patterns without structure, implying that no determinist rules are in place.

TERMINAL DYNAMICS

Many smooth and continuous mathematical functions are continuously differentiable and possess unique solutions of the Lipschitz type named after German mathematician, Rudolf Lipschitz (1832–1903). Other smooth and continuous mathematical functions are not continuously differentiable, have multiple solutions of the non-Lipschitz type, and are strictly non-deterministic and non-reversible in time (or space). Possible trajectories of one non-deterministic system is schematized in **Figure 5**. Starting at time zero (t_0), $f(x)$ is greater than 0 and the trajectory decays toward the horizontal axis. When the trajectory reaches this axis (t_e), instead of continuing through a single point to the region of negative values (as a Lipschitz type system would do), it is extinguished (halts). Mathematically, when $f(x) = 0$ all dynamic motion ceases and the system is rendered non-Lipschitzian. The only way for the system to be kicked back into action is for infinitesimal noise to jitter the system off of this singularity, forcing $f(x) \neq 0$. Since this dynamical action restart can happen at any time following the start of

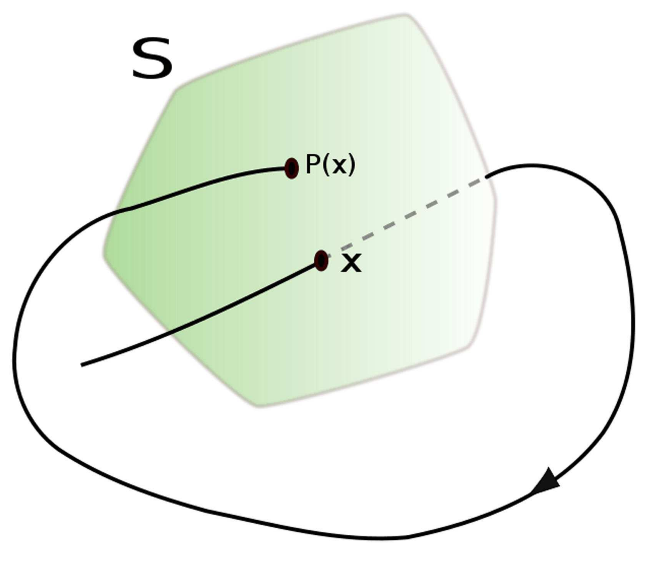

FIGURE 4 | Example of how a Poincaré section reduces the dimensionality of a dynamical system. Public source: http://en.wikipedia.org/wiki/File:Poincare_map.svg

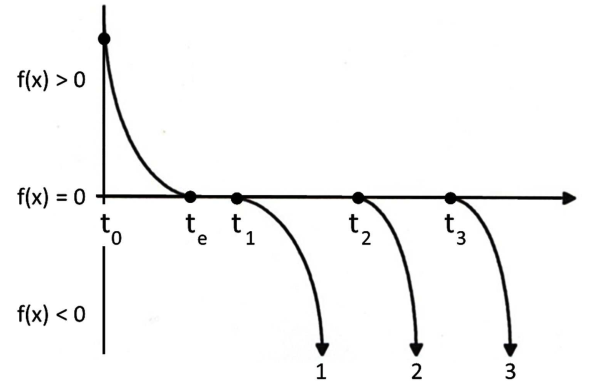

FIGURE 5 | Schematic of terminal dynamic with multiple trajectory selections. Adapted from Figure 24.8 of Zbilut et al. (1996).

the singularity, the solutions to the equation become numerous and variable, initiating new trajectories (1, 2, or 3) where f(x) is non-zero at different times (t_1, t_2, t_3, respectively). This trajectory selection is unique, flows with the direction of time, and is non-reversible through the singularity.

There are many real-world examples of non-deterministic systems which possess alternating deterministic trajectories and stochastic pauses. For example: jet aircraft land and pause at the gate before taking off again; pauses interrupt arm extensions and flexions; flatline isopotentials are recorded in the normal ECG between T-wave repolarizations and P-wave excitations; and the active running of ants is punctuated by stationary pauses. To best way to model such systems would be to describe the dynamical trajectories with differential equations interspersed with realistic (and stochastic) pauses between trajectories (system stop or pause).

RECURRENCE PLOTS

AUTO RECURRENCES (IMPLEMENTED BY PROGRAM RQD)

Recurrence is a theoretical mathematical concept that has practical utility in the real-world. Events can recur in time; places can be revised in space. For starters, take a time series, any digitized time series, which is by definition a linear vector of N points. Form two identical copies of this vector calling the first V_i and the second V_j. Compare each point in vector V_i with every point in vector V_j and compute the distance between them by taking the absolute differences between paired scalars according to this formula.

$$\left[Dij\right] = \left|\left(Di - Dj\right)\right| \text{ for } i = 1 \text{ to } N \text{and } j = 1 \text{ to } N \qquad (1)$$

This calculation will generate an $[N_i, N_j]$ square matrix called the distance matrix with $N \times N$ elements. Plotting the distances at each V_i, V_j coordinate produces an unthresholded recurrence plot which can be color coded. A ubiquitous line of identity (LOI) forms a central diagonal where i and j scalars are always identical (distances of 0). Likewise, the distances are exactly symmetrical to around this LOI since the distance from point i to point j is the necessarily the same as the distance from point j to point i. **Figure 6** (left) plots an unthresholded (global) recurrence plot that is color coded by distance (from blue = 0–10% to red = 90–100%). It can be noted that the dark blue rectangles in the recurrence plot correspond to the nadirs in the sun spot activities, but that the red recurrent points line up with the largest peak in sun spot activity.

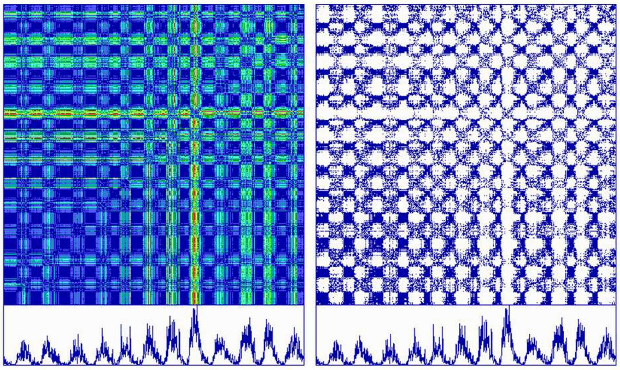

FIGURE 6 | Global (left) and local (right) recurrence plots of monthly sun spot activity from May 1874 to September 2005 (131 years, 5 months) obtained from the Royal Greenwich Observatory. Twelve cycles of 11 years each are duplicated as time series beneath the recurrence plots. With a delay of 1 and embedding dimension of 1, the distance matrices are scaled from 0 to 100%. With the threshold set to 100% (left) the entire matrix is plotted in 10 different colors representing 10% steps (saturated, unthresholded recurrence plot). With the threshold set to 1% (right) only a fraction of the first step is plotted in a single color (sparse, thresholded recurrence plot).

To generate a sparse recurrence matrix, the distance matrix must be thresholded. The formula for the recurrence matrix is given below where the epsilon threshold (ε) is some fraction of the maximum distance in the distance matrix and theta (Θ) is the Heaviside function that replaces the distance matrix with either 1 for distances below threshold (close or recurrent points) or 0 for distances above threshold (distant or non-recurrent points).

$$Ri,j := \Theta\left(\varepsilon_i - \left|x_i - x_j\right|\right), \quad i,j = 1, \ldots N \qquad (2)$$

Distance matrix thresholding is demonstrated in **Figure 6** (right) in which epsilon is set to 10% of the maximum distance. In this case, only the dark blue recurrent points are plotted, leaving the remainder of the area as white space (above threshold). Thresholding converts the saturated global recurrence plot (multicolored, 100% saturated) into a sparse recurrence plot (single colored, 5.835% saturated).

Typical recurrence plots from very different dynamical systems are illustrated in **Figure 7**. The fundamental observation is that parallel trajectories score as diagonal lines parallel to the central LOI. Periodic processes score with very long diagonals (panel 1) whereas deterministic chaotic processes score with short diagonals (panel 2). Auto-regressive processes have parallel trajectories that stack vertically, forming block patterns (panel 3). However, in the case of stochastic systems where each point in the time series is time-independent from all other points, recurrence plots lose these diagonal line structures (panel 4). Thus the key to discovering determinist rules in dynamical systems is to look for diagonal

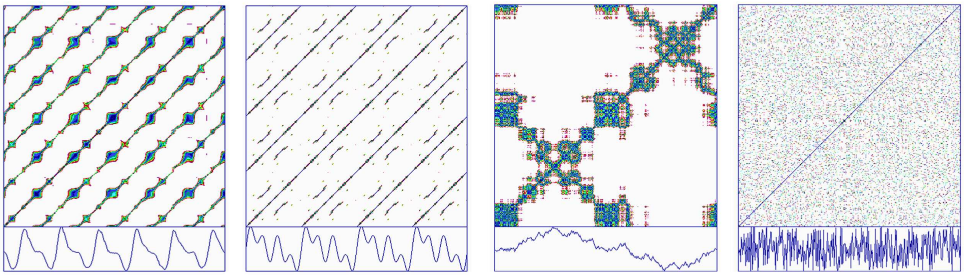

FIGURE 7 | Recurrence plots (top) of time series (bottom) including (left to right): tracheal pressure (rodent); pink noise (auto-regressive process of integrated white noise); Hénon chaotic attractor (*x* variable); white noise (caesium^{137} beta decay).

line structures, the length, number, positioning, etc. which convey insight into the organization of the dynamics.

The examples given above discuss (for simplicity) the recurrences between points. However, by implementing embedding procedures with lag delays between embedded points, it is possible to cast the dynamic into higher dimensional space. Typically, the Euclidean norm is used to compute vectors and then the Euclidean distances between all possible vectors are computed. If the distances fall below a threshold cutoff (epsilon), that vector pair is said to be recurrent. To find the proper embedding dimension, it is recommended to use the false nearest neighbor approach (Kennel et al., 1992). It is always better to overestimate the ideal embedding dimension than underestimate it so that the full dynamic can be captured in its proper dimension (as opposed to a projection to a lower-dimensional wall as it were). Then for embedding dimensions greater than 1, the proper time delay between embedded points must be found. This can be determined by looking at the first minimum in the autocorrelation function or the first minimum in the mutual information function (Fraser and Swiney, 1986). Typically, lag or delay values are greater than one for smooth flows. However, for discrete intervals (Poincaré sections of flows), lags of one works just fine.

CROSS RECURRENCES (IMPLEMENTED BY PROGRAM KRQD)

As discussed, auto recurrence looks for parallel trajectories within a single time series. Likewise, cross recurrence looks for parallel trajectories between two time series. As explained in the equation below, the distances between all vectors pairs, x_i and y_j are computed and thresholded to form a recurrence matrix. In this case the LOI and symmetry across the central diagonal are both lost if x_i and y_j vectors are different. There are practical implementation rules for computing cross recurrence plots (Webber, 2012). First, both signals must be digitized simultaneously at the same digitization rate. Second, both signals must be amplitude adjusted over the same range (e.g., the unit interval from 0 to 1) to minimize the distance between parallel but separated trajectories. Third, the signals must be smooth flows, not discrete intervals. Fourth, the lag intervals should be set to 1. Cross recurrence plots are useful in separating out events in one signal that lead, lag, or occur simultaneously with the second signal.

$$Ri,j := \Theta\left(\varepsilon_i - \left|x_i - y_j\right|\right), \quad i,j = 1, \ldots N \qquad (3)$$

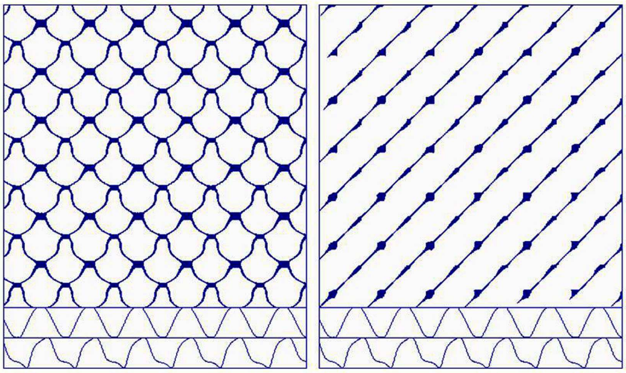

FIGURE 8 | Cross recurrence plot (left) and joint recurrence plot (right) of a fluid-coupled system consisting of an independent sinusoidal driver (upper trace) and dependent coupled rotor (lower trace).

Shockley et al. (2002) performed coupled-oscillator experiments on a fluid dynamical system. A gravity-driven rotor was freely spun within a tray filled with a fluid of selectable viscosity (low, medium, or high). Then the tray was pushed and pulled horizontally by a sinusoidal driver motor system. As shown in **Figure 8** (left) for a high viscosity medium, the sinusoidal motion of the driver tray distorted the motion of the rotor (lower two traces). The non-linear coupling of the rotor to the driver was then studied by cross recurrence plots which in this case shows the high degree of non-linearity along deterministic squiggles which form crossing patterns (due to the embedding dimension being selected as 1).

JOINT RECURRENCES (IMPLEMENTED BY PROGRAM JRQD)

The concept of joint recurrences is different from that of cross recurrences (Marwan et al., 2007). That is, instead of looking for parallel trajectories between two time series, joint recurrences look for recurrent points common to the auto recurrence plots of each signal separately. By this means joint recurrences can detect direction of phase synchronizations. Joint recurrence plots are expressed mathematically as the intersection of two individual auto recurrence plots of separate time series, *x* and *y*. It is advised that recurrence parameters be selected the same for each time series, but this is not absolutely necessary theoretically. The utility of joint recurrence plots awaits further exploration.

$$Ri,j := \left[\Theta\left(\varepsilon_i - \left|x_i - x_j\right|\right)\right] \cap \left[\Theta\left(\varepsilon_i - \left|y_i - y_j\right|\right)\right]$$
$$i,j = 1,\ldots N \tag{4}$$

Returning to the coupled-oscillator experiments of Shockley et al. (2002), the coupling of rotor to driver were reexamined by joint recurrence plots. In this case, **Figure 8** (right) shows the high degree of linearity along deterministic lines with bulges at periodic intervals. Taken together, this simple example highlights how joint-recurrences and cross recurrences are two different ways in which coupled system variables can be studied. (More work is required in this area.)

RECURRENCE QUANTIFICATIONS

The recurrence plot when first reported was heralded as a mathematical tool for revealing hidden rhythms within complex time series (Eckmann et al., 1987). And so it is. But it soon became apparent that recurrence plots had two inherent difficulties. First, there were numerous recurrence parameters that needed to be set logically to match the data set under investigation. These parameters included the threshold radius, embedding dimension, time delay between embedded points, selection of the distance norm (max, min, or Euclidean norm), rescaling of the distance matrix, a parameter that defined the shortest number of recurrent points forming a line segment (typically two), and the size of the recurrence window) short, medium, long. The author has written extensively on how to select recurrence parameters elsewhere (Webber and Zbilut, 2005).

The second difficulty with recurrence plots was the plots themselves. That is, how are the intricate and beautiful patterns to be interpreted? Instead of reading into recurrence plots patterns unique to the observer (I see a canoe in the clouds, you see a banana), recurrence quantification were born to extract from recurrence plots different aspects of the plots. To date there are eight unique features that are extracted from recurrence plots according to strict mathematical definitions. These recurrence variables, as they are called, include *percent recurrence* (recurrence density or recurrence rate), *percent determinism* (portion of recurrent points aligning into diagonal lines), $d_{\max}$ (length of longest diagonal line), *Shannon entropy* (complexity of line structure distributions), *trend* (homogeneity or inhomogeneity of recurrent points over plot), *percent laminarity* (portion of recurrence points aligning into vertical lines), $v_{\max}$ (length of longest vertical line), and *trapping time* (average vertical line length). The strict mathematical definition of these variables can be found elsewhere (Webber and Zbilut, 2007; Webber et al., 2011). The idea is that from a single time series (with auto recurrence plots) or double time series (with cross or joint recurrence plots) multiple reporters of the embedded dynamic are produced. It is the differential sensitivities of these recurrence variables depending upon the system under study that render RQA as a sensitive non-linear, multidimensional tool for exploring the so-called hidden rhythms in complicated signals. The beauty of this analysis is that no modeling assumptions on the time series are required, no statistical distributions are excluded, inherent noise in the signal does not stymy the analysis since the threshold is adjustable, short data sets ($n = 30$) can yield useful data, and outliers need not be dropped, clipped, substituted, or replaced.

MATHEMATICAL FRACTALS

FRACTALS AND RECURRENCE STRUCTURES

There is a natural linkage between fractals and recurrence. By definition, fractals are self-similar structures observed repeatedly or recurrently at different scales of magnitude. The natural world is filled with fractal examples such as mountains, clouds, trees. Thus small trigs from real trees conveniently pass as surrogates for full trees on HO train layouts. In physiology, the lungs form a fractal branching pattern from trachea to terminal alveoli with 23–27 branched generations. This fractal form minimizes the dead space volume of the conducting pathways (airways without alveoli), delivers oxygenated air quickly to the live space (airways with alveoli), and packs the entire lung within the thoracic space yet provide a huge surface area for gas exchange ($70\,\mathrm{m}^2$). Likewise, the human circulatory system starting with the large single aorta (2.5 cm diameter) branches numerous times to finally form the millions of tiny systemic capillaries ($7\,\mu\mathrm{m}$ diameter), only to collect them again from venules to vena cava and to repeat (recur) the process once again in the pulmonary circuit flowing through the lungs. The bronchiolar tree for air flow is also fractal and amenable to fractal modeling (Canals et al., 2004).

The theoretical study of fractals comes from the field of mathematics. Unlike natural fractals which have fundamental limits or minima (e.g., patent alveoli cannot be smaller than $100\,\mu\mathrm{m}$ and capillaries with blood flow cannot be smaller than $5\,\mu\mathrm{m}$), mathematical fractals are infinitely deep and unbounded. From the study of mathematical fractals comes the concept of self-similarity in which graphical depictions of systems at deep levels reveals (reflects, recurs) images of larger parent structures magnitudes of scales distant. And these are not simple structures of geometric forms, but complex structures of lace-like beauty waiting to be discovered using the computer as a digital microscope.

Mandelbrot (1924–2010) is the father of fractal geometry. He is famous for asking the question, "How long is the coast of Britain?" (Mandelbrot, 1967). The answer to this question is, surprisingly, the cumulative length depends upon the length of the measuring ruler! That is, the shorter the ruler, the longer is the measured length. The longest total length would be the integral of the boundary taken to the infinitesimal limit. The conclusion is that the quantitative description of structures is scale dependent. Because of this fact, Mandelbrot was able to construct artificial worlds from algorithmic computations on the computer that could pass as actual geography in the real-world. It is not overstating the situation to affirm that our natural world is not as geometric as it is fractal in design.

What follows are detailed descriptions of five mathematical fractals, the dynamics of which can be studied by recurrence strategies. The first two fractal systems are continuous flows, and the remaining three fractal systems are discontinuous maps. Sufficient information will be provided to allow the reader to study the dynamics of these fractals in detail. More questions will be raised than answered, but the intent of the author is to simulate further research into this fascinating field linking mathematical fractals with recurrence plots and quantifications. The methodology is fully applicable to fractal biological systems (Bassingthwaighte et al., 1994) which are not addressed herein because of space constraints.

LORENZ ATTRACTOR

Edward Lorenz (1917–2008) was an American mathematician and meteorologist who studied a simplified model of atmospheric convection using three ordinary differential equations. The way air swirled around the overhead atmosphere depended on three parameters (a, b, c) which dictated the interaction of three strongly coupled variables (x, y, z) as defined below.

$$\mathrm{d}x/\mathrm{d}t = a \times (y - x) \tag{5}$$

$$\mathrm{d}y/\mathrm{d}t = -b \times x - y - x \times z \tag{6}$$

$$\mathrm{d}z/\mathrm{d}t = -c \times z + x \times y \tag{7}$$

where:

$a = 10$ (ratio of the fluid viscosity of a substance to its thermal conductivity).

$b = 28$ (difference in temperature between the top and bottom of the gaseous system).

$c = 8/3$ (width to height ratio of the box being used to hold the gaseous system).

and

x = rate of rotation of convection cylinder.

y = temperature differential at opposite sides of the cylinder.

z = deviation of the system from a linear, vertical graphed line representing temperature.

Mathematical solution of the system of Lorenz equations results in a three-dimensional structure known as a dynamical attractor. Dynamical motion is captured on the single trajectory forming the attractor, but other negative spaces are devoid of legal trajectory pathways. The contrast between the presence and absence of trajectory pathways gives shape to the attractor which appears like the wings of a butterfly (with asymmetric donut holes) as shown in **Figure 9**.

What is remarkable about the Lorenz attractor (and consequently a fundamental principle of chaotic dynamics) is that not only can rich dynamics be continued within and expressed by simple non-linear systems (e.g., consisting of a mere three variables), but that the single dynamical trajectory shows sensitive dependence on initial conditions. What this means is that by just altering the initial conditions of just one variable by a smidgeon (non-mathematical term) will lead to two different trajectories over time. For example, if variables x_1 and x_2 differ numerically by just 10^{-5} ($x_1 = 0.10000$ and $x_2 = 0.10001$), everything else remaining exactly the same, then the pathways will eventually diverge. Such extreme sensitivity of chaotic systems to initial conditions has been called the "butterfly effect" in honor of insect shape of the Lorenz attractor.

To study the recurrence structure of the Lorenz system, the three system variables can be followed over time by solving the three ordinary differential equations using standard fourth-order Runge–Kutta estimations. Initial conditions can be set as variables $x = y = z = 0.1$ using fixed parameters $a = 10$, $b = 28$, and $c = 8/3$. The first points of the three-dimensional trajectory can be retained to follow the transients (off-attractor dynamics) before the dynamic settles on the attractor proper. The higher the time increment (e.g., $\mathrm{d}t = 0.01$), the longer will be the transient. The Lorenz attractor can be viewed in the x,y plane (two paper plates), the x,z plane (butterfly), and the y,z plane (owl mask) which are projections of the three-dimensional object.

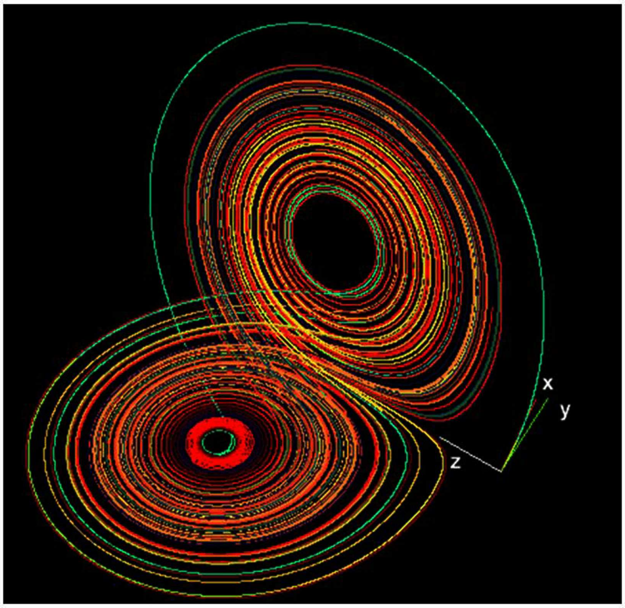

FIGURE 9 | The Lorenz strange attractor in its chaotic mode. Public source: http://en.wikipedia.org/wiki/Lorenz_system

Since the Lorenz attractor is a three-dimensional structure, auto recurrence plots can be generated on any one of the variables. Selecting an embedding dimension of 3 will suffice because the dimension of this attractor is fractal between 2 and 3. And any two variables can be paired to generate cross recurrence plots (KRQD x y; KRQD x z; KRQD y z) or joint recurrent plots (JRQD x y; JRQD x z; JRQD y z). See Webber (2012) for free RQA software and detailed explanations of proper implementation procedures.

RÖSSLER ATTRACTOR

Otto Rössler (1940–present) is a German biochemist responsible for the mathematical attractor that bears his name. The Rössler attractor is similar to the Lorenz attractor and consists of three coupled differential equations. Insofar that the first two equations are linear, the Rössler attractor turns out to be simpler than the Lorenz attractor and easier to analyze.

$$\mathrm{d}x/\mathrm{d}t = -y - z \tag{8}$$

$$\mathrm{d}y/\mathrm{d}t = x + a \times y \tag{9}$$

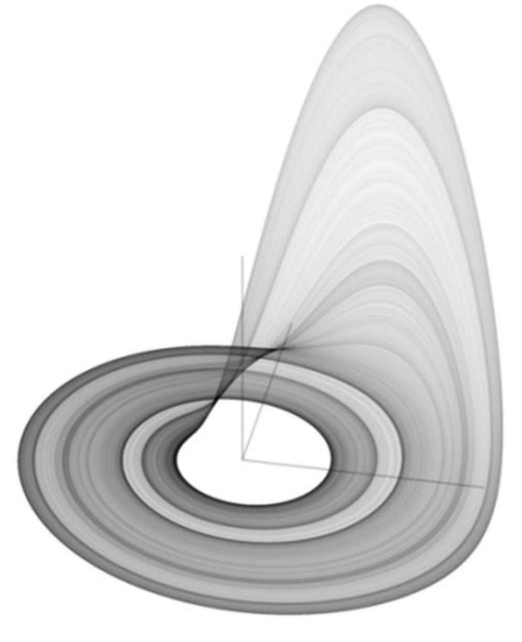

FIGURE 10 | The Rössler strange attractor in its chaotic mode. Public source: http://en.wikipedia.org/wiki/R%C3%B6ssler_attractor

$$\mathrm{d}z/\mathrm{d}t = b + z \times (x - c) \quad (10)$$

where:

$a = 0.2$, $b = 0.2$, and $c = 5.7$.

As shown in **Figure 10**, the Rössler attractor is a three-dimensional chaotic attractor, with unstable spiral orbits in the *x*,*y* plane that grow up into the *z* plane. The system has only one manifold and is fractal in nature. Like the Lorenz attractor, the Rössler attractor demonstrates sensitive dependence on initial conditions, the hallmark of chaos, and fracticality.

To study the recurrence structure of the Rössler system, the three system variables can followed over time by solving the three ordinary differential equations using a standard fourth-order Runge–Kutta estimation. For example, starting conditions can begin with variables $x = y = z = 0.1$ using fixed parameters $a = 0.2$, $b = 0.2$, and $c = 5.7$. Again the initial points the three-dimensional trajectory (transient or off-attractor dynamics) can be studied as can the following points (stable or on-attractor dynamics) using a high resolution time increment of $\mathrm{d}t = 0.01$. The *x*, *y*, and *z* variables can be examined using recurrence plots and quantifications.

As can be demonstrated for the Lorenz attractor, the Rössler attractor can be shown to possess steady state, periodic, and chaotic dynamics depending up the value of the *b* parameter. As parameter *b* decreases from 2 to about 1.44, the *x* variable settles on single point attractors. With further decreases in parameter *b*, the *x* variable falls into a period-2 then period-4, then period-8 stable periodic states until full chaos erupts with *b* values less than 0.7. There are brief periodic windows embedded within chaotic regimes for lower values of b approaching 0. But at $b = 0.2$ as is the typical choice, the Rössler attractor is in a strong chaotic mode.

LOGISTIC ATTRACTOR

Robert May (1938–present) called attention to the logistic map (May, 1976). This deceptively simple difference equation illustrates how complex dynamics can arise from non-linear recurrent interactions of a single variable. In this case, the next *x* is a function of the current x^2 term.

$$X_{n+1} = a \times X_n \times (1 - X_n) \quad (11)$$

where:

$a = 0$–4 and $0 \leq x \leq 1$.

As illustrated in **Figure 11**, the logistic map forms a "Saint Louis Arch" in the second dimension (**Figure 11A**) and a "roller coaster" in the third dimension (**Figure 11B**). Interestingly, as tuning parameter *a* is increased from 0 to 4, the dynamics of *x* follows a period-doubling pathway to chaos. Trulla et al. (1996) investigated these dynamics with RQA windows by adiabatically incrementing parameter *a*. Transitions between periodicity and chaoticity were easily distinguished by RQA variables, particularly DET and LMAX. In fact, 1/LMAX values positively correlated with Lyapunov exponents in the chaotic frames, confirming the postulate of Eckmann et al. (1987).

The principle difference between the Logistic attractor and the Lorenz and Rössler attractors is that it is an iterated map, not a continuous flow. Because sequential points are iterated, they resemble Poincaré sections not unlike how R–R intervals represent planes through the ECG flow dynamic. In any case, it is proper to select a delay of one point when dealing with iterated dynamics (difference equations as opposed to differential equations).

HÉNON ATTRACTOR

Another excellent example of an iterated map is the Hénon attractor named after French mathematician, Michel Hénon (1931–present). As explicitly defined in the equations below, this system consists of the interplay between *x* and *y* variables interlinked through two parameters, *a* and *b*, and a single constant, 1. The non-linearity of this two-dimensional system derives again from the x^2 term.

$$X_{n+1} = y_n + 1 - a \times X_n^2 \quad (12)$$

$$Y_{n+1} + b \times X_n \quad (13)$$

where:

$a = 1.4$ and $b = 0.3$.

The plane plot of the coupled *x*,*y* variables reveals the double crescent shape of the Hénon attractor as shown in **Figure 12**. Dark points show allowed positions of the dynamic, and white space reveals disallowed positions never part of the stable dynamic. Transients can be studied by examining the *x*,*y* variables starting at randomly selected initial conditions for x_0, y_0. The fracticality of the Hénon attractor can be demonstrated by focusing in on one of the single arms of the double crescent (magnify the scale) and discovering yet another double-banded structure. This unveiling of bands after band continues to infinity!

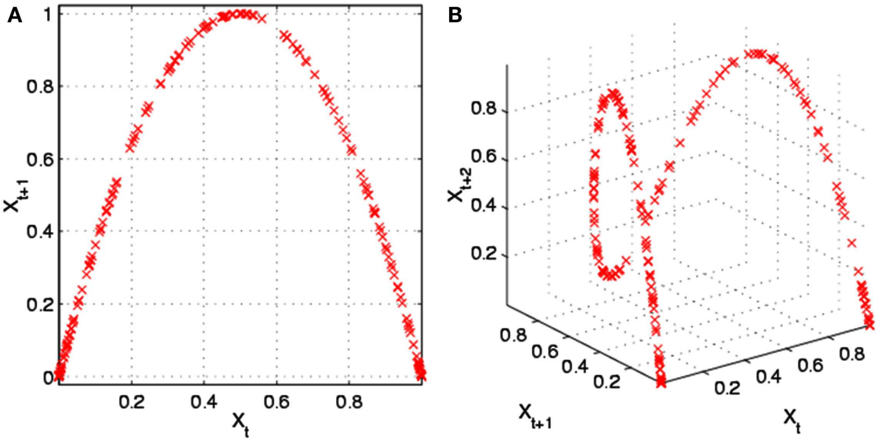

FIGURE 11 | The Logistic map in two-dimensions (A) and three-dimensions (B). Public source: http://en.wikipedia.org/wiki/File:Logistic_map_scatterplots_large.png

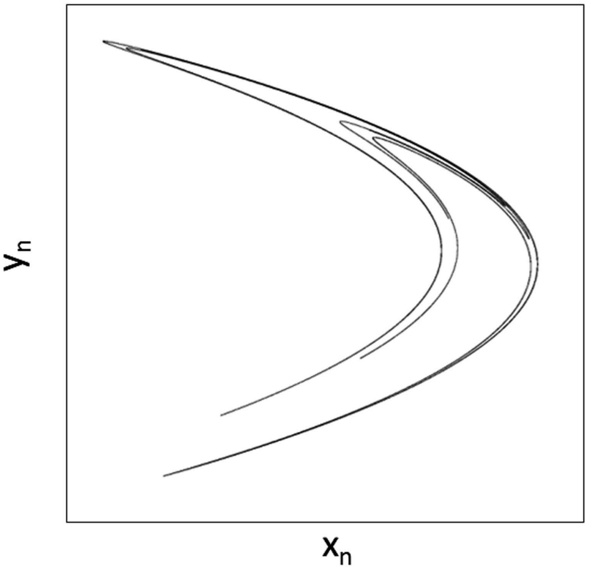

FIGURE 12 | The Hénon strange attractor in its chaotic mode. Adapted from public source: http://en.wikipedia.org/wiki/H%C3%A9non_map

It is very instructive to study the dynamics of the Hénon attractor by following the time courses of x, y individually and coupled in both the chaotic and periodic modes of the system. To get started, hints can be gleaned from Webber and Zbilut (1998).

MANDELBROT ATTRACTOR

Mandelbrot has already been introduced above as the father of fractal geometry. However, most interesting and beautiful is the mathematical set named after him. The Mandelbrot set is a flat structure with infinitely deep fractal patterns that lives in the complex plane. The intriguing and early book, *The Beauty of Fractals*, by Peitgen and Richter (1986) captures much of the essence of the Mandelbrot Set which stems from the simple iteration of the complex equation consisting of one complex variable, z, and one complex constant, c. The non-linear chaotic dynamics of this equation grows out of the complex and real parts of both the variable z (z real, z imaginary) and the constant c (c real, c imaginary), the former of which is squared according to the following equation.

$$z_{n+1} = z_n^2 + c \tag{14}$$

The Mandelbrot set (M set) is a black and white set meaning that complex point c either belongs to the M set (black) or does not belong to the M set (white). To keep things simple, the equation can be implemented by setting both z real and z imaginary to zero and setting c real from -2 to $+1$ and c imaginary from -1 to $+1$. Iteration of the equation will alter the z variable to either some type of converging dynamic (period 1, 2, 4, 8, etc. or chaotic) or diverging dynamic (tending toward infinity). If the system converges then constant c is a member of the M set and can be plotted as a black point on the complex plane of c imaginary versus c real. If the system fails to converge than constant c is a not a member of the M set as is plotted as a contrasting white point. The M set is illustrated in **Figure 13** in which characteristic cardioids are seen at both low and high magnifications, demonstrating the fractal structuring of the set. Mandelbrot conjectured that his set was discontinuous, meaning the some white space interspersed between points of the set. But Douady and Hubbard (1984/1985) proved that the M set was truly continuous. To visualize the continuity of the set requires high resolution computer graphics.

To illustrate recurrence properties of the M set, formula 14 was iterated 1000 times using as initial conditions: $z_{\text{real}} = 0.0$, $z_{\text{imag}} = 0.0$, $c_{\text{real}} = -0.75$, and $c_{\text{imag}} = 0.005$. In the c plane this is positioned deep within the seahorse valley, the gap between the large cardioid to the right and smaller circle to the left (**Figure 13**, left). The question is, is this specific point a member of the M set or not? In this case, variable z was iterated 632 times before it started going toward infinity. Thus complex point c is not a member of the M set, but still it took many iterations to determine this.

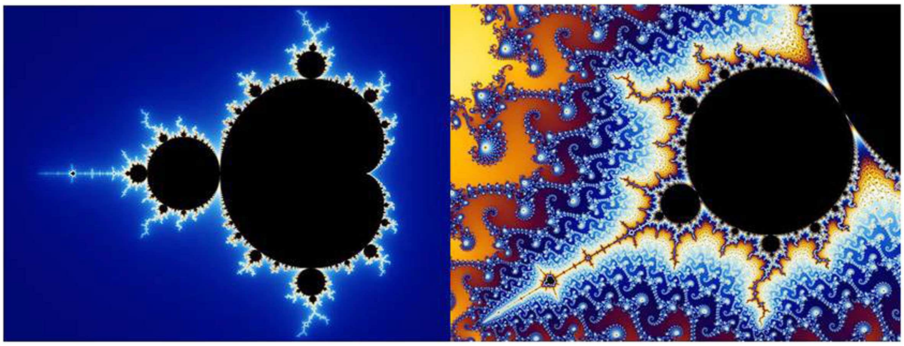

FIGURE 13 | Mandelbrot set low resolution (left) and high resolution (right). Public source: http://en.wikipedia.org/wiki/File:Mandel_zoom_00_mandelbrot_set.jpg

The dynamics of z_{real} and z_{imag} were studied individually by generating their respective recurrence plots as shown in **Figure 14**. Using a delay of one, embedding of five, no rescaling of the distance matrix, and absolute radius of 0.01 and color steps of 0.001 (dark blue to purple). It can be noted that z_{real} shows a gentle decrescendo in terms of amplitude whereas z_{imag} displays a gradual crescendo. Nevertheless, after 632 iterations the system explodes toward infinity. Thus imaginary point *c* is very close to the M set border, but never touches it.

The reader is challenged to study other transient dynamics of the complex *z* variable as it moves from 0.0 to either a steady state dynamic or a non-steady state dynamic depending upon the value of complex parameter *c*. The most complicated and most interesting dynamics are seen at the borders at very high magnifications deep within the M set. In these places the *c* parameter is taken out to the sixth decimal point or finer causing the *z* variable to go through hundreds of iterations before it diverges or converges. Here the user can examine *z* real and *z* imaginary variables either individually or coupled using recurrence programs. No space remains in this paper to carry this out, so the reader should take it as an assignment to discover the rich dynamics of the iterated equation in which are hidden all the exquisite beauty of the M set.

CONCLUSION

In this communication we have moved from (1) conceptual definitions of systems to (2) simple overview themes of recurrence quantifications for analysis of non-linear (and linear) systems to (3) practical implementation of recurrence analyses on systems of common fractals. By design (space limitations notwithstanding) much work has been left to the reader for study fractals on his/her own by combining these conceptual and practical ideas. For the experienced RQA user, it will be easy to move into the mathematical fractal world using recurrence strategies. For the new RQA user, it will be absolutely necessary to first read the long chapter (monograph) written by the author to learn the proper procedures for setting RQA parameters and interpreting RQA variables (Webber and Zbilut, 2005). Learning by doing is always the best teacher.

Deemphasized in this chapter is the specific application of recurrence plots and quantifications to real-world systems found in physics, chemistry, biology, and medicine, for example. The author has already addressed these things elsewhere (Webber and Zbilut, 2005). The value of this present chapter is to identify fractals as mathematical systems which possess deep-rooted complexity and repeating structures at different magnification scales. In this sense they become analogies for real-world systems which possess many of the same properties. Whether a system be mathematical or material, it is governed by dynamical rules which define boundaries, fuzzy or sharp, depending upon the state of the system (quasi-steady state or transient), and the presence of noise (numerical round-off or environmental).

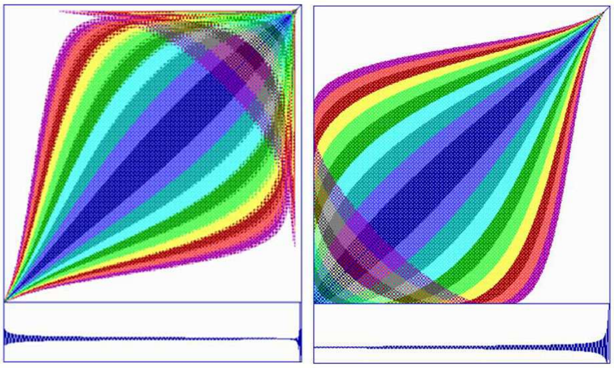

FIGURE 14 | Recurrence plot of z_{real} (left) and z_{imag} (right) scaled from point 1 to point 629 or the 633-point time series (lower traces). The system diverges toward infinity at the end of the each series, but the dynamics of the real and imaginary components are rather different.

The big idea of this chapter is that dynamical rules in complex, non-linear systems can be ferreted out as it were, by applying recurrence analyses to dynamical time series. Embedding procedures allow measured variables to serve as surrogates for unmeasured variables (Webber and Zbilut, 2005). The reader is challenged to apply RQA to systems of their choice. We live in a fractal world, nay fractal universe. And recurrence analysis is one way to delve into the mysteries which lie before us.

REFERENCES

Bassingthwaighte, J. B., Liebovitch, L. S., and West, B. J. (1994). *Fractal Physiology*. New York: Oxford University Press.

Canals, M., Novoa, F. F., and Rosenmann, M. (2004). A simple geometrical pattern for the branching distribution of the bronchial tree, useful to estimate optimally departures. *Acta Biotheor.* 52, 1–16.

Cannon, W. B. (1929). Organization for physiological homeostasis. *Physiol. Rev.* 9, 399–431.

Douady, A., and Hubbard, J. H. (1984/1985). *Étude dynamique des polynômes complexes I & II, Publications mathématiques, d'Orsay*, Vol. 2/4.

Eckmann, J.-P., Kamphorst, S. O., and Ruelle, D. (1987). Recurrence plots of dynamical systems. *Europhys. Lett.* 4, 973–977.

Fraser, A. M., and Swiney, H. L. (1986). Independent coordinates for strange attractors from mutual information. *Phys. Rev. A* 33, 1134–1140.

Grassberger, P., and Procaccia, I. (1983). Measuring the strangeness of strange attractors. *Physica D* 9, 189–208.

Gross, C. G. (1998). Claude Bernard and the constancy of the internal environment. *Neuroscientist* 4, 380–385.

Kennel, M. B., Brown, B., and Abarbanel, H. D. I. (1992). Determining embedding dimension for phase-space reconstruction using a geometrical construction. *Phys. Rev. A* 45, 3403–3411.

Lloyd, D., Aon, M. A., and Cortassa, S. (2001). Why homeodynamics, not homeostasis? *Sci. World J.* 1, 133–145.

Lorenz, E. N. (1963). Deterministic non-periodic flow. *J. Atmos. Sci.* 20, 130–141.

Mandelbrot, B. B. (1967). How long is the coast of Britain? Statistical self-similarity and fractional dimension. *Science* 156, 636–638.

Mandelbrot, B. B. (1983). *The Fractal Geometry of Nature*. London: Macmillan Publishers.

Marwan, N., Romano, M. C., Thiel, M., and Kurths, J. (2007). Recurrence plots for the analysis of complex systems. *Phys. Rep.* 438, 237–329.

May, R. M. (1976). Simple mathematical models with very complicated dynamics. *Nature* 261, 459–467.

Nyquist, H. (1924). Certain factors affecting telegraph speed. *Bell Syst. Tech. J.* 3, 324–346.

Parker, T. S., and Chua, L. O. (1989). *Practical Numerical Algorithms for Chaotic Systems*. New York: Springer-Verlag.

Peitgen, H.-O., and Richter, P. H. (1986). *The Beauty of Fractals: Images of Complex Dynamical Systems*. Berlin: Springer-Verlag.

Rasband, S. N. (1990). *Chaotic Dynamics of Nonlinear Systems*. New York: Wiley.

Shockley, K., Buttwill, M., Zbilut, J. P., and Webber, C. L. Jr. (2002). Cross recurrence quantification of coupled oscillators. *Phys. Lett. A* 305, 59–69.

Somjen, G. G. (1992). The missing error signal – regulation beyond negative feedback. *News Physiol. Sci.* 7, 184–185.

Trulla, L. L., Giuliani, A., Zbilut, J. P., and Webber, C. L. Jr. (1996). Recurrence quantification analysis of the logistic equation with transients. *Phys. Lett. A* 223, 255–260.

Webber, C. L. Jr. (2012). *Introduction to Recurrence Quantification Analysis*. RQA Version 14.1 README.PDF. Available at: http://homepages.luc.edu/∼cwebber/

Webber, C. L. Jr., Hu, Z., and Akar, J. (2011). Unstable cardiac singularities may lead to atrial fibrillation. *Int. J. Bifurcat. Chaos* 21, 1141–1151.

Webber, C. L. Jr., and Zbilut, J. P. (1998). "Recurrent structuring of dynamical and spatial systems," in *Complexity in the Living: A Modelistic Approach, Proceedings of an international meeting, February 1997*, ed. A. Colosimo (University of Rome "La Sapienza), 101–133.

Webber, C. L. Jr., and Zbilut, J. P. (2005). "Recurrence quantification analysis of nonlinear dynamical systems," in *Tutorials in Contemporary Nonlinear Methods for the Behavioral Sciences*, Chap. 2, eds M. A. Riley and G. Van Orden (Arlington, VA: National Science Foundation), 26–94.

Webber, C. L. Jr., and Zbilut, J. P. (2007). Recurrence quantifications: feature extractions from recurrence plots. *Int. J. Bifurcat. Chaos* 17, 3467–3475.

West, B. J. (2010). Homeostasis and gauss statistics: barriers to understanding natural variability. *J. Eval. Clin. Pract.* 16, 403–408.

Wiesenfeld, K., and Moss, F. (1995). Stochastic resonance and the benefits of noise: from ice ages to crayfish and SQUIDs. *Nature* 373, 33–36.

Zbilut, J. P., Hübler, A., and Webber, C. L. Jr. (1996). "Physiological singularities modeled by nondeterministic equations of motion and the effect of noise," in *Fluctuations and Order: The New Synthesis*, ed. M. M. Millonas (New York, NY: Springer-Verlag), 397–417.

Conflict of Interest Statement: The author declares that the research was conducted in the absence of any commercial or financial relationships that could be construed as a potential conflict of interest.

Received: 12 June 2012; accepted: 08 September 2012; published online: 01 October 2012.

Citation: Webber CL Jr. (2012) Recurrence quantification of fractal structures. Front. Physio. ***3****:382. doi: 10.3389/fphys.2012.00382*

This article was submitted to Frontiers in Fractal Physiology, a specialty of Frontiers in Physiology.

frontiers in
PHYSIOLOGY

METHODS ARTICLE
published: 24 January 2012
doi: 10.3389/fphys.2011.00110

Multiscale analysis of biological data by scale-dependent Lyapunov exponent

Jianbo Gao[1,2,3]*, Jing Hu[4], Wen-wen Tung[5] and Erik Blasch[6]

[1] PMB Intelligence LLC, West Lafayette, IN, USA
[2] State Key Laboratory of Non-linear Mechanics, Institute of Mechanics, Chinese Academy of Sciences, Beijing, China
[3] Mechanical and Materials Engineering, Wright State University, Dayton, OH, USA
[4] Affymetrix, Inc., Santa Clara, CA, USA
[5] Department of Earth and Atmospheric Sciences, Purdue University, West Lafayette, IN, USA
[6] Electrical Engineering, Wright State University, Dayton, OH, USA

Edited by:
John Holden, University of Cincinnati, USA

Reviewed by:
Michael A. Riley, University of Cincinnati, USA
John Holden, University of Cincinnati, USA
Damian Stephen, Harvard University, USA

***Correspondence:**
Jianbo Gao, PMB Intelligence LLC, PO Box 2077, West Lafayette, IN 47996, USA.
e-mail: jbgao.pmb@gmail.com

Physiological signals often are highly non-stationary (i.e., mean and variance change with time) and multiscaled (i.e., dependent on the spatial or temporal interval lengths). They may exhibit different behaviors, such as non-linearity, sensitive dependence on small disturbances, long memory, and extreme variations. Such data have been accumulating in all areas of health sciences and rapid analysis can serve quality testing, physician assessment, and patient diagnosis. To support patient care, it is very desirable to characterize the different signal behaviors on a wide range of scales simultaneously. The Scale-Dependent Lyapunov Exponent (SDLE) is capable of such a fundamental task. In particular, SDLE can readily characterize all known types of signal data, including deterministic chaos, noisy chaos, random $1/f^{\alpha}$ processes, stochastic limit cycles, among others. SDLE also has some unique capabilities that are not shared by other methods, such as detecting fractal structures from non-stationary data and detecting intermittent chaos. In this article, we describe SDLE in such a way that it can be readily understood and implemented by non-mathematically oriented researchers, develop a SDLE-based consistent, unifying theory for the multiscale analysis, and demonstrate the power of SDLE on analysis of heart-rate variability (HRV) data to detect congestive heart failure and analysis of electroencephalography (EEG) data to detect seizures.

Keywords: multiscale analysis, chaos, random fractal, scale-dependent Lyapunov exponent, EEG, heart-rate variability, intermittent chaos, non-stationarity

1. INTRODUCTION

Complex systems, such as physiological systems, usually are comprised of multiple subsystems that exhibit both highly non-linear deterministic, as well as, random characteristics, and are regulated hierarchically. These systems generate signals that exhibit complex characteristics such as sensitive dependence on small disturbances, long memory, extreme variations, and non-stationarity (i.e., mean and variance change with time). Examples of such signals in physiology are abundant (Bassingthwaighte et al., 1994). An example of heart-rate variability (HRV) data for a normal young subject (Physionet, 2011) is shown in **Figure 1**. Evidently, the signal is highly non-stationary and multiscaled (i.e., dependent on the spatial or temporal interval lengths), appearing oscillatory for some period of time (**Figures 1B,D**), and then varying as a $1/f$ process for another period of time (**Figures 1C,E**).

While the multiscale nature of signals such as shown in **Figure 1** cannot be fully characterized by existing methods, the non-stationarity of the data is even more troublesome, because it prevents direct application of spectral analysis, or methods based on chaos theory and random fractal theory. For example, in order to reveal that the HRV data is of $1/f$ nature (Akselrod et al., 1981; Kobayashi and Musha, 1982) with anti-persistent *long-range correlations* (i.e., algebraically decaying autocorrelation function; Peng et al., 1993; Ashkenazy et al., 2001) and multifractality (i.e., multiple power-law behavior; Ivanov et al., 1999), time series such as shown in **Figure 1A** has to be pre-processed to remove components (such as the oscillatory ones) that do not conform to fractal scaling analysis. However, automated segmentation of complex biological signals to remove undesired components is a significant open problem, since it is closely related to the challenging task of accurately detecting transitions from normal to abnormal states in physiological data.

Rapid accumulation of complex data in all areas of natural and health sciences has made it increasingly important to be able to analyze multiscale and non-stationary data. Since multiscale signals behave differently, depending upon the temporal and spatial scale at which the data are examined, it is of fundamental importance to develop measures that explicitly incorporate the concept of scale so that different data behaviors on varying scales can be simultaneously characterized.

Straightforward multiscale analysis include short-time Fourier transform based time-frequency analysis, wavelet analysis (Strang and Nguyen, 1997; Mallat, 2008), and time-domain adaptive filtering (Gao et al., 2011b; Tung et al., 2011). Multiscale analysis can also be based on chaos theory and random fractal theory (Gao et al., 2007). In many instances, the latter two theories are more

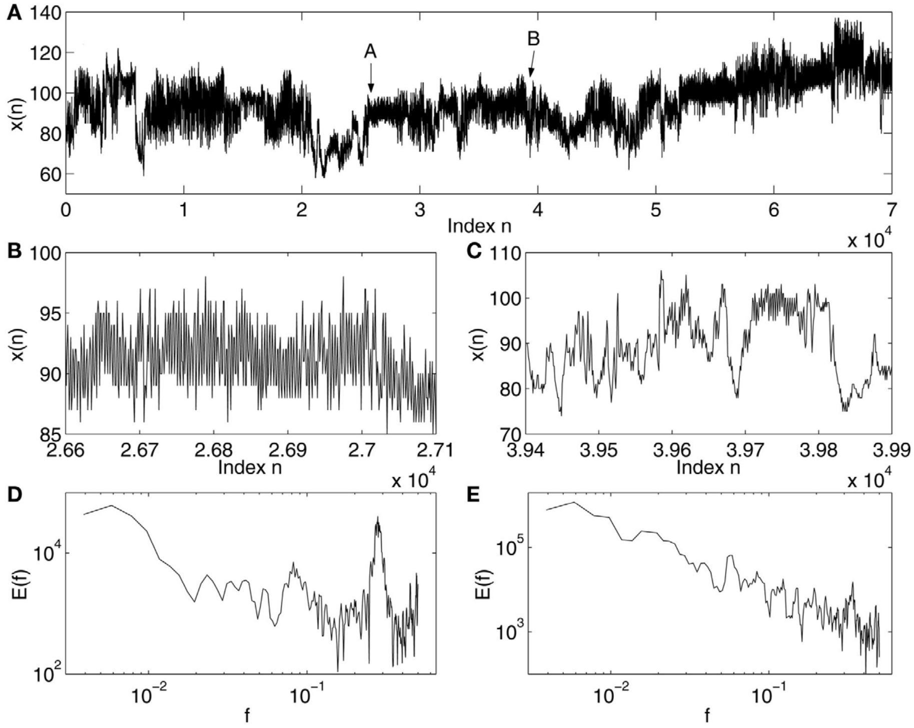

FIGURE 1 | Non-stationarity in HRV data: (A) The HRV data for a normal subject; (B,C) the segments of signals indicated as A and B in (A); (D,E) power spectral density $E(f)$ vs. frequency f for the signals shown in (B,C).

appealing, since measures from chaos or fractal theories can be associated with the complexity of the signal and the underlying physiological system, and thus can stimulate researchers to ask whether the complexity of the signal may change when certain pathology of the physiological system progresses, and if so, how. Indeed, they have been used extensively in physiology (Goldberger and West, 1987; Kaplan and Goldberger, 1991; Garfinkel et al., 1992; Peng et al., 1993; Bassingthwaighte et al., 1994; Fortrat et al., 1997; Ivanov et al., 1999; Kaneko and Tsuda, 2000; Ashkenazy et al., 2001; Gao et al., 2007, 2011b).

The key element of random fractal theory is *scale-invariance*, i.e., the statistical behavior of the signal is independent of a spatial or temporal interval length. With scale-invariance, only one or a few parameters are sufficient to describe the complexity of the signal across a wide range of scales where the fractal scaling laws hold. Because of the small number of parameters, fractal analyses are among the most parsimonious multiscale approaches. Chaos theory also provides a few multiscale approaches, including ε-entropy (Gaspard and Wang, 1993; where entropy is a way of measuring uncertainty), the finite size Lyapunov exponent (FSLE; Torcini et al., 1995; Aurell et al., 1996, 1997), multiscale entropy (MSE; Costa et al., 2005), and the scale-dependent Lyapunov exponent (SDLE; Gao et al., 2006b, 2007). FSLE and SDLE are in fact closely related – conceptually SDLE is partially inspired by FSLE. The algorithm for computing SDLE, which is derived from that for computing *time-dependent exponent curves* and will be defined shortly (Gao and Zheng, 1993, 1994a,b; Gao, 1997), is completely different from that for computing FSLE. This leads to a few important differences between FSLE and SDLE: (1) FSLE assumes the underlying dynamics to be divergent, and thus is positive; SDLE, however, is assumption-free, and therefore, can assume any value. Consequentially, SDLE possesses a unique *scale separation property*, i.e., different types of dynamics manifesting themselves on different scales. This allows SDLE to readily detect intermittent chaos and detect fractal structures from non-stationary signals, while FSLE does not. (2) It is much easier to analytically derive and numerically verify scaling laws for SDLE than for FSLE for various types of processes.

In this article, we aim to present SDLE in such a way that it can be readily understood and implemented by non-mathematically oriented researchers[1]. We shall focus on its capabilities that are not shared by other popular chaos or fractal analysis methods, such as detecting intermittent chaos, detecting fractal structures from non-stationary data, and characterizing fractal scaling laws for stochastic limit cycles. We shall also consider detection of epileptic seizures from electroencephalography (EEG) and certain cardiac disease from heart-rate variability (HRV) data, for the purposes of (1) shedding new light on the interpretation of complexity of physiological data, and (2) illustrating SDLE's clinical relevance.

The remainder of the paper is organized as follows. In Section 2, we first define SDLE, then apply it to characterize low-dimensional chaos, noisy chaos, and random $1/f^{\alpha}$ processes, and show how SDLE can readily detect intermittent chaos and deal with non-stationarity. As real world applications, in Section 3, we apply SDLE to characterize EEG and HRV data for detecting

---

[1] Implementation includes two files, sdle.m and lamda.m.

epileptic seizures and certain cardiac disease. Finally, in Section 4, we make a few concluding remarks, including a discussion of best practices for experimental data analysis using the SDLE approach.

2. SDLE: DEFINITIONS AND FUNDAMENTAL PROPERTIES

Chaos theory is a mathematical analysis of irregular behaviors of complex systems generated by non-linear deterministic (i.e., future behavior described by the initial conditions) interactions of only a few degrees of freedom without concern of noise or intrinsic randomness. Random fractal theory, on the other hand, assumes that the dynamics of the system are inherently random. One of the most important classes of random fractals is $1/f^{\alpha}$ processes with long-range correlations, where $1 < \alpha < 3$. Therefore, the foundations of chaos theory and random fractal theory are entirely different. Consequentially, different conclusions may be drawn depending upon which theory is utilized to analyze a data set. In fact, much of the research in the past has been devoted to determining whether a complex time series is generated by a chaotic or a random system (Grassberger and Procaccia, 1983a,b; Wolf et al., 1985; Sugihara and May, 1990; Kaplan and Glass, 1992; Gao and Zheng, 1994a,b; Pei and Moss, 1996; Gaspard et al., 1998; Dettmann and Cohen, 2000; Poon and Barahona, 2001; Hu et al., 2005). From past research, $1/f^{\alpha}$ processes have distinguished themselves as providing counter examples that invalidate commonly used tests for chaos (Osborne and Provenzale, 1989; Provenzale and Osborne, 1991; Hu et al., 2005). In fact, the two research communities, one favoring chaos theory, the other random fractal theory, often assume two polar positions, either rarely communicating or constantly debating with each other as to the applicability of their theories[2]. While this classic issue, distinguishing chaos from noise, is still important, the authors believe that chaos and random fractal theories should be used synergistically in order to comprehensively characterize the behaviors of signals over a wide range of scales. Based on this belief, we aim to develop a complexity measure that cannot only effectively distinguish chaos from noise, but also aptly extract the crucial or the defining parameters of a process generating the data, be it chaotic or random. SDLE is a measure that has these capabilities.

SDLE stems from two important concepts, the time-dependent exponent curves (Gao and Zheng, 1993, 1994a,b; Gao, 1997) and the finite size Lyapunov exponent (Torcini et al., 1995; Aurell et al., 1996, 1997). SDLE was first introduced by (Gao et al., 2006b, 2007), and has been further developed in (Gao et al., 2009, in press) and applied to characterize EEG (Gao et al., 2011a), HRV (Hu et al., 2009a, 2010), Earth's geodynamo (Ryan and Sarson, 2008), and non-autonomous Boolean chaos (Blakely et al., under review). To better understand SDLE, it is beneficial to consider an ensemble forecasting framework. An example is shown in **Figure 2**, where we observe that 2500 close by initial conditions rapidly evolve to fill the entire attractor. A fundamental question is, how do we characterize such evolutions?

SDLE is a concept derived from a high-dimensional phase space. Assume that all that is known is a scalar time series $x[n] = x(1), x(2), \ldots, x(n)$. How can we obtain a phase space? This can be achieved by the time delay embedding technique (Packard et al., 1980; Takens, 1981; Sauer et al., 1991). This technique is perhaps the most significant contribution of chaos theory to practical data analysis, since non-trivial dynamical systems usually involve many state variables, and therefore, have to be described by a high-dimensional state (or phase) space. The embedding technique consists of creating vectors of the form:

$$V_i = [x(i), x(i+L), \ldots, x(i+(m-1)L)], \quad i = 1, \ldots, N_p \tag{1}$$

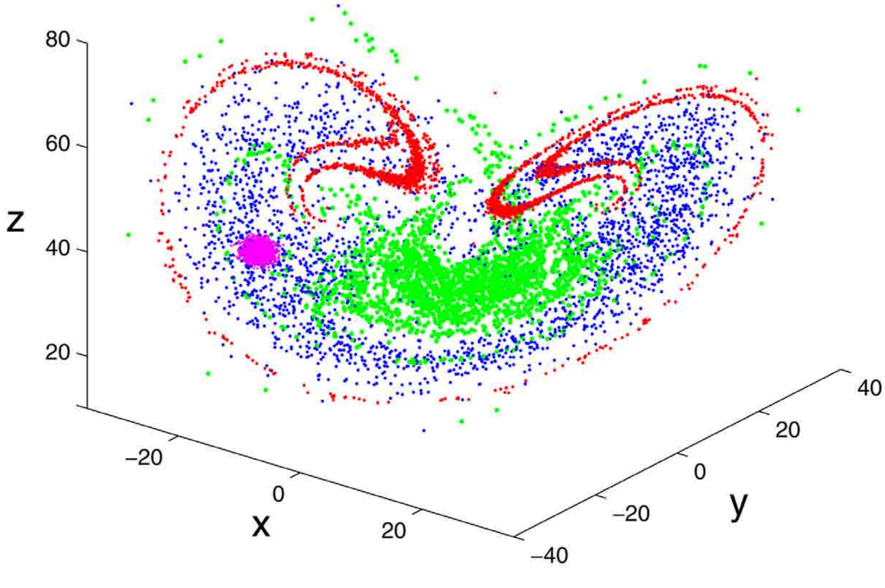

FIGURE 2 | Error growth in the chaotic Lorenz system (Lorenz, 1963) illustrated using an ensemble forecasting framework, where 2500 initial conditions, initially represented by the pink color, evolve to those represented by the red, green, and blue colors at $t = 2$, 4, and 6 units.

---

[2] This statement is a little over-simplified; singular measure based multifractal theory can be applied to both deterministic chaos and random processes.

where $N_p = n - (m-1)L$ is the total number of reconstructed vectors, and the embedding dimension m and the delay time L are chosen according to certain optimization criteria (Gao et al., 2007). Specifically, L alone may be determined by computing the first zero of the autocorrelation or the first minimal point of mutual information (Fraser and Swinney, 1986), while joint determination of m and L may be achieved using false nearest neighbor method (Liebert et al., 1991; Kennel et al., 1992), which is a static geometrical method, or time-dependent exponent method (Gao and Zheng, 1993, 1994b), which is a dynamical method. Note that when the time series is random, the embedding procedure transforms the self-affine (i.e., x and t have to be stretched differently in order to make the curve look "similar," since the units for x and t are different) stochastic process into a self-similar (i.e., part of the curve in the high-dimensional space looks similar to another part or the whole when it is magnified or shrinked, since all the axes have the same unit) process in phase space. In this case, the specific value of m is not important, so long as $m > 1$.

After a proper phase space is re-constructed, we consider an ensemble of trajectories. We denote the initial separation between two nearby trajectories by ε_0, and their *average separation* at time t and $t + \Delta t$ by ε_t and $\varepsilon_{t+\Delta t}$, respectively. The trajectory separation is schematically shown in **Figure 3**. We can then examine the relation between ε_t and $\varepsilon_{t+\Delta t}$, where Δt is small. When $\Delta t \to 0$, we have,

$$\varepsilon_{t+\Delta t} = \varepsilon_t e^{\lambda(\varepsilon_t)\Delta t}, \tag{2}$$

where $\lambda(\varepsilon_t)$ is the SDLE given by

$$\lambda\left(\varepsilon_t\right) = \frac{\ln \varepsilon_{t+\Delta t} - \ln \varepsilon_t}{\Delta t}. \tag{3}$$

Equivalently, we can express this as,

$$\frac{d\varepsilon_t}{dt} = \lambda\left(\varepsilon_t\right)\varepsilon_t. \tag{4}$$

Given a time series data, the smallest Δt possible is the sampling time τ.

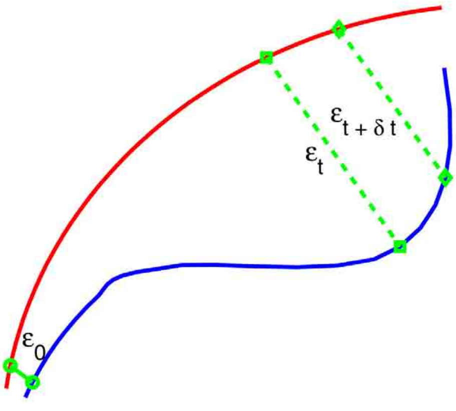

FIGURE 3 | A schematic showing 2 arbitrary trajectories in a general high-dimensional space, with the distance between them at time 0, *t*, and *t* + δt being ε_0, ε_t, and $\varepsilon_{t+\delta t}$, respectively.

Note that the classic algorithm of computing the Lyapunov exponent λ_1 (Wolf et al., 1985) amounts to assuming $\varepsilon_t \sim \varepsilon_0 e^{\lambda_1 t}$ and estimating λ_1 by $(\ln \varepsilon_t - \varepsilon_0)/t$. Depending on ε_0, this may not be the case even for truly chaotic systems, such as shown in **Figure 2**. This is emphasized in the schematic of **Figure 3** – $\varepsilon_{t+\delta t}$ could in fact be smaller than ε_t. A greater difficulty with such an assumption is that for any type of noise, λ_1 can always be greater than 0, leading to misclassifying noise as chaos. This is because ε_t will be closer to the most probable separation so long as ε_0 is small (for a more quantitative discussion of this issue, see Gao and Zheng, 1994b). On the other hand, Eq. 2 does not involve any assumptions, except that Δt is small. As we will see, chaos amounts to $\lambda(\varepsilon)$ being almost constant over a range of ε.

To compute SDLE, we check whether pairs of vectors (V_i, V_i) defined by Eq. 1 satisfy the following *Inequality*,

$$\varepsilon_k \leqslant \left\| V_i - V_j \right\| \leqslant \varepsilon_k + \Delta\varepsilon_k,\ k = 1, 2, 3, \ldots, \tag{5}$$

where ε_k and $\Delta\varepsilon_k$ are arbitrarily chosen small distances, and

$$\left\| V_i - V_j \right\| = \sqrt{\sum_{w=1}^{m} \left(x_{i+(w-1)L} - x_{j+(w-1)L}\right)^2} \tag{6}$$

Geometrically, *Inequality* (5) defines a high-dimensional shell (which reduces to a ball with radius $\Delta\varepsilon_k$ when $\varepsilon_k = 0$; in a 2-D plane, a ball is a circle described by $(x-a)^2 + (y-b)^2 = r^2$, where (a, b) is the center of the circle, and r is the radius). We then monitor the evolution of all such vector pairs (V_i, V_j) within a shell and take the ensemble average over indices i, j. Since we are most interested in exponential or power-law functions, we assume that taking logarithm and averaging can be exchanged, then Eq. 3 can be written as

$$\lambda\left(\varepsilon_t\right) = \frac{\left\langle \ln \left\| V_{i+t+\Delta t} - V_{j+t+\Delta t} \right\| - \ln \left\| V_{i+t} - V_{j+t} \right\| \right\rangle}{\Delta t} \tag{7}$$

where t and Δt are integers in units of the sampling time, the angle brackets denote the average over indices i, j within a shell, and

$$\varepsilon_t = \left\| V_{i+t} - V_{j+t} \right\| = \sqrt{\sum_{w=1}^{m} \left(x_{i+(w-1)L+t} - x_{j+(w-1)L+t}\right)^2} \tag{8}$$

Note that the initial set of shells for computing SDLE serve as initial values of the scales; through evolution of the dynamics, the scales will automatically converge to the range of inherent scales – which are the scales that define Eqs 3 and 4. This point will be clearer after we introduce the notion of *characteristic scale* below.

Also note that when analyzing chaotic time series, the condition

$$\left| j - i \right| \geqslant t_{uncorrelated} \tag{9}$$

needs to be imposed when finding pairs of vectors within a shell, where $t_{uncorrelated}$ denotes a time scale beyond which the two vectors V_i and V_j are no longer along the tangential motions (i.e., close orbital motions similar to two cars driving in the same lane, one following the other closely) of the same trajectory (Gao and Zheng, 1994b). Often $t_{uncorrelated} > (m-1)L$ is sufficient to ensure the elimination of the effects of *tangential motions* and the convergence of initial scales to the inherent scales (Gao et al., 2007).

Finally, we note that

$$\Lambda(t) = \left\langle \ln \left\| V_{i+t} - V_{j+t} \right\| - \ln \left\| V_i - V_j \right\| \right\rangle \tag{10}$$

is called the *time-dependent exponent curves* by Gao and Zheng (1993, 1994a,b). Since $\Lambda(t) = \ln \varepsilon_t - \ln \varepsilon_0$, we immediately see that SDLE amounts to the local slopes of such curves vs.

$$\varepsilon_t = \varepsilon_0 e^{\Lambda(t)}. \tag{11}$$

With this realization, the algorithm for computing SDLE can be summarized by the following pseudo code (the actual Fortran, C, and Matlab codes are available from the authors, or at http://www.gao.ece.ufl.edu/GCTH_Wileybook/programs/lambda_k_curves/):

```
(1) (More or less arbitrarily) choose the scale parameters $\varepsilon_k$, $\Delta\varepsilon_k$,
    $k = 1, 2, 3, \ldots$; properly choose $m$ and $L$ to reconstruct a suitable phase space
    from a scalar time series using Eq. 1; also choose $t_{uncorrelated}$. These are the
    basic parameters needed for lambda.m in step (2).
(2) Compute the time-dependent exponent $\Lambda(t)$ curves:
        for $i = 1{:}N_p - t_{uncorrelated} - T_{max}$
        for $j = i + t_{uncorrelated}{:}N_P - T_{max}$
        check Inequality (5); if valid,
        save $\Lambda(t) = \ln \left|\left|V_{i+t} - V_{j+t}\right|\right|$, $t = 0, 1, \ldots, T_{max}$
        end
        end
(3) Estimate SDLE as the local slopes of $\Lambda(k)$. Specifically, at time $t = k\delta t$,
    where $\delta t$ is the sampling time, the scale parameter $\varepsilon_t$ is given by Eq. 11,
    while the local slope of $\Lambda(k)$ may be estimated by

        $(\Lambda(k+1) - \Lambda(k-1))/2k\delta t$.
```

Equivalently, the local slope may be estimated based on $\ln \varepsilon_t$, where ε_t is given by Eq. 11. To improve estimation of the local slope of $\Lambda(k)$, filtering may be used to suppress local variations.

2.1. SCALING LAWS FOR SDLE

SDLE has distinctive scaling laws for chaotic signals and $1/f^{\alpha}$ processes. First we analyze the chaotic Lorenz system (shown in **Figure 2**) with stochastic forcing:

$$\begin{aligned} dx/dt &= -16(x-y) + D\eta_1(t), \\ dy/dt &= -xz + 45.92x - y + D\eta_2(t), \\ dz/dt &= xy - 4z + D\eta_3(t). \end{aligned} \tag{12}$$

where $\eta_i(t)$, $i = 1, 2, 3$ are independent Gaussian noise forcing terms with zero mean and unit variance. When $D = 0$, the system is clean. **Figure 4** (top) shows a few $\Lambda(t)$ curves for the clean Lorenz system; the bottom of the Figure shows five SDLE curves, for the cases with $D = 0, 1, 2, 3, 4$. The computations are done with 10000 points and $m = 4$, $L = 2$. We observe the following interesting features:

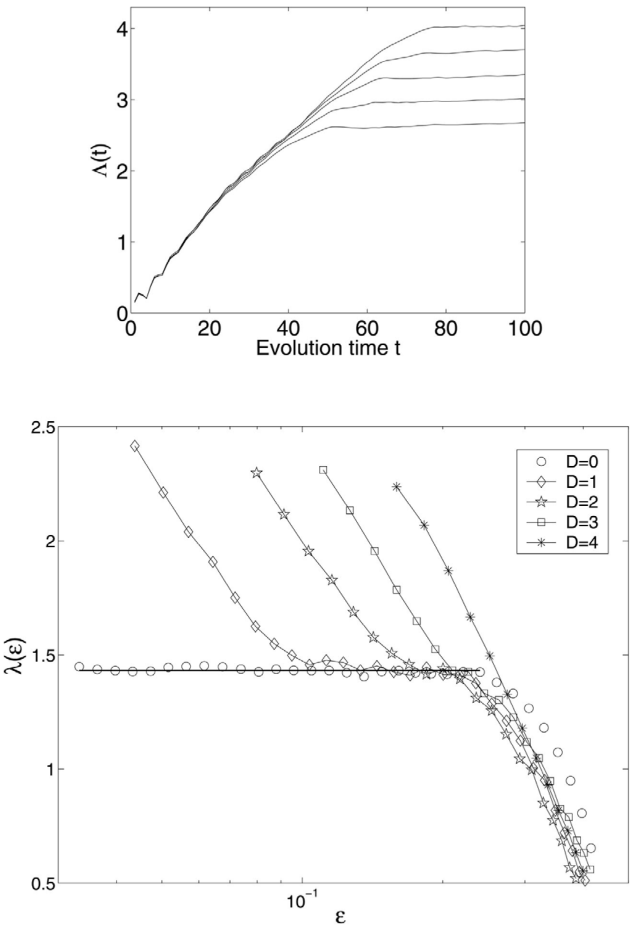

FIGURE 4 | Top: $\Lambda(t)$ curves for the clean Lorenz system; bottom: SDLE $\lambda(\varepsilon)$ curves for clean and noisy Lorenz systems.

(1) For the *clean chaotic signal*, $\lambda(\varepsilon)$ fluctuates slightly around a constant. As is expected, this constant is the very largest positive Lyapunov exponent, λ_1,

$$\lambda(\varepsilon) = \lambda_1. \tag{13}$$

The small fluctuation in $\lambda(\varepsilon)$ is due to the fact that the divergence (i.e., expansion) rate on the Lorenz attractor is not uniform (i.e., varies from one region to another). This nonuniform divergence is the origin of multifractality in chaotic systems.

(2) When there is *stochastic forcing*, $\lambda(\varepsilon)$ is no longer a constant when ε is small, but diverges to infinity as $\varepsilon \to 0$ according the following scaling law,

$$\lambda(\varepsilon) \sim -\gamma \ln \varepsilon, \tag{14}$$

where γ is a coefficient controlling the speed of loss of information (i.e., defined as the measure of uncertainty involved in predicting the value of a random variable). This feature suggests that entropy generation is infinite when the scale ε approaches zero.

(3) When the *noise* is increased, the part of the curve with $\lambda(\varepsilon) \sim -\gamma \ln \varepsilon$ shifts to the right. In fact, the plateau (i.e., the chaotic signature) can no longer be identified when D is increased beyond 3.

To facilitate practical applications, we emphasize that there are two features that are important in real data analysis: (i) the location of the $-\gamma \ln \varepsilon$ curve; this includes the slope and the position of the "transition" point from $-\gamma \ln \varepsilon$ curve to the plateau scaling; and (ii) the width of the plateau.

Note that similar results to those shown in **Figure 4** have been observed in other model chaotic systems, such as the Mackey-Glass delay differential equation with multiple positive Lyapunov exponents (Mackey and Glass, 1977). Also note that Eq. 14 characterizes various types of noise, including independent identically distributed random variables, or noise with correlations (including long-range correlation) for time scale up to the embedding window, $(m-1)L$. This means SDLE is close to zero if *Inequality* (9) is imposed when it is computed.

At this point, it is beneficial to introduce a concept, *characteristic scale,* or *limiting scale*, ε_∞, which is defined as the scale where SDLE is close to 0. In terms of the $\Lambda(t)$ curves, this amounts to where the curves are flat, as shown in the top plot of **Figure 4**. If one starts from $\varepsilon_0 \ll \varepsilon_\infty$, then, regardless of whether the data is deterministically chaotic or simply random, ε_t will initially increase with time and gradually settle around ε_∞. Consequentially, $\lambda(\varepsilon_t)$ will be positive before ε_t reaches ε_∞. On the other hand, if one starts from $\varepsilon_0 \gg \varepsilon_\infty$, then ε_t will simply decrease, yielding negative $\lambda(\varepsilon_t)$, again regardless of whether the data are chaotic or random. When $\varepsilon_0 \sim \varepsilon_\infty$, then $\lambda(\varepsilon_t)$ will stay around 0. For stationary noise processes, the only scale available after $t > (m-1)L$ would be this limiting scale, since SDLE will always close to 0. *In other words, for noise, the only scale resolvable is* ε_∞. Note however, for some dynamical systems, ε_∞ may not be a single point, but a function of time, such as a periodic function of time. When this is the case, the motion can be said to have large scale coherent motions. This is often the case for physiological data.

Next we consider $1/f^\alpha$ processes. Such type of processes is ubiquitous in science and engineering (see Gao et al., 2007 and references therein). Two important prototypical models for such processes are fractional Brownian motion (fBm) process (Mandelbrot, 1982) and ON/OFF intermittency with power-law distributed ON and OFF periods (Gao et al., 2006a). For convenience, we introduce the Hurst parameter $0 < H < 1$ through a simple equation,

$$\alpha = 2H + 1. \tag{15}$$

Depending on whether H is smaller than, equal to, or larger than 1/2, the process is said to have anti-persistent correlation, short-range correlation, and persistent long-range correlation (Gao et al., 2006a). Note that $D = 1/H$ is the fractal dimension of such processes, and Kolmogorov's 5/3 law for the energy spectrum of fully developed turbulence (Frisch, 1995) corresponds to $H = 1/3$.

It is well-known that the variance of such stochastic processes increases with t as $t^{2\mathrm{H}}$. Translating this into the average distance between nearby trajectories, we immediately have

$$\varepsilon_t = \varepsilon_0 t^H. \tag{16}$$

To obtain SDLE from Eq. 16, we can use the defining Eq. 3 to obtain $\lambda(\varepsilon_t) \sim H/t$. Expressing t by ε_t, we obtain

$$\lambda\left(\varepsilon_t\right) \sim H\varepsilon_t^{-1/H} \tag{17}$$

Equation 17 can be readily verified by calculating $\lambda(\varepsilon_t)$ from such processes. Therefore, SDLE offers a new means of estimating H. In fact, SDLE improves analysis over commonly used fractal analysis methods in two important situations: (i) in some non-stationary environments where commonly used fractal analysis methods fail to detect fractal structures from the data, SDLE may still be able to; this will be shown shortly; and (ii) Eq. 17 also characterizes stochastic limit cycles. This is true for many model systems (Gao et al., 1999a,b, 2006b; Hwang et al., 2000), as well as essential and Parkinsonian tremors (Gao and Tung, 2002).

SDLE also has distinct scaling laws for random Levy processes, and complex motions with multiple scaling laws on different scale ranges. For the details, we refer to Gao et al. (2006b, 2007).

2.2. DETECTING INTERMITTENT CHAOS BY SDLE

Intermittent chaos is a type of complex motion where regular (i.e., periodic) and chaotic motions alternate. It is a crucial ingredient of the intermittent route to chaos, one of the most famous and universal routes to chaos (Gao et al., 2007). One can envision that intermittent chaos may be associated with the physiological transitions from normal to abnormal states, and *vice versa*. Therefore, studying intermittent chaos can be very important for physiology in general and pathology in particular. Since intermittent chaos is a universal phenomena to many dynamical systems, without loss of generality and to ease repeatability, we examine the logistic map

$$x_{n+1} = ax_n\left(1 - x_n\right), \tag{18}$$

with $a = 3.8284$. An example of the time series is shown in **Figure 5A**. We observe that time intervals exhibiting chaos are very short compared with those exhibiting periodic motions. Traditional methods for computing Lyapunov exponent, being based on global average, is unable to quantify chaos in such intermittent situations, since the laminar phase dominates. Neither can FSLE, since it requires that divergence dominates most of the time. Interestingly, the SDLE curve shown in **Figure 5B** clearly indicates existence of chaotic motions, since the plateau region extends almost one decade in the scale (see arrow A in the Figure).

One might wonder why **Figure 5B** is more complicated than **Figure 4** (bottom), even though the model system is a simpler logistic map. The reason is that the motion now is intermittent. Realizing intermittent transitions, we can readily understand all the features in **Figure 5B**: the scale regions indicated by arrows B and C in **Figure 5B** are due to the transitions from periodic to chaotic motions, and *vice versa.* To understand the transition, consider two very close trajectories in the laminar region. So far as they stay in the laminar region, ε will remain small. When both trajectories enter the chaotic region, the distance between them will become greater – this divergence becomes stronger when the trajectories get deeper into the chaotic region, till it stabilizes at the plateau region, after it is fully within the chaotic region. This

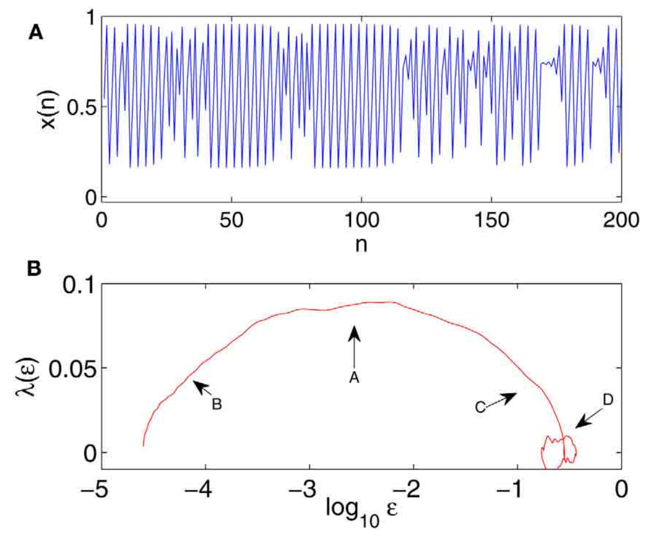

FIGURE 5 | (A) An intermittent time series generated by the logistic map with $a = 3.8284$. **(B)** The SDLE curve for a time series of 10000 points, with $m = 4$, $L = 1$, and a shell size of $(2^{-13.5}, 2^{-13})$. A plateau, indicated by arrow A, is clearly visible. Regions indicated by arrows B and C are due to transitions between periodic and chaotic motions, and arrow D indicates the region of oscillatory motions.

argument is equally valid when the motion gets out of the chaotic region.

The discussion above can be readily extended to understand the circular structure, indicated as arrow D, in **Figure 5B**. This structure is caused by the large scale laminar flows (i.e., oscillatory motions). Region D is an example of a limiting scale being not a constant. Such a feature can often arise in physiological data, as we will see shortly in Section 4.

In summary, we conclude that the oscillatory part of the data only affects the scale range where $\lambda(\varepsilon) \sim 0$. It cannot affect the positive portion of $\lambda(\varepsilon)$. Therefore, SDLE has a unique scale separation property such that different motions are manifested on different scales.

2.3. DETECTING FRACTAL STRUCTURE FROM NON-STATIONARITY DATA

The HRV data shown in **Figure 1A** motivates us to consider complicated processes generated by the following two scenarios. One is to randomly concatenate $1/f^{2H+1}$ and oscillatory components. Another is to superimpose oscillatory components on $1/f^{2H+1}$ processes at randomly chosen time intervals. Either scenario generates signals that appear quite similar to that shown in **Figure 1A**. The $\lambda(\varepsilon)$ curves for such processes are shown in **Figure 6**, for a wide range of the H parameter instances. We observe well-defined power-law relations, consistent with Eq. 17, when $\lambda(\varepsilon) > 0.02$. **Figure 6** clearly shows that oscillatory components in the signals can only affect the SDLE where $\lambda(\varepsilon)$ is close to 0. The effects of oscillatory components on SDLE observed in these scenarios is another manifestation of SDLE's scale separation property. It is most important to emphasize that none of other commonly used fractal analysis methods are able to detect fractal structure from such non-stationary data.

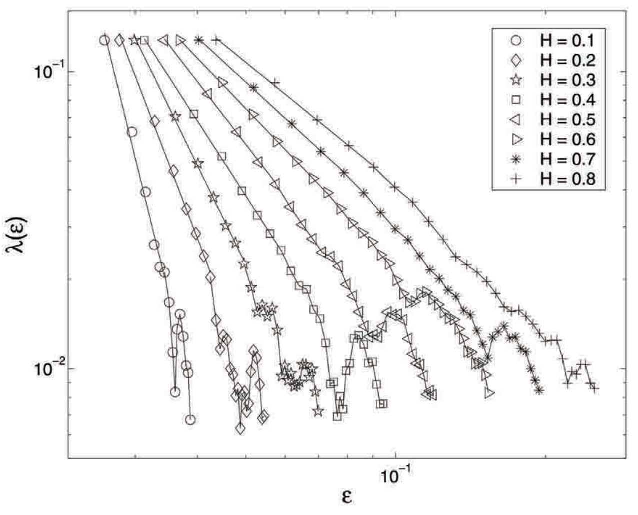

FIGURE 6 | SDLE λ(ε) vs. ε curves for the simulation data. Eight different H values are considered. To put all the curves on one plot, the curves for different H values (except the smallest one considered here) are arbitrarily shifted rightward.

Now, let us ask: when we perturb chaotic data by similar procedures, will we still be able to detect chaos? The answer is yes. In fact, the intermittent chaos discussed above may be viewed as an example of such a procedure.

We are now ready to fully understand why the SDLE can deal with the types of non-stationary data constructed here. One type of non-stationarity causes shifts of the trajectory in phase space – the greater the non-stationarity, the larger the shifts. SDLE, however, cannot be significantly affected by trajectory shifts, especially large ones, since it is based on the co-evolution of pairs of vectors within chosen small shells. The other type is related to oscillatory components. The oscillatory components only affect SDLE where it is close to zero, therefore, will not alter the distinct scaling for chaos and fractal processes.

3. APPLICATIONS: BIOLOGICAL DATA ANALYSIS

As we have mentioned, the popularity of chaos and fractal theories in modeling physiology is closely related to the desire of learning whether a healthy brain, heart, etc., may be associated with greater complexity, greater chaoticity, or greater adaptability due to properties such as long-range correlations. While such complexity interpretations are very appealing, one has to envision that the reality is more difficult, since disease diagnosis is complicated by many factors where the cause is unknown. For example, as man-made chemicals are designed and used, it has yet to know how they affect the body. To (1) shed new light on the interpretation of complexity of physiological data, and (2) illustrate SDLE's clinical relevance, in this section, we apply SDLE to examine two types of physiological data, HRV and EEG. As we shall see, the most relevant scaling law for these data is Eq. 14, which cannot be obtained by standard chaos or conventional random fractal analysis. Due to space limitations, we shall only briefly describe a complexity measure, when it is used for comparison with SDLE.

3.1. EEG ANALYSIS

EEG signals provide a wealth of information about brain dynamics, especially related to cognitive processes and pathologies of the brain such as epileptic seizures. To understand the nature of brain dynamics as well as to develop novel methods for the diagnosis of brain pathologies, a number of complexity measures have been used in the analysis of EEG data. These include the Lempel-Ziv (LZ) complexity (Lempel and Ziv, 1976), the permutation entropy (Cao et al., 2004), the Lyapunov exponent (LE; Wolf et al., 1985), the Kolmogorov entropy (Grassberger and Procaccia, 1983b), the correlation dimension D_2 (Grassberger and Procaccia, 1983a; Martinerie et al., 1998), and the Hurst parameter (Peng et al., 1994; Hwa and Ferree, 2002; Robinson, 2003). Since foundations of information theory, chaos theory, and random fractal theory are different, and brain dynamics are complicated, involving multiple spatial-temporal scales, it is natural and important for us to ask whether there exist relations among these complexity measures, and if so, how to understand those relations.

The EEG signals analyzed here were measured intracranially by the Shands hospital at the University of Florida (Gao et al., 2011a). Such EEG data are also called *depth EEG* and are considered cleaner and more free of artifacts than scalp (or surface) EEG. Altogether, we have analyzed 7 patients' multiple channel EEG data, each with a duration of a few hours, with a sampling frequency of 200 Hz. When analyzing EEG for epileptic seizure prediction/detection, it is customary to partition a long EEG signal into short windows of length W points, and calculate the measure of interest for each window. The criterion for choosing W is such that the EEG signal in each window is fairly stationary, is long enough to reliably estimate the measure of interest, and is short enough to accurately resolve localized activities such as seizures. Since seizure activities usually last about 1–2 min, in practice, one often chooses W to be about 10 sec. When applying methods from random fractal theory such as *detrended fluctuation analysis* (DFA) (Peng et al., 1994), it is most convenient when the length of a sequence is a power of 2. Therefore, we have chosen $W = 2 \times 1024 = 2048$ when calculating various measures. We have found, however, that the variations of these measures with time are largely independent of the window size W. The relations among the measures studied here are the same for all the 7 patients' EEG data, so we illustrate the results based on only one patient's EEG signals.

We have examined the variation of $\lambda(\varepsilon)$ with ε is for each segment of the EEG data. Two representative examples for seizure and non-seizure segments are shown in **Figure 7**. We observe that on a specific scale ε^*, the two curves cross. Loosely, we may term any $\varepsilon < \varepsilon^*$ as small scale, while any $\varepsilon > \varepsilon^*$ as large scale. Therefore, on small scales, $\lambda(\varepsilon)$ is smaller for seizure than for non-seizure EEG, while on large scales, the opposite is true. The variations of $\lambda_{\mathrm{small}-\varepsilon}$ and $\lambda_{\mathrm{large}-\varepsilon}$ with time for this patient's data, where small $-\ \varepsilon$ and large $-\ \varepsilon$ stand for (more or less arbitrarily) chosen fixed small and large scales, are shown in **Figures 8A,B**, respectively. We observe two interesting features: (i) the pattern of variation of $\lambda_{\mathrm{small}-\varepsilon}(t)$ is reciprocal of that of $\lambda_{\mathrm{large}-\varepsilon}(t)$. This result can be expected from **Figure 7**. (ii) The variations in $\lambda_{\mathrm{small}-\varepsilon}(t)$ and $\lambda_{\mathrm{large}-\varepsilon}(t)$ clearly indicate the two seizure events. Therefore, either $\lambda_{\mathrm{small}-\varepsilon}(t)$ or $\lambda_{\mathrm{large}-\varepsilon}(t)$ can be used to accurately detect epileptic seizures.

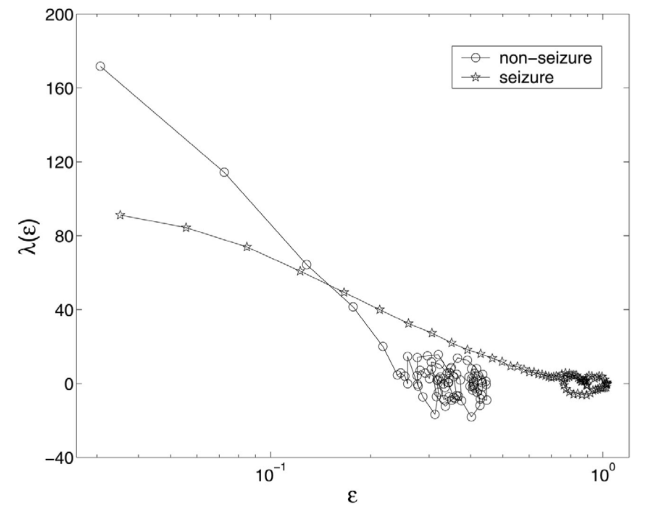

FIGURE 7 | Representative SDLE λ(ε) (per second) vs. ε for a seizure and non-seizure EEG segment.

We now compare the SDLE with three commonly used measures from chaos theory, the largest positive Lyapunov exponent (LE), which we have discussed earlier; the correlation entropy (Grassberger and Procaccia, 1983b), and the correlation dimension (Grassberger and Procaccia, 1983a). We also choose one measure from random fractal theory, the Hurst parameter. We discuss the three measures from chaos theory first.

As we have discussed, LE is a dynamic quantity, characterizing the exponential growth of an infinitesimal line segment, $\varepsilon_t \sim \varepsilon_0 e^{\lambda_1 t}, \varepsilon_0 \to 0$. For truly chaotic signals, $1/\lambda_1$ gives the prediction time scale of the dynamics. Also, it is well-known that the sum of all the positive Lyapunov exponents in a chaotic system equals the Kolmogorov-Sinai (KS) entropy. The KS entropy characterizes the rate of creation of new information (or loss of prior knowledge) in a system. It is zero, positive, and infinite for regular, chaotic, and random motions, respectively. However, it is difficult to compute. Therefore, one usually computes the *correlation entropy* K_2, which is a tight lower bound of the KS entropy. Similarly, the box-counting dimension, which is a geometrical quantity characterizing the minimal number of variables that are needed to fully describe the dynamics of a motion, is difficult to compute, and one often calculates the correlation dimension D_2 instead. Again, D_2 is a tight lower bound of the box-counting dimension. For in-depth discussions of K_2 and D_2, we refer to Gao et al. (2012).

From the above brief descriptions, one would expect that $\lambda_1(t)$ and $K_2(t)$ are similar, while $D_2(t)$ has little to do with either $\lambda_1(t)$ or $K_2(t)$. Surprisingly, from **Figures 8C,D,E**, we observe that this is not the case: $\lambda_1(t)$ is similar to $D_2(t)$, but reciprocal of $K_2(t)$. In a moment, we shall explain how these puzzling relations may be understood based on $\lambda_{\mathrm{small}-\varepsilon}(t)$ and $\lambda_{\mathrm{large}-\varepsilon}(t)$.

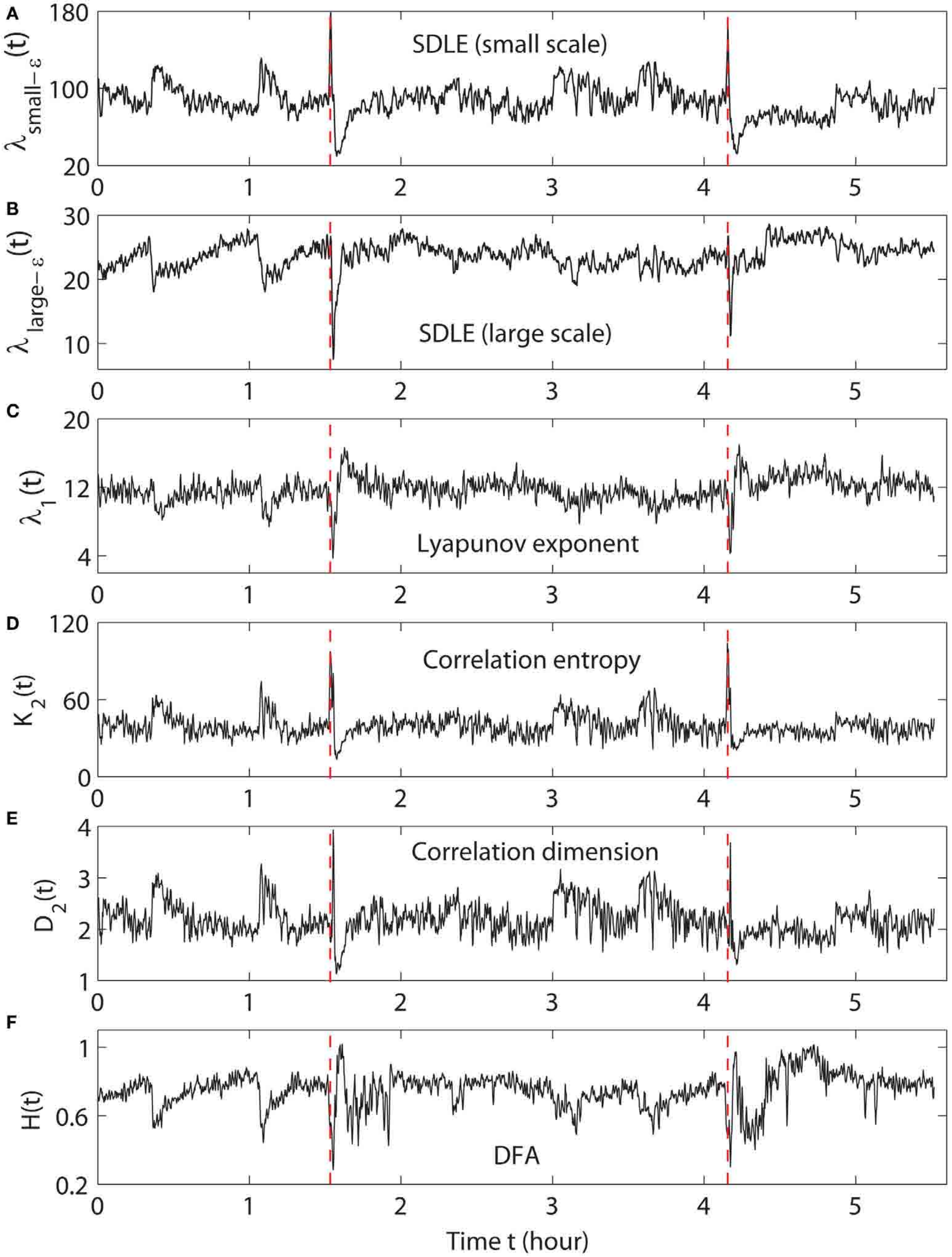

FIGURE 8 | The variation of (A) $\lambda_{small-\varepsilon}$, (B) $\lambda_{large-\varepsilon}$, (C) the LE, (D) the K_2 entropy, (E) the D_2, and (F) the Hurst parameter with time for EEG signals of a patient. The vertical dashed lines in **(A–F)** indicate seizure occurrence times determined by medical experts.

Next we consider the calculation of the Hurst parameter H. As pointed out earlier, H characterizes the long-term correlations in a time series. There are many different ways to estimate H. We have chosen DFA (Peng et al., 1994), since it is more reliable (Gao et al., 2006a), and has been used to study EEG data (Hwa and Ferree, 2002; Robinson, 2003).

Figure 8F shows $H(t)$ for our EEG data. We observe that the pattern of $H(t)$ is very similar to that of $\lambda_1(t)$, but reciprocal to $K_2(t)$ and $D_2(t)$. Such relations cannot be readily understood intuitively, since the foundations for chaos theory and random fractal theory are entirely different.

Let us now resolve all of the curious relations observed between $\lambda_1(t)$, $K_2(t)$, $D_2(t)$, and $H(t)$.

(1) Generally, entropy measures the randomness of a dataset. This pertains to small scale. Therefore, $K_2(t)$ should be similar to $\lambda_{\text{small}-\varepsilon}(t)$. This is indeed the case. We should point out that we have also calculated other entropy-related measures, such as the Lempel-Ziv complexity (Lempel and Ziv, 1976), which is closely related to the Shannon entropy, and the permutation entropy (Cao et al., 2004), and observed similar variations. Therefore, we can conclude that the variation of the entropy is represented by $\lambda_{\text{small}-\varepsilon}(t)$, regardless of how entropy is defined.

(2) To understand why $\lambda_1(t)$ calculated by the algorithm of Wolf et al. (1985) corresponds to $\lambda_{\text{large}-\varepsilon}(t)$, we note that the algorithm of Wolf et al. (1985) involves a scale parameter that whenever the divergence between a reference and a perturbed trajectory exceeds this chosen scale, a renormalization procedure is performed. When the algorithm of Wolf et al. (1985) is applied to a time series with only a few thousand points, in order to obtain a well-defined LE, a fairly large scale parameter has to be chosen. This is the reason that the LE and $\lambda_{\text{large}-\varepsilon}$ are similar. In fact, the scale we have chosen to calculate $\lambda_1(t)$ is even larger than that for calculating $\lambda_{\text{large}-\varepsilon}(t)$. This is the reason that the value of $\lambda_1(t)$ shown in **Figure 8C** is smaller than that of $\lambda_{\text{large}-\varepsilon}(t)$ shown in **Figure 8B**.

(3) It is easy to see that if one fits the $\lambda(\varepsilon)$ curves shown in **Figure 7** by a straight line, then the variation of the slope with time should be similar to $\lambda_{\text{small}-\varepsilon}(t)$ but reciprocal of $\lambda_{\text{large}-\varepsilon}(t)$. Such a pattern will be preserved even if one takes the logarithm of $\lambda(\varepsilon)$ first and then does the fitting. Such a discussion makes it clear that even if EEG is not ideally of the $1/f^{2H+1}$ type, qualitatively, the relation $\lambda(\varepsilon) \sim \varepsilon^{-1/H}$ holds. This in turn implies $D_2 \sim 1/H$. With these arguments, it is clear that the seemingly puzzling relations among the measures considered here can be readily understood by the $\lambda(\varepsilon)$ curves. More importantly, we have established that commonly used complexity measures can be related to the values of the SDLE at specific scales.

As we have pointed out, around the characteristic scale ε_∞, $\lambda(\varepsilon)$ is always close to 0. The pattern of $\lambda(\varepsilon)$ around ε_∞ is governed by the structured components in the data, such as the α, γ, β, and δ brain waves. From **Figure 7**, we observe that the patterns for seizure and non-seizure EEG segments are very different. In particular, the pattern of the limiting scale for seizure EEG resembles that of the intermittent chaos indicated by arrow D in **Figure 5**. Since the brain dynamics on this scale are different from those on smaller scales, such information is clearly helpful in preliminary detection or prediction of seizures. However, we shall not pursue this issue further here, as further use of the SDLE methods for seizure forewarning would require coordination with clinical verification.

3.2. HRV ANALYSIS

HRV is an important dynamical variable of the cardiovascular function. Its most salient feature is the spontaneous fluctuation, even when the environmental parameters are maintained constant and no perturbing influences can be identified. Since the observation that HRV is related to various cardiovascular disorders (Hon and Lee, 1965), a number of methods have been proposed to analyze HRV data. They include methods based on simple statistics from time and frequency domain analyses (see Malik, 1996 and references therein), as well as those derived from chaos theory and random fractal theory (Kobayashi and Musha, 1982; Goldberger and West, 1987; Babyloyantz and Destexhe, 1988; Kaplan and Goldberger, 1991; Pincus and Viscarello, 1992; Bigger et al., 1996; Ho et al., 1997). We shall now show that the SDLE can readily characterize the hidden differences in the HRV under healthy and diseased conditions, and shed new light on the dynamics of the cardiovascular system.

We examine two types of HRV data, one for healthy subjects, and another for subjects with the congestive heart failure (CHF), a life-threatening disease. The data were downloaded from the (Physionet, 2011). There are 18 healthy subjects and 15 subjects with CHF. Part of these datasets were analyzed by random fractal theory. In particular, 12 of the 15 CHF datasets were analyzed by wavelet based multifractal analysis (Ivanov et al., 1999), for the purpose of distinguishing healthy subjects from CHF patients. For ease of comparison, we take the first 3×10^4 points of both groups of HRV data for analysis. In **Figures 9A,B**, we have shown two typical $\lambda(\varepsilon)$ vs. ε curves, one for a healthy subject, and another for a patient with CHF. We observe that for the healthy subject, $\lambda(\varepsilon)$ linearly decreases with $\ln \varepsilon$ before λ reaches around 0, or, before ε settles around the characteristic scale, ε_∞. Recall that this is a characteristic of noisy dynamics (**Figure 4**). For the CHF case plotted in **Figure 9B**, we observe that the $\lambda(\varepsilon)$ is oscillatory, with its value always close to 0, and hence, the only scale resolvable is around ε_∞. Since the length of the time series used in our analysis for the healthy and the CHF subjects is the same, the inability of resolving the $\lambda(\varepsilon)$ behavior on scales much smaller than ε_∞ for patients with CHF strongly suggests that the dimension of the dynamics of the cardiovascular system for CHF patients is considerably higher than that for healthy subjects.

We now discuss how to distinguish between healthy subjects and patients with CHF from HRV analysis. We have devised two simple measures, or features. The first feature characterizes how well the linear relation between $\lambda(\varepsilon)$ and $\ln \varepsilon$ can be defined. We have quantified this by calculating the error between a fitted straight line and the actual $\lambda(\varepsilon)$ vs. $\ln \varepsilon$ plots of **Figures 9A,B**. The second feature is to characterize how well the characteristic scale ε_∞ is defined. This is quantified by the ratio between two scale ranges, one is from the 2nd to the 6th point of the $\lambda(\varepsilon)$ curves, and another is from the 7th to the 11th point of the $\lambda(\varepsilon)$ curves. Now each subject's data can be represented as a point in the feature plane, as shown in **Figure 10**. We observe that for healthy subjects, feature 1 is generally very small, but feature 2 is large, indicating that the dynamics of the cardiovascular system is like a non-linear system with stochasticity, (i.e., with resolvable small scale behaviors and well-defined characteristic scale ε_∞). The opposite is true for the patients with CHF: feature 1 is large, but feature 2 is small,

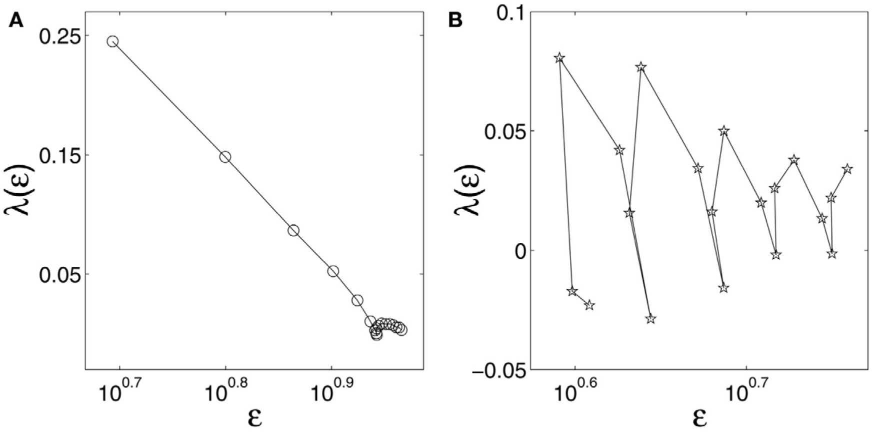

FIGURE 9 | λ(ε) (per beat) vs. ε (in semi-log scale) for HRV data of (A) a healthy subject and (B) a subject with CHF.

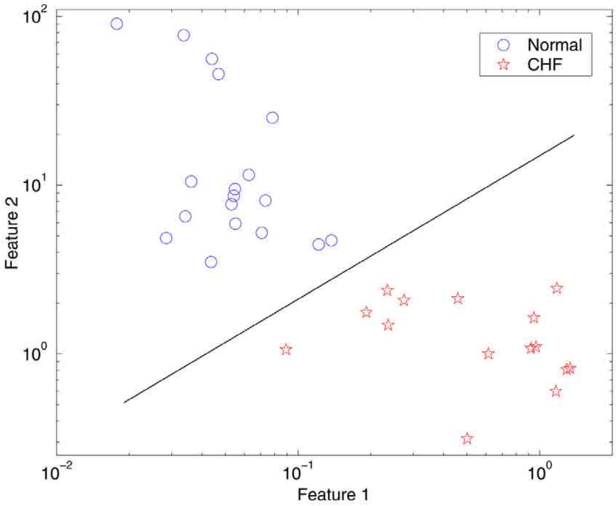

FIGURE 10 | Feature plane separating normal subjects from subjects with CHF, where Feature 1 quantifies the goodness-of-fit of Eq. 14 to the actual SDLE curve, and Feature 2 is related to how well the characteristic scale ε_∞ is defined.

indicating that not only small scale behaviors of the λ(ε) curves cannot be resolved, but also that the characteristic scale ε_∞ is not well-defined. Very interestingly, these two simple features separate completely the normal subjects from patients with CHF. The results show that no formal methods of statistical clustering are needed and that presentation of the feature space can be readily usable for diagnostics. In fact, each feature alone can almost perfectly separate the two groups of subjects studied here.

It is interesting to note that for the purpose of distinguishing normal HRV from CHF HRV, the features derived from SDLE are much more effective than other metrics including the Hurst parameter, the sample entropy, and multiscale entropy. For the details of the comparisons, we refer to Hu et al. (2010).

Finally, we emphasize that the results presented here should not be interpreted as 100% accurate in distinguishing normal from CHF patients, since only 18 normal and 15 CHF HRV data sets were available to us and analyzed here. It merits noting, however, that other approaches, such as wavelet based multifractal analysis (Ivanov et al., 1999), are not able to achieve the classification rate of SDLE, when all these data were used. The preliminary analysis demonstrates that SDLE could be used over collected HRV data as a first indication of possible non-healthy cardiovascular issues. The use of SDLE could provide valuable complementary information in patient testing.

4. CONCLUDING REMARKS

In this paper, we have discussed a multiscale complexity measure, the SDLE. We have shown that it can readily (1) characterize low-dimensional chaos, random $1/f^\alpha$ processes, and stochastic limit cycles, (2) detect intermittent chaos, and (3) conveniently deal with non-stationarity, especially to detect fractal from non-stationary data. Furthermore, we have shown that SDLE can accurately detect epileptic seizures from EEG and distinguish healthy subjects from patients with CHF from HRV. More importantly, we have established that commonly used complexity measures for EEG can be related to the value of the SDLE at specific scales, and that the pattern of the SDLE around the characteristic scale ε_∞ contains a lot of useful information on the structured components of the data that may greatly help detect significant patterns. Because of the ubiquity of chaos-like motions and $1/f^\alpha$-type processes and the complexity of HRV and EEG data, our analyses strongly suggest that the SDLE is potentially important for clinical practice, and provides a comprehensive characterization of complex data arising from a wide range of fields in science and engineering.

Our analyses have a number of important implications.

(1) To comprehensively characterize the complexity of complicated data such as HRV or EEG data, a wide range of scales has to be considered, since the complexity may be different on different scales. For this purpose, the entire λ(ε) curve, where ε is such that λ(ε) is positive, provides a good solution. Using the entire λ(ε) curve is particularly important when one wishes to compare the complexity between two signals – the complexity for one signal may be higher on some scales, but

lower on other scales. The situation shown in **Figure 7** may be considered one of the simplest.

(2) For detecting important events such as epileptic seizures, $\lambda_{\text{small}-\varepsilon}$ and $\lambda_{\text{large}-\varepsilon}$ appear to provide better defined features than other commonly used complexity measures. This may be due to the fact that $\lambda_{\text{small}-\varepsilon}$ and $\lambda_{\text{large}-\varepsilon}$ are evaluated at fixed scales, while other measures are not. In other words, scale mixing may blur the features for events being detected, such as seizures.

(3) In recent years, there has been much effort in searching for cardiac chaos (Goldberger and West, 1987; Babyloyantz and Destexhe, 1988; Kaplan and Goldberger, 1991; Garfinkel et al., 1992; Fortrat et al., 1997; Kaneko and Tsuda, 2000). Due to the inability of unambiguously distinguishing deterministic chaos from noise by calculating the largest positive Lyapunov exponent and the correlation dimension, it is still unclear whether the control mechanism of cardiovascular system is truly chaotic or not. Our analysis here highly suggests that if cardiac chaos does exist, it is more likely to be identified in healthy subjects than in pathological groups. This is because the dimension of the dynamics of the cardiovascular system appears to be lower for healthy than for pathological subjects. Intuitively, such an implication makes sense, because a healthy cardiovascular system is a tightly coupled system with coherent functions, while components in a malfunctioning cardiovascular system are somewhat loosely coupled and function incoherently.

As example applications, we have focused on the analyses of HRV and EEG data here. It is evident that SDLE will be useful for other kinds of physiological data analyses. While much of the past as well as current research has been focused on determining whether some experimental data are chaotic or not, the scaling laws of SDLE suggest that it is often feasible to obtain the defining parameters of the data under study, without a focus on assessing the chaotic nature of the data. While in principle, SDLE is able to do so without pre-processing of the data under study, suitable detrending and denoising may help. A particularly simple and versatile procedure is the smooth adaptive filter developed by the authors, which has been successfully applied to recover chaos in an extremely noisy environment (Hu et al., 2009b; Gao et al., 2010, 2011b; Tung et al., 2011).

ACKNOWLEDGMENTS

This work is supported in part by U.S. NSF grants CMMI-1031958 and 0826119 as well as by the State Key Laboratory of Non-linear Mechanics (LNM), Institute of Mechanics, Chinese Academy of Sciences, Beijing, People's Republic of China. We also thank Dr. Jay Holden and two anonymous reviewers, for their many constructive comments which have considerably improved the manuscript.

REFERENCES

Akselrod, S., Gordon, D., Ubel, F., Shannon, D., Barger, M., and Cohen, R. (1981). Power spectrum analysis of heart rate fluctuation: a quantitative probe of beat-to-beat cardiovascular control. *Science* 213, 220–222.

Ashkenazy, Y., Ivanov, P., Havlin, S., Peng, C., Goldberger, A., and Stanley, H. (2001). Magnitude and sign correlations in heartbeat fluctuations. *Phys. Rev. Lett.* 86, 1900–1903.

Aurell, E., Boffetta, G., Crisanti, A., Paladin, G., and Vulpiani, A. (1996). Growth of non-infinitesimal perturbations in turbulence. *Phys. Rev. Lett.* 77, 1262.

Aurell, E., Boffetta, G., Crisanti, A., Paladin, G., and Vulpiani, A. (1997). Predictability in the large: an extension of the concept of Lyapunov exponent. *Physica A* 30, 1–26.

Babyloyantz, A., and Destexhe, A. (1988). Is the normal heart a periodic oscillator? *Biol. Cybern.* 58, 203–211.

Bassingthwaighte, J., Liebovitch, L., and West, B. (1994). *Fractal Physiology.* New York: Oxford University Press.

Bigger, J., Steinman, R., Rolnitzky, L., Fleiss, J., Albrecht, P., and Cohen, R. (1996). Power law behavior of rr-interval variability in healthy middle-aged persons, patients with recent acute myocardial infarction, and patients with heart transplants. *Circulation* 93, 2142–2151.

Cao, Y., Tung, W., Gao, J., Protopopescu, V., and Hively, L. (2004). Detecting dynamical changes in time series using the permutation entropy. *Phys. Rev. E Stat. Nonlin. Soft Matter Phys.* 70, 046217.

Costa, M., Goldberger, A., and Peng, C. (2005). Multiscale entropy analysis of biological signals. *Phys. Rev. E Stat. Nonlin. Soft Matter Phys.* 71, 021906.

Dettmann, C., and Cohen, E. (2000). Microscopic chaos and diffusion. *J. Stat. Phys.* 101, 775–817.

Fortrat, J., Yamamoto, Y., and Hughson, R. (1997). Respiratory influences on non-linear dynamics of heart rate variability in humans. *Biol. Cybern.* 77, 1–10.

Fraser, A., and Swinney, H. (1986). Independent coordinates for strange attractors from mutual information. *Phys. Rev. A* 33, 1134–1140.

Frisch, U. (1995). *Turbulence – The Legacy of A.N. Kolmogorov*. Cambridge: University Press.

Gao, J. (1997). Recognizing randomness in a time series. *Physica D* 106, 49–56.

Gao, J., Cao, Y., Tung, W., and Hu, J. (2007). *Multiscale Analysis of Complex Time Series – Integration of Chaos and Random Fractal Theory, and Beyond.* Hoboken, NJ: Wiley.

Gao, J., Chen, C., Hwang, S., and Liu, J. (1999a). Noise-induced chaos. *Int. J. Mod. Phys. B* 13, 3283–3305.

Gao, J., Hwang, S., and Liu, J. (1999b). When can noise induce chaos? *Phys. Rev. Lett.* 82, 1132–1135.

Gao, J., Hu, J., Mao, X., and Tung, W. (in press). *Detecting Low-Dimensional Chaos by the "Noise Titration" Technique: Possible Problems and Remedies.* Chaos, Solitons, & Fractals.

Gao, J., Hu, J., and Tung, W. (2011a). Complexity measures of brain wave dynamics. *Cogn. Neurodyn.* 5, 171–182.

Gao, J., Hu, J., and Tung, W. (2011b). Facilitating joint chaos and fractal analysis of biosignals through nonlinear adaptive filtering. *PLoS ONE* 6, e24331. doi:10.1371/journal.pone.0024331

Gao, J., Hu, J., and Tung, W. (2012). Entropy measures for biological signal analysis. *Nonlinear Dyn.* doi: 10.1007/s11071-011-0281-2

Gao, J., Hu, J., Tung, W., Cao, Y., Sarshar, N., and Roychowdhury, V. (2006a). Assessment of long range correlation in time series: how to avoid pitfalls. *Phys. Rev. E Stat. Nonlin. Soft Matter Phys.* 73, 016117.

Gao, J., Hu, J., Tung, W., and Cao, Y. (2006b). Distinguishing chaos from noise by scale-dependent Lyapunov exponent. *Phys. Rev. E Stat. Nonlin. Soft Matter Phys.* 74, 066204.

Gao, J., Sultan, H., Hu, J., and Tung, W. (2010). Denoising nonlinear time series by adaptive filtering and wavelet shrinkage: a comparison. *IEEE Signal Process. Lett.* 17, 237–240.

Gao, J., and Tung, W. (2002). Pathological tremors as diffusional processes. *Biol. Cybern.* 86, 263–270.

Gao, J., Tung, W., and Hu, J. (2009). Quantifying dynamical predictability: the pseudo-ensemble approach (in honor of Professor Andrew Majda's 60th birthday). *Chi. Ann. Math. Series B* 30, 569–588.

Gao, J., and Zheng, Z. (1993). Local exponential divergence plot and optimal embedding of a chaotic time series. *Phys. Lett. A* 181, 153–158.

Gao, J., and Zheng, Z. (1994a). Direct dynamical test for deterministic chaos. *Europhys. Lett.* 25, 485–490.

Gao, J., and Zheng, Z. (1994b). Direct dynamical test for deterministic chaos and optimal embedding of a chaotic time series. *Phys. Rev. E Stat. Nonlin. Soft Matter Phys.* 49, 3807–3814.

Garfinkel, A., Spano, M., Ditto, W., and Weiss, J. (1992). Controlling cardiac chaos. *Science* 257, 1230–1235.

Gaspard, P., Briggs, M., Francis, M., Sengers, J., Gammons, R., Dorfman, J., and Calabrese, R. (1998). Experimental evidence for microscopic chaos. *Nature* 394, 865–868.

Gaspard, P., and Wang, X. (1993). Noise, chaos, and (ε,τ)-entropy per unit time. *Phys. Report.* 235, 291–343.

Goldberger, A., and West, B. (1987). Applications of nonlinear dynamics to clinical cardiology. *Ann. N. Y. Acad. Sci.* 504, 155–212.

Grassberger, P., and Procaccia, I. (1983a). Characterization of strange attractors. *Phys. Rev. Lett.* 50, 346–349.

Grassberger, P., and Procaccia, I. (1983b). Estimation of the Kolmogorov entropy from a chaotic signal. *Phys. Rev. A* 28, 2591–2593.

Ho, K., Moody, G., Peng, C., Mietus, J., Larson, M., Levy, D., and Goldberger, A. (1997). Predicting survival in heart failure cases and controls using fully automated methods for deriving nonlinear and conventional indices of heart rate dynamics. *Circulation* 96, 842–848.

Hon, E., and Lee, S. (1965). Electronic evaluations of the fetal heart rate patterns preceding fetal death: further observations. *Am. J. Obstet. Gynecol.* 87, 814–826.

Hu, J., Gao, J., and Tung, W. (2009a). Characterizing heart rate variability by scale-dependent Lyapunov exponent. *Chaos* 19, 028506.

Hu, J., Gao, J., and Wang, X. (2009b). Multifractal analysis of sunspot time series: the effects of the 11-year cycle and Fourier truncation. *J. Stat. Mech.* doi: 10.1088/1742-5468/2009/02/P02066.

Hu, J., Gao, J., Tung, W., and Cao, Y. (2010). Multiscale analysis of heart rate variability: a comparison of different complexity measures. *Ann. Biomed. Eng.* 38, 854–864.

Hu, J., Tung, W., Gao, J., and Cao, Y. (2005). Reliability of the 0-1 test for chaos. *Phys. Rev. E Stat. Nonlin. Soft Matter Phys.* 72, 056207.

Hwa, R., and Ferree, T. (2002). Scaling properties of fluctuations in the human electroencephalogram. *Phys. Rev. E Stat. Nonlin. Soft Matter Phys.* 66, 021901.

Hwang, S., Gao, J., and Liu, J. (2000). Noise-induced chaos in an optically injected semiconductor laser. *Phys. Rev. E Stat. Nonlin. Soft Matter Phys.* 61, 5162–5170.

Ivanov, P., Amaral, L., Goldberger, A., Havlin, S., Rosenblum, M., Struzik, Z., and Stanley, H. (1999). Multifractality in human heartbeat dynamics. *Nature* 399, 461–465.

Kaneko, K., and Tsuda, I. (2000). *Complex Systems: Chaos and Beyond.* Berlin: Springer.

Kaplan, D., and Glass, L. (1992). Direct test for determinism in a time-series. *Phys. Rev. Lett.* 68, 427–430.

Kaplan, D., and Goldberger, A. (1991). Chaos in cardiology. *J. Cardiovasc. Electrophysiol.* 2, 342–354.

Kennel, M., Brown, R., and Abarbanel, H. (1992). Determining embedding dimension for phase-space reconstruction using a geometrical construction. *Phys. Rev. A* 45, 3403–3411.

Kobayashi, M., and Musha, T. (1982). 1/f fluctuation of heart beat period. *IEEE Trans. Biomed. Eng.* 29, 456–457.

Lempel, A., and Ziv, J. (1976). On the complexity of finite sequences. *IEEE Trans. Inform. Theory* 22, 75–81.

Liebert, W., Pawelzik, K., and Schuster, H. (1991). Optimal embedding of chaotic attractors from topological considerations. *Europhys. Lett.* 14, 521–526.

Lorenz, E. (1963). Deterministic nonperiodic flow. *J. Atmos. Sci.* 20, 130–141.

Mackey, M., and Glass, L. (1977). Oscillation and chaos in physiological control-systems. *Science* 197, 287–288.

Malik, M. (1996). Task force of the European society of cardiology and the North American society of pacing and electrophysiology: heart rate variability: standards of measurement, physiological interpretation,and clinical use. *Circulation* 93, 1043–1065.

Mallat, S. (2008). *A Wavelet Tour of Signal Processing*, 3rd Edn. Amsterdam: Academic Press.

Mandelbrot, B. (1982). *The Fractal Geometry of Nature.* San Francisco: Freeman.

Martinerie, J., Adam, C., Quyen, M., Baulac, M., Clemenceau, S., Renault, B., and Varela, F. (1998). Epileptic seizures can be anticipated by non-linear analysis. *Nat. Med.* 4, 1173–1176.

Osborne, A., and Provenzale, A. (1989). Finite correlation dimension for stochastic-systems with power-law spectra. *Physica D* 35, 357–381.

Packard, N., Crutchfield, J., Farmer, J., and Shaw, R. (1980). Geometry from time-series. *Phys. Rev. Lett.* 45, 712–716.

Pei, X., and Moss, F. (1996). Characterization of low-dimensional dynamics in the crayfish caudal photoreceptor. *Nature* 379, 618–621.

Peng, C., Buldyrev, S., Havlin, S., Simons, M., Stanley, H., and Goldberger, A. (1994). On the mosaic organization of DNA sequences. *Phys. Rev. E Stat. Nonlin. Soft Matter Phys.* 49, 1685–1689.

Peng, C., Mietus, J., Hausdorff, J., Havlin, S., Stanley, H., and Goldberger, A. (1993). Long-range anticorrelations and non-Gaussian behavior of the heartbeat. *Phys. Rev. Lett.* 70, 1343–1346.

Physionet. (2011). MIT-BIH normal sinus rhythm database and BIDMC congestive heart failure. Available at: http://www.physionet.org/physiobank/database/#ecg

Pincus, S., and Viscarello, R. (1992). Approximate entropy: a regularity statistic for fetal heart rate analysis. *Obstet. Gynecol.* 79, 249–255.

Poon, C., and Barahona, M. (2001). Titration of chaos with added noise. *Proc. Natl. Acad. Sci. U.S.A.* 98, 7107–7112.

Provenzale, A., and Osborne, A. (1991). Convergence of the k2 entropy for random noises with power law spectra. *Physica D* 47, 361–372.

Robinson, P. (2003). Interpretation of scaling properties of electroencephalographic fluctuations via spectral analysis and underlying physiology. *Phys. Rev. E Stat. Nonlin. Soft Matter Phys.* 67, 032902.

Ryan, D., and Sarson, G. (2008). The geodynamo as a low-dimensional deterministic system at the edge of chaos. *Europhys. Lett.* 83, 49001.

Sauer, T., Yorke, J., and Casdagli, M. (1991). Embedology. *J. Stat. Phys.* 65, 579–616.

Strang, G., and Nguyen, T. (1997). *Wavelet and Filter Banks.* New York: Wellesley-Cambridge Press.

Sugihara, G., and May, R. (1990). Nonlinear forecasting as a way of distinguishing chaos from measurement error in time series. *Nature* 344, 734–741.

Takens, F. (1981). "Detecting strange attractors in turbulence," in *Dynamical Systems and Turbulence, Lecture Notes in Mathematics*, eds D. A. Rand and L. S. Young (New York, NY: Springer-Verlag), 366.

Torcini, A., Grassberger, P., and Politi, A. (1995). Error propagation in extended chaotic systems. *J. Phys. A Math. Gen.* 28, 4533.

Tung, W., Gao, J., Hu, J., and Yang, L. (2011). Recovering chaotic signals in heavy noise environments. *Phys. Rev. E Stat. Nonlin. Soft Matter Phys.* 83, 046210.

Wolf, A., Swift, J., Swinney, H., and Vastano, J. (1985). Determining Lyapunov exponents from a time series. *Physica D* 16, 285–317.

Conflict of Interest Statement: The authors declare that the research was conducted in the absence of any commercial or financial relationships that could be construed as a potential conflict of interest.

Received: 11 November 2011; accepted: 08 December 2011; published online: 24 January 2012.

Citation: Gao J, Hu J, Tung W-w and Blasch E (2012) Multiscale analysis of biological data by scale-dependent Lyapunov exponent. Front. Physio. ***2****:110. doi: 10.3389/fphys.2011.00110*

This article was submitted to Frontiers in Fractal Physiology, a specialty of Frontiers in Physiology.

frontiers in
PHYSIOLOGY

METHODS ARTICLE
published: 19 October 2012
doi: 10.3389/fphys.2012.00405

Measuring group synchrony: a cluster-phase method for analyzing multivariate movement time-series

Michael J. Richardson[1]*, Randi L. Garcia[2], Till D. Frank[2,3], Madison Gergor[4] and Kerry L. Marsh[2,3]

[1] Department of Psychology, Center for Cognition, Action, and Perception, University of Cincinnati, Cincinnati, OH, USA
[2] Department of Psychology, University of Connecticut, Storrs, CT, USA
[3] Center for the Ecological Study of Perception-Action, University of Connecticut, Storrs, CT, USA
[4] Department of Psychology, Colby College, Waterville, ME, USA

Edited by:
John G. Holden, University of Cincinnati, USA

Reviewed by:
Fred Hasselman, Radboud University Nijmegen, Netherlands
Dirk Cysarz, Witten/Herdecke University, Germany

***Correspondence:**
Michael J. Richardson, Department of Psychology, Assistant Professor, Center for Cognition, Action, and Perception, ML 0376, 4150-B Edwards C1, University of Cincinnati, Cincinnati, OH 45221-0376, USA.
e-mail: michael.richardson@uc.edu

A new method for assessing group synchrony is introduced as being potentially useful for objectively determining degree of group cohesiveness or entitativity. The cluster-phase method of Frank and Richardson (2010) was used to analyze movement data from the rocking chair movements of six-member groups who rocked their chairs while seated in a circle facing the center. In some trials group members had no information about others' movements (their eyes were shut) or they had their eyes open and gazed at a marker in the center of the group. As predicted, the group level synchrony measure was able to distinguish between situations where synchrony would have been possible and situations where it would be impossible. Moreover, other aspects of the analysis illustrated how the cluster phase measures can be used to determine the type of patterning of group synchrony, and, when integrated with multi-level modeling, can be used to examine individual-level differences in synchrony and dyadic level synchrony as well.

Keywords: cluster phase method, group synchrony, interpersonal coordination, group processes, multivariate analysis

A common feature of many social activities, including a group of friends walking to class together, an audience swaying to the music of their favorite rock band at a concert, or a highly trained rowing team racing down a river, is the synchrony or coordination that occurs between the movements of the actors involved. Although the magnitude or stability of movement synchrony can differ across different social situations, it is a natural part of interpersonal behavior (Bernieri and Rosenthal, 1991; Fowler et al., 2008; Marsh et al., 2009; Miles et al., 2009; Richardson et al., 2010) and can result both intentionally due to intrinsic task requirements (i.e., when rowing) and spontaneously (i.e., when friends are walking to class) due to the myriad of perceptual-motor couplings that exist during social interaction (Schmidt et al., 1998; Repp and Penel, 2004; Schmidt and Richardson, 2008).

Movement synchrony may be a fundamental means of becoming a social unit with others (Marsh et al., 2009; Marsh, 2010), and of blending the boundaries of one's self with another (Paladino et al., 2010). Synchrony helps build rapport with others (Bernieri et al., 1996; Chartrand and Bargh, 1999; Hove and Risen, 2009; Marsh et al., 2009), and telegraphs to outsiders that individuals are a social unit and have rapport (Macrae et al., 2008; Lakens, 2010; Lakens and Stel, 2011). Being psychologically distanced from another individual can cause a reduction in interpersonal synchrony (Miles et al., 2010). Synchrony not only facilitates memory for those we synchronize with (Miles et al., 2010) but can more generally facilitate performance of cognitive or linguistic tasks (Richardson et al., 2005; Shockley et al., 2009). Thus, developing a detailed understanding of why and when it does or does not occur has significant implications for understanding social behavior.

It should come as no surprise then that there is a large body of research that has attempted to examine and model such behavior (see Schmidt and Richardson, 2008; Marsh et al., 2009, for reviews). Despite the fact that movement synchrony presumably can occur between 3 or more individuals, research on between-person movement synchronization has, with rare exception, been limited to the movement coordination of dyads. Typically, these studies involve recording the movements of a single limb from each participant (e.g., each participant's leg, arm, or hand movements) under different intentional and social constraints (e.g., Boker and Rotondo, 2003). Movement synchrony or coordination is then quantified using various bivariate measures, such as relative phase, frequency difference, frequency, or cross-spectral coherence, cross-correlation, and cross-recurrence analysis. Interaction between two subsystems, in general, and phase synchronization between two dynamical systems, in particular, can also be quantified by means of various entropy measures (Tass et al., 1998; Wojcik et al., 2001), mutual information (Palus, 1997), phase distribution (Frank et al., 2000), and phase diffusion index measures (e.g., Pikovsky et al., 2001; Schelter et al., 2007). The most commonly used quantifications are the mean and SD of the relative phase time-series ($\overline{\phi}$ and $SD\phi$, respectively) that occurs between the movements of the two participants, where the relative phase time-series, $\phi(t)$, is calculated as the difference between the phase angles, $\theta(t)$, of the two movement time-series [i.e., $\theta_2(t) - \theta_1(t)$]. For 1-to-1 frequency locked synchrony, $\overline{\phi}$ is used to identify the degree to which the pattern of coordination is equal to or shifted away from one of the two stable states of interlimb coordination, namely $\overline{\phi} = 0°$ and $180°$ (referred to as inphase and antiphase coordination, respectively). $SD\phi$ is used to determined the stability of the coordination, with greater values of $SD\phi$ corresponding to weaker or less stable states of coordination (e.g., Schmidt et al., 1990; Richardson et al., 2007). The distribution of $\phi(t)$ has also been used to quantify the degree of spontaneous synchrony, in that observing a greater number of relative phase angles around 0° and 180° is indicative of intermittent or relative coordination (Schmidt and O'Brien, 1997; Richardson et al., 2007).

What about the movement synchrony or coordination that involves more than two people? There are important theoretical reasons why studying synchrony at a group level may be important. Whereas dyadic interpersonal coordination forms the basis for joint action (Clark, 1996), communication, rapport, and the formation of relationships (Tickle-Degnen and Rosenthal, 1990; Fiske, 1992), group-level synchrony may be an important behavioral indicator of group cohesiveness, the degree to which a group has a sense of "groupness," or existence as an *entity* (i.e., group entitativity, a term coined by Campbell, 1958). Group cohesiveness, entitativity, and social identification are viewed as crucial processes in understanding a range of phenomena, from dysfunctional group decision-making (Janis, 1982), to social influence (Festinger et al., 1950), intergroup conflict, and social identity processes (Simon and Pettigrew, 1990; Tsui and Gutek, 1999; Tajfel and Turner, 2004). To date, however, nearly all means of assessing degree of groupness involves self-report (Lickel et al., 2000). We hypothesize that, as occurs with dyadic interpersonal synchrony (Miles et al., 2010), group synchrony may occur when individuals have mutual interpersonal connection with others. These may be due to valence bonds (friendship and liking) or due to some functional reasons for their connection (belonging to a family, or a workgroup that must cooperate). Thus, a behavioral means of assessing group synchrony could potentially revolutionize the study of group processes. Furthermore, if group synchrony measures are integrated with methodological techniques that allow for multi-level modeling of data it would provide the ability to look at both dyadic and individual level synchrony within a group, as well as group-level differences in synchrony, that is, the ability to empirically determine the level at which synchrony is occurring (Bond and Kenny, 2002). For example, being able to identify individual differences in synchrony with the group provides the potential to understand how some individuals within a group may be strongly pulled to coordinate with others, whereas others may tend to be relatively impervious to such social influence.

Almost no research studies have examined the movement synchronization that occurs between 3 or more individuals. One exception is work by Néda et al. (2000a,b) in which they examined the synchronized clapping of an audience in a naturalistic setting. As this latter work points out, group process research requires that researchers examine not only consequent emergent synchrony as a final product, but also the individual level movements that contribute to synchrony or group coordination. Being able to assess the movements of each individual in the process of examining group synchrony is therefore critical. One reason for the lack of such research concerns the inability of researchers to simultaneously record the limb and body movements of multiple individuals. However, recent technical advances in multi-sensor motion tracking systems (e.g., NDI's optical tracking systems, Polhemus's Liberty, or Latus magnetic tracking systems) that can provide time series records of the limb or body movements of many individuals means that this is no longer a barrier.

A second reason for the limited group synchrony research is a lack of verified statistics for quantifying the magnitude and stability of the synchrony that can occur between multiple movement time-series. This latter issue is really a two-fold issue. First, how can one effectively measure the overall synchrony of a group of individuals as a whole? Second, how can one effectively measure the degree to which the movements of any one individual in the group are synchronized to the movements of a group as a whole? Here, we address these questions by adapting and testing a *cluster phase* method recently proposed by Frank and Richardson (2010). The method is based on the Kuramoto order parameter[1] (Kuramoto, 1984, 1989), which has been used previously to examine the phase synchronization of many-body systems (e.g., a large set of oscillators), such as the synchronized firefly flashing and chirping of crickets, (see Strogatz, 2000, for a review), and synchronized applause (Néda et al., 2000a,b). The method directly quantifies phase synchronization in noisy experimental multivariate data.

CLUSTER PHASE QUANTIFICATION OF GROUP SYNCHRONY

The Kuramoto based cluster phase method proposed by Frank and Richardson (2010) can be used to quantify phase synchronization in noisy experimental multivariate data as follows.

First, for n movement (participant) times-series, $x_1(t_i), \ldots, x_k(t_i)$, where $k = 1, \ldots, n$ and $i = 1, \ldots, T$ time steps, calculate the phase times-series for each movement, θ_k, in radians $[-\pi\ \pi]$. This can be done either using the Hilbert transform or a frequency normalized continuous phase calculation (see Pikovsky et al. (2001) for an overview of these standard phase calculation methods).

Second, calculate the group phase time-series or *cluster* phase $q(t_i)$ from:

$$\acute{q}(t_i) = \frac{1}{n}\sum_{k=1}^{n} \exp(i\theta_k(t_i))$$

and

$$q(t_i) = \mathrm{atan2}(\acute{q}(t_i))$$

---

[1] Classically, the Kuramoto method is defined in the thermodynamic limit (i.e., for systems composed of an extremely large number N of oscillatory units such that the limit $N \to \infty$ can be considered as a good approximation; Kuramoto, 1984, 1989). Frank and Richardson, however, described how this method can be adapted to quantify phase synchronization in multivariate time series when the number N of movement time-series or trajectories is relatively small compared to the thermodynamic limit (i.e., N can be 5, 10, 25, 50, or 100).

where n = the number of movements, $i = \sqrt{-1}$ (when not used as a time step index), and $\hat{q}(t_i)$ and $q(t_i)$ are the resulting cluster phase in complex and radian $[-\pi\,\pi]$ form, respectively.

Third, calculate the relative phases for the individual movements with respect to the cluster phase as:

$$\phi_k(t_i) = \theta_k(t_i) - q(t_i)$$

where $k = 1, \ldots, n$ and ϕ_k is the relative phase times for each movement (participant).

Forth, compute the mean relative phase $\overline{\phi}_k$ and the degree of synchrony ρ_k for every movement k with respect to the group behavior q from:

$$\overline{\acute{\phi}}_k = \frac{1}{N}\sum_{i=1}^{N}\exp(i\phi_k(t_i))$$

$$\overline{\phi}_k = \operatorname{atan2}(\overline{\acute{\phi}}_k),$$

and

$$\rho_k = \left|\overline{\acute{\phi}}_k\right|$$

where N is the number of time steps t_i, $\overline{\acute{\phi}}_k$ and $\overline{\phi}_k$ is the mean cluster phase in complex and radian $[-\pi\ \pi]$ form, and $\rho_k \in [0, 1]$. Here, ρ_k corresponds to the inverse of the circular variance[2] of $\phi_k(t_i)$. Thus, if $\rho_k = 1$ the movement is in complete synchronization with the group (i.e., the phase of the movement at any time step t_i is equivalent to the group phase shifted by a constant phase). If $\rho_k = 0$ the movement is completely unsynchronized to the group. Note that $\overline{\phi}_k$ captures the phase shift of a movement with respect to the group behavior q. For stable synchrony (i.e., ρ_k tending toward 1) it can be used to compare if movements have the same mean phase with the group and, thus, determine the between movement relative phase relations. For instance, if $\overline{\phi}_n = \overline{\phi}_m$ then the mean relative phase between movement (participant) m and n is zero and they are perfectly inphase with one another.

Finally, the degree of synchronization of the group as a whole ρ_{group} at every time step t_i is defined by:

$$\rho_{\text{group},i} = \left|\frac{1}{n}\sum_{k=1}^{n}\exp\{i(\phi_k(t_i) - \overline{\phi}_k)\}\right|$$

where $\rho_{\text{group},i} \in [0, 1]$ and the mean degree to group synchronization is computed as:

$$\rho_{\text{group}} = \frac{1}{N}\sum_{i=1}^{N}\rho_{\text{group},i}$$

As with ρ_k above, the larger the value of $\rho_{\text{group},i}$ and ρ_{group} (i.e., the closer to 1) the larger the degree of group synchronization.

Note that ρ_{group} provides a single measure of group synchrony for a behavioral period (trial), whereas $\rho_{\text{group},i}$ provides a continuous measure of group synchrony[3].

EXPERIMENTAL TEST OF METHOD

To test the effectiveness of the above method, we conducted a study of group synchrony in which groups of six participants, arranged in a circle, rocked in rocking chairs at a self-selected or predetermined frequency. This social coordination paradigm was chosen for two reasons. First, the rocking chair movements of many participants could be recorded easily by placing motion tracking sensors unobtrusively behind the head rest of each participant's chair. Second, previous research has found that the natural period of rocking chairs is quite stable such that the individual differences in participant weight has a negligible effect on movement frequency (Richardson et al., 2007). Third, previous research (Richardson et al., 2007) has demonstrated that rocking chair movements can be synchronized, but only when participants have information about their co-participant's movements (e.g., can see each other). In short, this methodology provided a way to examine the effectiveness of the cluster phase statistics in determining the phase synchronization of multivariate time-series movement data under intentional (eyes-open) and chance (eyes-closed) levels of coordination.

METHOD

PARTICIPANTS

Eight groups of six participants (48 participants in mixed gender groups) were recruited for the study. All participants were Colby college undergraduate students who completed the experiment for partial course credit or monetary incentive (US \$6.00). All participants were naïve to the study's purpose and had not previously participated in a study on rhythmic or social movement coordination[4].

MATERIALS

Participants sat and rocked in six identical wooden rocking chairs. The chairs were positioned evenly around a central 10 × 10 cm target that stood on a 5 cm wide by 1.2 m high stand. The chairs formed a circle with a radius of 1.25 m, with the radius assessed from the center of target to the front of the chairs. The Euclidean *x*-*y*-*z* movements of each rocking chair was recorded at 120 Hz using a magnetic tracking system (Polhemus Liberty, Polhemus Corporation, Colchester, VT), with the motion sensors attached unobtrusively to the back of each chairs' headrest.

PROCEDURE

Upon arrival each participant was randomly assigned to one of the six chairs. Participants were instructed to rock at a self-selected frequency (*groups 101–104*) or at a frequency of 0.6 Hz[5]

---

[2] Circular variance is a circular or directional statistic that measures the spread of a set of dihedral angles. See Fisher (1993) for more details.

[3] Although not demonstrated here, $\rho_{\text{group},i}$ could be used to determine transient and stationary behavior across a behavioral period.

[4] The participants and data presented here are not the same as reported by Frank and Richardson (2010).

[5] Extensive pilot testing revealed that individuals naturally rocked at between 0.5 and 0.7 Hz. Thus, 0.6 Hz was chosen as it represented the average self-selected (comfort mode) frequency of individuals.

(*groups 201–204*). With respect to the latter groups, a metronome beat was presented to participants for 30 s prior to beginning the experiment trials so that participants could practice rocking at this frequency. The metronome was *not* presented during the experimental trials. This metronome condition was employed to ensure that participants rocked at a tempo more consistent with the natural rocking tempo of the chairs, as deviations from a systems natural movement frequency can decrease coordination stability (e.g., Richardson et al., 2007; Schmidt and Richardson, 2008).

Every group completed three 3 min trials in the following order: one *eyes closed* trial; and two *eyes open* trials. For the eyes closed trial, participants were instructed to either rock at their own self-selected tempo or at the practice (0.6 Hz) frequency (depending on group) with their eyes closed. This trial allowed for a measure of chance level synchrony as participants had no visual information about their co-participants' movements. For the eyes open trials, participants were instructed to rock at a self-selected frequency or at the practice frequency (depending on group) while attempting to synchronize their rocking chair movements as a group. To control for looking direction, all participants were instructed to look at the central target. No instructions as to the form or pattern of synchrony were provided.

DATA REDUCTION AND SIGNAL PROCESSING

Due to the circular arrangement of the chairs the z-direction (up-down) of movement was extracted from the movement recordings for analysis as it was the only uniform direction (motion time-series) across chairs (see **Figure 1**). Prior to performing the analysis, the movement time-series were down-sampled from 120 to 60 Hz, centered around zero, and low-pass filtered using a 10 Hz Butterworth filter. The Hilbert transform was employed to calculate the phase times-series for each movement. In addition to performing the cluster phase analysis defined above, a peak-picking algorithm was used to obtain the mean frequency (Hz) of the chair movements for each trial and was calculated as the inverse of the mean time between the points of maximum extension. This frequency analysis revealed that participants produced the equivalent movement frequencies in both the self-paced ($M = 0.58$, $SD = 0.06$) and metronome paced ($M = 0.60$, $SD = 0.04$) conditions and for both the eyes-closed ($M = 0.59$, $SD = 0.08$) and eyes-open ($M = 0.50$, $SD = 0.03$) conditions. This is consistent with previous rocking chair research (Richardson et al., 2007), and reflects the tendency of participants to produced movements close to a systems natural or resonant frequency (Kugler and Turvey, 1987; Richardson et al., 2007). Given that an initial analysis of the data revealed no significant effects of whether individuals' pacing was set by the experimenter or not, this factor was removed from the analysis and the eight groups were treated as equivalent with respect to pacing.

RESULTS AND DISCUSSION

The aim of the current experiment was to demonstrate that the cluster phase method proposed by Frank and Richardson (2010) could be used to effectively measure group synchrony. As a way of illustrating the effectiveness of the differing cluster phase statistics we first present a qualitative assessment of $\rho_{\text{group},i}$ (which provides a continuous measure of group synchrony) and the cluster phase calculations of mean and SD of relative phase (which can be used to illustrate the patterning of the synchrony). Following this, we then present a quantitative (statistical) analysis of the cluster phase statistics ρ_{group}, ρ_k, and ρ_d (see below for definitions) to objectively determine the effectiveness with which they can be used to (1) measure the presence and magnitude of group movement synchrony as a whole, (2) the degree to which the different individuals in the group were synchronized to the movements of the group as a whole, respectively, and (3) the degree to which two individuals within the group are synchronized with each other.

Recall that the eyes-closed condition enabled a measure of chance level coordination, that is, a statistical magnitude by which actual coordination could be assessed against. Thus, while the overall magnitude of the cluster phase statistics, $\rho_{\text{group},i}$, ρ_{group}, and ρ_k (i.e., the closer to 1) is indicative of greater synchrony, the instructive comparison for both the qualitative and quantitative analysis presented below is the magnitude difference between the eyes-closed and eyes-open conditions. Specifically, the magnitude of the cluster phase statistics, $\rho_{\text{group},i}$, ρ_{group}, and ρ_k should be greater for the eyes-open condition compared to the eyes-closed condition.

QUALITATIVE ANALYSIS

An inspection of **Figure 2**, which plots $\rho_{\text{group},i}$ averaged across group as a function of time, provides preliminary support for the

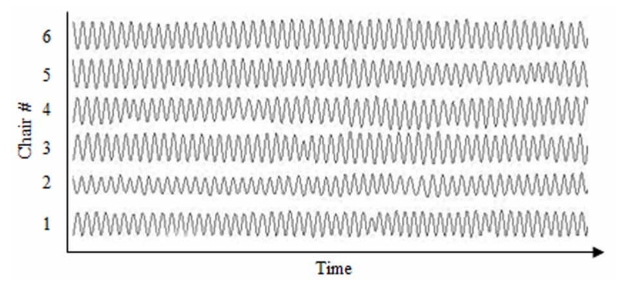

FIGURE 1 | Example time-series of the rocking chairs' z-direction (up-down) movements over time.

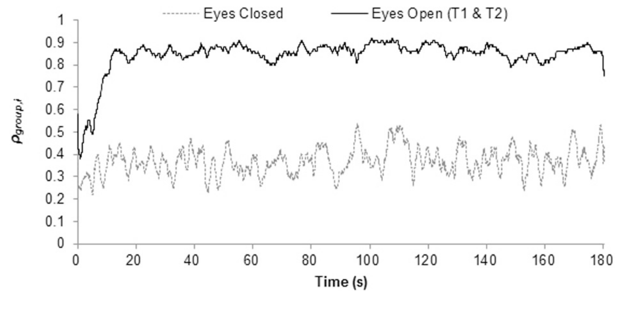

FIGURE 2 | Continuous group synchrony, $\rho_{\text{group},i}$ averaged across group and trial.

cluster phase method. Specifically, the data presented in **Figure 2** reveals how following an initial transient period of approximately 15 s, $\rho_{\text{group},i}$ for both of the eyes-open trials remained at a much greater level across the course of the trials than that observed for the eyes-closed condition. A similar pattern was exhibited for each of the eight groups, with $\rho_{\text{group},i}$ ranging between approximately 0.7 and 0.9 for the coordination (eyes-open) condition and between approximately 0.2 and 0.4 for the chance level (eyes-closed) condition.

With respect to the patterning of the synchrony that emerged during the intentional coordination (eyes-open) trials, individuals within a group tended to exhibit an inphase pattern of coordination to the group as a whole (as measured by $\overline{\phi}_{\text{clus.}}$, $M = 0.38$, $SD = 15.21$), with a modest degree of stability (as measured by $SD\phi_{\text{clus.}}$, $M = 41.34$, $SD = 20.94$). The individual measures, by chair number, of $\overline{\phi}_{\text{clus.}}$ and $SD\phi_{\text{clus.}}$ are displayed in **Table 1**. Note that although $\overline{\phi}_{\text{clus.}}$ and $SD\phi_{\text{clus.}}$ could be determined for the eyes-closed condition the circular nature of relative phase means that such calculations are trivial for chance (or intermittent) coordination and do not reflect a meaningful synchrony relationship.

QUANTITATIVE ANALYSIS

The ρ_{group} and ρ_k measures for the eyes-closed and both eyes-open trials are displayed in **Table 2**. To assess the validity of the ρ_{group} statistic in measuring group based synchrony, a One-Way repeated measures ANOVA was conducted to compare the three trials (*eyes closed*, *eyes-open trial one*, and *eyes-open trial two*). If ρ_{group} is a valid measure of group synchrony then it should be a significantly greater (closer to 1) in the eyes-open conditions than in the eyes-closed condition, where any synchrony that occurs is simply due to chance. This was indeed the case, with the omnibus ANOVA revealing a significant effect of trial, $F_{(2,\,14)} = 189.10$, $p < 0.01$, $\eta^2 = 0.96$ (see **Figure 3**) and a *post-hoc* analysis (Tukey-HSD) finding that the two eyes-open trials were significant greater than the eyes-closed condition (both $p < 0.01$), but were not significantly different from each other ($p > 0.95$).

In addition to the group-based measure of synchrony, ρ_{group}, Frank and Richardson (2010) also proposed that the cluster phase statistic of ρ_k could be used to measure the extent to which each individual is synchronizing with his or her group. Just as in the analyses using group based synchrony above, this would be validated by finding significantly more individual synchrony, greater magnitudes of ρ_k (closer to 1), in the eyes open compared to the eyes-closed condition. Of more import is the possibility that ρ_k can be used to examine the variation in the extent to which differing individuals within a group are synchronized with their group as a whole. This latter possibility was investigated using multilevel modeling with 2 levels (individual crossed with trial is level 1 and

Table 1 | Mean (SD) cluster relative phase ($\overline{\phi}_{\text{clus.}}$ and $SD\phi_{\text{clus.}}$, respectively).

Group no.	Trial	Chair number					
		1	2	3	4	5	6
101	Eyes Closed	–	–	–	–	–	–
	Eyes Open (T1)	−12.4 (17.6)	−3.9 (23)	3.4 (13.6)	5.2 (24)	−4.5 (49.3)	10.5 (12.1)
	Eyes Open (T2)	−9.9 (18.3)	1.2 (21)	−2.3 (17.5)	4.5 (27.1)	−6.2 (23.3)	12.7 (15.8)
102	Eyes Closed	–	–	–	–	–	–
	Eyes Open (T1)	−3.6 (30)	−10.8 (28.6)	−0.9 (29.2)	0.8 (20.4)	56 (69.5)	−0.1 (20.1)
	Eyes Open (T2)	6.3 (35.1)	−21.7 (22.5)	15.2 (27.4)	7 (19.6)	−4.7 (32.4)	−1.7 (28)
103	Eyes Closed	–	–	–	–	–	–
	Eyes Open (T1)	−0.5 (18.5)	−4.2 (22.9)	7.5 (19)	13.2 (28.3)	2.6 (46.6)	−48.4 (64.2)
	Eyes Open (T2)	−3.4 (22.1)	−5.9 (23.8)	0.8 (21)	−2.5 (28.9)	0.7 (44.9)	39.2 (69.7)
104	Eyes Closed	–	–	–	–	–	–
	Eyes Open (T1)	−1.8 (17)	31.1 (37.9)	−5.9 (19.7)	−21.4 (46)	11.9 (24)	−13.7 (23.3)
	Eyes Open (T2)	10 (32.4)	27.1 (30.6)	−19.7 (36)	−14.2 (32.5)	5.6 (28)	−9 (21.9)
201	Eyes Closed	–	–	–	–	–	–
	Eyes Open (T1)	−15.3 (13.2)	4.8 (30.2)	15.3 (17.5)	10.7 (16.5)	−11.7 (24.2)	−3.5 (16.2)
	Eyes Open (T2)	−21.3 (17.1)	3.1 (45)	4.8 (18.9)	4.2 (17.5)	16.6 (25)	−5.8 (15.1)
202	Eyes Closed	–	–	–	–	–	–
	Eyes Open (T1)	11.1 (24.7)	−0.8 (23.4)	−12 (54.1)	−20.5 (30.3)	14.4 (36.7)	3.9 (34)
	Eyes Open (T2)	0.3 (27.2)	7.1 (22.4)	−8.3 (62)	−13.8 (43.5)	19.4 (26.3)	−30.3 (64.3)
203	Eyes Closed	–	–	–	–	–	–
	Eyes Open (T1)	13 (43.6)	−8.9 (21.8)	−8.1 (21.2)	−9 (23.8)	8.8 (24.2)	8.1 (32.7)
	Eyes Open (T2)	12.2 (62)	−4.4 (31.4)	12.8 (24)	−1 (25.5)	6.8 (50.3)	−32.9 (56.3)
204	Eyes Closed	–	–	–	–	–	–
	Eyes Open (T1)	−30.3 (33.5)	−4.8 (23.7)	6 (33.3)	13.6 (26.4)	7.9 (30.3)	5.3 (31)
	Eyes Open (T2)	−18.7 (24)	−0.9 (23)	2.7 (24)	−9.2 (24.7)	20.7 (32.4)	6.9 (23.3)

Table 2 | Individual (ρ_k) and group (ρ_{group}) cluster amplitudes.

Group no.	Trial	Chair number						
		1	2	3	4	5	6	ρ_{group}
101	Eyes Closed	0.30	0.27	0.42	0.40	0.38	0.31	0.36
	Eyes Open (T1)	0.95	0.92	0.97	0.91	0.63	0.98	0.89
	Eyes Open (T2)	0.95	0.93	0.95	0.89	0.92	0.96	0.93
102	Eyes Closed	0.31	0.42	0.14	0.32	0.34	0.46	0.36
	Eyes Open (T1)	0.86	0.88	0.87	0.94	0.26	0.94	0.80
	Eyes Open (T2)	0.81	0.92	0.89	0.94	0.84	0.88	0.88
103	Eyes Closed	0.36	0.34	0.30	0.35	0.34	0.40	0.36
	Eyes Open (T1)	0.95	0.92	0.95	0.88	0.67	0.37	0.80
	Eyes Open (T2)	0.93	0.91	0.93	0.87	0.69	0.26	0.77
104	Eyes Closed	0.36	0.35	0.41	0.39	0.38	0.36	0.38
	Eyes Open (T1)	0.96	0.78	0.94	0.68	0.91	0.92	0.87
	Eyes Open (T2)	0.84	0.86	0.80	0.84	0.88	0.93	0.86
201	Eyes Closed	0.33	0.38	0.48	0.41	0.30	0.25	0.37
	Eyes Open (T1)	0.97	0.86	0.95	0.96	0.91	0.96	0.94
	Eyes Open (T2)	0.96	0.69	0.95	0.95	0.91	0.97	0.90
202	Eyes Closed	0.40	0.22	0.32	0.43	0.58	0.30	0.41
	Eyes Open (T1)	0.91	0.92	0.55	0.86	0.79	0.82	0.81
	Eyes Open (T2)	0.89	0.92	0.41	0.71	0.90	0.37	0.71
203	Eyes Closed	0.37	0.47	0.17	0.39	0.35	0.34	0.36
	Eyes Open (T1)	0.71	0.93	0.93	0.91	0.91	0.84	0.87
	Eyes Open (T2)	0.42	0.85	0.91	0.90	0.61	0.52	0.71
204	Eyes Closed	0.35	0.41	0.34	0.33	0.46	0.33	0.38
	Eyes Open (T1)	0.83	0.91	0.83	0.89	0.86	0.85	0.87
	Eyes Open (T2)	0.91	0.92	0.91	0.91	0.84	0.92	0.90

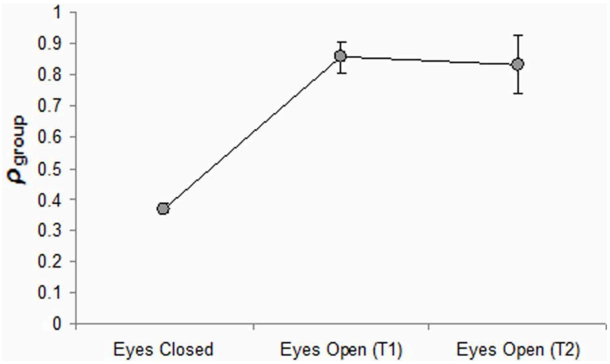

FIGURE 3 | Mean group synchrony, ρ_{group}, as a function of condition and trial (T).

group is level 2). The variable Condition (fixed effect at level 1) was dummy coded with two indicator variables: an eyes closed indicator variable, as well as an eyes open trial 1 variable; thus, eyes open trial 2 was the comparison group. As in the group-based synchrony analyses above we found a significant difference in individual synchrony between the eyes closed condition and the eyes open trial 2 condition ($b = -0.47$, $p < 0.01$) with the eyes closed condition eliciting less individual synchrony. Furthermore, there was no statistically significant difference in individual synchrony between eyes open, trial 1 and eyes open, trial 2 ($b = 0.02$, $p = 0.32$).

Interestingly there was statistically significant individual variance in this synchrony in all three trials with the most individual synchrony in the eyes open conditions, as would be expected; however, it was not large (eyes closed: $\hat{\sigma}^2_{\rho_{k,\text{individual}}} = 0.006$, $p < 0.01$; eyes open trial 1: $\hat{\sigma}^2_{\rho_{k,\text{individual}}} = 0.02$, $p < 0.01$; eyes open trial 2: $\hat{\sigma}^2_{\rho_{k,\text{individual}}} = 0.03$, $p < 0.01$). Variance in synchrony at the individual level measures whether or not some individuals are more synchronized with their groups than other individuals in each condition. There was also statistically significant covariance between individual synchrony in the first eyes open trial and in the second, $\hat{\sigma}^2_{\rho_{k,\text{individual}}} = 0.55$, $p < 0.01$, which indicates that there is some consistency in individual synchrony across trials; that is, those who individually synchronize to their groups in the first eyes open trial tended to individually synchronize in the second eyes open trial. The covariances between the eyes open trials and the eyes closed trial were zero—as one would expect since the individuals who become synchronized in the eyes closed trials are random and not necessarily the ones who *tend* to synchronize. Likewise, we also tested if there was group based individual synchrony. This effect measures the extent to which some groups' *members* are more synchronized with the group than other groups' members. For example, some groups may have individuals that are strongly influenced by others (regardless of whether there is a group-level synchrony that is emerging) whereas others might not. Since there were no systematic differences in how groups were created we might not expect there to be any group-based variance. Indeed this is the case, there was no group variance—thus groups do not vary in their overall levels of individual synchrony.

DYADIC SYNCHRONY

While the Frank and Richardson (2010) cluster phase method examined here enables a measure of group synchrony (ρ_{group}) and the degree to which each individual is synchronizing with the group (ρ_k), one should still examine dyadic synchrony (i.e., the synchrony between pairs of individuals in a group). That is, for each pair of phase time series θ_k and $\theta_{k'}$, with $k \neq k'$, one should examine the degree of dyadic synchronization, ρ_d. This can be obtained by first calculating the relative phases for each pair of individuals within a group,

$$\phi_d(t_i) = \theta_k(t_i) - \theta_{k'}(t_i)$$

where $k = 1, \ldots, n$ and ϕ_d is the relative phase times series for each pair $d = 1, \ldots, n$, and then by computing the degree of dyadic synchrony, ρ_d for every pair d from:

$$\overline{\acute{\phi}}_d = \frac{1}{N}\sum_{i=1}^{N} \exp(i\phi_d(t_i))$$

and

$$\rho_d = \left|\overline{\acute{\phi}}_d\right|$$

where N is the number of time steps t_i, $\overline{\acute{\phi}}_d$ is the mean dyadic relative phase in complex form, and $\rho_d \in [0, 1]$. Again, ρ_d corresponds to the inverse of the circular variance of $\phi_d(t_i)$, where $\rho_d = 0$ reflects no synchrony and $\rho_d = 1$ reflects perfect dyadic synchrony.

See **Table 3** for the ρ_d values by dyad within each group. Multilevel modeling, with dyad as the unit of analysis (level 1) controlling for individual and group as level 2, was again used to test for variation in dyadic synchrony at the individual and group levels. A Social Relations Model (Kenny, 1994) approach to the decomposition of variance was used with constraints to account for the symmetric nature of the measurement (i.e., group member A's synchrony with group member B is equal to group member B's synchrony with group member A). For this analysis, only the eyes open trial two condition was used. Interestingly, there was statistically significant individual variance in dyadic synchrony, $\sigma^2_{d,\text{individual}} = 0.014$, $p < 0.01$. That is, some individuals were more synchronized with the others in the group, on a pairwise basis. There was no group-based variance in dyadic synchrony however, $\sigma^2_{d,\text{group}} = 0.017$, $p = 0.13$. Group-based variance here measures the extent to which some groups had pairs of members that were more synchronized with each other than were pairs in other groups. Even though group-based variance was not found in this context, in either the dyadic or individual measure of synchrony, there may be other contexts in which we would expect variation across groups to be present. For example, if some groups had pairs of friends in a group and other groups did not, then group-level differences in dyadic synchrony would be expected.

Table 3 | Dyadic, ρ_{Dyad}, Cluster Amplitudes.

Group no.	Chair no.	Chair number				
		2	**3**	**4**	**5**	**6**
101	1	0.90	0.88	0.85	0.83	0.89
	2	–	0.85	0.89	0.82	0.88
	3	–	–	0.84	0.91	0.95
	4	–	–	–	0.84	0.83
	5	–	–	–	–	0.90
102	1	0.70	0.70	0.76	0.69	0.86
	2	–	0.84	0.90	0.82	0.77
	3	–	–	0.91	0.68	0.78
	4	–	–	–	0.73	0.82
	5	–	–	–	–	0.78
103	1	0.87	0.86	0.81	0.63	0.19
	2	–	0.85	0.78	0.59	0.21
	3	–	–	0.82	0.61	0.21
	4	–	–	–	0.50	0.18
	5	–	–	–	–	0.14
104	1	0.70	0.61	0.62	0.82	0.73
	2	–	0.67	0.68	0.76	0.76
	3	–	–	0.66	0.68	0.70
	4	–	–	–	0.67	0.82
	5	–	–	–	–	0.80
201	1	0.62	0.91	0.91	0.82	0.93
	2	–	0.59	0.60	0.63	0.67
	3	–	–	0.91	0.85	0.90
	4	–	–	–	0.84	0.91
	5	–	–	–	–	0.85
202	1	0.84	0.24	0.67	0.83	0.28
	2	–	0.29	0.68	0.90	0.29
	3	–	–	0.17	0.27	0.52
	4	–	–	–	0.69	0.10
	5	–	–	–	–	0.25
203	1	0.25	0.29	0.29	0.18	0.39
	2	–	0.90	0.86	0.42	0.33
	3	–	–	0.91	0.50	0.36
	4	–	–	–	0.49	0.35
	5	–	–	–	–	0.30
204	1	0.84	0.78	0.81	0.72	0.83
	2	–	0.81	0.79	0.72	0.84
	3	–	–	0.81	0.83	0.80
	4	–	–	–	0.71	0.83
	5	–	–	–	–	0.74

Addressing such an issue, however, is beyond the scope of the current paper; more detailed features of the groups were not manipulated nor assessed in the study. Although low levels of dyadic synchrony would constrain the ability to have group synchrony, it is important to note that a group could have a high mean level of dyadic synchrony (e.g., $\rho_{d,\text{group}}$ close to 1), without having high levels of group synchrony (e.g., ρ_{group} approximately 0.5), since they are measuring different processes. The distinction between group mean dyadic synchrony and group synchrony is that group synchronization measures the extent to which at any moment in time the interactions between all group members establish a "central" group behavior that acts in turn as an attractor for every individual member, whereas dyadic synchronization measures the degree to which two particular group members synchronize their behavior over the course of time when we considered them isolated from the remaining group members. This central group behavior reflects a mutuality and interdependence of influence. This attractor might not even be an observed state that an individual or a dyad is achieving—much as a prototype for a given cognitive category captures something about category members as a whole and might not be something ever specifically observed in any members (Rosch and Lloyd, 1978). Thus, measures of group level synchrony would be expected to relate to psychological and physical factors that lead to a strong sense of "groupness"—group entitativity or cohesiveness. The benefits of investigating these other levels of synchrony, individual, and dyadic, are that they allow us to empirically test the extent with which the synchrony process is a process that emerges as a result of relatively unidirectional influences.

CONCLUSION

Here we presented and tested an analysis method proposed by Frank and Richardson (2010) for measuring the magnitude and patterning of the movement synchrony that can occur between the movements of a group of individuals. We experimentally tested the multivariate time-series method using a group-based rocking chair paradigm in which six participants positioned in a circle rocked in rocking chairs. In addition to instructing participants to intentionally coordinate their rocking chair movements with their eyes-open, we also instructed groups to rock in an eyes-closed condition in order to test whether the cluster phase statistics could effectively differentiate between intentional and chance levels of group synchrony. In particular we were interested in determining (1) whether the cluster phase statistic ρ_{group} could effectively measure the overall synchrony of a group of individuals as a whole and, (2) the degree to which ρ_k could effectively determine whether the movements of any one individual in the group are synchronized to the movements of a group as a whole.

The results revealed that ρ_{group} and ρ_k did provide effective measures of (1) and (2), respectively, in that both statistics could statistically differentiate between the intentional (eyes-open) and chance level (eyes-closed) conditions (see **Figures 2** and **3**). In addition, the results revealed that the cluster phase measures of the mean and SD of relative phase (i.e., $\overline{\phi}_{\text{clus.}}$ and $SD\phi_{\text{clus.}}$, respectively) can be used to identify the patterning of the synchrony that emerges. More specifically, the data presented in **Table 1** demonstrates how $\overline{\phi}_{\text{clus.}}$ and $SD\phi_{\text{clus.}}$ can be used to determine whether individuals are coordinated to the group as a whole in an inphase (0°) or antiphase (180°) manner, or in some other stable relative-phase relation (e.g., 90°, 45°). Consistent with past research using rocking chairs (Richardson et al., 2007), relative phases near inphase were the dominant pattern.

We also illustrated how this analysis can be conducted within the context of considering all levels of influence (dyadic as well as group) within a group. Although we did not have any manipulations in this study that would lead dyadic processes to be crucial factors, we have illustrated how such analyses would be conducted. In situations where pairs of allies are present within a group of strangers or allies are absent, and in situations where one individual is a group leader versus when a leader is absent, the patterns of dyadic level synchrony should distinguish these different groups.

At present the cluster phase method presented here cannot account for coupling delays or leading/following behavior. However, it is plausible to assume that the method could be generalized to take such effects into account. First, the Kuramoto model with delay has been studied in the literature (e.g., Huber and Tsimring, 2003) and data analysis techniques have been developed to determine the underlying evolution equations of such stochastic delay systems (see e.g., Frank et al., 2004, 2005). The challenge in this context is that it is difficult to distinguish between the two kinds of couplings that lead to the same observation: a coupling without delay such that the attractor is at a particular phase difference different from zero and a coupling with delay e.g., with an in-phase attractor. Therefore, generalizing the current approach to account for delays is not a trivial matter. Mathematical models for leading/following behavior have been proposed for example for group and jury decision-making (e.g., Boster et al., 1991). It might be possible, therefore, for the Kuramoto model and cluster phase method presented here to be generalized in an analogous way and, thus, future work should be directed accordingly.

In the current study, we employed an eyes-closed condition as a control condition by providing a measure of chance level coordination. It is worth noting, however, that one could generate surrogate data for control purposes—i.e., by shuffled recorded data or by generating data with known random influences based on the recorded data (see e.g., Schreiber and Schmitz, 2000). Such surrogate data analysis would enable one to quantify chancel level group synchrony (as well as individual and dyadic synchrony) without the need for a control condition or control trials (i.e., no visual or non-coupled movement trials). For some experimental designs this may be preferable. For instance, when multiple trials or specific control trials may unduly influence participants' movements or may reveal the true nature of the study (i.e., when investigating spontaneous or unintentional coordination).

Researchers may have some concerns regarding whether these methods are constrained to situations where group members are seated, and seated in rocking chairs in particular. Although the analyses presented here all involve analysis of rhythmic (periodic) behavior, it is important to note that the analyses could be extended to situations where the movements involve natural gestural or postural movements during conversation (Schmidt et al., 2011) or movement during dance (Himberg and Thompson, 2010; Van Dyck et al., 2010). It is also possible that the analysis proposed could even be adapted to quantify group cognitive behavior and performance (e.g., Woolley et al., 2010).

By validating the cluster phase method proposed by Frank and Richardson (2010) the current study provides a practical demonstration of how researchers interested in group synchrony can objectively measure the magnitude of such synchrony. Accordingly, the cluster phase statistics could be used in future research to determine whether and how the magnitude and stability of group synchrony influences the social dynamics of group interaction. In particular, we would predict that strength of group synchrony is correlated with self (and perceiver) reports of group entitativity, cohesiveness, and identification with the group. More broadly, it seems likely that the cluster phase method will aid social scientists interested in investigating the dynamic time-dependent structure of group behavior, with respect not only to movement synchrony and group dynamics, but a broad spectrum of human perception and action phenomena.

AUTHOR NOTE

Example MATLAB code for the cluster phase method can be downloaded from http://homepages.uc.edu/~richamo/downloads.html. Example data can also be downloaded for demonstration purposes and for testing the analysis code.

ACKNOWLEDGMENTS

This research was supported in part by NSF [BCS-0750190].

REFERENCES

Bernieri, F. J., and Rosenthal, R. (1991). “Interpersonal coordination: behavior matching and interactional synchrony,” in *Fundamentals of Nonverbal Behavior. Studies in Emotion and Social Interaction,* eds R. S. Feldman and B. Rime (New York, NY: Cambridge University Press), 401–432.

Bernieri, F. J., Gillis, J. S., Davis, J. M., and Grahe, J. E. (1996). Dyad rapport and the accuracy of its judgment across situations: a lens model analysis. *J. Pers. Soc. Psychol.* 71, 110–129.

Boker, S. M., and Rotondo, J. L. (2003). “Symmetry building and symmetry breaking in synchronized movement,” in *Mirror Neurons and the Evolution of Brain and Language,* eds M. Stamenov and V. Gallese (Amsterdam: John Benjamins), 163–171.

Bond, C., and Kenny, D. (2002). The triangle of interpersonal models. *J. Pers. Soc. Psychol.* 83, 355–366.

Boster, F. J., Hunter, J. E., and Hale, J. L. (1991). An information processing model for jury-decision making. *Commun. Res.* 18, 524–547.

Campbell, D. T. (1958). Common fate, similarity, and other indices of the status of aggregates of persons as social entities. *Behav. Sci.* 3, 14–25.

Chartrand, T. L., and Bargh, J. A. (1999). The chameleon effect: the perception-behavior link and social interaction. *J. Pers. Soc. Psychol.* 76, 893–910.

Clark, H. H. (1996). *Using Language.* New York, NY: Cambridge University Press.

Festinger, L., Schachter, S., and Back, K. W. (1950). *Social Pressures in Informal Groups: A Study of Human Hactors in Housing*. New York, NY: Harper.

Fisher, N. I. (1993). *Statistical Analysis of Circular Data*. Cambridge, MA: Cambridge University Press.

Fiske, A. P. (1992). The four elementary forms of sociality: framework for a unified theory of social relations. *Psychol. Rev.* 99, 689–723.

Fowler, C. A., Richardson, M. J., Marsh, K. L., and Shockley, K. D. (2008). “Language use, coordination, and the emergence of cooperative action,” in *Coordination: Neural, Behavioral and Social Dynamics*, eds A. Fuchs and V. K. Jirsa (Heidelberg: Springer-Verlag), 261–279.

Frank, T. D., Beek, P. J., and Friedrich, R. (2004). Identifying noise sources of time-delayed feedback systems. *Phys. Lett. A* 327, 146–151.

Frank, T. D., Beek, P. J., and Friedrich, R. (2005). Identifying and comparing states of time-delayed systems: phase diagrams and applications to human movements. *Phys. Lett. A* 338, 74–80.

Frank, T. D., Daffertshofer, A., Peper, C. E., Beek, P. J., and Haken, H. (2000). H-theorem for a mean field model describing coupled oscillator systems under external forces. *Physica D* 144, 62–86.

Frank, T. D., and Richardson, M. J. (2010). On a test statistic for the Kuramoto order parameter of synchronization: with an illustration for group synchronization during rocking chairs. *Physica D* 239, 2084–2092.

Himberg, T., and Thompson, M. R. (2010). “Dyadic entrainment and interaction in African dance,” in *Proceedings of the 11th International Conference on Music Perception and Cognition (ICMPC11)*, eds S. M. Demorest, S. J. Morrison, and P. S. Campbell, (Seattle, WA, Washington), 658–663.

Hove, M. J., and Risen, J. L. (2009). It’s all in the timing: interpersonal synchrony increases affiliation. *Soc. Cogn.* 27, 949–961.

Huber, D., and Tsimring, L. S. (2003). Dynamics of an ensemble of noisy bistable elements with global time delayed coupling. *Phys. Rev. Lett.* 91, 260601.

Janis, I. L. (1982). *Groupthink: Psychological Studies of Policy Decisions and Fiascoes, 2nd Edn.* Boston, MA: Houghton Mifflin.

Kenny, D., (1994). *Interpersonal Perception: A Social Relations Analysis*. New York, NY, US: Guilford Press.

Kugler, P. N., and Turvey, M. T. (1987). *Information, Natural law, and the Self-assembly of Rhythmic Movement.* Hillsdale, NJ: Erlbaum.

Kuramoto, Y. (1984). *Chemical Oscillations, Waves, and Turbulence.* Berlin: Springer.

Kuramoto, Y. (1989). *Cooperative Dynamics in Complex Physical Systems*. Berlin: Springer.

Lakens, D. (2010). Movement synchrony and perceived entitativity. *J. Exp. Soc. Psychol.* 46, 701–708.

Lakens, D., and Stel, M. (2011). If they move in sync, they must feel in sync: movement synchrony leads to attributed feelings of rapport. *Soc. Cogn.* 29, 1–14.

Lickel, B., Hamilton, D. L., Wieczorkowska, G., Lewis, A., Sherman, S. J., and Uhles, A. N. (2000). Varieties of groups and the perception of group entitativity. *J. Pers. Soc. Psychol.* 78, 223–246.

Macrae, C. N., Duffy, O. K., Miles, L. K., and Lawrence, J. (2008). A case of hand waving: action synchrony and person perception. *Cognition* 109, 152–156.

Marsh, K. L. (2010). “Sociality from an ecological, dynamical perspective,” in *Grounding Sociality: Neurons, Minds, and Culture,* eds G. R. Semin and G. Echterhoff (London: Psychology Press), 43–71.

Marsh, K. L., Richardson, M. J., and Schmidt, R. C. (2009). Social connection through joint action and interpersonal coordination. *Top. Cogn. Sci.* 1, 320–339.

Miles, L. K., Griffiths, J. L., Richardson, M. J., and Macrae, C. N. (2010). Too late to coordinate: contextual influences on behavioral synchrony. *J. Exp. Soc. Psychol.* 40, 52–60.

Miles, L. K., Nind, L. K., and Macrae, C. N. (2009). The rhythm of rapport: interpersonal synchrony and social perception. *J. Exp. Soc. Psychol.* 45, 585–589.

Néda, Z., Ravasz, E., Brechet, Y., Vicsek, T., and Barabási, A. L. (2000a). The sound of many hands clapping, *Nature* 403, 849–850.

Néda, Z., Ravasz, E., Brechet, Y., Vicsek, T., and Barabási, A. L. (2000b). Physics of rhythmic applause. *Phys. Rev. E* 61, 6987–6992.

Paladino, M. P., Mazzurega, M., Pavani, F., and Schubert, T. W. (2010). Synchronous multisensory stimulation blurs self-other boundaries. *Psychol. Sci.* 21, 1202–1207.

Palus, M. (1997). Detecting phase synchronization in noisy systems. *Phys. Lett. A* 235, 341–351.

Pikovsky, A., Rosenblum, M., and Kurths, J. (2001) *Synchronization: A Universal Concept in Nonlinear Sciences*. New York, NY: Cambridge University Press.

Repp, B. H., and Penel, A. (2004). Rhythmic movement is attracted more strongly to auditory than to visual rhythms. *Psychol. Res.* 68, 252–270.

Richardson, M. J., Marsh, K. L., Isenhower, R., Goodman, J., and Schmidt, R. C. (2007). Rocking together: dynamics of intentional and unintentional interpersonal coordination. *Hum. Mov. Sci.* 26, 867–891.

Richardson, M. J., Marsh, K. L., and Schmidt, R. C. (2005). Effects of visual and verbal information on unintentional interpersonal coordination. *J. Exp. Psychol. Hum. Percept. Perform.* 31, 62–79.

Richardson, M. J., Marsh, K. L., and Schmidt, R. C. (2010). “Challenging egocentric notions of perceiving, acting, and knowing,” in

The Mind in Vontext, eds. L. F. Barrett, B. Mesquita, and E. Smith (New York, NY: Guilford), 307–333.

Rosch, E., and Lloyd, B. B. (eds.). (1978). *Cognition and Categorization*. Hillsdale, NJ: Lawrence Erlbaum, 27–48.

Schelter, B., Peifer, M., Winterhalder, M., and Timmer, J. (2007). Testing for phase synchronization. *Phys. Lett. A* 366, 382–390.

Schreiber, T., and Schmitz, A. (2000). Surrogate time series. *Physica D* 142, 346–382.

Schmidt, R. C., Bienvenu, M., Fitzpatrick, P. A., and Amazeen, P. G. (1998). A comparison of intra- and interpersonal interlimb coordination: coordination breakdowns and coupling strength. *J. Exp. Psychol. Hum. Percept. Perform.* 24, 884–900.

Schmidt, R. C., Carello, C., and Turvey, M. T. (1990). Phase transitions and critical fluctuations in the visual coordination of rhythmic movements between people. *J. Exp. Psychol. Hum. Percept. Perform.* 16, 227–247.

Schmidt, R. C., Fitzpatrick, P. A., Caron, R., and Mergeche, J. (2011). Understanding social motor coordination. *Hum. Mov. Sci.* 30, 834–845.

Schmidt, R. C., and O'Brien, B. (1997). Evaluating the dynamics of unintended interpersonal coordination. *Ecol. Psychol.* 9, 189–206.

Schmidt, R. C., and Richardson, M. J. (2008). "Dynamics of interpersonal coordination," in *Coordination: Neural, Behavioral and Social Dynamics*, eds A. Fuchs and V. K. Jirsa (Heidelberg: Springer-Verlag), 281–308.

Shockley, K., Richardson, D. C., and Dale, R. (2009). Conversation and coordinative structures. *Top. Cogn. Sci.* 1, 305–319.

Simon, B., and Pettigrew, T. (1990). Social identity and perceived group homogeneity: evidence for the ingroup homogeneity effect. *Eur. J. Soc. Psychol.* 20, 269–286.

Strogatz, S. H. (2000). From Kuramoto to Crawford: exploring the onset of synchronization in populations of coupled nonlinear oscillators. *Physica D* 143, 1–20.

Tajfel, H., and Turner, J. (2004). "The social identity theory of intergroup behavior," in *Political Psychology: Key Readings* eds J. Sidanius and J. T. Jost (New York, NY: Psychology Press), 276–293.

Tass, P., Rosenblum, M. G., Weule, J., Kurths, J., Pikovsky, A., Volkmann, J., et al. (1998). Detection of *n:m* phase locking from noisy data: application to magnetoencephalography. *Phys. Rev. Lett.* 81, 3291–3294.

Tickle-Degnen, L., and Rosenthal, R. (1990). The nature of rapport and its nonverbal correlates. *Psychol. Inq.* 1, 285–293.

Tsui, A. S., and Gutek, B. A. (1999). *Demographic Differences in Organizations: Current Research and Future Directions*. New York, NY: Lexington Books/Macmillan.

Van Dyck, E., Moelants, D., Demey, M., Coussement, P., Deweppe, A., and Leman, M. (2010). "The impact of the bass drum on body movement in spontaneous dance," in *Proceedings of the 11th International Conference on Music Perception and Cognition (ICMPC11)*, eds S. M. Demorest, S. J. Morrison, and P. S. Campbell, (Seattle, WA,), 429–434.

Wojcik, D., Nowak, A., and Kus, M. (2001). Dimension of interaction dynamics. *Phys. Rev. E* 63, 3.

Woolley, A. W., Chabris, C. F., Pentland, A., Hashmi, N., and Malone, T. (2010). Evidence for a collective intelligence factor in the performance of human groups. *Science* 330, 686–688.

Conflict of Interest Statement: The authors declare that the research was conducted in the absence of any commercial or financial relationships that could be construed as a potential conflict of interest.

Received: 28 June 2012; paper pending published: 26 July 2012; accepted: 01 October 2012; published online: 19 October 2012.

Citation: Richardson MJ, Garcia RL, Frank TD, Gergor M and Marsh KL (2012) Measuring group synchrony: a cluster-phase method for analyzing multivariate movement time-series. Front. Physio. ***3****:405. doi: 10.3389/fphys.2012.00405*

This article was submitted to Frontiers in Fractal Physiology, a specialty of Frontiers in Physiology.